University of Nottingham
UK | CHINA | MALAYSIA

Simulating neutral hydrogen across cosmic time: the 21-cm forest in late reionization models and the global 21-cm signal at cosmic dawn

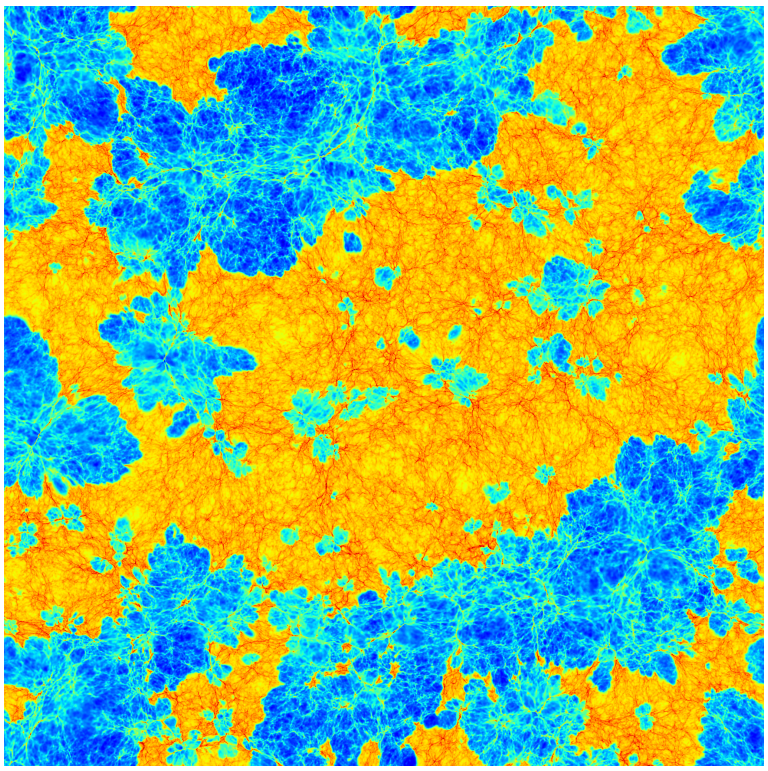

Tomáš Šoltinský

Thesis submitted to the University of Nottingham
for the degree of Doctor of Philosophy

29 October 2022

Cover: Projection of the neutral hydrogen fraction at redshift 7 in a Sherwood-Relics simulation with volume $(40h^{-1}\,\mathrm{cMpc})^3$. In this model the reionization ends late, at $z = 5.3$. The blue regions correspond to highly ionized gas while the orange regions are still neutral. Image taken from the Sherwood-Relics website. Credit: Ewald Puchwein/Leibniz-Institut für Astrophysik.

... we are still pioneers. And we've barely begun. And that our greatest accomplishments cannot be behind us, that our destiny lies above us.

– Cooper, *Interstellar* (2014)

Supervisors:	Dr James Bolton	
	Dr Nina Hatch	
Examiners:	Dr Jonathan Pritchard	(Imperial College London)
	Prof. Michael Merrifield	(University of Nottingham)
Submitted:	29.10.2022	
Examined:	30.1.2023	
Final version:	23.2.2023	

Contents

Abstract

The 21-cm line has the potential to be a powerful probe of the intergalactic medium (IGM) during the cosmic dawn era and the epoch of reionization. Various observatories such as LOFAR and SKA aim to observe this line in the near future. To aid these observational efforts, I use cosmological simulations to model the 21-cm forest during the epoch of reionization and sky-averaged 21-cm signal during cosmic dawn. I use simulations drawn from the Sherwood-Relics programme in which a novel hybrid approach of coupling hydrodynamical simulations with radiative transfer is implemented.

Recent Lyα absorption observations showing large spatial fluctuations in opacity can be explained by reionization which is completed at $z \simeq 5.3$ (i.e. later than previously thought). In this scenario, large islands of neutral hydrogen are expected to persist in the diffuse IGM until $z \simeq 6$. In this context, I predict the incidence of strong 21-cm forest absorbers ($\tau_{21} \gtrsim 10^{-2}$) and find that if the IGM is not pre-heated above $\simeq 10^2\,\mathrm{K}$, the 21-cm forest should be detectable at redshift as low as $z \simeq 6$. I consider the effect of the pressure smoothing arising from the patchiness of reionization, redshift space distortions, Lyα coupling and soft X-ray background pre-heating of the IGM on the observability of the 21-cm forest signal. While the pressure smoothing affects the 21-cm forest signal only modestly, inclusion of redshift space distortions increases the largest τ_{21} by up to a factor of ~ 10. In addition, the soft X-ray background can completely suppress the signal. However, a null detection of strong 21-cm forest absorbers at $z \simeq 6$ in the spectra of ~ 10 sufficiently radio-bright background sources with SKA1-low and possibly LOFAR can provide informative, model-dependent lower limits on the soft X-ray background at high redshift.

Furthermore, I model the effect of quasar radiation on the ionization and thermal state of the IGM. The gas in close proximity to a quasar is ionized enough such that it becomes transparent to Lyα photons. The size of this Lyα transmission window, the Lyα near-zone, has been used to inform us about the quasar optical/UV bright lifetime. The majority of measurements are consistent with lifetimes of $\sim 10^5 - 10^7\,\mathrm{yr}$; however, the smallest Lyα near-zones suggest lifetimes shorter than $\sim 10^4\,\mathrm{yr}$. Such short lifetimes pose a challenge for the growth of black holes with masses of $\sim 10^9\,\mathrm{M}_\odot$ at $z \gtrsim 6$. Models of black holes accreting in an obscured phase or quasars with a time-varying spectrum (flickering) have been proposed to alleviate this problem. However, it is challenging to discern between young quasars and old quasars driven by episodic accretion with the Lyα forest alone. Motivated by this, I model the 21-cm forest absorption in the vicinity of $z \gtrsim 6$ radio-loud quasars. The distance between a quasar and the closest 21-cm forest absorber with $\tau_{21} \gtrsim 10^{-2}$ is sensitive to the heating of the

IGM by quasar X-rays. Hence, the extent of the proximate 21-cm forest is sensitive to the integrated quasar lifetime due to the long gas cooling time. I find that a detection of a strong 21-cm forest absorber within $\sim 3\,\mathrm{pMpc}$ of a quasar would suggest a quasar lifetime of $\lesssim 10^5\,\mathrm{yr}$. On the other hand, a larger distance between the quasar and the closest strong 21-cm forest absorber in combination with a small Lyα near-zone would be consistent with a quasar that is old and flickering.

Finally, I study the effect of IGM density fluctuations on the amplitude of the cosmic dawn absorption feature in the sky-averaged 21-cm spectrum. The density distribution of the IGM is extracted from the Sherwood-Relics simulations. I find that the density fluctuations suppress the signal by $6.4 - 11.3\%$, depending on the mass resolution of the simulation. Higher mass resolution results in a larger suppression of the signal. This effect makes the discrepancy between standard theoretical models and the recent observation by EDGES even larger.

Acknowledgements

First and foremost, I am immensely grateful to my supervisors Jamie and Nina for their amazing mentoring, guidance, support and all the enlightening discussions over the past three and a bit years. I would like to thank them for their time, energy and patience, because having a student who spent $\sim 2/3$ of his PhD outside the country is probably not easy. In spite of my application getting lost, I ended up doing my PhD at the University of Nottingham thanks to them and with them, which I am happy about. I am very thankful to Jamie for introducing me to the Sherwood-Relics collaboration. This led me to securing my future job and our collaborators were a great help when we were working on our papers.

I was very lucky to have such awesome office mates. I would like to express my appreciation towards Margherita for helping me with research, answering my numerous questions and calming me down when I panicked. I am thankful to Maggie for pleasant conversations and for proof-reading this thesis. I am very happy that I could share memes about Slovak politics with Marta on many occasions. Also, I thank Emma (in the nearby office) for discussions about 21-cm line observations.

I would like to express my gratitude towards Phil, the CAPT IT king, who helped me with many issues ranging from the smooth transition to remote working to rebooting my desktop computer when I crashed it and was $\sim 2000\,\mathrm{km}$ away from it during the pandemic. I thank Ella for being so efficient and helpful when I dealt with movie nights, lunch talks and student representative responsibilities. I acknowledge the University of Nottingham for supporting my PhD and funding it via the Vice Chancellor's Scholarship for Research Excellence (EU). I am also thankful to Eva Balejčíková and Jozef Smrek for preparing me for Physics competitions before my undergraduate studies, and hence exciting my interest in the subject, Jose Oñorbe for inducing my interest in 21-cm physics and Philip Best for recommending applying for a PhD programme at the University of Nottingham.

A huge thank you to my fellow classmates/colleagues - Roan, Mick, Jacob, Liza, Leonardo, Karel, CB, Steph, Kellie, Dan, Lizzie, Matt, Swagat, Sergio, Kieran, Brad, Sukhi, Simon, Chad, Jimi, Jordan, Harry, Jen, Mikey, Joel, Finlay, Charutha, Tom, Tom, Ben, James, Sunny, Shaun, Ulli, Amelia, Shuang, Agustín, Vitor, etc. – for all the support and fun time over pints in Boat Inn, movie nights, cinemas, trip to Tenerife, lunches, when I annoyed you while I was waiting for my tea to brew... and for many of you becoming my close friends. I hope there will be room for *wraauu* in your hearts forever. I was fortunate to meet Denis and Patrik who brought a piece of Slovakia with themselves to Nottingham. I also

thank Jess for proof-reading this thesis. I am also grateful for my friends from back home - Vlado, Rast'o, Jančo, Lukáš, Tomáš, Pišta, Temný pán Tomčisko, Dodo, Alica, Daniela, Paľo, Matúš, etc. - for keeping me sane during the pandemic and throughout my PhD studies.

Speaking of home, words are not enough to express how much I am thankful for my family - Mamka, Oco, Jarka, Nikuška, Mat'o - for their love and support, for my mum's delicious cooking and for tennis games with my dad. Last but not least, I am extremely lucky that I have met Alenka. I am grateful for every second we spent together in person and online, and for her love and support which was very much needed especially in the last few months (ňus ňus).

In summary, thank you all who have contributed to my PhD experience, during and before.

List of Figures

List of Tables

Abbreviations

ΛCDM – Lambda Cold Dark Matter.
AGN – Active Galactic Nuclei.
CMB – Cosmic Microwave Background.
EDGES – Experiment to Detect the Global EoR Signature.
EoR – Epoch of Reionization.
FoF – Friends-of-Friends.
GMRT – Giant Metrewave Radio Telescope.
IGM – Intergalactic Medium.
JWST – James Webb Space Telescope.
LOFAR – Low Frequency Array.
LOS – Line of Sight.
Lyα – Lyman-alpha.
MWA – Murchison Widefield Array.
PDF – Probability Density Function.
QSO – Quasi-Stellar Object.
RT – Radiative Transfer.
SED – Spectral Energy Distribution.
SKA – Square Kilometre Array.
SPH – Smoothed Particle Hydrodynamics.
UV – Ultraviolet.

Chapter 1

Introduction

1.1 The cosmological history of Universe

Our understanding of the Universe has greatly advanced since the beginning of modern cosmology, which is usually associated with Einstein's article from 1917 (Einstein, 1917). Currently, the findings favour a flat ΛCDM model (Planck Collaboration, 2020) in which the Universe expanded (Lemaître, 1927; Hubble, 1929) from a hot and dense state and hierarchically forms structures via gravitational instability. The evolution (e.g. expansion) of the space itself is governed by the Friedmann equations (Friedmann, 1922)

$$H^2 = \left(\frac{\dot{a}}{a}\right)^2 = \frac{8\pi G}{3}\left(\rho_\mathrm{r} + \rho_\mathrm{m}\right) - \frac{kc^2}{a^2} + \frac{\Lambda c^2}{3} \tag{1.1}$$

and

$$\frac{\ddot{a}}{a} = -\frac{4\pi G}{3}\left(\rho_\mathrm{r} + \rho_\mathrm{m} + \frac{3p}{c^2}\right) + \frac{\Lambda c^2}{3}, \tag{1.2}$$

where a is the scale factor, $G = 6.67 \times 10^{-11}\,\mathrm{m^3\,kg^{-1}\,s^{-2}}$ is the gravitational constant, ρ_r and ρ_m are the radiation and mass density, respectively, p is the pressure, k is the spatial curvature of the Universe, c is the speed of light in vacuum, Λ is the cosmological constant and H is the redshift dependent Hubble parameter. The first equation can be expressed in terms of redshift, $z = 1/a - 1$, and the present day radiation, matter, "spatial curvature" and "dark energy" density parameters, Ω_r, Ω_m, Ω_k and Ω_Λ, respectively:

$$H^2(z) = H_0^2 \left(\Omega_\mathrm{r} (1+z)^4 + \Omega_\mathrm{m} (1+z)^3 + \Omega_\mathrm{k} (1+z)^2 + \Omega_\Lambda\right). \tag{1.3}$$

The Hubble constant, H_0, is the Hubble parameter at present day.

However, the ΛCDM model faces cosmological fine-tuning problems. For example, current measurements of the total density parameter $\Omega = \Omega_\mathrm{r} + \Omega_\mathrm{m} + \Omega_\Lambda$ are close to the specific value required for the Universe to be flat (Planck Collaboration, 2020). This is known as the flatness problem. Another fine-tuning problem, the horizon problem, arises from cosmic microwave background (CMB) observations in which causally disconnected regions appear to be homogeneous. Inflation, an exponential growth of spacetime, was proposed by Starobinsky (1980), Guth (1981) and Linde (1982) to solve these problems. The inflationary models naturally explain how the initial conditions were set and how they lead to primordial density perturbations which result in structures we observe today (Mukhanov & Chibisov, 1981; Hawking, 1982; Guth & Pi, 1982; Starobinsky, 1982).

After the first second of the Universe's life, the first baryons formed and the Universe was composed of a photon-baryon fluid. Minutes later, the plasma that composed the early Universe reached high enough pressure and

temperature that it formed nuclei heavier than those of hydrogen, namely deuterium (^{2}H), tritium (^{3}H), helium (^{3}He and ^{4}He), lithium (^{7}Li) and beryllium (^{7}Be). This is a process known as Big Bang nucleosynthesis, first discussed in Gamow (1946) and Alpher et al. (1948). During this period, the Universe was dominated by radiation (i.e. Ω_r dominates the Eq. (1.3)).

Approximately 47 000 years later, the Universe expanded enough for matter to dominate (matter energy density evolves as $\propto (1+z)^3$, while radiation energy density as $\propto (1+z)^4$), but matter was still coupled with radiation. Meanwhile, plasma in overdense regions was compressed due to gravity, which was counteracted by the pressure generated by the photons. These forces caused baryons to oscillate in a similar way to sound waves (Sunyaev & Zeldovich, 1970; Peebles & Yu, 1970).

Around 370 000 years after the Big Bang, the Universe expanded further such that the temperature and density of baryons decreased to the values that allow nuclei to recombine with free electrons and the first neutral atoms formed. As a consequence the Universe became transparent and the radiation decoupled from the baryons. This radiation has been dubbed the CMB, which was observed serendipitously by Penzias & Wilson (1965) for the first time. The CMB behaves as a nearly perfect black body with a temperature of $T_\mathrm{CMB} = 2.7\,\mathrm{K}(1+z)$ (Fixsen, 2009) and is rich in information about the primordial density distribution, geometry and composition of the Universe (e.g. Planck Collaboration, 2020). A map of the CMB is shown on the left side of Fig. 1.1.

After the photons decouple from the baryons, there is no radiation pressure to oppose the compression due to gravity, and an imprint of the pre-decoupling plasma oscillations is left in the baryon matter distribution.

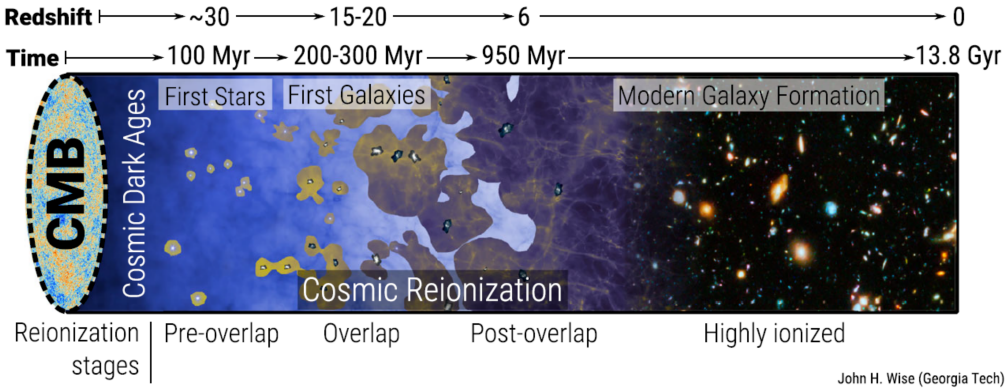

Figure 1.1: The cosmological evolution of the Universe after recombination. On the left, we show the map of the CMB, the background radiation released at cosmic recombination. Afterwards, the first luminous sources appear which create ionization bubbles (yellow colour marks highly ionized gas, dark blue colour indicates low ionization). After the Universe is reionized it enters the era of modern galaxy formation. Figure edited from Wise (2019).

This phenomenon is known as baryonic acoustic oscillations, and has been observed in the CMB temperature power spectrum (e.g. Bennett et al., 2013; Planck Collaboration, 2020), galaxy surveys (e.g. Cole et al., 2005; Eisenstein et al., 2005, see the end of this section for more details) and Lyα forest (e.g. Busca et al., 2013; Delubac et al., 2015).

After recombination, the baryons are able to collapse further under gravity which they were prevented from before by radiation pressure. The dominant gravitational component is dark matter. If the dark matter becomes non-relativistic early and dominates the matter content of the Universe, it sets the matter power spectrum and leads to the formation of structures as we know today (Peebles, 1984; Davis et al., 1985). The ΛCDM model assumes that the dark matter is cold, meaning it consists of particles with mass of $\sim 1\,\mathrm{GeV}$. An alternative is warm dark matter with particle masses of $\approx 1\,\mathrm{keV}$ (Dodelson & Widrow, 1994). Such dark matter would stay relativistic for a longer time and hence free-stream over larger scales resulting

in reduced power at small scales (Colombi et al., 1996; Viel et al., 2005).

The rest of Fig. 1.1 illustrates the cosmic timeline after the cosmic recombination. During the cosmic dark ages (before the first luminous sources were formed), the baryon kinetic temperature, $T_{\rm K}$, was coupled to the CMB temperature via Compton scattering until $z_{\rm dec} = 147.8$ (Furlanetto et al., 2006). Afterwards, the Universe adiabatically cooled (i.e. $T_{\rm K} \propto (1+z)^2$) due to its expansion. Meanwhile, the growth of structure is non-linear and numerical approaches are required to model it. An important advance in large scale structure studies has been achieved by an N-body simulation of 2160^3 collisionless dark matter particles within a volume of $500h^{-1}\,$cMpc - The Millennium simulation (Springel et al., 2005). Since 2005, dark matter only N-body simulations have advanced considerably (Angulo & Hahn, 2022) to the level where they can track trillions of dark matter particles in a few $h^{-1}\,$Gpc boxes. Such simulations include the Cosmo-π simulation (Cheng et al., 2020), the Euclid Flagship simulation (Potter et al., 2017) and the Uchuu simulation (Ishiyama et al., 2021). An example of a density field slice from the Uchuu simulation is shown in the left panel of Fig. 1.2 (but note that this is at $z = 0$). One can clearly see the filamentary structure of the cosmic web.

Given that the matter budget is dominated by the dark matter, baryons trace this structure. However, this happens only to a degree because the baryons, as opposed to the dark matter, interact hydrodynamically as well. If a spherical gas cloud of mass $M_{\rm gc}$ and radius $R_{\rm gc}$ has a uniform mass density $\rho_{\rm gc} = 4\pi M_{\rm gc}/3R_{\rm gc}^3$ and temperature $T_{\rm gc}$, then it will collapse on a free-fall timescale $t_{\rm ff} \sim (\pi/G\rho_{\rm gc})^{1/2}$. To restore the hydrostatic equilibrium and prevent the collapse, the required change in pressure must reach the

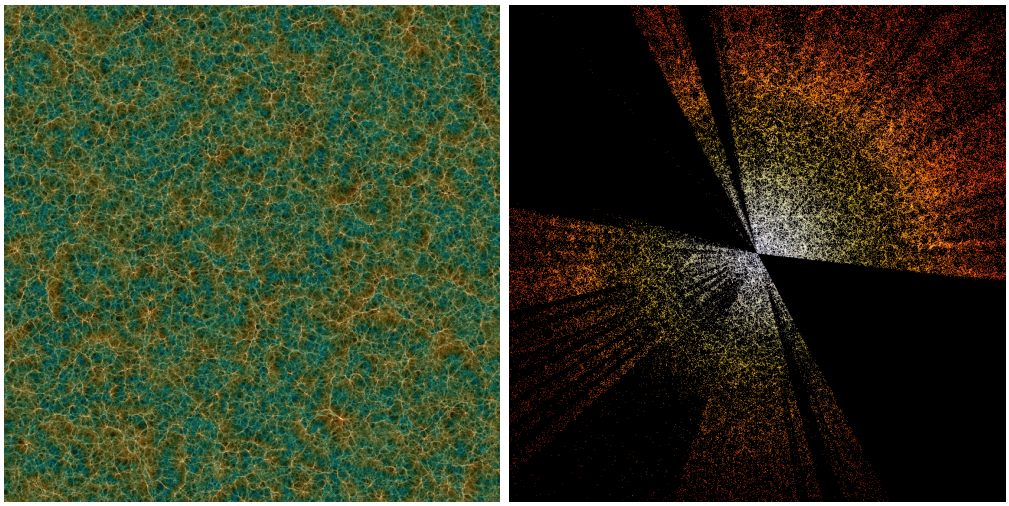

Figure 1.2: *Left panel:* 2D slice of density field from the Uchuu simulation at $z = 0$. The slice has a width of $2h^{-1}$ cGpc and a thickness of $25h^{-1}$ cMpc. Figure from the Uchuu simulation website[1]. *Right panel:* Galaxy distribution mapped by DESI. Plotted are 400 000 galaxies, with the furthest at ≈ 3 Gpc distance. Credit: D. Schlegel/Berkeley Lab using data from DESI, M. Zamani/NSF's NOIRLab[2].

centre of the gas cloud before $t_{\rm ff}$. This pressure change propagates as sound waves with speed

$$c_{\rm s} = \left(\frac{5k_{\rm B}T_{\rm gc}}{3\mu m_{\rm H}}\right)^{1/2}, \tag{1.4}$$

where μ is the molecular weight (e.g. $\mu = 1.158$ for a fully ionized hydrogen and helium with $Y_{\rm p} = 0.24$) and $m_{\rm H}$ is the hydrogen atom mass. This leads to a condition for which the gas cloud is stable, defined as the Jeans length (Gnedin & Hui, 1998; Garzilli et al., 2015)

$$\begin{aligned}\lambda_{\rm J} &= c_{\rm s}t_{\rm ff}, \\ &\simeq 9.8h^{-1}\,{\rm ckpc}\left[\left(\frac{10}{1+\delta}\right)\left(\frac{1.22}{\mu}\right)\left(\frac{T_{\rm gc}}{10^2\,{\rm K}}\right)\left(\frac{10}{1+z}\right)\right]^{1/2}.\end{aligned} \tag{1.5}$$

If the gas cloud has size larger than $\lambda_{\rm J}$, the gravitational force will overcome the pressure and it will collapse. Within such high density pockets of

[1] http://skiesanduniverses.org/Simulations/Uchuu/
[2] https://noirlab.edu/public/images/noirlab2203a/

hydrogen, the first stars are born and the dark ages end with their advent (Silk, 1983; Bromm et al., 1999; Abel et al., 2002). The period during which the first generation of stars and galaxies form is known as the cosmic dawn. I discuss this cosmological era in more detail in Section 1.2 and Chapter 5.

The radiation emitted from the first galaxies drives the last phase transition of the Universe, the epoch of reionization (EoR), during which the cold and neutral Universe turns hot and ionized (e.g. Wise, 2019). While the baryonic matter followed mainly the dark matter structures during the dark ages, the behaviour of the baryons becomes more complex during the EoR as it hydrodynamically reacts to the heating and ionization caused by the radiation from the galaxies. Not only does the baryonic matter become important during the EoR, at small scales it becomes even dominant (Zaroubi, 2012). Understanding how the intergalactic medium (IGM) is affected by these processes is crucial for later galaxy formation and evolution. The EoR is the main focus of this thesis. An overview of both observational and theoretical studies of this epoch is presented in Section 1.3 and in Chapters 3 and 4.

Approximately 1 Gyr years after the Big Bang, the Universe is completely reionized and filled with galaxies which evolve to spirals and ellipticals that become the dominant galaxy populations at $z \lesssim 2.5$ (Mortlock et al., 2013; Conselice, 2014; Whitney et al., 2021). These galaxies form popII and popI stars (i.e. metal-poor and metal-rich stars, respectively) from pre-processed gas enriched by metals. The cosmic star formation rate density is at its peak at around 3.5 Gyr after the Big Bang (Madau & Dickinson, 2014).

One of the last known cosmological milestones takes place 9.8 Gyr after

the Big Bang when dark energy starts to dominate the Universe (i.e. the Ω_Λ term in Eq. (1.3)). Dark energy has been proposed to be the engine behind the accelerated expansion of the Universe which was inferred from observations of type Ia supernovae (Riess et al., 1998; Perlmutter et al., 1999). There are surveys aiming to measure the effect of dark energy by mapping the distribution of galaxies. For instance, the Dark Energy Spectroscopic Instrument (DESI) aims to measure the spectra of 4×10^7 galaxies and quasars (Abareshi et al., 2022). A version of the preliminary DESI map with 400 000 galaxies is shown in the right panel of Figure 1.2, which shows similar structure to the cosmic web from the Uchuu simulation (the left panel). Furthermore, earlier galaxy surveys such as the 2dF Galaxy Redshift Survey (2dFGRS, Cole et al., 2005), the 6dF Galaxy Survey (6dFGS, Beutler et al., 2011), the Baryon Oscillation Spectroscopic Survey (BOSS, Anderson et al., 2012; Chen et al., 2022c), the Sloan Digital Sky Survey (SDSS, Eisenstein et al., 2005; Zhao et al., 2022) and the WiggleZ Dark Energy Survey (Blake et al., 2011) detect baryon acoustic oscillations in two-point correlation functions and power spectra.

1.1.1 Challenges for ΛCDM model

In summary, ΛCDM is a very successful model in explaining the CMB and its structure, the abundance of hydrogen and helium isotopes, the accelerated expansion of the Universe and the distribution of galaxies on large scales. However, there are also some challenges. For example, the abundance of ^{7}Li predicted by the Big Bang nucleosynthesis models is overestimated by a factor of $3 - 4$ compared to observations (Fields, 2011; Hou et al., 2017). This is known as the cosmological lithium problem.

Figure 1.3: The mass distribution from weak lensing in blue overlayed with the map of hot gas from the X-ray observations in pink in the colliding galaxy cluster. The offset of these two components shows that the baryons lag behind the bulk of the matter which suggests that most of the matter is collisionless dark matter. *Left:* Bullet cluster. Credit: X-ray: NASA/CXC/CFA/ Markevitch et al. (2004); Optical/Lensing: NASA/STScI; ESO WFI; MAGELLAN/U. Arizona/Clowe et al. (2006). *Right:* MACS J0025.4-1222 cluster. Credit: X-ray: NASA/CXC/Stanford/Allen et al. (2008); Optical/Lensing: NASA/STScI/UC Santa Barbara/Bradač et al. (2008).

In addition, one of the main building blocks of the ΛCDM, dark matter, has never been observed directly. More than 80 years ago, stellar orbits and galaxy dynamics in clusters suggested that both galaxies and clusters contain matter which interacts via gravity but not electromagnetically - dark matter (e.g. Kapteyn, 1922; Zwicky, 1933). Since then many phenomena have been explained with the aid of dark matter including the rotation curves in galaxies (e.g. Rubin et al., 1962; Rubin & Ford, 1970; Freeman, 1970; Corbelli & Salucci, 2000), the difference between optical observations of the stellar mass in galaxy clusters and their total mass measurements from X-ray observations, gravitational lensing dark matter maps of substructures inside galaxy clusters (e.g. Natarajan et al., 2017) and large scale structure (e.g. Hong et al., 2021; Jeffrey et al., 2021). The arguably most convincing evidence of dark matter are the observations of galaxy clusters, namely the Bullet Cluster (Clowe et al., 2006) and MACS J0025.4-1222 (Bradač et al., 2008) shown in Fig. 1.3. These maps show that hot gas

detected by X-ray observations (pink colour, Markevitch et al., 2004; Allen et al., 2008) lags behind the bulk of the matter detected by weak lensing (blue colour, Clowe et al., 2006; Bradač et al., 2008). This suggests that most of the matter in these clusters does not interact electromagnetically and is collisionless, i.e. is dark matter.

However, all of the above are indirect detections of dark matter and the nature of dark matter is still a question of active research. Dark matter candidates range from objects consisting of baryons such as primordial black holes (Espinosa et al., 2018; Clesse & García-Bellido, 2018) and massive astrophysical compact halo objects (Paczynski, 1986; Griest, 1993) to non-baryonic particles such as weakly interacting massive particles (Griest, 1993; Jungman et al., 1996) and neutrinos (Boyarsky et al., 2019).

Furthermore, there is a discrepancy between the measurements of a key cosmological parameter - H_0 (see Eq. (1.3)). There has been a myriad of measurements of H_0 (see Di Valentino et al., 2021, for review, especially their figure 1). These are usually divided into two groups. The early Universe measurements of $H_0 \approx 67 - 68\,\mathrm{km\,s^{-1}\,Mpc^{-1}}$ involve the observations of CMB and baryon acoustic oscillations (e.g. Grieb et al., 2017; Planck Collaboration, 2020). The late Universe measurements are based on observations of standard candles such as Cepheids and supernovae Ia and result usually in $H_0 \approx 73 - 74\,\mathrm{km\,s^{-1}\,Mpc^{-1}}$ (e.g. Riess et al., 2022; Brout et al., 2022). With improved data these measurements became more precise over time and the difference between the early and late Universe H_0 measurements now reaches a significance of $4 - 6\sigma$. This is known as the Hubble tension. Recently, new approaches of measuring H_0 such as observations of gravitational waves (Mukherjee et al., 2020) and lensing systems (Denzel

et al., 2021) were developed. However, these measurements have large uncertainties at the moment and hence agree with both the early and late H_0 measurements. If the source of this discrepancy is not systematic, physics beyond the ΛCDM model is needed. Examples of such new physics include various models of dark energy (e.g. Kumar & Nunes, 2016; Di Valentino et al., 2017; Poulin et al., 2019; Banihashemi et al., 2020) and modifications to gravity (e.g. Nunes, 2018; Lin et al., 2019).

Similarly, the S_8 tension, which is an inconsistency between the early and late Universe measurements of $S_8 = \sigma_8\sqrt{\Omega_\mathrm{m}/0.3}$, has arisen in recent years. Here, σ_8 is defined as the amplitude of the matter power spectrum on the scale of $8h^{-1}\,\mathrm{Mpc}$. Similarly to the case of H_0, the early Universe measurements are taken from the CMB observations. These have been constrained to $S_8 = 0.830 \pm 0.013$ by the Planck Collaboration (2020). The weak lensing and galaxy clustering studies are used as the late Universe measurements of S_8. Recently, joint analysis of these have been performed resulting in $S_8 \approx 0.77$ and a $2{-}3\sigma$ discrepancy with the CMB measurements (Heymans et al., 2021; Abbott et al., 2022). Consistent with these results, the mean value of S_8 inferred from galaxy cluster counts measurements is 0.789 ± 0.12 Pratt et al. (2019). For a comprehensive summary of S_8 measurements, see figure 4 in Abdalla et al. (2022). While this issue is not as severe as the Hubble tension, it poses another challenge for the ΛCDM model. However, solving one of these tensions usually makes the other one worse, and hence one needs to tackle both at the same time (Abdalla et al., 2022). For instance, Bhattacharyya et al. (2019) and Kumar (2021) argue that models of dark energy interacting with dark matter can alleviate both problems.

1.2 Cosmic Dawn

The first stars, dubbed population III (popIII) stars, are formed from pristine gas as there was no mechanism present to form large amounts of metals. Therefore, popIII stars should have a metal-free composition. The main coolant is molecular hydrogen, which can decrease the cloud temperature to $\sim 200\,\mathrm{K}$ resulting in gas fragments which can collapse and form stars (Silk, 1983; Abel et al., 2002; Clark et al., 2011). Numerical modelling of such systems (e.g. Bromm et al., 1999; Abel et al., 2002; Clark et al., 2011; Bovino et al., 2014; Dutta et al., 2015) shows that the masses of popIII stars are high, $10 - 1000\,\mathrm{M}_\odot$ (Hosokawa et al., 2011; Hirano et al., 2014). Hence, popIII stars are expected to be short lived (but see Dutta et al., 2020) and hard to detect.

On the other hand, the highest redshift at which galaxies are observed has been pushed to cosmic dawn times. While the most distant spectroscopically confirmed galaxy the Hubble Space Telescope detected is GN-z11 at $z = 11.09$ (Oesch et al., 2016), the first observations from the James Webb Space Telescope (JWST) have already provided galaxy candidates at redshifts up to $z \approx 15.4$ (Adams et al., 2022). However, reported masses of the galaxy candidates (Labbé et al., 2022) are in tension with the limits on the stellar mass density and number density of these galaxies expected from the ΛCDM cosmology (Boylan-Kolchin, 2022). Nevertheless, these are still early days of the JWST observations and these results are yet to be confirmed.

The evolution of the popIII stars and the first galaxies and how they affect their surroundings has been studied with numerical simulations (e.g.

Wise et al., 2014). For example, the first generation stars enrich the gas with metals and hence build up nurseries for the next generation of stars (Bromm & Loeb, 2003; Chiaki et al., 2018; Jaacks et al., 2018). On larger scales, the radiation from these sources ionizes and heats up the gas during the process known as reionization (Wyithe & Loeb, 2003; Sokasian et al., 2004). I discuss the details of the reionization epoch below.

1.3 The epoch of reionization

In this section, I will present the evidence that shows how the Universe evolved from neutral to ionized over $\approx 1\,\mathrm{Gyr}$ of its life due to the sources which formed at cosmic dawn and later. I will describe the current probes of the EoR, namely the Lyα forest in Section 1.3.1 and CMB in Section 1.3.3. I will also outline the present day understanding of reionization, in particular what is known about its morphology, timing and sources of ionizing photons in Section 1.3.2 to 1.3.4, respectively. Section 1.3.5 is devoted to the numerical modelling of reionization.

1.3.1 Lyα forest signal

As the light from a distant quasar travels through the Universe and redshifts to a wavelength of $\lambda_\alpha = 1215.67\,\text{Å}$, it is absorbed due to the transition between the $n = 1$ and $n = 2$ state of the neutral hydrogen, leaving absorption features in the quasar spectrum. This is known as the Lyα forest signal.

As an example I show the spectrum of the $z = 5.98$ quasar ULAS

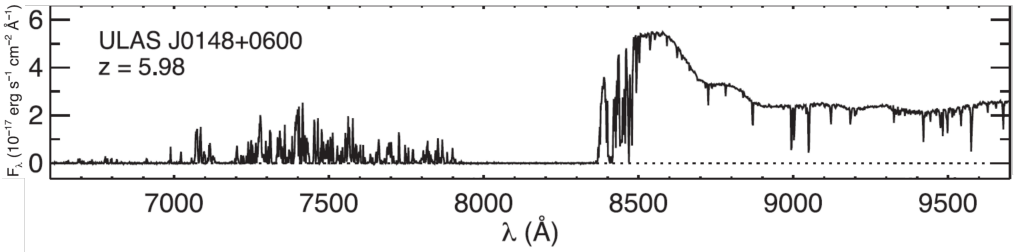

Figure 1.4: Lyα forest in the spectrum of ULAS J0148+0600, a quasar at $z = 5.98$. Note the long absorption trough at $7900\,\text{Å} \lesssim \lambda \lesssim 8350\,\text{Å}$ and Lyα transmission spikes at bluer wavelengths. Figure edited from Becker et al. (2015b)

J0148+0600 in Fig. 1.4 which exhibits a very long absorption trough blueward of the quasar Lyα restframe emission known as the Gunn-Peterson trough (Becker et al., 2015b). At lower wavelengths one can observe Lyα transmission spikes (Becker et al., 2015b). The Gunn-Peterson optical depth is

$$\tau_{\text{GP}} = \frac{\sigma_\alpha c}{H(z)} n_{\text{HI}}(z) \approx 3.9 \times 10^5 x_{\text{HI}} \left(\frac{1+z}{7}\right)^{3/2}, \tag{1.6}$$

where σ_α is the Lyα cross-section and n_{HI} is the neutral hydrogen number density. This shows that the optical depth at a given redshift is directly proportional to the amount of neutral hydrogen. It has been found that τ_{GP} increases faster with redshift than could be accounted by redshift evolution of the density of the Universe. This implies decreasing x_{HI} over time (Fan et al., 2006) and hence suggests that reionization has happened.

The first use of the Lyα forest signal to put constraints on the amount of neutral hydrogen in the IGM was done by Gunn & Peterson (1965) using a $z = 2.01$ quasar (Schmidt, 1965). The Lyα forest spectra from the EoR was observed decades later (Djorgovski et al., 2001). In addition to the measurements of the ionization state of the IGM during the EoR (e.g. Fan et al., 2006; McGreer et al., 2015; Davies et al., 2018; Greig et al.,

2022), the Lyα forest has been used for other EoR measurements including the thermal state of the IGM (e.g. Bolton et al., 2012; Boera et al., 2019; Walther et al., 2019; Gaikwad et al., 2020), UV background radiation (e.g Calverley et al., 2011; Becker & Bolton, 2013; D'Aloisio et al., 2018) and the timing of the reionization. I discuss the latter in Section 1.3.3.

However, given the large σ_α, the IGM becomes opaque to Lyα photons if $x_{\rm HI} \gtrsim 10^{-4}$. Hence, a quasar's spectrum will be completely suppressed and exhibit a Gunn-Peterson trough at $z \gtrsim 6$ when the IGM was just slightly neutral. The exception are regions surrounding quasars that are photo-ionized by the quasar UV radiation to levels that allow the Lyα photons to be transmitted. These regions are known as quasar near-zones (or proximity zones) and have been used to explore host quasar properties such as their lifetimes (e.g Eilers et al., 2017, 2021; Davies et al., 2020). Furthermore, the quasar near-zones in the Lyα forest were proposed to be used as probes of their surroundings, particularly the density fields (Chen & Gnedin, 2021b,a) and temperature profiles (Chen et al., 2022a) with the former already measured by Chen et al. (2022b). I further discuss the use of quasar near-zones in Chapter 4.

1.3.2 Morphology

In the ΛCDM model the galaxies which reionize the Universe form in overdense regions and hence cluster together. Therefore, the morphology of the reionization is expected to be patchy rather than homogeneous. The large scatter in the Lyα forest transmission supports this picture (e.g. Lidz et al., 2006; Becker et al., 2015b; Bosman et al., 2018; Eilers et al., 2018).

In the patchy reionization models the sources generate photons with energies of 13.6 eV or higher (i.e. UV photons). This radiation creates highly ionized H II bubbles. The IGM in these regions reaches photo-ionization equilibrium with the UV background radiation given by

$$n_{\rm e} n_{\rm p} \alpha \left(T_{\rm K}\right) = n_{\rm HI} \Gamma_{\rm HI}, \tag{1.7}$$

where $n_{\rm e}$, $n_{\rm p}$ and $n_{\rm HI}$ are the number densities of electrons, protons and neutral hydrogen atoms, respectively, $\alpha\left(T_{\rm K}\right)$ is the recombination coefficient dependent on the gas kinetic temperature, $T_{\rm K}$, and $\Gamma_{\rm HI}$ is the photo-ionization rate. The recombination coefficient has been fitted by Verner & Ferland (1996) with

$$\begin{aligned} \alpha\left(T_{\rm K}\right) &= a \left(\sqrt{\frac{T_{\rm K}}{T_0}} \left(1 + \sqrt{\frac{T_{\rm K}}{T_0}}\right)^{1-b} \left(1 + \sqrt{\frac{T_{\rm K}}{T_1}}\right)^{1+b} \right)^{-1} \\ &\approx 4.1 \times 10^{-13} \left(\frac{T_{\rm K}}{10^4\,{\rm K}}\right)^{-0.72} {\rm cm}^3\,{\rm s}^{-1}, \end{aligned} \tag{1.8}$$

where $a = 7.982 \times 10^{-11}\,{\rm cm}^3\,{\rm s}^{-1}$, $b = 0.748$, $T_0 = 3.148\,{\rm K}$ and $T_1 = 7.036 \times 10^5\,{\rm K}$ for H I. The H II bubbles grow and overlap creating a "swiss-cheese" structure of ionized and neutral hydrogen. Over time, the ionized regions disconnect the neutral regions leading to islands of neutral hydrogen until the whole Universe is ionized (e.g. Barkana & Loeb, 2001; Lee et al., 2008; Chen et al., 2019). An example of patchy reionization is depicted in Fig. 1.5 which shows the results of a numerical simulation of the evolution of the neutral hydrogen fraction, $x_{\rm HI}$, between $z = 5$ and 8. One can clearly see this reonization process outlined above with ionization bubbles in blue and neutral gas in brown.

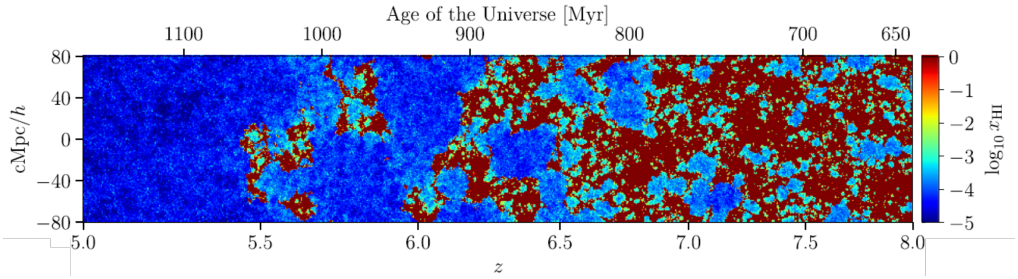

Figure 1.5: Evolution of the neutral hydrogen fraction during the epoch of reionization. The brown colour corresponds to neutral hydrogen and the blue colour to highly ionized gas. Figure edited from Kulkarni et al. (2019).

Studies of the H II bubbles have advanced from the first theoretical modelling dating back to Arons & McCray (1970) and Arons & Wingert (1972), in which the authors stated that the techniques at the time cannot detect these objects, to the present day research which suggests the presence of the ionization bubbles at $z = 7.7$ from the Lyα spectra of distant galaxies (Tilvi et al., 2020). However, many details are still under debate. For example, Lin et al. (2016) show that, depending on the algorithm, numerical simulations predict 2-10 times larger effective radii of the H II bubbles than analytical predictions do (Furlanetto et al., 2004a).

Various techniques have been designed to measure the H II bubble size distribution from ionization fields. For instance, in the Mean Free Path (MFP) method one selects a random ionized region, casts a ray in a random direction and tracks it until stopping criteria are met (Mesinger & Furlanetto, 2007). The spherical average (SPA) technique finds the largest sphere around each H II location in which the average ionization fraction exceeds some threshold (Zahn et al., 2007). Another method is to connect constant values of the ionization field and treat these as contours. This is known as the watershed algorithm (Lin et al., 2016). Otherwise, one can use a Friends-of-Friends (FoF) algorithm to map the ionization bub-

bles (Iliev et al., 2006). While the SPA method is strongly biased, the MFP and watershed algorithm are unbiased (e.g. Friedrich et al., 2011; Lin et al., 2016; Giri et al., 2018). The FoF method is not directly comparable to the others because instead of measuring the radii of the H II bubbles, it measures the volume of topologically connected ionized regions. I will discuss what future observations might contain information about the ionization bubbles and their sizes in Section 1.4.2.

1.3.3 Timing

Another uncertain aspect of reionization is its timing. I have discussed in Section 1.2 that the hunt for the first stars and galaxies (and hence the beginning of the reionization) is still ongoing. However, one can use CMB and Lyman series photons to constrain the timing of reionization.

As the CMB photons travel to Earth from recombination they may interact with free electrons via Thomson scattering (a low energy limit of Compton scattering). The integrated effect of this mechanism is quantified with the Thomson scattering optical depth, which is inferred from the CMB power spectrum to fit observed data. The Thomson scattering optical depth is given by

$$\tau_{\rm e} = \int_0^{z_{\rm dec}} \frac{\sigma_{\rm T} n_{\rm e} c}{(1+z) H_0 \sqrt{\Omega_{\rm m}(1+z)^3 + \Omega_\Lambda}} dz, \tag{1.9}$$

where $\sigma_{\rm T} = 6.65 \times 10^{-25}\,{\rm cm}^2$ is the Thomson scattering cross-section. From this, one can infer the timing of reionization. However, given that different assumptions for $n_{\rm e}$ in Eq. (1.9) can result in the same $\tau_{\rm e}$, the implied constraints on the reionization timing are highly model-dependent. For example, Pagano et al. (2020) assume a tanh function for $n_{\rm e}$ and suggest

that the Universe was half ionized at $z = 8.14 \pm 0.60$.

In addition to the onset of the EoR, the time at which reionization is completed is not fully constrained either. Recently, large spatial fluctuations in the Lyα forest opacity at $z > 5$ (Becker et al., 2015b; Eilers et al., 2018; Bosman et al., 2022) have motivated models for a late end to reionization. In such models, reionization is ongoing until as late as $z \approx 5.3$ (Kulkarni et al., 2019; Nasir & D'Aloisio, 2020; Qin et al., 2021). A late end to reionization is also consistent with the observed deficit of Lyα emitting galaxies around extended Lyα absorption troughs (Kashino et al., 2020; Keating et al., 2020; Christenson et al., 2021), the clustering of Lyα emitters (Weinberger et al., 2019), the thermal widths of Lyα forest transmission spikes at $z > 5$ (Gaikwad et al., 2020), long dark gaps in the Lyβ forest (Zhu et al., 2022), and the mean free path of ionizing photons at $z = 6$ (Becker et al., 2021). This picture is also consistent with the above measurement of $\tau_{\rm e}$.

1.3.4 Sources

Naturally, both the morphology and timing of the reionization is dictated by the sources of ionizing radiation. However, their nature is still a matter of active research. The sources that have been investigated include star-forming galaxies, active galactic nuclei (AGN), X-ray binaries and the diffuse interstellar medium (e.g. Eide et al., 2018, 2020). However, X-ray binaries are expected to play a more important role in the heating of the IGM rather than ionizing it (Fialkov et al., 2014). Currently, the observational evidence such as the Thomson scattering optical depth (see Section 1.3.3

for more details on this observable), galaxy UV luminosity function and star formation rate of individual galaxies suggest that hydrogen reionization is driven by star-forming galaxies (e.g. Robertson et al., 2015; Bouwens et al., 2015; Matsuoka et al., 2018; Endsley et al., 2021, 2022). The AGN contribution to the hydrogen reionization is subdominant (e.g. Volonteri & Gnedin, 2009; Grissom et al., 2014; Parsa et al., 2018; Wang et al., 2019; Zeltyn & Trakhtenbrot, 2022; Jiang et al., 2022) but important to model because they are the only sources producing photons which can reionize He II by $z \sim 3$ (e.g. Furlanetto & Oh, 2008; Eide et al., 2020; Trebitsch et al., 2021). Quasars might also drive the large-scale opacity fluctuations in the Lyα forest signal (Chardin et al., 2017). This picture of the relative contributions to reionization has been reproduced by numerical simulations too (e.g. Finkelstein et al., 2019; Lewis et al., 2020; Eide et al., 2020; Trebitsch et al., 2021, 2022). However, see Madau & Haardt (2015) for an AGN-dominated reionization model.

AGN's extreme luminosity is driven by matter infalling into their central supermassive black hole (SMBH) through the accretion disk surrounding the black hole. Hence, the AGN luminosity is

$$L = \epsilon \dot{M} c^2, \tag{1.10}$$

where ϵ is the radiative efficiency of the accretion process and $\dot{M}$ is the accretion rate. There is a limit to the AGN luminosity beyond which the pressure from the radiation produced by the central SMBH exerted on the infalling mass would overcome the gravitational pull applied on this mass. If the AGN was emitting at a luminosity higher than this limit, accretion

will halt. This limit is known as the Eddington luminosity and is given by

$$L_{\mathrm{E}} = \frac{4\pi c G m \mu M_{\mathrm{BH}}}{\sigma_{\mathrm{T}}}, \tag{1.11}$$

where M_{BH} is the mass of the central black hole. The accretion of mass on the SMBH is given by the differential equation

$$\frac{\mathrm{d}M_{\mathrm{BH}}}{\mathrm{d}t} = (1-\eta)\,\dot{M}, \tag{1.12}$$

where η is the accretion efficiency. Setting $L = L_{\mathrm{E}}$ and combining Eq. (1.10) with Eq. (1.12) results in exponential SMBH growth

$$M_{\mathrm{BH}} = M_{\mathrm{seed}} \exp\left(\frac{t_{\mathrm{Q}}}{t_{\mathrm{S}}}\right). \tag{1.13}$$

Here the SMBH grows from a seed of mass M_{seed} with an e-folding time of

$$t_{\mathrm{S}} = \frac{\epsilon}{1-\eta}\frac{c\sigma_{\mathrm{T}}}{4\pi G \mu m_{\mathrm{p}}} = 4.33\times10^{7}\,\mathrm{yr}\left(\frac{L}{L_{\mathrm{E}}}\right)^{-1}\left(\frac{\epsilon}{0.1}\right)\left(\frac{1-\eta}{0.9}\right)^{-1}. \tag{1.14}$$

There have been more than 400 quasars detected at $z > 5.7$ when the Universe was only $\approx 1\,\mathrm{Gyr}$ old (Bosman, 2022). Some extreme examples are ULAS J1342+0928 at $z = 7.54$ with $M_{\mathrm{BH}} = 7.8\times10^{8}\,\mathrm{M}_{\odot}$ (Bañados et al., 2018b), and SDSS J0100+2802 at $z = 6.3$ with $M_{\mathrm{BH}} = 1.2\times10^{10}\,\mathrm{M}_{\odot}$ (Wu et al., 2015). If we assume the black hole seeds of the most massive popIII stars from Hirano et al. (2014) (i.e. $M_{\mathrm{seed}} = 1000\,\mathrm{M}_{\odot}$) accreting with radiative and accretion efficiency of $\epsilon = \eta = 0.1$, it would take $\approx 0.6 - 0.7\,\mathrm{Gyr}$ to grow a SMBH similar to the two mentioned above. This is comparable with the age of the Universe at these redshifts and requires a duty cycle, the fraction of the time the AGN is active, of $f_{\mathrm{duty}} = 1$.

Obviously, meeting such conditions is difficult, which was pointed out by Turner (1991) with a quasar sample at even lower redshifts. A shorter accretion timescale would be required if the seeds were $\sim 10^5\,\mathrm{M}_\odot$. Such seeds can be formed from supermassive stars (e.g. Hosokawa et al., 2013) or in gas clouds in which the H_2 molecules are photo-dissociated and hence cannot cool the gas (e.g. Bromm & Loeb, 2003; Omukai et al., 2008). The latter mechanism can be provided by the bombardment of the collapsing gas cloud by Lyman-Werner photons of $11.2-13.6\,\mathrm{eV}$ generated by a nearby star-burst halo which can destroy molecular hydrogen (Dijkstra et al., 2008; Regan et al., 2017). Another solution to this problem are thin accretion disks which would provide radiatively inefficient, super-Eddington growth (e.g. Madau et al., 2014; Volonteri et al., 2015; Pezzulli et al., 2016; Davies et al., 2019). Further discussion on this matter is presented in Chapter 4.

A crucial quantity for the study of reionization sources is the escape fraction of the ionizing photons, f_{esc}. This is the fraction of ionizing photons that are released to the IGM from all ionizing photons produced by the sources. This is still uncertain, but various studies find $f_{\mathrm{esc}} < 0.15$ at $z \sim 3-3.5$ (e.g Grazian et al., 2017; Naidu et al., 2018; Steidel et al., 2018). In addition, Begley et al. (2022) find that young, low metallicity, dust-free galaxies at $z > 6$ are capable of having $f_{\mathrm{esc}} \geq 0.1$, which is required to reionize the Universe (Finkelstein et al., 2019). However, this is complicated by recent measurement of short mean free path of ionizing photons (Becker et al., 2021) which means that the required ionizing photons budget for the reionization is larger than previously thought (Davies et al., 2021).

1.3.5 Simulations

Numerical simulations are required to capture all the complexity of reionization, such as its patchiness. However, to include the effect of radiation on the IGM, one needs to implement radiative transfer (RT). Unfortunately, adding more elements that the simulation must track (i.e. photons) increases the computational cost of the simulation. There has been a lot of effort to optimize RT. For example, one can apply a reduced speed of light while still capturing the propagation of ionization fronts (Gnedin & Abel, 2001; Gnedin, 2016). One way to model reionization in a relatively cheap way is using semi-numerical methods. For example, DRAGONS (Poole et al., 2016) and ASTRAEUS (Hutter et al., 2021) are simulations which apply semi-analytic modelling of galaxy formation and evolution to N-body simulations of collisionless dark matter. While this method allows one to explore a large parameter space due to its low computational cost, physical mechanisms have to be approximated.

The opposite approach is to fully couple RT to hydrodynamical simulations. This results in more realistic modelling but is significantly more expensive. This is further complicated by the dynamic range requirements. To sample cosmic variance one needs to simulate boxes of $\gtrsim 200h^{-1}$ cMpc on a side (Iliev et al., 2014). On the other hand, small scales of $\lesssim 20h^{-1}$ ckpc must be resolved to model the Lyα forest properly (Lukić et al., 2015). However, the dynamic range is still too large and subgrid models (e.g. for star formation and AGN feedback) are necessary. Unfortunately, running simulations with large enough volumes and high enough resolution is infeasible with current computational resources. Therefore, there are various projects focusing on large simulated volumes including CROC (Gnedin,

2014), THESAN (Kannan et al., 2022) and CoDaIII (Lewis et al., 2022) which itself is built on its predecessors CoDaII (Ocvirk et al., 2020) and CoDa (Ocvirk et al., 2016). On the other hand, SPHINX (Rosdahl et al., 2018) simulations have ~ 10 times smaller volume but resolve galaxies better. An intermediate step (both in volume and resolution) was achieved by OBELISK simulation performed by Trebitsch et al. (2021).

Recently, a hybrid approach of coupling RT to hydrodynamical simulations has emerged. Such modelling is less expensive than fully coupled simulations but still self-consistently follows the hydrodynamical response of the gas to the reionization. Two examples are the Nyx (Almgren et al., 2013; Oñorbe et al., 2019) and Sherwood-Relics (Puchwein et al., 2022) simulation suites. The modelling in my thesis is based on the latter. See Section 2.1 for details.

For more information on the reionization simulations see Gnedin & Madau (2022). Despite these advances in the modelling of patchy reionization, the details of its morphology, such as the size distribution of the ionized regions or the clustering of the sources driving them, is still not well known. Given the limited utility of the Lyα forest signal at earlier stages of reionization, different methods for exploring the above are desired. Another signal with a high potential for exploring the EoR is the 21-cm signal, which is the main focus of this thesis that I discuss in the next section. For more detailed reviews of the EoR see Barkana & Loeb (2001), Zaroubi (2012) and Wise (2019).

1.4 21-cm signal

In 1930s, observers detected a radio signal with an unknown origin (Jansky, 1932, 1933, 1935, 1937; Whipple & Greenstein, 1937; Reber, 1940). It was thought that the source of this signal was from the centre of our galaxy. Inspired by Oort, the physicist van de Hulst made a theoretical prediction that this signal originates from the hyperfine structure of the neutral hydrogen (van de Hulst, 1945, 1998). The ground state energy level of an H I atom is split into a singlet and triplet state which is determined by the relative orientation of the proton and electron spin. The energy difference between these two hyperfine levels is $E_{10} = 5.874\,\mu\text{eV}$. This means that a transition between these two states can be induced by a photon with rest-frame wavelength $\lambda_{21} = 21.11\,\text{cm}$, or equivalently frequency $\nu_{21} = 1420.41\,\text{MHz}$. Hence, the signal originating from this spin-flip transition was dubbed the 21-cm signal. This theoretically predicted H I line was detected for the first time by Ewen & Purcell (1951) with closely following detections by Muller & Oort (1951) and Pawsey (1951). The signal was of Galactic origin in all three cases. In the next decade various astronomers aimed to detect the 21-cm signal in the IGM, particularly in the spectra of radio sources (e.g. Goldstein, 1963; Penzias & Wilson, 1969) which even preceded discovery of quasars. Meanwhile, the ν_{21} has been measured to high accuracy in laboratories (e.g. Goldenberg et al., 1960; Essen et al., 1971).

Decades later, there have been multiple detections of H I absorption along the lines of sight toward radio sources at low and intermediate redshifts (i.e. $z \approx 0 - 4$) (e.g. Curran et al., 2010; Srianand et al., 2010, 2022; Gupta et al., 2013; Zwaan et al., 2015; Dutta & Srianand, 2022). These

observations suggested the presence of damped Lyα absorbers and further strengthened the role of the 21-cm signal as a powerful tracer of neutral hydrogen. On the other hand, non-detection of 21-cm absorption indicates a lack of neutral gas along the line of sight (Curran & Whiting, 2012).

High redshift observations of the 21-cm signal have the potential to be used to explore cosmological eras from the dark ages through the cosmic dawn until the epoch of reionization. Topics that can be addressed with the 21-cm line physics are the properties of the first galaxies and popIII stars, and the history of X-ray sources and ionization bubbles to name a few (e.g. Furlanetto et al., 2006; Furlanetto, 2019; Pritchard & Loeb, 2012). In addition, it may also help to constrain the dark matter particle mass and the sum of neutrino masses (e.g. Shimabukuro et al., 2014). Operational radio observatories such as BIGHORNS (Sokolowski et al., 2015), EDGES (Monsalve et al., 2017), GMRT (Swarup et al., 1991), HERA (DeBoer et al., 2017), LEDA (Price et al., 2018), LOFAR (van Haarlem et al., 2013), MWA (Bowman et al., 2013), PAPER (Parsons et al., 2010), PRIZM (Philip et al., 2019), SARAS 3 (Nambissan T. et al., 2021), and SCI-HI (Voytek et al., 2014), and radio observatories which will be built in the next decade including ASSASSIN (McKinley et al., 2020), REACH (de Lera Acedo et al., 2022), SKA (Dewdney et al., 2009) and SITARA (Nambissan T. et al., 2022) mean this is a very active field.

While some of the above mentioned observatories already provide measurements of the high-redshift 21-cm signal (see Section 1.4.2 and 1.4.3 for details) there is still not enough observational data to draw many conclusions. On the theoretical front, astrophysicists use numerical methods to devise observational strategies for these experiments and to aid the inter-

pretation of data. In addition to the simulations modelling cosmic dawn and the EoR described in Section 1.3.5, there is software developed specifically for 21-cm signal studies. For example, 21CMFAST[3] generates 3D density, ionization, peculiar velocity and temperature fields, which are relevant for 21-cm physics, using a semi-numerical approach (Mesinger et al., 2011; Murray et al., 2020). Building on this, MCMC parameter estimation software 21CMMC[4] has been developed by Greig & Mesinger (2015). Another example of semi-numerical software built for the 21-cm signal modelling is SIMFAST21[5] (Santos et al., 2010). In addition to the software that generates 3D fields of various quantities, a tool with the main purpose of creating mock 21-cm signal observations by post-processing data from cosmological simulations, TOOLS21CM[6], has been developed by Giri et al. (2020).

1.4.1 21-cm line basics

The classical measure of the "brightness" of a radiation field is the specific intensity J_ν (in units of $\mathrm{W\,m^{-2}\,sr^{-1}\,Hz^{-1}}$). Considering the absorption and emission of the radiation by the gas element given by α_ν and j_ν, respectively, along a path s, the radiation field follows the radiative transfer equation

$$\frac{\mathrm{d}J_\nu}{\mathrm{d}s} = j_\nu - \alpha_\nu J_\nu. \tag{1.15}$$

[3] https://github.com/21cmfast/21cmFAST
[4] https://github.com/21cmfast/21CMMC
[5] https://github.com/mariogrs/Simfast21
[6] https://github.com/sambit-giri/tools21cm

For a black body of temperature T, the specific intensity is given by

$$J_\nu = \frac{h_\mathrm{p}\nu^3}{c^2}\frac{1}{e^{\frac{h_\mathrm{p}\nu}{k_\mathrm{B}T}}-1}, \tag{1.16}$$

where $h_\mathrm{p} = 6.626 \times 10^{-34}\,\mathrm{m^2\,kg\,s^{-1}}$ is the Planck constant. In the limit of $h_\mathrm{p}\nu \ll k_\mathrm{B}T$ (Rayleigh-Jeans limit) this becomes

$$J_\nu = \frac{2k_\mathrm{B}\nu^2 T}{c^2}. \tag{1.17}$$

This limit becomes $T \gg T_* \equiv \frac{h_\mathrm{p}\nu_{21}}{k_\mathrm{B}} = 0.068\,\mathrm{K}$ for the 21-cm line, so we have always been in this limit as the $T_\mathrm{CMB} = 2.73\,\mathrm{K}(1+z)$ (Fixsen, 2009). It is conventional to use this relation between the specific intensity and temperature to define a brightness temperature T_b, a theoretical temperature of an object emitting at specific intensity J_ν if it was a black body. Hence, one can replace J_ν with T_b. Now consider a background radio source, with brightness temperature T_R, which emits light that travels through a cloud of optical depth $\tau = \int \alpha_\nu \mathrm{d}s$ and excitation temperature T_ex. The solution to the radiative transfer equation, Eq. (1.15), in terms of the brightness temperature becomes

$$T_\mathrm{b}^\mathrm{obs} = T_\mathrm{R}e^{-\tau} + T_\mathrm{ex}\left(1-e^{-\tau}\right), \tag{1.18}$$

where $T_\mathrm{b}^\mathrm{obs}$ is the observed brightness temperature of the background radio source.

The excitation temperature, T_ex, for the 21-cm line is the spin temperature T_S. The spin temperature is a measure of the relative number densities of hydrogen atoms in the singlet (denoted 0) versus triplet (denoted 1) state

defined as

$$\frac{n_1}{n_0} = \frac{g_1}{g_0} e^{-\frac{T_*}{T_S}}, \tag{1.19}$$

where n_1/n_0 is the ratio of the number densities of each state and $g_1/g_0 = 3$ is the ratio of the spin degeneracy factors of each state. The spin temperature can couple to the radio background temperature T_γ, gas kinetic temperature T_K, and effective colour temperature of the Lyα radiation T_α, which is closely coupled to T_K. Hence, (Field, 1958)

$$T_S^{-1} = \frac{T_\gamma^{-1} + x_\alpha T_\alpha^{-1} + x_c T_K^{-1}}{1 + x_\alpha + x_c}, \tag{1.20}$$

where x_c and x_α are the collisional and Lyα coupling coefficients, respectively. The spin temperature couples to the radio background temperature if $x_c + x_\alpha \ll 1$ or to the gas kinetic temperature if $x_c + x_\alpha \gg 1$.

The spin temperature couples to the radio background temperature when the 21-cm photons are absorbed (emitted) from (to) the radio background. Usually, either a radio-loud point source (see Section 1.4.4 for more details) or the CMB is considered as a radio background source. However, there are studies which include an excess radio background in addition to the CMB in their modeling of the 21-cm signal (e.g. Feng & Holder, 2018; Ewall-Wice et al., 2018; Yang, 2018; Fialkov & Barkana, 2019; Reis et al., 2020; Natwariya, 2021; Mittal et al., 2022; Mittal & Kulkarni, 2022b). Sources that were considered to generate the excess radio background include accreting black holes (Ewall-Wice et al., 2014; Ewall-Wice et al., 2018; Mittal & Kulkarni, 2022a), supernovae from popIII stars (Biermann et al., 2014; Jana et al., 2019) and high redshift galaxies (Mirocha & Furlanetto, 2019; Reis et al., 2020), but see Singal et al. (2018) for an

overview. Furthermore, the excess radio background above the CMB has been already measured at $3-90\,\mathrm{GHz}$ by ARCADE 2 (Fixsen et al., 2011) and at $40-80\,\mathrm{MHz}$ by LWA1 (Dowell & Taylor, 2018).

Otherwise, as mentioned above, T_S can couple to T_K. One way to do so is via collisions between the H I atoms and various other particles which can induce the spin-flip transition. The strength of collisional coupling is determined by

$$x_\mathrm{c} = \sum_i \frac{n_i \kappa_{10}^i T_*}{A_{10} T_\gamma}, \tag{1.21}$$

where κ_{10}^i is the specific rate coefficient for spin deexcitation by collisions with species i. In this thesis, I consider the collisions between H I atoms and other H I atoms (HH), protons (pH) and electrons (eH). I use fitting functions for the HH collisions

$$\kappa_{10}^\mathrm{HH}(T_\mathrm{K}) = 3.1\times10^{-11} T_\mathrm{K}^{0.357} e^{-32/T_\mathrm{K}} + 10^{-12.885+0.45e^{-6(\log_{10}(T_\mathrm{K}/7))^2}} \tag{1.22}$$

and the pH collisions

$$\kappa_{10}^\mathrm{pH}(T_\mathrm{K}) = 2\kappa_{10}^\mathrm{HH} + 10^{-9.35-(\log_{10}(T_\mathrm{K}/3))^2/3.5} \tag{1.23}$$

from Kuhlen et al. (2006) which I modify to better fit the tabulated data in Zygelman (2005), Furlanetto (2006a) and Furlanetto & Furlanetto (2007b), respectively. The fitting function for the eH collisions

$$\kappa_{10}^\mathrm{eH}(T_\mathrm{K}) = 10^{-9.607+\log_{10}(\sqrt{T_\mathrm{K}})e^{-(\log_{10}(T_\mathrm{K}))^{4.5}/1800}} \tag{1.24}$$

is taken from Liszt (2001) and fits data from Furlanetto & Furlanetto (2007a). All three fitting functions, and the tabulated data, are shown

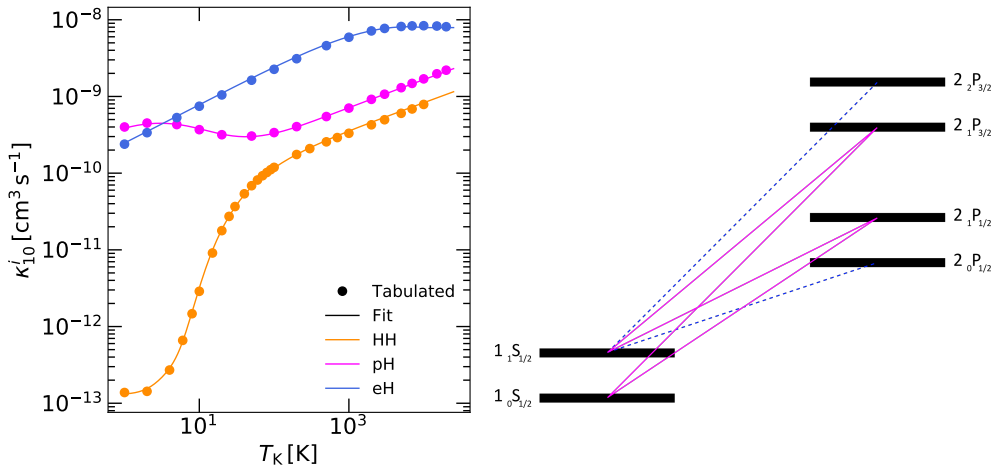

Figure 1.6: *Left:* De-excitation rate coefficients for the collisions between H I atoms and other H I atoms (orange), protons (fuchsia) and electrons (blue). Tabulated data from Zygelman (2005), Furlanetto (2006a), Furlanetto & Furlanetto (2007b) and Furlanetto & Furlanetto (2007a) are shown as points, and modified fitting functions from Kuhlen et al. (2006) and Liszt (2001) are shown as curves. *Right:* Schematic of the Wouthuysen-Field effect (Wouthuysen, 1952; Field, 1959). The horizontal black lines show the hyperfine levels of the 1S and 2P states of the neutral hydrogen atom. The other lines show allowed transitions, both which contribute (solid fuchsia lines) and which do not contribute to the spin-flip transition (dashed blue lines). Figure adapted from Pritchard & Furlanetto (2006).

in the left panel of Fig. 1.6. Note that these fitting function are appropriate only over the range $1\,\mathrm{K} \leq T_\mathrm{K} \leq 10^4\,\mathrm{K}$. The collisional coupling is efficient only in dense gas and becomes inefficient at later times, since density scales as $\propto (1+z)^3$.

However, once the luminous sources are formed during Cosmic Dawn and the EoR, they provide the second channel for the T_S decoupling from the radio background temperature in the form of resonant scattering with Lyα photons. The Lyα photons can mix the hyperfine states via the transitions between an intermediate excitation state, a mechanism known as the Wouthuysen-Field effect (Wouthuysen (1952) and Field (1958)) which is depicted in the right panel of Fig. 1.6. This figure shows the hyperfine

structure of the neutral hydrogen atom in its 1S and 2P states and the allowed transitions between them. Let us assume a H I atom is initially in the state $1\,{}_0\mathrm{S}_{1/2}$ (singlet). Here I use $n^{\mathrm{q}}\,{}_{F^{\mathrm{q}}}L^{\mathrm{q}}_{J^{\mathrm{q}}}$ notation, where n^{q}, L^{q} and J^{q} is the radial, angular orbital and total angular momentum quantum number, respectively, and F^{q} is the sum of the nuclear spin and J^{q}. If this atom absorbs a Lyman series photon, it can be excited to either $2\,{}_1\mathrm{P}_{1/2}$ or $2\,{}_1\mathrm{P}_{3/2}$ level, which is shown as the transitions along the solid fuchsia lines. Afterwards, this atom can spontaneously emit a Lyman series photon resulting in the de-excitation to either of the 1S levels. If the final state is $1\,{}_1\mathrm{S}_{1/2}$, the spin-flip transition has occurred. Similarly, the spin-flip transition can happen the opposite way too. The dashed blue lines illustrate transitions that are permitted but do not contribute to the mixing of the ground level hyperfine states. Other transitions between the 1S and 2P states are not allowed by the dipole selection rules. This mechanism couples the spin temperature to T_α. However, the large number of scatterings of Lyα photons bring the radiation field and gas into local equilibrium resulting in $T_\alpha \approx T_{\mathrm{K}}$ (Field, 1959). The coupling coefficient for this channel is given by

$$x_\alpha = \frac{2T_\star \lambda_\alpha^3 \Lambda_\alpha}{9T_{\mathrm{CMB}} A_{10} h_{\mathrm{p}} c} S_\alpha J_\alpha, \tag{1.25}$$

where $\Lambda_\alpha = 6.265 \times 10^8\,\mathrm{s}^{-1}$ is the Einstein spontaneous emission coefficient for the Lyα transition, $A_{10} = 2.85 \times 10^{-15}\,\mathrm{s}^{-1}$ is the spontaneous decay rate of the spin-flip transition and J_α is the Lyα photon flux. S_α is a correction of order unity that describes the detailed structure of the photon distribution in the neighbourhood of the Lyα resonance. There are several papers that study relevant effects determining this correction such as Hirata (2006), Pritchard & Furlanetto (2006), Furlanetto & Pritchard (2006) and

Chuzhoy & Shapiro (2006) to name a few.

The optical depth of a neutral hydrogen cloud is given by

$$\tau_{21} = \int \frac{3c^2 A_{10}}{8\pi\nu^2} \left(1 - e^{-\frac{h_{\rm p}\nu_{21}}{k_{\rm B}T_{\rm S}}}\right) \phi(\nu) n_0 {\rm d}s, \tag{1.26}$$

where $\phi(\nu)$ is the line profile. The line profile should incorporate natural, thermal, pressure and velocity (both from Hubble flow and peculiar motion of the gas) broadening. Neglecting peculiar velocities, Eq. (1.26) yields an approximation for the 21-cm optical depth at a given redshift (Furlanetto et al., 2006; Furlanetto, 2019)

$$\tau_{21}(z) = \frac{3h_{\rm p}c^3 A_{10}}{32\pi\nu_{21}^2 k_{\rm B}} \frac{n_{\rm HI}(z)}{T_{\rm S}(z)H(z)}, \tag{1.27}$$

where $n_{\rm HI}(z)$ is the neutral hydrogen number density. To include large peculiar velocity gradients (and to avoid unphysical results) a more careful calculation is required (e.g. Mao et al., 2012; Semelin, 2016; Chapman & Santos, 2019). Furlanetto et al. (2006), Pritchard & Loeb (2012) and Furlanetto (2019) describe the physics of the 21-cm line in more depth. This is also discussed further in Chapter 3.

1.4.2 21-cm tomography and power spectrum

As explained above, the 21-cm signal should be observed relative to a radio background. Given that we live in a CMB photon bath with temperature $T_{\rm R}$, the useful measure of the signal is the differential brightness tempera-

ture $\delta T_{\rm b}$. Using Eq. (1.18) one acquires

$$\delta T_{\rm b} = \frac{T_{\rm S} - T_{\rm R}}{1+z}\left(1 - e^{-\tau_{21}}\right). \tag{1.28}$$

Expanding the exponential (assuming the optical depth for the 21-cm is small), assuming a matter-dominated Universe, and using

$$n_{\rm HI} = x_{\rm HI}\Delta\frac{\Omega_{\rm b}X_{\rm H}}{m_{\rm p}}(1+z)^3, \tag{1.29}$$

where overdensity $\Delta = 1 + \delta$ and δ is the density contrast, $\Omega_{\rm b}$ is the baryon energy density parameter, $X_{\rm H}$ is the fraction of the baryons that are hydrogen and $m_{\rm p} = 1.67 \times 10^{-27}\,{\rm kg}$ is the proton mass, this results in

$$\delta T_{\rm b} \approx 9 x_{\rm HI}\Delta(1+z)^{1/2}\frac{T_{\rm S} - T_{\rm R}}{T_{\rm S}}\frac{H(z)/(1+z)}{{\rm d}v_\parallel/{\rm d}r_\parallel}. \tag{1.30}$$

Note that the factor of 9 is cosmology dependent. With this definition, the 21-cm signal is in absorption if $\delta T_{\rm b} < 0$ and in emission if $\delta T_{\rm b} > 0$. Even with this approximate expression for $\delta T_{\rm b}$, the 21-cm signal can inform us about the ionization state of the IGM, the IGM structures and the history of the light sources (encapsulated in $T_{\rm S}$).

Given that the CMB can be measured as a 2D map of the sky, in principle, tomographic measurements of the 21-cm line should be possible too. During the EoR, the 21-cm signal is expected to be in emission (see Fig. 1.8) but its tomographic maps will contain regions with no signal corresponding to H II bubbles (Furlanetto et al., 2006). Various techniques have been developed to measure the size distribution of these regions, some of which are described in Section 1.3.2 (e.g. Zahn et al., 2007; Mesinger

& Furlanetto, 2007). Studies make predictions for the observability of the H II bubbles in the $\delta T_{\rm b}$ maps by GMRT (Majumdar et al., 2012), LOFAR (Rhook & Haehnelt, 2006; Datta et al., 2012; Dixon et al., 2016), MWA (Geil & Wyithe, 2008) and SKA (Kakiichi et al., 2017; Giri et al., 2018; Ma et al., 2020; Davies et al., 2021; Bianco et al., 2021). In addition, some studies suggest that such observations could be used as probes of the reionization history (Kohler et al., 2005) and quasar lifetimes (Datta et al., 2012; Ma et al., 2020). On the other hand, Giri et al. (2019) suggest exploring neutral hydrogen islands from the 21-cm line tomography acquired by SKA.

However, the tomographic features of the 21-cm signal are expected to be comparable to or even fainter than telescope noise (Furlanetto et al., 2006). Instead of exploring individual features, one can measure statistics such as the dimensionless power spectrum Δ^2_{21} which quantifies the variance of the signal at scales $x = 2\pi/k$, where k is the spatial frequency. The 21-cm differential brightness temperature variance is caused by density, neutral fraction, temperature, Lyα coupling and velocity fluctuations (see Eq. (1.30)), many of which are dictated by the reionization sources. Therefore, Δ^2_{21} can inform us about the properties of these sources such as their escape fraction (e.g. Kim et al., 2013; Seiler et al., 2019; Shaw et al., 2020) and the contribution of AGN to reionization (e.g. Kulkarni et al., 2017; Hassan et al., 2018). In addition to exploring astrophysics, the 21-cm power spectrum has been proposed for cosmological studies too, particularly to constrain cosmological parameters (e.g. McQuinn et al., 2006; Mao et al., 2008; Liu & Parsons, 2016; Kern et al., 2017), inflation (e.g. Barger et al., 2009; Adshead et al., 2011) and neutrino mass (e.g. Pritchard & Pierpaoli, 2008; Oyama et al., 2013; Pal & Guha Sarkar, 2016).

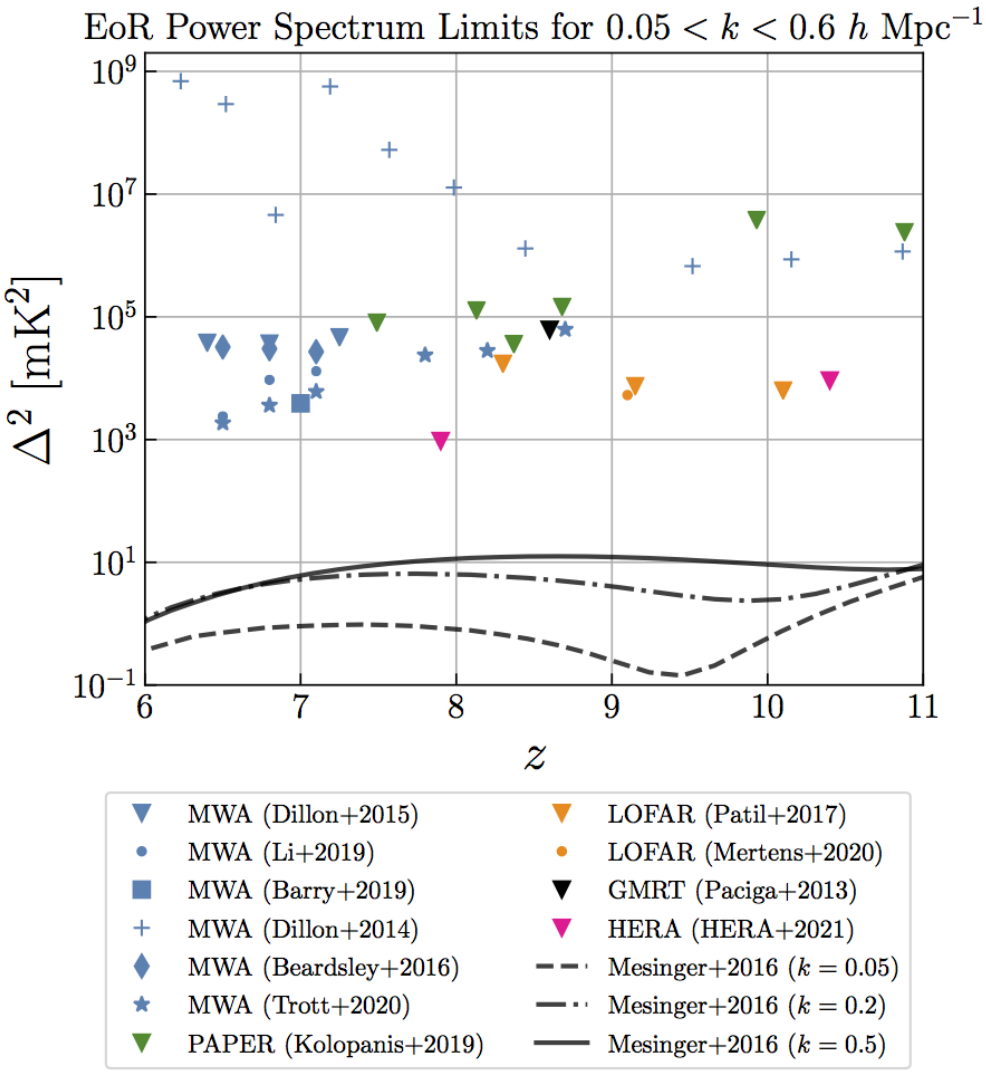

Figure 1.7: The 21-cm power spectrum upper limits measured by MWA (blue points, Dillon et al., 2014, 2015; Beardsley et al., 2016; Barry et al., 2019; Li et al., 2019; Trott et al., 2020), PAPER (green points, Kolopanis et al., 2019), LOFAR (orange points, Patil et al., 2017; Mertens et al., 2020), GMRT (black point, Paciga et al., 2013) and HERA (pink points, The HERA Collaboration, 2022b). For comparison theoretical predictions from Mesinger et al. (2016) are shown (black curves). Figure taken from the HERA website[7].

To date, there are numerous upper limit measurements of the 21-cm power spectrum at a wide range of redshifts. For example, GMRT acquired measurements from the post-reionization IGM (Chakraborty et al., 2021) and the 21-cm power spectrum from the Cosmic Dawn was measured by MWA (Ewall-Wice et al., 2016), LOFAR (Gehlot et al., 2019) and OVRO-LWA (Eastwood et al., 2019). Furthermore, Fig. 1.7 shows the measurements from the EoR and how they have improved over the years. These include observations from GMRT (black point, Paciga et al., 2013), LOFAR (orange points, Patil et al., 2017; Mertens et al., 2020), PAPER (green points, Kolopanis et al., 2019) and MWA (blue points, Dillon et al., 2014, 2015; Beardsley et al., 2016; Barry et al., 2019; Li et al., 2019; Trott et al., 2020). The results from the latter two were used to guide the HERA measurements (pink points, The HERA Collaboration, 2022b) which put the tightest constraints on the 21-cm power spectrum to date. However, even this upper limit is two orders of magnitude larger than expected from cosmological simulations (e.g. Mesinger et al., 2016; Kulkarni et al., 2017; Hassan et al., 2018).

The signal is orders of magnitude weaker than the foreground contaminants (Chapman & Jelić, 2019). The radio signal that needs to be filtered out is of terrestrial, galactic and extragalactic origin. For instance, the radio frequency interference and ionospheric effects need to be mitigated (e.g. Wilensky et al., 2019; Yoshiura et al., 2021; Kariuki Chege et al., 2022). The galactic foregrounds include synchrotron radiation from cosmic ray electrons and free-free emission from the ionized interstellar medium, and the extragalactic foregrounds originate from star forming galaxies and

[7] http://reionization.org/science/public-data-release-1/

AGN (Chapman & Jelić, 2019). There has been a lot of effort to model these foregrounds (e.g. Jelić et al., 2008, 2010; Spinelli et al., 2018), develop methods to mitigate them (e.g. Morales et al., 2012; Pober et al., 2013; Gu et al., 2013) and generate sky maps to assist in this process (e.g. Byrne et al., 2019, 2022). However, observatories deal with foregrounds differently, and hence techniques specialized for LOFAR (e.g. Chapman et al., 2012; Harker et al., 2010), MWA (e.g. Kariuki Chege et al., 2022) and SKA (e.g. Chapman et al., 2015, 2016) are designed. In the future, SKA will have higher sensitivity and hence will be able to provide tighter limits on Δ^2_{21} (Mellema et al., 2013; Koopmans et al., 2015).

However, even the currently available measurements can be used to constrain reionization astrophysics. For example, Mondal et al. (2020) used LOFAR data to constrain the excess radio background. Furthermore, Greig et al. (2021a,b) and The HERA Collaboration (2022a) inferred 95% confidence constraints on $T_{\rm S}$ (see Fig. 2.3 for the values) from the MWA, LOFAR and HERA measurements, respectively, which disfavour models of very cold IGM (i.e. some pre-heating of the IGM is expected according to these measurements). In addition, HERA observations rule out the parameter space in which the radio background is high and X-ray background is low (The HERA Collaboration, 2022a).

1.4.3 Global 21-cm signal

Instead of looking at the maps of the 21-cm brightness temperature, one can average the signal over the sky and explore how the 21-cm signal behaves globally. Even though this method collapses the signal to 1D, it still retains

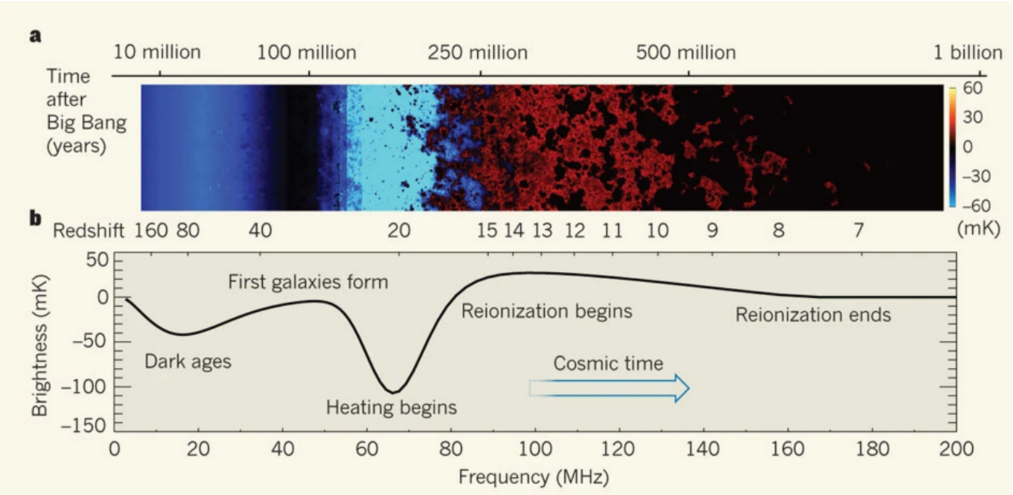

Figure 1.8: *Top:* 2D lightcone of the 21-cm brightness temperature based on the simulations from Santos et al. (2008). This shows how the signal evolves. The blue colour corresponds to the signal in absorption, red colour to the emission and black colour to no signal. *Bottom:* Redshift evolution of the sky-averaged 21-cm signal from the Dark Ages to the end of the Epoch of Reionization. Figure taken from Pritchard & Loeb (2010b).

rich information. Fig. 1.8 shows how such a transformation from a 2D lightcone of $\delta T_{\rm b}$ (the top panel) to the global 21-cm signal (the bottom panel) would look. Below I will describe the general shape of the global 21-cm signal as expected if assuming only the CMB as the radio background (i.e. $T_{\rm R} = T_\gamma = T_{\rm CMB}$) and only adiabatic cooling due to the expansion of the Universe, as in Pritchard & Loeb (2010b), Cohen et al. (2017) and Villanueva-Domingo et al. (2020), for example.

During the dark ages, the collisions between the H I atoms and other species are frequent and $x_{\rm c}$ is large. Hence, according to Eq. (1.19), the spin temperature couples to the gas kinetic temperature. The gas kinetic temperature decreases adiabatically due to the expansion of the Universe with $T_{\rm K} \propto (1+z)^2$ as opposed to the CMB temperature with $T_{\rm CMB} \propto (1+z)$ and hence $T_{\rm K} < T_{\rm CMB}$. The combination of these two effects leads to $T_{\rm S} < T_{\rm CMB}$ and hence the signal is in absorption. However, as the

Universe expands, the collisions between particles become inefficient and $T_{\rm S}$ gradually couples to the $T_{\rm CMB}$. This is seen as a turn in $\delta T_{\rm b}$ at $z \approx 80$ in Fig. 1.8, followed by an increase of $\delta T_{\rm b}$ until $T_{\rm S} \approx T_{\rm CMB}$ and the signal is lost.

The first luminous sources produced at the cosmic dawn emit Lyα photons which provide the second channel of $T_{\rm S}$ coupling to $T_{\rm K}$ via the Wouthuysen-Field effect, and hence the spin temperature decouples from the radio background once again. The gas kinetic temperature is still lower than the CMB temperature, and hence the signal shows another absorption feature. However, in addition to the Lyα coupling, the Lyα photons heat the IGM. The latter requires more Lyα photons than the former (Pritchard & Loeb, 2012) and hence the gas is significantly heated after the signal enters the absorption phase. Once the hydrogen is heated enough, the absorption feature reaches its maximum amplitude and $\delta T_{\rm b}$ rises (at $z \gtrsim 20$ in Fig. 1.8). The shape, timing and amplitude of this global 21-cm absorption feature at cosmic dawn is determined by the heating and coupling by Lyα photons but also heating mechanisms such as X-ray photo-heating (e.g. Villanueva-Domingo et al., 2020) and shocks.

As reionization progresses, the gas kinetic temperature increases further and eventually becomes higher than the CMB temperature. At this point, the global 21-cm signal switches to emission. However, as the reionization bubbles grow and the neutral hydrogen is depleted, the signal diminishes.

The complexity of the global 21-cm signal, particularly how it depends on various physical mechanisms, has motivated a number of experiments with the goal to detect it. All of the currently ongoing experiments are ground-based, namely BIGHORNS (Sokolowski et al., 2015), EDGES

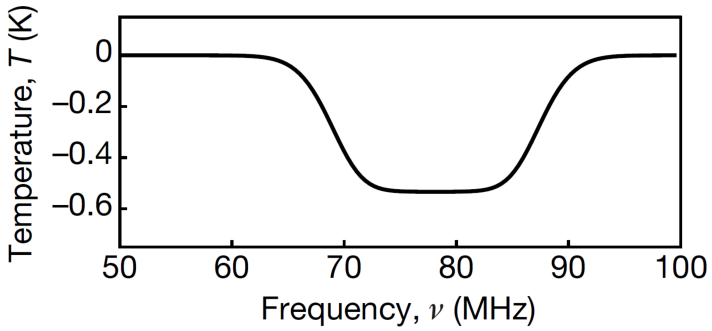

Figure 1.9: Model of the global 21-cm signal (the temperature represents the differential brightness temperature) recovered from the EDGES measurement. The absorption feature is centred at 78 ± 1 MHz with the maximum amplitude of $0.5^{+0.5}_{-0.2}$ K. Figure taken from Bowman et al. (2018).

(Monsalve et al., 2017), LEDA (Price et al., 2018), LOFAR (van Haarlem et al., 2013), MIST[8], PRIZM (Philip et al., 2019), SARAS 3 (Nambissan T. et al., 2021) with its precursors SARAS 2 (Singh et al., 2018) and SARAS (Patra et al., 2013) and SCI-HI (Voytek et al., 2014). The frequencies at which these facilities observe range from 10 MHz to 240 MHz, meaning that they aim to explore the EoR, Cosmic Dawn and Dark Ages.

Currently, only EDGES has successfully measured δT_b. Bowman et al. (2018) reported the measurement of $\delta T_\mathrm{b} = -0.5^{+0.5}_{-0.2}$ K at 78 ± 1 MHz (i.e. $z \approx 17.2$). The model signal which fits the measured data is shown in Fig. 1.9. This measurement is surprising because the absorption feature has a factor of a few larger amplitude, compared to standard models (e.g. the bottom panel in Fig. 1.8).

According to Eq. (1.30), to make this absorption feature deeper the difference between T_S and T_R must be increased. One way is to include other cooling mechanisms in addition to the adiabatic expansion of the Universe that decrease T_K below adiabatic cooling and hence decrease T_S too. For instance, interactions between dark matter particles and baryons

[8] http://www.physics.mcgill.ca/mist/

could induce such cooling (e.g. Muñoz & Loeb, 2018; Fialkov et al., 2018; Barkana et al., 2018). In such a scenario the global 21-cm signal can be used to constrain the dark matter particle mass (e.g. Safarzadeh et al., 2018; Houston et al., 2018).

On the other hand, an excess radio background (i.e. increased $T_{\rm R}$) could also explain this deep feature (e.g. Feng & Holder, 2018; Fraser et al., 2018; Ewall-Wice et al., 2018). The measurements of the radio background by ARCADE2 (Fixsen et al., 2011) and LWA1 (Dowell & Taylor, 2018) make this explanation plausible. Such models have been already used to constrain high redshift star formation (Fialkov & Barkana, 2019) and primordial black holes (Mittal et al., 2022).

Furthermore, the steep edge at the lower frequency end of the EDGES signal requires a very quick coupling of $T_{\rm S}$ to $T_{\rm K}$, which has to happen at $z \approx 19 - 21$. The large amount of UV photons required by this can be generated by stars in rare and massive halos (Kaurov et al., 2018) or by popIII stars (Mittal & Kulkarni, 2022b). Mittal & Kulkarni (2022b) also showed that for the appropriate evolution of the star formation, Lyα and X-ray radiation can result in a $\delta T_{\rm b}$ model that fits the flat bottom and the sharp edge at the higher frequency of the 21-cm signal measured by the EDGES.

However, before using the sky-averaged 21-cm spectrum to precisely constrain quantities such as the dark matter particle mass and star formation at high redshifts, the details of standard models must be clarified. For instance, recent studies (e.g. Venumadhav et al., 2018; Meiksin, 2021) improved the modelling of the heating mechanisms induced by Lyα and CMB photons. Moreover, given that the global 21-cm signal is an aver-

aged quantity, $\delta T_{\rm b}$ is usually calculated at the cosmic mean density only. Recently, Xu et al. (2018) incorporated density fluctuations in their analytical calculation of $\delta T_{\rm b}$ which resulted in a 40% reduction of the global 21-cm absorption feature amplitude in comparison with the case in which the IGM density is homogeneous. This suppression of the global 21-cm signal was reduced to $\approx 15\%$ when hydrodynamical simulations were used (Villanueva-Domingo et al., 2020; Xu et al., 2021). This is still a significant difference which makes the discrepancy between the EDGES signal and theoretical predictions from the standard ΛCDM model even larger. I study this issue further in Chapter 5.

More experiments with the goal of detecting the sky-averaged 21-cm spectrum are being designed. These include ground-based observatories such as ASSASSIN, HYPERION[9], SITARA and REACH. Unfortunately, the ionosphere can partially reflect radio waves and hence disrupt or even completely block the 21-cm signal from high redshifts. Therefore, lunar orbiters have been proposed as 21-cm signal observatories, namely DAPPER (Burns et al., 2021), DARE (Burns et al., 2012) and DSL (Chen et al., 2021).

1.4.4 21-cm forest signal

A different approach for observing the 21-cm line is to use a radio-loud point source as a background. Suitable background sources are radio-loud quasars (Carilli et al., 2002; Carilli et al., 2007; Mack & Wyithe, 2012; Ciardi et al., 2013; Ciardi et al., 2015a; Ewall-Wice et al., 2014) and gamma-ray bursts (Ioka & Mészáros, 2005; Xu et al., 2011; Ciardi et al., 2015b). The radio

[9] https://github.com/karakundert/HYPERION-project-doc

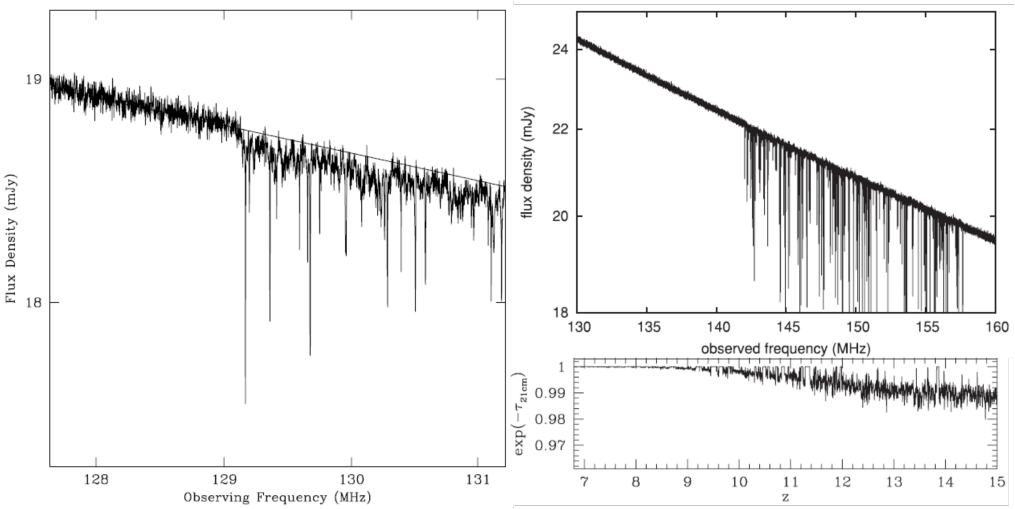

Figure 1.10: Simulated 21-cm forest absorption in the spectrum of a radio source with a similar SED as Cygnus A at $z = 10$ (left panel, figure taken from Carilli et al. (2002)) and $z = 9$ (top right panel, figure edited from Mack & Wyithe (2012)). Both spectra were created incorporating SKA instrumental features. The bottom right panel shows the redshift evolution of the normalized 21-cm forest spectrum assuming no instrumental features (figure edited from (Ciardi et al., 2013)).

brightness of these sources is expected to be much larger than the 21-cm line, and hence the 21-cm signal will always be in absorption (Pritchard & Loeb, 2012). Such a signal is analogous to the Lyα forest. As the light from a background source travels through the Universe, the photons that redshift to λ_{21} are absorbed by neutral hydrogen structures, imprinting absorption features in the spectrum of the source. This is known as the 21-cm forest signal. Examples of synthetic 21-cm forest spectra are shown in Fig. 1.10, but see also Chapter 3 and 4. The left and top right panel show a spectrum of a source with a SED similar to Cygnus A, a radio galaxy, located at $z = 10$ and 9 simulated by Carilli et al. (2002) and Mack & Wyithe (2012), respectively.

The 21-cm forest signal is complementary to tomography, the power spectrum, and sky-averaged measurements of the 21-cm line because it is

detectable even if $T_S = T_R$. Furthermore, the only requirement for 21-cm forest observations is a high signal-to-noise spectrum (Furlanetto et al., 2006; Pritchard & Loeb, 2012). Hence, the 21-cm forest detection is subject to different systematics and in principle is less complicated to perform than other 21-cm line observations. However, the 21-cm forest observations face different challenges. For example, it requires radio-bright sources, whose abundance is not known at high redshifts. There have been attempts to estimate the number of such sources (Xu et al., 2009; Saxena et al., 2017; Bolgar et al., 2018). Encouragingly, 9 radio-loud quasars have been confirmed at $z > 6$ (Belladitta et al., 2020; Liu et al., 2021; Bañados et al., 2021; Ighina et al., 2021; Endsley et al., 2022; Gloudemans et al., 2022) and hundreds more are expected to be detected by the GMRT all sky radio survey at 150 MHz (Intema et al., 2017), the LOFAR Two-metre Sky Survey (LoTSS, Shimwell et al., 2017; Kondapally et al., 2021), and the Galactic and Extragalactic All-sky MWA survey (GLEAM, Wayth et al., 2015). This search can be aided by large spectroscopic follow-up programmes such as the WEAVE-LOFAR survey (Smith et al., 2016).

Another advantage of the 21-cm forest signal is that it is sensitive to small scale structures (Furlanetto et al., 2006). Hence, it can be used to track minihaloes (Furlanetto & Loeb, 2002; Furlanetto, 2006a; Yue et al., 2009; Xu et al., 2011; Meiksin, 2011; Kadota et al., 2022). Currently, the main limitation is the spectral resolution of telescopes. Instead of detecting individual absorption features, a statistical detection of average 21-cm absorption has been suggested (e.g. Ciardi et al., 2013; Thyagarajan, 2020), for example to constrain the thermal history of the IGM (Mack & Wyithe, 2012; Ewall-Wice et al., 2014). On the other hand, Xu et al. (2009) and Xu

et al. (2011) show that the thermal state of the IGM can be probed with individual 21-cm absorbers too. However, the pre-heating of the IGM (e.g. by X-ray background) poses another challenge for the detection of 21-cm absorbers because if the gas becomes too hot, the signal will be suppressed (Xu et al., 2011; Mack & Wyithe, 2012, and Chapter 3 in this thesis). Such a strong pre-heating by X-ray background is not ruled out as the X-ray background is not well constrained yet (The HERA Collaboration, 2022a).

Naturally, the ionization state of the IGM has a large impact on the observability of the 21-cm forest. This is clearly shown in the bottom right panel of Fig. 1.10 in which the gas becomes more transparent to the 21-cm photons over time as reionization progresses. This makes the 21-cm forest signal complementary to the Lyα forest, which is observable at the end of the EoR but it is hard to detect beyond $z \sim 6$. This is because the IGM is opaque to the Lyα radiation for $x_{\rm HI} \gtrsim 10^{-4}$ (see Section 1.3.1) due to the Lyα transition cross-section being 10^7 times larger than the spin-flip transition cross-section.

In addition to being a potential probe of the EoR, the 21-cm forest has been suggested for cosmological studies too. These include constraining the dark matter, neutrino mass and cosmological parameters (Shimabukuro et al., 2014; Shimabukuro et al., 2020; Kadota et al., 2021; Villanueva-Domingo & Ichiki, 2022). However, the modelling of the 21-cm forest signal must improve to prevent misinterpretation of such measurements. This includes the modelling of redshift space distortions, Lyα coupling, minihaloes, reionization and the hydrodynamical response of the gas to the reionization (Gnedin & Hui, 1998; Meiksin, 2011; Kulkarni et al., 2015; Semelin, 2016; Park et al., 2016; D'Aloisio et al., 2020; Nakatani et al., 2020, and

Chapter 3 in this thesis). This will also aid the observational strategies of facilities such as LOFAR and SKA in the future (Xu et al., 2011; Mack & Wyithe, 2012; Ciardi et al., 2013; Ciardi et al., 2015a,b; Shimabukuro et al., 2014; Semelin, 2016; Kadota et al., 2021).

1.5 Summary

The 21-cm signal has a potential to be used as a probe of both astrophysics and cosmology throughout the dark ages, cosmic dawn and the epoch of reionization. While some of measurements and upper limits of the 21-cm line have been used to constrain astrophysics (e.g. The HERA Collaboration, 2022a; Mittal et al., 2022), the observations of the 21-cm signal are still very limited. However, forthcoming surveys such as the ones planned with LOFAR and SKA motivate theoretical modelling efforts to aid the observational strategies of these surveys.

In this thesis I will use hydrodynamical and radiative transfer simulations drawn from the Sherwood-Relics simulation suite (Puchwein et al., 2022), which I describe in Chapter 2, with the aim of addressing the following questions:

Q1: What are the prospects of detecting the 21-cm forest signal if reionization ends late?

In Chapter 3 I study what affects the observability of strong 21-cm absorbers. This includes heating by the X-ray background, Lyα coupling, redshift space distortions, pressure smoothing caused by the patchiness of the reionization and the reionization history. This is

done in the context of late-end reionization in which the reionization is completed by $z \approx 5.3$. In such a scenario, large islands of neutral hydrogen are expected to be present as late as $z \approx 6$ (Lidz et al., 2007; Mesinger, 2010) and hence there is a chance of detecting strong 21-cm absorbers at such low redshifts.

Q2: Can the 21-cm forest signal be used to constrain quasar lifetimes?

In Chapter 4 I model the effect of quasar radiation on proximate 21-cm absorption, in analogy to Lyα forest near-zones (e.g. Fan et al., 2006; Eilers et al., 2021). I explore the sensitivity of the 21-cm forest signal to the properties of quasars for both constant and time-varying quasar SED models (Davies et al., 2021; Satyavolu et al., 2022). Of particular interest is the potential of proximate 21-cm absorption distinguishing between quasar models that Lyα forest near-zones (e.g. Eilers et al., 2017, 2020) cannot.

Q3: How do density fluctuations of the intergalactic medium affect the global 21-cm signal at cosmic dawn?

In Chapter 5 I model the sky-averaged 21-cm signal in the context of the EDGES measurement (Bowman et al., 2018). Instead of evaluating it at the cosmic mean density as is usually done in the literature, Xu et al. (2018, 2021) and Villanueva-Domingo et al. (2020) assumed a distribution of densities. They found that density fluctuations significantly reduce the amplitude of the global 21-cm signal at cosmic dawn. Omitting this effect could lead to the incorrect interpretation of the signal (e.g. Fialkov et al., 2018; Mittal et al., 2022). However, Xu et al. (2021) assume strong Lyα coupling of spin temperature. On the other hand, Villanueva-Domingo et al. (2020) perform full

calculation of the spin temperature, but use simulations with now disfavoured cosmology. Therefore, I follow the approach described in Villanueva-Domingo et al. (2020), but use more recent simulations, to study how the effect of the IGM density fluctuations on the amplitude of the sky-averaged 21-cm spectrum changes in more realistic models.

Finally, Chapter 6 serves as a summary of the main conclusions of the above work and the outlook for this research field in the next decade.

Chapter 2

Numerical modeling of the intergalactic medium during reionization

The work contained in this chapter is adapted from Section 2 and Appendix B in the paper Šoltinský et al. (2021) in Monthly Notices of Royal Astronomical Society Volume 506, Issue 4, Pages 5818-5835.

2.1 Hydrodynamical simulations with radiative transfer

Throughout this thesis, the 21-cm forest during inhomogeneous reionization and the global 21-cm signal at Cosmic Dawn is modelled using a subset of the high resolution cosmological hydrodynamical simulations drawn from the Sherwood-Relics simulation programme (see Puchwein et al., 2022,

for an overview)[1]. The Sherwood-Relics simulations were performed with a modified version of the P-GADGET-3 code – which is itself an updated version of the GADGET-2 code described in Springel (2005) – and uses the same initial conditions as the earlier Sherwood simulation suite (Bolton et al., 2017). In this work we adopt a flat ΛCDM cosmology with $\Omega_\Lambda = 0.692$, $\Omega_\mathrm{m} = 0.308$, $\Omega_\mathrm{b} = 0.0482$, $\sigma_8 = 0.829$, $n_\mathrm{s} = 0.961$, $h = 0.678$, consistent with Planck Collaboration (2014), and a primordial helium fraction by mass of $Y_\mathrm{p} = 0.24$ (Hsyu et al., 2020).

The simulations have a volume $(40h^{-1}\mathrm{cMpc})^3$ and track 2×2048^3 dark matter and gas particles. This yields a dark matter particle mass of $7.9 \times 10^5\,\mathrm{M}_\odot$ and resolves dark matter haloes with masses greater than $\sim 2.5 \times 10^7\,\mathrm{M}_\odot$. This high mass resolution is necessary for capturing the small-scale intergalactic structure probed by the 21-cm forest (cf. Semelin, 2016). We furthermore adopt a simple but computationally efficient scheme for converting high density gas into collisionless particles that robustly predicts the properties of the IGM. If a gas particle has an overdensity $\Delta = 1 + \delta > 1000$ and kinetic temperature $T_\mathrm{K} < 10^5\,\mathrm{K}$, it is converted into a collisionless star particle (Viel et al., 2004). We have verified this simplified approach is sufficient for modelling the 21-cm forest in the diffuse IGM by direct comparison to a full sub-grid star formation model (see Section 3.3.2, particularly Fig. 3.4, for further details). The main effect of this approximation is the removal of dense gas from haloes, which slightly reduces the number of strong 21-cm absorbers in models with no X-ray heating.

In order to include the effect of inhomogeneous reionization by UV

[1] https://www.nottingham.ac.uk/astronomy/sherwood-relics/

photons on the IGM, the Sherwood-Relics simulations are combined with the moment-based, M1-closure radiative transfer code ATON (Aubert & Teyssier, 2008). We adopt a novel hybrid approach that captures the small-scale hydrodynamical response of the gas in the simulations to patchy heating during reionization (see also Oñorbe et al., 2019, for a related approach). Our hybrid RT/hydrodynamical simulations use inputs in the form of 3D maps of the reionization redshift and H I photo-ionization rate, produced by ATON simulations performed on the P-GADGET-3 outputs in post-processing (see e.g. image on thesis front page). These maps are then fed back into a re-run of the P-GADGET-3 model, where they are called within a non-equilibrium thermo-chemistry solver (Puchwein et al., 2015). Following Kulkarni et al. (2019), the ionizing sources in the ATON simulations have luminosities proportional to the halo mass with a redshift-dependent normalization, and the mean energy of ionizing photons is assumed to be 18.6 eV. Further details can be found in Gaikwad et al. (2020) and Puchwein et al. (2022). The main advantage of this approach is that since the post-processing step using the ATON radiative transfer simulations is computationally cheap compared to the hydrodynamical simulations, we may empirically calibrate the source model to yield a reionization history that is consistent with a wide range of observational constraints. This avoids many of the uncertainties associated with direct hydrodynamical modelling of the source population.

Note, however, the relatively small volume of our simulations means the patchy structure of reionization will not be fully captured on scales larger than the box size. This will lead to smaller neutral islands and an earlier percolation of ionized regions relative to simulations performed in a

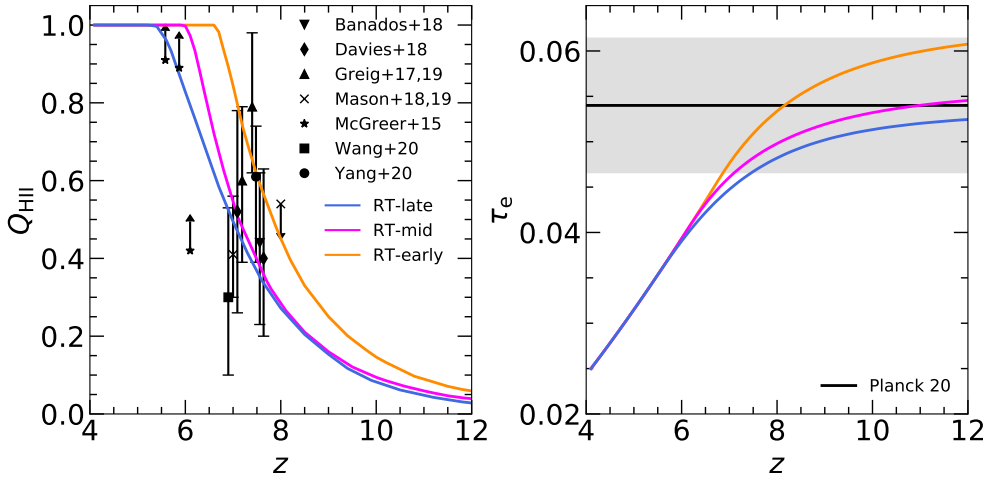

Figure 2.1: *Left*: The filling factor of ionized gas in the RT-late (blue curve), RT-mid (fuchsia curve) and RT-early (orange curve) simulations, compared to observational constraints from dark gaps in the Lyα forest (McGreer et al., 2015), the damping wing in high redshift quasar spectra (Bañados et al., 2018a; Davies et al., 2018; Greig et al., 2017, 2019; Wang et al., 2020; Yang et al., 2020a) and Lyα emitting galaxies (Mason et al., 2018, 2019). For clarity of presentation a small offset has been added to the redshifts of some of the data points. *Right*: The Thomson scattering optical depth to cosmic microwave background photons. The black line with the shaded region shows the Planck Collaboration (2020) measurement.

larger volume (Iliev et al., 2014; Kaur et al., 2020). We therefore adjust the ionizing emissivity in the models by hand to achieve a given reionization history; this scaling is equivalent to varying the escape fraction of ionizing photons. In addition, while our ATON simulations self-consistently follow the propagation of ionizing photons using a 2048^3 Cartesian grid, self-shielded regions below the size of the grid cells ($\lesssim 20h^{-1}$ ckpc) will not be resolved. We attempt to partially correct for this by implementing a correction for the self-shielding of dense gas in all our simulations in post-processing, using the results of Chardin et al. (2018). We find, however, that this correction makes almost no difference to our final results, as the majority of the strong 21-cm absorbers in our simulations arise from the diffuse IGM.

Table 2.1: Hydrodynamical simulations used in this work. From left to right, the columns give the name of the simulation, the nature of the reionization model, the redshift when the IGM is fully reionized, and the prescription for converting dense gas into collisionless star particles, which follows either Viel et al. (2004) or Puchwein & Springel (2013). The first four simulations are part of the Sherwood-Relics suite (Puchwein et al., 2022). The final two models are optically thin simulations with rapid reionization at $z \simeq 15$. All models have a volume of $(40h^{-1}\mathrm{cMpc})^3$ and include 2×2048^3 dark matter and gas particles.

Name	Reionization	z_R	Star formation
RT-late	Hybrid RT/hydro	5.3	VHS04
Homog-late	Homogeneous, matches RT-late	5.3	VHS04
RT-mid	Hybrid RT/hydro	6.0	VHS04
RT-early	Hybrid RT/hydro	6.7	VHS04
QLyα	Rapid, optically thin	~ 15	VHS04
PS13	Rapid, optically thin	~ 15	PS13

In this work we analyse Sherwood-Relics runs that use three reionization histories first described by Molaro et al. (2022), in which reionization completes at $z_\mathrm{R} = 5.3$, $z_\mathrm{R} = 6.0$ and $z_\mathrm{R} = 6.6$ (labelled RT-late, RT-mid and RT-early, respectively). Here we define z_R as the redshift where the volume averaged neutral fraction first falls below $\langle x_\mathrm{HI}\rangle \sim 10^{-3}$. The filling fraction of ionized gas and the Thomson scattering optical depth predicted by these models are displayed in Fig. 2.1. All three models are consistent with current observational constraints on the timing of reionization. As already discussed, the reionization model that ends at $z = 5.3$ is furthermore consistent with the large fluctuations in the Lyα forest transmission observed at $z \simeq 5.5$ (Becker et al., 2015b; Kulkarni et al., 2019; Keating et al., 2020; Bosman et al., 2022; Zhu et al., 2022). Finally, we also use a simulation (Homog-late) that has been constructed to give exactly the same globally averaged reionization history as the RT-late model, but using a spatially uniform ionizing background. A comparison between the

RT-late and Homog-late simulations therefore allows us to estimate the uncertain effect that spatial fluctuations in the pressure smoothing (from e.g. UV photo-heating) may have on the gas in the pre-reionization IGM (see Section 3.3.2). All the simulations used in this work are listed in Table 2.1, where the final two models listed are used only to test the effect of the star formation prescription on our results.

2.2 Heating of neutral gas by the X-ray and Lyα backgrounds

Absorption features in the 21-cm forest arise from neutral hydrogen in the IGM. In addition to modelling the inhomogeneous reionization of the IGM by UV photons, we must therefore also consider the temperature and ionization state of gas that is optically thick to Lyman continuum photons. This heating is attributable to adiabatic compression and shocks – which are already included within our hydrodynamical simulations – and the X-ray and (to a lesser extent) Lyα radiation backgrounds at high redshift (Ciardi et al., 2010), which are not. Hence, we now describe the procedure we use to include spatially uniform X-ray and Lyα heating in our simulations, by recalculating the density dependent temperature and ionization state of the neutral gas in our hybrid simulations in post-processing.

As we do not directly model the star formation rate in our simulations, rather than using a detailed model for the number and spectral energy distribution of X-ray sources at high redshift, for simplicity and ease of comparison to the existing literature we instead follow the approach introduced

by Furlanetto (2006b) for parameterising the comoving X-ray background emissivity. This uses the observed relationship between the star formation rate, SFR, and hard X-ray band luminosity (2–10 keV) for star-forming galaxies at $z = 0$ (Gilfanov et al., 2004; Lehmer et al., 2016). Furlanetto (2006b) adopt the normalisation

$$L_{\rm X} = 3.4 \times 10^{40}\,{\rm erg\,s^{-1}}\, f_{\rm X} \left(\frac{\rm SFR}{1\,{\rm M_\odot\,yr^{-1}}} \right), \tag{2.1}$$

for the total X-ray luminosity at photon energies $> 0.2\,{\rm keV}$, assuming a power-law spectral index $\alpha_{\rm Xb} = 1.5$. The X-ray efficiency, $f_{\rm X}$, parameterises the large uncertainty in the extrapolation of Eq. (2.1) toward higher redshift. Using the conversion $\epsilon_{\rm X,0.2\,keV} = L_{\rm X}(\alpha_{\rm Xb} - 1)/\nu_{\rm 0.2keV}$, the corresponding comoving X-ray emissivity is

$$\begin{aligned} \epsilon_{{\rm X},\nu}(z) = \; & 3.5 \times 10^{21} f_{\rm X}\,{\rm erg\,s^{-1}\,Hz^{-1}\,cMpc^{-3}} \\ & \times \left(\frac{\nu}{\nu_{0.2\,{\rm keV}}} \right)^{-\alpha_{\rm Xb}} \left(\frac{\rho_{\rm SFR}(z)}{10^{-2}\,{\rm M_\odot\,yr^{-1}\,cMpc^{-3}}} \right). \end{aligned} \tag{2.2}$$

We assume a power-law spectrum with $\alpha_{\rm Xb} = 1.5$, and use the fit to the observed comoving star formation rate density from Puchwein et al. (2019) (their eq. 21), where

$$\rho_{\rm SFR}(z) = 0.01\,{\rm M_\odot\,yr^{-1}\,cMpc^{-3}} \frac{(1+z)^{2.7}}{1 + [(1+z)/3.0]^{5.35}}. \tag{2.3}$$

We assume that $\rho_{\rm SFR} = 0$ at redshifts $z > z_\star = 14$, and have verified that adopting $z_\star > 14$ does not change our predictions for 21-cm absorption at $z \leq 12$. Note however, that we use $z_\star = 21$ in Chapter 5 when we investigate the IGM during Cosmic Dawn.

The X-ray background is primarily responsible for ionizing and heating the intergalactic medium prior to reionization. The proper specific intensity of the X-ray background, $J_{\mathrm{X},\nu}$ [erg s^{-1} cm^{-2} Hz^{-1} sr^{-1}], is given by the solution to the cosmological radiative transfer equation (Haardt & Madau, 1996; Mirocha, 2014)

$$J_{\mathrm{X},\nu}(z) = \frac{c(1+z)^3}{4\pi} \int_z^{z_\star} \frac{\epsilon_{\mathrm{X},\nu'}(z')}{H(z')(1+z')} e^{-\bar{\tau}_\nu(z,z')}\, dz', \tag{2.4}$$

where $\epsilon_{X,\nu}$ is the comoving X-ray emissivity, $z_\star$ is the redshift when X-ray emitting sources first form, and the emission frequency, ν' of a photon emitted at redshift z' and observed at frequency ν and redshift z is

$$\nu' = \nu \frac{(1+z')}{(1+z)}. \tag{2.5}$$

The optical depth encountered by a photon observed at frequency ν is

$$\bar{\tau}_\nu(z,z') = c \sum_i \int_z^{z'} \frac{\bar{n}_i(z'')\sigma_{\nu'',i}}{H(z'')(1+z'')}\, dz'', \tag{2.6}$$

where the sum is over the species $i = $ H I, He I, He II, and $\sigma_{\nu,i}$ are the photo-ionization cross-sections (Verner et al., 1996).

The photo-ionization rates for species $i = $ H I, He I, He II are

$$\Gamma_{\mathrm{i}} = 4\pi \int_{\nu_i}^{\infty} \frac{J_{\mathrm{X},\nu}}{h_{\mathrm{p}}\nu}\sigma_{\nu,i} + 4\pi \sum_j \Phi_i(h_{\mathrm{p}}(\nu-\nu_j), x_{\mathrm{e}}) \int_{\nu_j}^{\infty} \frac{J_{\mathrm{X},\nu}}{h_{\mathrm{p}}\nu}\sigma_{\nu,j}\, d\nu, \tag{2.7}$$

where ν_i is the frequency of the ionization threshold for species i. The second term in Eq. (2.7) arises from secondary ionizations due to collisions with energetic photo-electrons, where Φ_{i} is the number of secondary ion-

izations per primary photo-electron of energy $h_{\rm p}(\nu - \nu_{\rm i})$ for a free electron fraction of $x_{\rm e}$ (Shull & van Steenberg, 1985). The corresponding photo-heating rates are

$$\mathscr{H}_i = 4\pi n_i \phi_{\rm heat}(h_{\rm p}(\nu - \nu_i), x_{\rm e}) \int_{\nu_{\rm i}}^{\infty} \frac{J_{{\rm X},\nu}(\nu - \nu_i)}{\nu} \sigma_{\nu,i}\, d\nu, \tag{2.8}$$

where $\phi_{\rm heat}$ is the fraction of the primary photo-electron energy that contributes to the heating of the gas. We use the tabulated results from Furlanetto & Stoever (2010) for $\Phi_{\rm i}$ and $\phi_{\rm heat}$.

The Compton scattering of free electrons off X-ray background photons will also heat the IGM (Madau & Efstathiou, 1999). The Compton heating rate is

$$\mathscr{H}_{\rm C} = \frac{4\pi n_{\rm e} \sigma_{\rm T}}{m_{\rm e} c^2} \int_0^{\infty} J_{{\rm X},\nu}(h_{\rm p}\nu - 4k_{\rm B}T_{\rm K})\, d\nu, \tag{2.9}$$

where $\sigma_{\rm T} = 6.65 \times 10^{-25}\,{\rm cm}^2$ is the Thomson cross-section, appropriate for X-rays with energy $\lesssim 100\,{\rm keV}$ (i.e. relativistic effects may be ignored).

The UV background emissivity at the Lyα wavelength from stars in our model is instead given by

$$\begin{aligned} \epsilon_\alpha(z) = {} & 8.7 \times 10^{25} f_\alpha\, {\rm erg\,s^{-1}\,Hz^{-1}\,cMpc^{-3}} \\ & \times \left(\frac{\rho_{\rm SFR}(z)}{10^{-2}\,{\rm M_\odot\,yr^{-1}\,cMpc^{-3}}} \right), \end{aligned} \tag{2.10}$$

where we have used the conversion between SFR and UV luminosity at 1500 Å from Madau & Dickinson (2014) and assumed a flat spectrum ($\epsilon_\nu \propto \nu^0$) in the UV, where the Lyα efficiency f_α parameterises the uncertain amplitude. We adopt $f_\alpha = 1$ as the fiducial value in this work, but note that this parameter is uncertain and the Lyα emissivity should furthermore vary

spatially (see e.g. Fig. 4 in Semelin, 2016). For illustrative purposes we therefore also show some results in Chapter 3 for the much smaller value of $f_\alpha = 0.01$ (but note that in practise f_α and the reionization history are not fully decoupled). The primary effect of increasing the Lyα efficiency is to produce a tighter coupling of the H I spin and kinetic temperatures while decreasing f_α weakens this coupling. A smaller value of f_α may be more appropriate for absorbers that are distant from the sources of Lyα background photons. Instead of a flat UV spectrum we also considered the power-law population II and III spectra used by Pritchard & Furlanetto (2006), but the strength of the Lyα coupling in our model is not very sensitive to this choice at the redshifts we consider.

The Lyα background has two contributions: emission from stars, and Lyα photons produced by the excitation of H I atoms by X-ray photons. The proper Lyα specific intensity from stars, $J_{\alpha,\star}$, requires consideration of both Lyα and higher order Lyman series photons. This is because the Lyn photons redshift into resonance at redshift z and generate Lyα photons via a series of radiative cascades to lower energies (Pritchard & Furlanetto, 2006), such that

$$J_{\alpha,\star}(z) = \frac{c(1+z)^3}{4\pi} \sum_{n=2}^{n_{\rm max}} f_{\rm n} \int_z^{z_{\rm max}(n)} \frac{\epsilon_{\alpha,\nu'_{\rm n}}(z')}{H(z')(1+z')}\, dz', \tag{2.11}$$

where $f_{\rm n}$ is the probability of producing a Lyα photon from a cascade from level n, $\nu'_{\rm n}$ is the emission frequency at redshift z' that corresponds to absorption by level n at redshift z,

$$\nu'_{\rm n} = \nu_{\rm LL}\left(1 - \frac{1}{n^2}\right)\left(\frac{1+z'}{1+z}\right), \tag{2.12}$$

and $z_{\rm max}(n)$ is the maximum redshift from which an emitted photon will redshift into the Lyn resonance,

$$z_{\rm max}(n) = (1+z)\frac{1-(n+1)^{-2}}{1-n^{-2}} - 1. \tag{2.13}$$

We use the tabulated values for $f_{\rm n}$ from Pritchard & Furlanetto (2006) and assume $n_{\rm max} = 23$ (Barkana & Loeb, 2005). The contribution from H I excitation by X-ray photons is (Pritchard & Furlanetto, 2007)

$$J_{\alpha,{\rm X}}(z) = \frac{\lambda_\alpha}{4\pi H(z)} \sum_i \frac{\phi_\alpha(h_{\rm p}(\nu-\nu_i), x_{\rm e})}{\phi_{\rm heat}(h_{\rm p}(\nu-\nu_i), x_{\rm e})} \mathscr{H}_i, \tag{2.14}$$

where ϕ_α is the fraction of the primary photo-electron energy that is deposited in Lyα photons (Furlanetto & Stoever, 2010).

The Lyα background photons will also heat the IGM by scattering off H I atoms (Chen & Miralda-Escudé, 2004; Chuzhoy & Shapiro, 2007; Ciardi & Salvaterra, 2007; Mittal & Kulkarni, 2021), although this effect is usually small compared to heating by X-ray photons (Ciardi et al., 2010). The Lyα heating rate is

$$\mathscr{H}_\alpha = \frac{4\pi b H(z)}{c\lambda_\alpha} \left(J_{\alpha,\star,{\rm c}}(z) I_{\rm c} + [J_{\alpha,\star,{\rm i}}(z) + J_{\alpha,{\rm X}}(z)] I_{\rm i}\right), \tag{2.15}$$

where $J_{\alpha,\star,{\rm c}}$ is the specific intensity of continuum ($n = 2$) Lyα photons, $J_{\alpha,\star,{\rm i}}$ is the specific intensity of recombination photons injected at the line centre ($n > 2$), and $I_{\rm c}$, $I_{\rm i}$ are the integrals over the Lyα line profile. We use the approximations provided by Furlanetto & Pritchard (2006) for $I_{\rm c}$ and $I_{\rm i}$.

Given the photo-ionization and heating rates, the evolution of the ion-

ization and thermal state of the IGM at fixed gas density may be obtained by solving four coupled differential equations (Bolton & Haehnelt, 2007). We assume all gas is initially neutral and has a kinetic temperature set by adiabatic heating and cooling only,

$$T_{\rm ad} = T_{\rm ad,0}(1+\delta)^{2/3} = 2.73\,{\rm K}\frac{(1+z)^2(1+\delta)^{2/3}}{(1+z_{\rm dec})}, \tag{2.16}$$

where we assume the gas with overdensity δ thermally decouples from the CMB at $z_{\rm dec} = 147.8$ (Furlanetto et al., 2006). The first three differential equations then describe the number density of ionized hydrogen, singly ionized and double ionized helium,

$$\frac{dn_{\rm HII}}{dt} = n_{\rm HI}(\Gamma_{\rm HI} + n_{\rm e}\Gamma_{\rm c,HI}) - n_{\rm HII}n_{\rm e}\alpha_{\rm HII}, \tag{2.17}$$

$$\frac{dn_{\rm HeII}}{dt} = n_{\rm HeI}(\Gamma_{\rm HeI} + n_{\rm e}\Gamma_{\rm c,HeI}) - n_{\rm HeII}n_{\rm e}(\alpha_{\rm HeII} + \alpha_{\rm d}) - \frac{dn_{\rm HeIII}}{dt}, \tag{2.18}$$

$$\frac{dn_{\rm HeIII}}{dt} = n_{\rm HeII}(\Gamma_{\rm HeII} + n_{\rm e}\Gamma_{\rm c,HeII}) - n_{\rm HeIII}n_{\rm e}\alpha_{\rm HeIII}, \tag{2.19}$$

where $\alpha_{\rm i}$ and $\Gamma_{{\rm c},i}$ are, respectively, the recombination rates (Verner & Ferland, 1996) and collisional ionization rates (Voronov, 1997) for species $i = {\rm H\,I}$, ${\rm He\,I}$, ${\rm He\,II}$, and $\alpha_{\rm d}$ is the ${\rm He\,II}$ dielectronic recombination coefficient (Aldrovandi & Pequignot, 1973). The number density of neutral hydrogen, neutral helium and free electrons is

$$n_{\rm HI} = n_{\rm H} - n_{\rm HII}, \tag{2.20}$$

$$n_{\rm HeI} = \frac{Y_{\rm p}}{4(1-Y_{\rm p})}n_{\rm H} - n_{\rm HeII} - n_{\rm HeIII}, \tag{2.21}$$

$$n_{\rm e} = n_{\rm HII} + n_{\rm HeII} + 2n_{\rm HeIII}. \tag{2.22}$$

The fourth differential equation describes the kinetic temperature for gas at fixed overdensity

$$\frac{dT_{\rm K}}{dt} = \frac{2\mu m_{\rm H}}{3k_{\rm B}\rho}[\mathscr{H}_{\rm tot} - \Lambda_{\rm tot}] + \frac{T_{\rm K}}{\mu}\frac{d\mu}{dt} - 2H(t)T_{\rm K}, \tag{2.23}$$

where μ is the mean molecular weight and $\mathscr{H}_{\rm tot}$, $\Lambda_{\rm tot}$ are the total heating and cooling rates per unit volume, respectively.[2]

The total heating rate is

$$\mathscr{H}_{\rm tot} = \mathscr{H}_{\alpha} + \mathscr{H}_{C} + \sum_{i} \mathscr{H}_{i}, \tag{2.24}$$

and the total cooling rate is

$$\Lambda_{\rm tot} = \sum_{i} \Lambda_{{\rm c},i} + \sum_{i} \Lambda_{{\rm ex},i} + \sum_{j} \Lambda_{{\rm rec},j} + \Lambda_{\rm brem} + \Lambda_{\rm C}, \tag{2.25}$$

where the sums are over species $i = {\rm H\,I}, {\rm He\,I}, {\rm He\,II}$ and $j = {\rm H\,II}, {\rm He\,II}, {\rm He\,III}$. We consider contributions to the total cooling rate from collisional ionization, collisional excitation, recombination, bremsstrahlung and inverse Compton scattering of electrons off CMB photons, respectively (cf. Katz et al., 1996). We use the collisional excitation cooling rates from Cen

[2]Note that for X-ray heated gas we can safely neglect the missing $[2T_{\rm K}/3(1+\delta)](d\delta/dt)$ term in Eq. (2.23), as this is small compared to the photo-heating term for gas in the diffuse IGM. Instead, prior to any X-ray or Lyα heating, we just assume the gas kinetic temperature follows the solution of Eq. (2.23) for adiabatic heating and cooling (i.e. Eq. (2.16)). This simplification is advantageous, as a non-local calculation of the heating from adiabatic compression is significantly more complex (see also the discussion of this point in Villanueva-Domingo et al., 2020). In practice, however, we find that even if we ignore the heating from adiabatic compression and assume an initially isothermal IGM, the change to our results in Chapter 3 and 4 (i.e. associated with the 21-cm forest) is negligible. This is because all our heating models in these chapters have experienced appreciable X-ray and Lyα heating by $z = 6$. Finally, recall also that heating from adiabatic compression and shocks for gas with temperatures greater than the $T_{\rm K}$ predicted by Eq. (2.23) is already included self-consistently within our hydrodynamical simulations.

(1992), the inverse Compton cooling rate from Weymann (1965) and the bremsstrahlung cooling rate from Theuns et al. (1998). The recombination and collisional ionization cooling rates are derived from the Verner & Ferland (1996) and Voronov (1997) fits, respectively.

With the emissivities given by Eq. (2.2) and (2.10) in hand, we may evaluate the solution to the cosmological radiative transfer equation (i.e. Eq. (2.4)) to obtain the X-ray specific intensity at photon energies 0.2–30 keV (Pritchard & Loeb, 2012) and similarly obtain the specific intensity of the Lyα background by evaluating Eq. (2.11), following Pritchard & Furlanetto (2006). Fig. 2.2 shows the redshift evolution of the specific intensity of the Lyα background from stellar emission, $J_{\alpha,\star}(z)$, and the specific intensity of the X-ray background at three different energies, 0.2 keV, 1 keV and 2 keV. The dashed curves show the X-ray specific intensities in the optically thin limit, i.e. when the optical depth of the intervening IGM to X-ray photons is set to zero in Eq. (2.4). Note that $J_{2.0\,\mathrm{keV}}$ remains almost unchanged in the optically thin limit, implying the IGM is transparent to photons emitted with energies ≥ 2 keV at $z \lesssim 10$ (cf. McQuinn, 2012).

The unresolved soft X-ray background at $z = 0$ places an upper limit on the contribution of high redshift sources to the hard X-ray background, because these photons may redshift without significant absorption to $z = 0$ (Dijkstra et al., 2004; McQuinn, 2012). When assuming $f_{\mathrm{X}} = 1.8$, integrating our model specific intensity in the soft X-ray band (0.5-2 keV) at $z = 0$ yields $J_{0.5-2\mathrm{keV}} = 2.9 \times 10^{-12}\,\mathrm{erg\,s^{-1}cm^{-2}\,deg^{-2}}$. This value is consistent with the unresolved soft X-ray background obtained from Chandra observations of the COSMOS legacy field, $J_{0.5-2\mathrm{keV}} = 2.9 \pm$

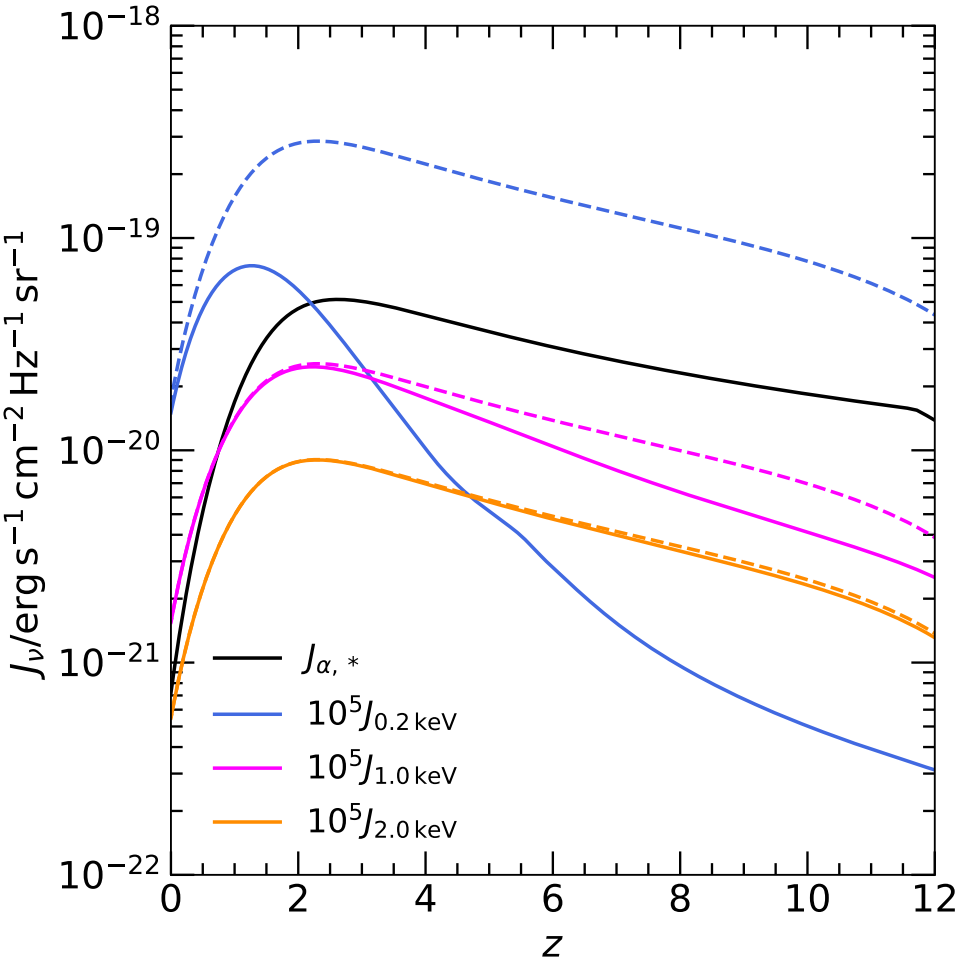

Figure 2.2: The redshift evolution of the specific intensity of the Lyα background from stars for a Lyα efficiency $f_\alpha = 1$ (solid black curve) and the specific intensity of the X-ray background for photon energies 0.2 keV (blue curve), 1 keV (fuchsia curve) and 2 keV (orange curve), assuming an X-ray efficiency of $f_{\rm X} = 1$. The X-ray specific intensities have been multiplied by a factor of 10^5 for presentation purposes. For comparison, the dashed curves show the X-ray specific intensities evaluated in the optically thin limit.

$0.16 \times 10^{-12}\,\mathrm{erg\,s^{-1}cm^{-2}\,deg^{-2}}$ (Cappelluti et al., 2017). Note, however, the $z = 0$ soft X-ray background does not provide a direct constraint on the very uncertain soft X-ray background at high redshift (see e.g. Dijkstra et al., 2012; Fialkov et al., 2017). Recently, Greig et al. (2021a)

have presented the first weak, model dependent lower limits on the soft X-ray background emissivity at $6.5 \leq z \leq 8.7$ using the Murchison Wide-field Array (MWA) upper limits on the 21-cm power spectrum (Trott et al., 2020), where $\epsilon_{\rm X,0.5-2\,keV} \gtrsim 10^{34.5}{\rm erg\,s^{-1}\,cMpc^{-3}}$. For comparison, for an X-ray efficiency of $f_{\rm X} = 0.01$, our X-ray background model gives $\epsilon_{\rm X,0.5-2\,keV} = 10^{36.0}\,{\rm erg\,s^{-1}\,cMpc^{-3}}$ at $z = 8.1$, which is well above the Greig et al. (2021a) lower limit.

Given the specific intensities of the X-ray and Lyα radiation backgrounds, we next compute the thermal evolution of the IGM that remains optically thick to UV photons, but is heated by X-ray and Lyα backgrounds that are assumed to be spatially uniform on the scale of our simulated volume. Given that the mean free path to X-ray photons is

$$\lambda_{\rm X} = 5\,{\rm cMpc}\,x_{\rm HI}^{-1}(1+\delta)^{-1}(E/0.2\,{\rm keV})^{2.8}[(1+z)/10]^{-2}, \tag{2.26}$$

fluctuations in the temperature of soft X-ray heated gas on $\sim 10\,{\rm cMpc}$ scales are thus expected (Pritchard & Furlanetto, 2007; Ross et al., 2017; Eide et al., 2018). These fluctuations would not, however, be adequately captured in our small simulation volume. We follow the procedure described above for this purpose. Fig. 2.3 displays the temperature evolution of a gas parcel at mean density for five different values of the X-ray efficiency parameter $f_{\rm X}$. An approximate lower limit on $f_{\rm X}$ is provided by the recent constraints on the spin temperature from upper limits on the 21-cm power spectrum at $z \simeq 9.1$ obtained with LOFAR (Mertens et al., 2020) and at $z = 6.5 - 8.7$ from MWA (Trott et al., 2020). These data disfavour very cold reionization models with no X-ray heating (Ghara et al., 2020;

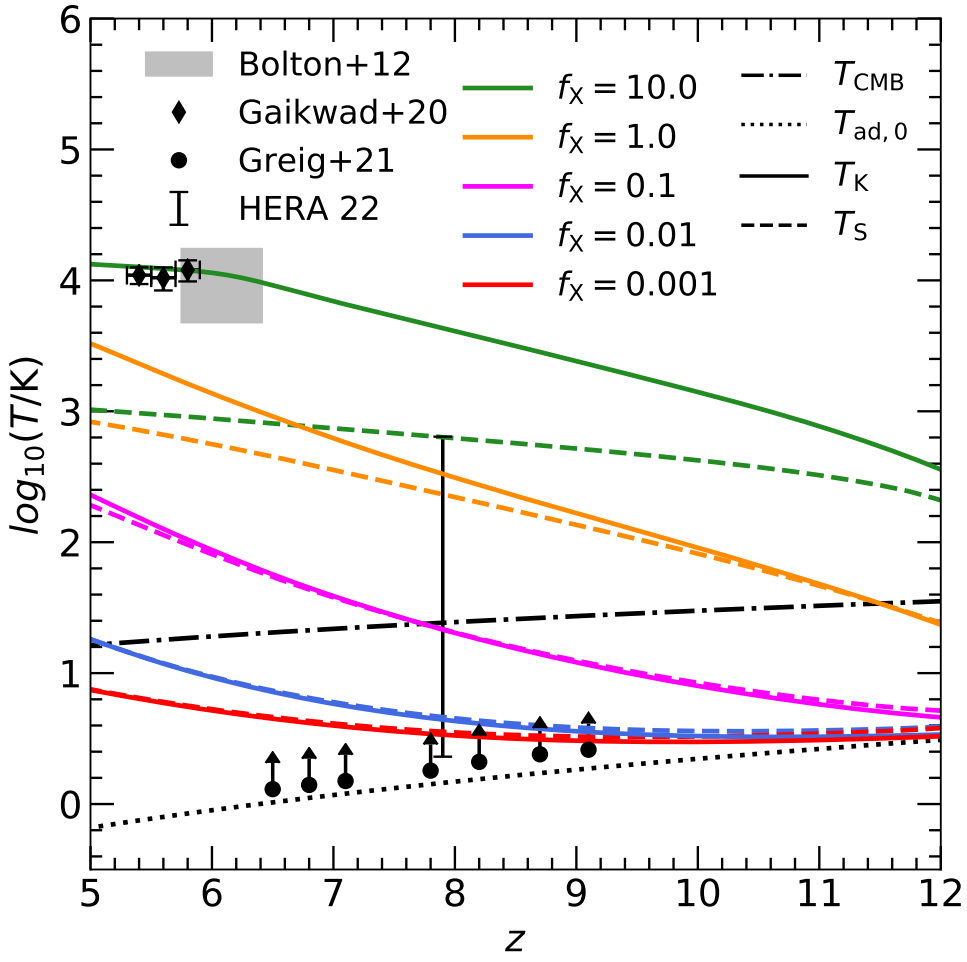

Figure 2.3: The redshift evolution of the gas kinetic temperature, T_K, (solid curves) and spin temperature, T_S, (dashed curves) at mean density following X-ray background heating by photons with $E = 0.2$–$30\,\mathrm{keV}$. The different coloured curves correspond to efficiency parameter $f_X = 10$ (green curves), 1 (orange curves), 0.1 (fuchsia curves), 0.01 (blue curves) and 0.001 (red curves). For comparison, the CMB temperature, $T_{CMB} = 2.73\,\mathrm{K}(1+z)$ corresponds to the dot-dashed curve, and the kinetic temperature for adiabatic heating and cooling only, $T_{ad,0} = 2.73\,\mathrm{K}(1+z)^2/(1+z_{dec})$, is shown by the dotted curve. We assume the gas thermally decouples from the CMB at $z_{dec} = 147.8$ (Furlanetto et al., 2006). The filled diamonds and grey shading correspond to the gas kinetic temperature measurements from Lyα transmission spikes in quasar spectra (Gaikwad et al., 2020) and Lyα absorption lines in quasar proximity zones (Bolton et al., 2012), respectively. The filled circles show the model dependent lower limits on the H I spin temperature obtained from LOFAR (Greig et al., 2021b) and MWA (Greig et al., 2021a). The black vertical line indicates the 95% confidence interval for T_S from HERA (The HERA Collaboration, 2022a).

Mondal et al., 2020; Greig et al., 2021a,b). Furthermore, an approximate upper limit on $f_{\rm X}$ at $z > 6$ is provided by Lyα absorption measurements of the kinetic temperature at $z \simeq 5$–6, after the IGM has been photo-ionized and heated by UV photons (Bolton et al., 2012; Gaikwad et al., 2020). These data are consistent with $f_{\rm X} \simeq 10$. Adopting larger X-ray efficiencies in our model would overheat the low density IGM by $z = 6$. In addition, at $z = 7.9$ this model predicts an IGM spin temperature at the mean density of $T_{\rm S} = 3.6\,{\rm K}$–$634.6\,{\rm K}$ for $f_{\rm X} = 0.001$–10, which is consistent with the recent constraint of $2.3\,{\rm K} < T_{\rm S} < 640\,{\rm K}$ (95 per cent confidence) from The HERA Collaboration (2022a) inferred from upper limits on the 21-cm power spectrum acquired by HERA (The HERA Collaboration, 2022b).

2.3 Summary

In this chapter I have described numerical simulations based on a novel approach of combining hydrodynamics with radiative transfer which are a part of Sherwood-Relics simulation suite. These simulations are calibrated such that they broadly agree with various observations including the neutral hydrogen fraction and Thomson scattering optical depth (see Fig. 2.1). All simulations follow 2×2048^3 dark matter and baryonic particles in $(40h^{-1}\,{\rm cMpc})^3$ volume. While the rarest and largest neutral hydrogen islands are not captured in these simulation, high mass resolution allows the modelling of small scale structure which is important for the 21-cm forest studies. Furthermore, the heating by Lyα and X-ray background radiation is missing in these simulations and hence I include it in the post-processing. I will explore a wide range of X-ray background efficiencies

spanning from $f_{\rm X} = 0.001$ to 10 which are consistent with multiple measurements of the 21-cm power spectrum (Greig et al., 2021a,b; The HERA Collaboration, 2022a) and the gas kinetic temperature at $z \approx 6$ (Bolton et al., 2012; Gaikwad et al., 2020). I will use two reionization models in which the reionization is completed by $z_{\rm R} = 5.3$ (RT-late) and $z_{\rm R} = 6.6$ (RT-early) in Chapter 3. In addition to these models, I will use RT-mid reionization model with $z_{\rm R} = 6$ in Chapter 4. The novel RT-late model is the main focus of my thesis.

Chapter 3

The detectability of strong 21-cm forest absorbers from the diffuse intergalactic medium in late reionization models

This chapter is based on the published paper Šoltinský et al. (2021) in Monthly Notices of Royal Astronomical Society Volume 506, Issue 4, Pages 5818-5835. Appendix A and C have been moved to appropriate places in the body of this chapter. Other modifications include a shortened introduction and minor formatting changes.

3.1 Introduction

At present, the premier technique for examining the small-scale structure of intergalactic neutral hydrogen approaching the reionization era is Lyman

series absorption in the spectra of luminous quasars (Becker et al., 2015b; Eilers et al., 2017; Bosman et al., 2018; Yang et al., 2020b). However, it is challenging to probe the intergalactic medium (IGM) much beyond redshift $z \simeq 6$ with this approach. The large cross-section for Lyα scattering means the IGM becomes opaque to Lyα photons at neutral hydrogen fractions as low as $x_{\rm HI} \simeq 10^{-4}$. An alternative transition that overcomes this limitation is the hyperfine 21-cm line, which has a cross-section that is a factor $\sim 10^7$ smaller than the Lyα transition[1]. If radio-bright sources such as high redshift quasars (Bañados et al., 2021) or gamma-ray bursts (e.g. Ioka & Mészáros, 2005; Ciardi et al., 2015b) can be identified during the reionization era, the intervening neutral IGM may be observed as a 21-cm forest of absorption lines in their spectra. This can be achieved either through the direct identification of individual absorption features (Carilli et al., 2002; Furlanetto & Loeb, 2002; Meiksin, 2011; Xu et al., 2011; Ciardi et al., 2013; Semelin, 2016; Villanueva-Domingo & Ichiki, 2022), or by the statistical detection of the average 21-cm forest absorption (Mack & Wyithe, 2012; Ewall-Wice et al., 2014; Thyagarajan, 2020). This approach is highly complementary to proposed tomographic studies of the redshifted 21-cm line and measurements of the 21-cm power spectrum during reionization (e.g. Mertens et al., 2020; Trott et al., 2020), as it is subject to a different set of systematic uncertainties (Furlanetto et al., 2006; Pritchard & Loeb, 2012).

However, any detection of the 21-cm forest relies on the identification of sufficient numbers of radio-loud sources and the existence of cold, neutral

[1]Low ionization metal lines such as O I (Oh, 2002; Keating et al., 2014) and Mg II (Hennawi et al., 2021) can also be used to trace neutral intergalactic gas, although the uncertain metallicity of the high redshift IGM further complicates their interpretation.

gas in the IGM at $z \gtrsim 6$. While neither of these criteria are guaranteed, the prospects for both have improved somewhat in the last few years. Approximately ~ 10 radio-loud active galactic nuclei are now known at $5.5 < z < 6.5$ (e.g. Bañados et al., 2018b, 2021; Liu et al., 2021; Ighina et al., 2021), including the $z = 6.1$ blazar PSO J0309+27 with a flux density $S_{147\,\mathrm{MHz}} = 64.2 \pm 6.2\,\mathrm{mJy}$ (Belladitta et al., 2020). The Low Frequency Array (LOFAR) Two-metre Sky Survey (LoTSS, Shimwell et al., 2017; Kondapally et al., 2021), the Giant Metrewave Radio Telescope (GMRT) all sky radio survey at 150 MHz (Intema et al., 2017), and the Galactic and Extragalactic All-sky Murchison Widefield Array survey (GLEAM, Wayth et al., 2015) are also projected to detect hundreds of bright $z > 6$ radio sources, particularly if coupled with large spectroscopic follow-up programmes such as the William Herschel Telescope Enhanced Area Velocity Explorer (WEAVE)-LOFAR survey (Smith et al., 2016).

Furthermore, there is now growing evidence that reionization ended rather late, and possibly even extended to redshifts as late as $z \simeq 5.3$ (Kulkarni et al., 2019; Nasir & D'Aloisio, 2020; Qin et al., 2021). This picture is motivated by the large spatial fluctuations observed in the Lyα forest transmission at $z \simeq 5.5$ (Becker et al., 2015b; Eilers et al., 2018). More observations supporting this scenario are discussed in Section 1.3. If this interpretation proves to be correct (but see D'Aloisio et al., 2015; Davies & Furlanetto, 2016; Chardin et al., 2017; Meiksin, 2020, for alternative explanations), then there should still be large islands of neutral hydrogen in the IGM as late as $z = 6$ (e.g. Lidz et al., 2007; Mesinger, 2010). If this neutral gas has not already been heated to kinetic temperatures $T_\mathrm{K} \gtrsim 10^3\,\mathrm{K}$ by the soft X-ray background, then it may be possible to detect 21-cm absorbers

in the pre-reionization IGM at $z \simeq 6$. Alternatively, a null-detection could provide a useful lower limit on the soft X-ray background at high redshift.

The goal of this work is to investigate this possibility further. We use a set of high resolution hydrodynamical cosmological simulations drawn from the Sherwood-Relics simulation programme (Puchwein et al., 2022). Using a novel hybrid approach, these are combined with the ATON radiative transfer code (Aubert & Teyssier, 2008) to model the small-scale structure of the IGM. Following Kulkarni et al. (2019), we consider a model with late reionization ending at $z = 5.3$, and contrast this with a simulation that has an earlier end to reionization at $z = 6.6$ (i.e. RT-early and RT-late, see Fig.2.1). We pay particular attention to some of the common assumptions adopted in previous models of the 21-cm forest that affect the absorption signature on small scales. This includes the treatment of gas peculiar motions and thermal broadening, the coupling of the spin temperature to the Lyα background, and the effect of pressure (or Jeans) smoothing on the IGM. Our approach is therefore closest to the earlier work by Semelin (2016), although we do not follow spatial variations in the X-ray and Lyα backgrounds. Instead, we attempt to explore a broader range of parameter space for spatially uniform X-ray heating using hydrodynamical simulations that use several different reionization histories and have an improved mass resolution (by a factor ~ 27). Note, however, that even the high resolution cosmological simulations considered here will still only capture the 21-cm absorption that arises from the diffuse IGM. We therefore do not model the (uncertain amount of) absorption from neutral gas in haloes below the atomic cooling threshold, or from the cold interstellar medium in much rarer, more massive haloes that host high redshift galaxies

(see e.g. Furlanetto & Loeb, 2002; Meiksin, 2011).

This chapter is structured as follows. We start by describing our calculation of the 21-cm optical depths in Section 3.2. We examine how different modelling assumptions affect the observability of strong 21-cm forest absorbers in Section 3.3.1 and 3.3.2, and estimate how a null-detection of strong 21-cm absorbers at redshift $z \simeq 6$ with LOFAR or the Square Kilometre Array (SKA) could constrain the high redshift soft X-ray background in Section 3.3.3. Finally, we conclude in Section 3.4.

3.2 The 21-cm forest optical depth

Firstly, we will describe the calculation of the 21-cm optical depth. The 21-cm line arises from the hyperfine structure of the hydrogen atom, and is determined by the relative orientation of the proton and electron spin, where the ground state energy level is split into a singlet and triplet state. A photon with rest-frame wavelength $\lambda_{21} = 21.11\,\mathrm{cm}$, or equivalently frequency $\nu_{21} = 1420.41\,\mathrm{MHz}$, can induce a transition between these two states.

In the absence of redshift space distortions, the optical depth to 21-cm photons at redshift z is

$$\begin{aligned} \tau_{21}(z) &= \frac{3h_{\mathrm{p}}c^3A_{10}}{32\pi\nu_{21}^2k_{\mathrm{B}}}\frac{n_{\mathrm{HI}}(z)}{T_{\mathrm{S}}(z)H(z)}, \\ &= 0.27x_{\mathrm{HI}}\left(\frac{1+\delta}{10}\right)\left(\frac{T_{\mathrm{S}}}{10\,\mathrm{K}}\right)^{-1}\left(\frac{1+z}{10}\right)^{3/2}, \end{aligned} \tag{3.1}$$

where n_{HI} is the H I number density, T_{S} is the spin temperature, $A_{10} = 2.85 \times 10^{-15}\,\mathrm{s}^{-1}$ is the Einstein spontaneous emission coefficient for the

hyperfine transition, δ is the gas overdensity and $H(z)$ is the Hubble parameter (Madau et al., 1997). Note the factor of 0.27 in the second equality is cosmology dependent. Absorption will therefore be most readily observable for dense, cold and significantly neutral hydrogen gas. The H I spin temperature, a measure of the relative occupation numbers of the singlet and triplet states, is (Field, 1958)

$$T_{\rm S}^{-1} = \frac{T_{\rm CMB}^{-1} + x_\alpha T_\alpha^{-1} + x_{\rm c} T_{\rm K}^{-1}}{1 + x_\alpha + x_{\rm c}}, \tag{3.2}$$

where $T_{\rm CMB} = 2.73(1+z)\,{\rm K}$ is the temperature of the cosmic microwave background (CMB, Fixsen, 2009), T_α is the Lyα colour temperature and $x_{\rm c}$, x_α are the coupling coefficients for collisions and Lyα photon scattering, respectively. If $x_{\rm c} + x_\alpha \gg 1$, the H I spin temperature is coupled to the gas kinetic temperature, and if $x_{\rm c} + x_\alpha \ll 1$ it is coupled to the CMB temperature.

The collisional coupling coefficient is

$$x_{\rm c} = \frac{T_\star}{A_{10} T_{\rm CMB}} (\kappa_{10}^{\rm HH} n_{\rm H} + \kappa_{10}^{\rm eH} n_{\rm e} + \kappa_{10}^{\rm pH} n_{\rm p}), \tag{3.3}$$

where $T_\star = h_{\rm p}\nu_{21}/k_{\rm B}$, and $\kappa_{10}^{\rm HH}$, $\kappa_{10}^{\rm eH}$, $\kappa_{10}^{\rm pH}$ are the temperature dependent de-excitation rates for collisions between hydrogen atoms, electrons and hydrogen atoms, and protons and hydrogen atoms, respectively. We use the convenient fitting functions to the de-excitation rates from Kuhlen et al. (2006) and Liszt (2001), modified to better agree with tabulated values for $\kappa_{10}^{\rm HH}$ (Furlanetto et al., 2006), $\kappa_{10}^{\rm eH}$ (Furlanetto & Furlanetto, 2007a), and $\kappa_{10}^{\rm pH}$ (Furlanetto & Furlanetto, 2007b) over the range $1\,{\rm K} \leq T_{\rm K} \leq 10^4\,{\rm K}$.

The coupling coefficient for Lyα scattering is (Wouthuysen, 1952; Field,

1958; Madau et al., 1997)

$$x_\alpha = \frac{2T_\star \lambda_\alpha^3 \Lambda_\alpha}{9T_{\rm CMB} A_{10} h_{\rm p} c} S_\alpha J_\alpha, \tag{3.4}$$

where $\lambda_\alpha = 1215.67$ Å, $\Lambda_\alpha = 6.265 \times 10^8\,{\rm s}^{-1}$ is the Einstein spontaneous emission coefficient for the Lyα transition, S_α is a factor of order unity that corrects for the spectral distortions in the Lyα spectrum, and J_α is the proper Lyα specific intensity in units ${\rm erg\,s^{-1}\,cm^{-2}\,Hz^{-1}\,sr^{-1}}$. We use the fits provided by Hirata (2006) to calculate T_α and S_α, where $T_{\rm S}$, T_α and S_α must be solved for iteratively.

In this work we also include the effect of redshift space distortions on the 21-cm forest absorption features. In our calculation of the 21-cm optical depth, we therefore include a convolution with the Gaussian line profile and incorporate the gas peculiar velocities from our hybrid RT/hydrodynamical simulations. The optical depth in Eq. (3.1) may then be calculated in discrete form as (e.g. Furlanetto & Loeb, 2002)

$$\tau_{21,i} = \frac{3h_{\rm p}c^3 A_{10}}{32\pi^{3/2}\nu_{21}^2 k_{\rm B}} \frac{\delta v}{H(z)} \sum_{j=1}^{N} \frac{n_{{\rm HI},j}}{b_j T_{{\rm S},j}} \exp\left(-\frac{(v_{{\rm H},i} - u_j)^2}{b_j^2}\right), \tag{3.5}$$

for pixel i with Hubble velocity $v_{{\rm H},i}$ and velocity width[2] δv. Here $b = (2k_{\rm B}T_{\rm K}/m_{\rm H})^{1/2}$ is the Doppler parameter, $T_{\rm K}$ is the gas kinetic temperature, $u_j = v_{{\rm H},j} + v_{{\rm pec},j}$, and $v_{\rm pec}$ is the peculiar velocity of the gas. We evaluate Eq. (3.5) in our simulations by extracting a total of 5000 periodic lines of sight, drawn parallel to the simulation box axes at redshift intervals of

[2]Note the width of the pixel must be smaller than the typical thermal width of an absorber, $\Delta\nu_{21} = 0.61(T_{\rm K}/10^2\,{\rm K})^{1/2}\,{\rm kHz}$, to ensure the optical depths obtained using Eq. (3.5) are converged. In this work we resample the simulation outputs using linear interpolation to achieve the required pixel size. Alternatively, the line profile may be evaluated using error functions (Meiksin, 2011; Hennawi et al., 2021).

$\Delta z = 0.1$ over the range $5 \leq z \leq 12$. The total path length we use to make our mock 21-cm forest spectra at each output redshift is therefore $200h^{-1}$ cGpc.

The redshift evolution of the transmission, $F = e^{-\tau_{21}}$, for a random selection of 21-cm forest spectra drawn from the RT-late simulation is shown in Fig. 3.1, for three different X-ray efficiencies. No instrumental features have been added to the simulated data. The detailed small-scale structure of the 21-cm absorption is displayed in the insets. One can see the strong effect that X-ray heating has on the 21-cm absorption as the X-ray efficiency parameter is increased from $f_{\rm X} = 0.01$ in the top panel, to $f_{\rm X} = 1$ in the bottom panel (cf. Xu et al., 2011; Mack & Wyithe, 2012). The redshift evolution due to the increasing filling factor of warm ($T_{\rm K} \sim 10^4$ K), photo-ionized gas is also apparent. In particular, the occurrence of gaps in the 21-cm forest absorption due to extended regions of ionized gas increases toward lower redshift.

In order to better identify the gas associated with the absorption, we calculate the optical depth weighted density, $\Delta_{\rm w} = 1 + \delta_{\rm w}$, and optical depth weighted kinetic temperature, $T_{\rm K,w}$, for each pixel in our RT-late mock spectra for $f_{\rm X} = 0.1$. This is analogous to the approach used to study the properties of gas responsible for absorption in the Lyα forest (Schaye et al., 1999); peculiar motions (and to a much lesser extent, line broadening) would otherwise distort the mapping between 21-cm optical depth, temperature and gas density. The results are shown in Fig. 3.2, where the temperature-density plane is displayed for the RT-late simulation at three different redshifts: $z = 9$ (top), 7.5 (middle) and 6 (bottom). The colour bar and contours show the average 21-cm optical depth and the

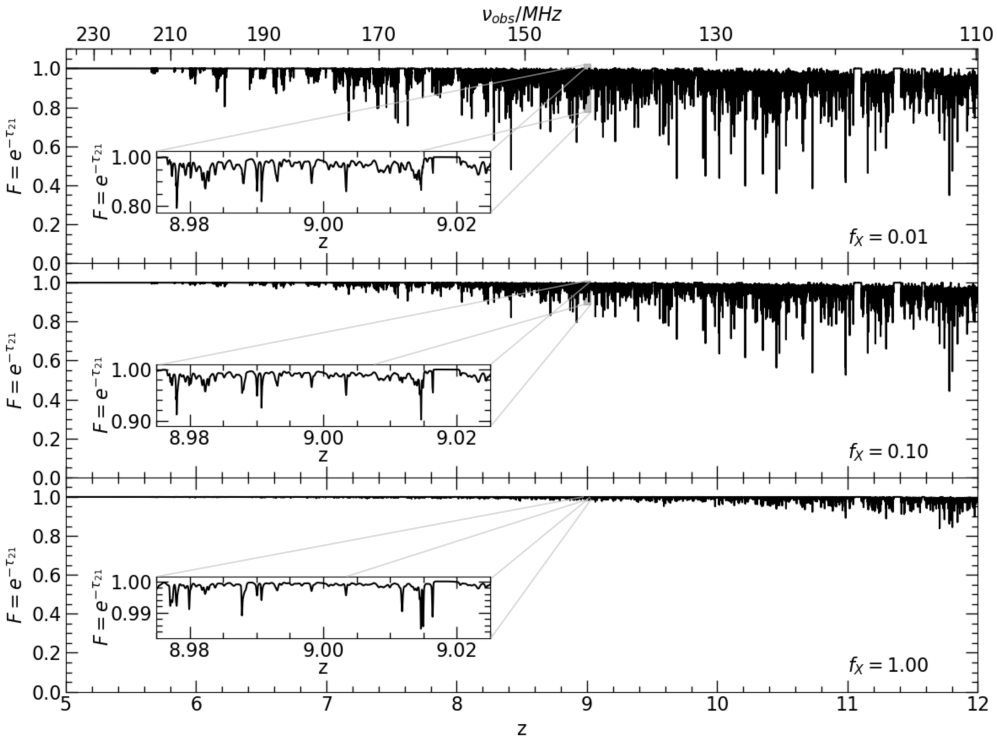

Figure 3.1: The redshift evolution of the 21-cm forest transmission, $F = e^{-\tau_{21}}$, in the RT-late simulation for a Lyα efficiency $f_\alpha = 1$ and an X-ray efficiency of $f_{\rm X} = 0.01$ (top), 0.1 (middle) and 1 (bottom). The inset displays a zoom-in on part of the 21-cm forest at redshift $z \sim 9$ – note the different scales on the vertical axes of the inset. The incidence of gaps in the 21-cm forest, which are associated with large regions of ionized gas, increases toward lower redshift, and become particularly apparent in the $f_{\rm X} = 0.01$ model at redshift $z < 7$. No instrumental features have been added to the spectra.

relative number density of the pixels, respectively.

The gas distribution in Fig. 3.2 is bimodal, with the bulk of the pixels associated with either warm ($T_{\rm K} \sim 10^4\,{\rm K}$), photo-ionized gas or cold ($T_{\rm K} \leq 10^2\,{\rm K}$), significantly neutral regions (see also Ciardi et al., 2013; Semelin, 2016). The plume of gas at intermediate temperatures has been heated by shocks from structure formation. Note, furthermore, that in this very late reionization model the IGM is still not fully ionized by $z = 6$. The largest optical depths in the model arise not from the highest density gas,

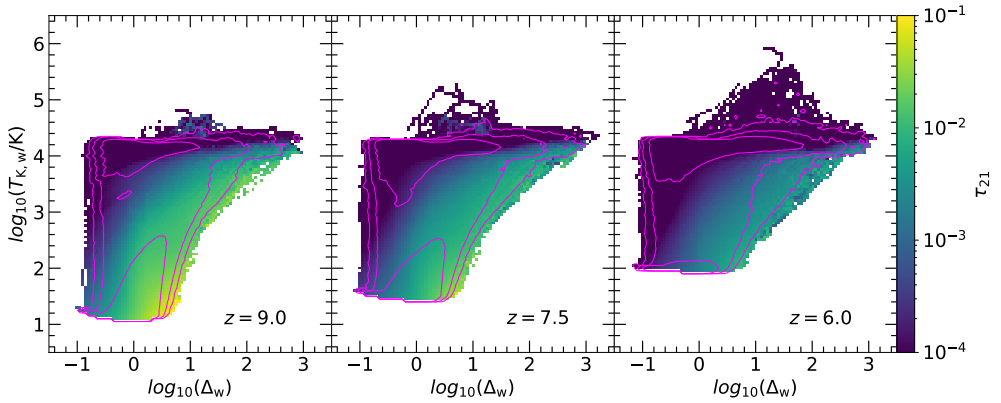

Figure 3.2: The optical depth weighted temperature-density plane for gas in the RT-late simulation at redshift $z = 9$ (left panel), 7.5 (middle panel) and 6 (right panel), for an X-ray efficiency $f_{\rm X} = 0.1$ and Lyα efficiency $f_\alpha = 1$. The colour scale shows the average 21-cm optical depth at each point in the plane. The number density of points increases by 1 dex for each contour level.

but the cold, diffuse IGM with $3 < \Delta < 10$. This is because gas at higher densities is typically reionized early due to proximity to the ionizing sources, and also because gas around haloes (with $\Delta \gtrsim 100$) is shock-heated and partially collisionally ionized. Toward lower redshift, the increase in the minimum kinetic temperature of the neutral gas due to X-ray heating, the partial ionization of the H I by secondary electrons and collisions, and the decrease in the proper number density of gas at fixed overdensity, all conspire to lower the maximum optical depth. The contours furthermore show that the regions with the largest optical depths are at least 100 times rarer than the bulk of the cold, neutral gas. Nevertheless, in this very late reionization model, it remains possible that some detectable 21-cm absorption may persist as late as $z \simeq 6$. We now explore this possibility in more detail.

3.3 The detectability of 21-cm forest absorption for very late reionization

3.3.1 The volume averaged 21-cm optical depth

We first consider the redshift evolution of the volume averaged 21-cm optical depth, $\langle\tau_{21}\rangle$, in the RT-late simulation, displayed as the solid curves in Fig. 3.3 for our fiducial model with $f_\alpha = 1$. In the left panel, we test the common assumption that, as a result of the Wouthuysen-Field effect, the spin temperature becomes strongly coupled to the gas kinetic temperature during the later stages of reionization, such that $T_\mathrm{S} = T_\mathrm{K}$ (e.g. Xu et al., 2009; Mack & Wyithe, 2012; Ciardi et al., 2013). This is shown by the dashed curves in the left panel of Fig. 3.3. As also noted by Semelin (2016), a full calculation of T_S using Eq. (3.2) can either reduce or enhance 21-cm optical depths relative to the value obtained assuming strong coupling. This is caused by a partial coupling of the spin temperature to the CMB temperature; if $T_\mathrm{K} < T_\mathrm{CMB}$, the full calculation will result in a higher spin temperature and smaller 21-cm optical depth, and vice versa.

This can be observed in Fig. 3.3 for $f_\mathrm{X} = 0.1$ (fuchsia curves), where $\langle\tau_{21}\rangle$ for the full calculation assuming $f_\alpha = 1$ (solid curves) is smaller than the $T_\mathrm{S} = T_\mathrm{K}$ case (dashed curves) at $z \gtrsim 8$, but is greater at lower redshifts. This coincides with the temperature evolution shown in Fig. 2.3, particularly the transition from $T_\mathrm{K} < T_\mathrm{CMB}$ (and $T_\mathrm{S} > T_\mathrm{K}$) at $z > 8$ to $T_\mathrm{K} > T_\mathrm{CMB}$ (and $T_S < T_K$) at $z < 8$. Similarly, in the case of a weaker ($f_\mathrm{X} = 0.01$, blue curves) or stronger ($f_\mathrm{X} = 1$, orange curves) X-ray background, the full T_S calculation respectively decreases or increases $\langle\tau_{21}\rangle$ relative to the strong

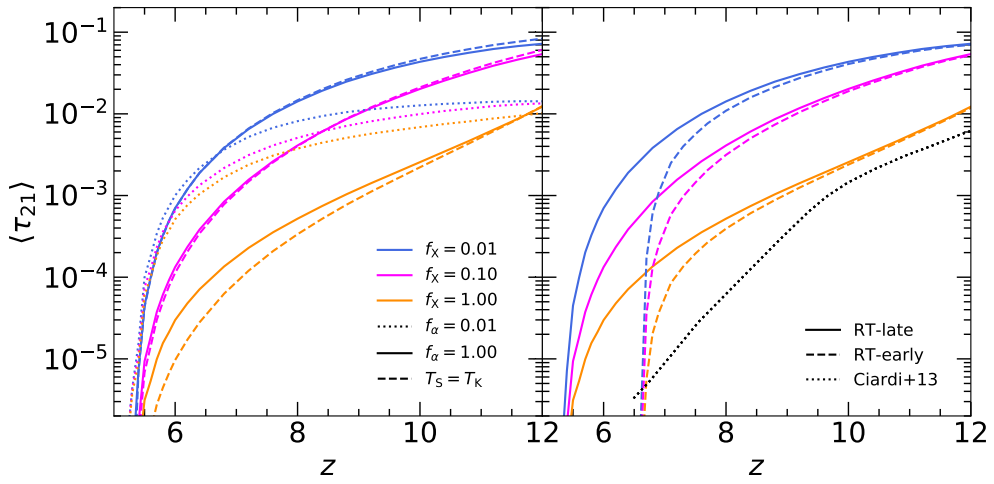

Figure 3.3: Redshift evolution of the volume averaged 21-cm optical depth in the RT-late model (solid curves) for a Lyα efficiency $f_\alpha = 1$ and an assumed X-ray efficiency of $f_X = 0.01$ (blue curves), 0.1 (fuchsia curves) and 1 (orange curves). In the left panel, this is compared to results from the same hybrid RT/hydrodynamical simulation, but with 21-cm optical depths calculated under the assumption of strong (i.e. $T_S = T_K$, shown by the dashed curves) and weak Lyα coupling ($f_\alpha = 0.01$, shown by the dotted curves). In the right panel, the dashed curves instead show $\langle\tau_{21}\rangle$ for the hybrid model with an earlier end to reionization (RT-early). The dotted black curve in the right panel corresponds to the RT+Lyα+x model from fig. 2 of Ciardi et al. (2013).

coupling approximation. The dotted curves furthermore show the $\langle\tau_{21}\rangle$ redshift evolution for significantly weaker Lyα coupling, with $f_\alpha = 0.01$. In this case T_S is now decoupled from T_K and has a value similar to T_{CMB}. The weak coupling means $\langle\tau_{21}\rangle$ is significantly increased in the models with efficient X-ray heating. Hence, while the assumption of strong coupling, $T_S = T_K$, remains a reasonable approximation if $f_\alpha = 1$, this will not be the case if the background Lyα emissivity is significantly overestimated in our fiducial model (i.e. $f_\alpha \ll 1$).

The right panel of Fig. 3.3 instead shows $\langle\tau_{21}\rangle$ for the two different reionization histories in Fig. 2.1. Both of these reionization models are broadly consistent with existing constraints on the timing of reionization, and the

RT-late model furthermore successfully reproduces the large fluctuations in the Lyα forest opacity at $z = 5.5$ (Kulkarni et al., 2019). For comparison, we also show $\langle \tau_{21} \rangle$ from Ciardi et al. (2013) as the dotted curve. This includes X-ray and Lyα heating following Ciardi et al. (2010), and is most similar to our RT-early simulation with $f_{\rm X} \simeq 1$. The differences between this work and Ciardi et al. (2013) are due to different assumptions for the X-ray emissivity and the reionization history. A later end to reionization means $\langle \tau_{21} \rangle$ in Fig. 3.3 remains significantly larger than earlier reionization models at redshifts $6 \lesssim z \lesssim 7$. If reionization does indeed complete late, such that large neutral islands persist in the IGM at $z \simeq 6$ (e.g. Lidz et al., 2007; Mesinger, 2010), this suggests 21-cm forest absorption lines may be more readily observable than previously thought at these redshifts.

3.3.2 The differential number density of 21-cm absorption lines

We now consider the number density of individual absorption lines in our high resolution mock spectra. We present this as the total number of lines, N, within a given optical depth bin, per unit redshift (see also Furlanetto, 2006a; Shimabukuro et al., 2014), where

$$f(\tau_{21}, z) = \frac{\partial^2 N}{\partial \tau_{21} \partial z}. \tag{3.6}$$

The absorption lines in our simulated 21-cm forest spectra are identified following a similar method to Garzilli et al. (2015), who identify absorption lines in mock Lyα forest spectra as local optical depth maxima located between two minima. In this work, we require that the local maxima must

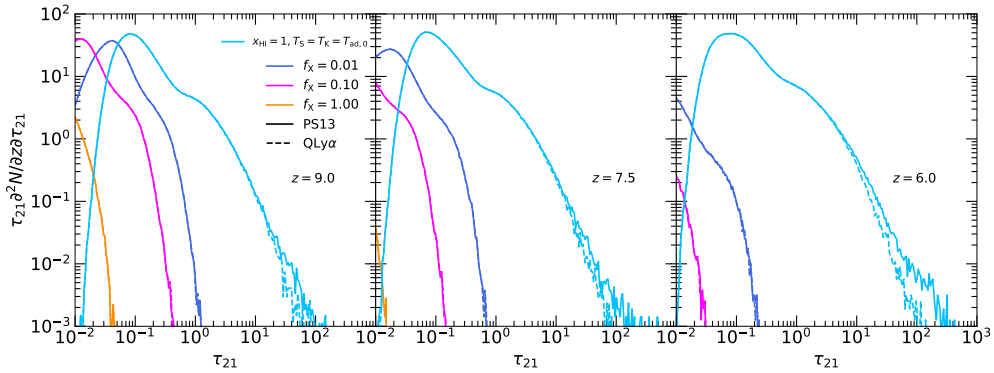

Figure 3.4: The differential line number density distribution for 21-cm forest absorption features in simulations that use two different implementations for the treatment of dense gas. The dashed curves displays the simplified approach used in this work (the QLyα simulation), whereas the solid curves use the sub-grid star formation and feedback model from Puchwein & Springel (2013) (the PS13 simulation, solid line). The results are shown at three different redshifts: $z = 9$ (top), 7.5 (middle) and 6 (bottom). The X-ray efficiencies are $f_{\rm X} = 0.01$ (blue curves), 0.1 (fuchsia curves) and 1 (orange curves). For comparison, the cyan curves show the distribution for fully neutral, unheated gas with temperature equal to the adiabatic temperature at mean density (i.e. $x_{\rm HI} = 1$ and $T_{\rm S} = T_{\rm K} = T_{\rm ad,0}$).

have a prominence (i.e. be higher by a certain value than the minima) that corresponds to a factor of 1.001 difference in the transmitted flux, $F = e^{-\tau_{21}}$, between the line base and peak. We then define the optical depth for each identified line as being equal to the local maximum. We find this method is robust for lines with $\tau_{21} \geq 10^{-2}$ (i.e. $F = e^{-\tau_{21}} \leq 0.99$), but for optical depths below this threshold the number of lines is sensitive to the choice for the prominence, and is thus unreliable.

Firstly, we will use the number density distributions, $\tau_{21} f(\tau_{21}, z)$, to test whether our approximate prescription for converting dense gas into collisionless particles affects our results for the 21-cm forest. As discussed in Section 2.1, we adopt a simplified scheme for the treatment of dense, star forming gas in the Sherwood-Relics simulations, where all gas particles with density $\Delta > 1000$ and temperature $T_{\rm K} < 10^5$ K are converted to collisionless

star particles (Viel et al., 2004). As a consequence, very dense, cold halo gas is not included in the Sherwood-Relics models. In Fig. 3.4 we compare two models drawn from the Sherwood simulation suite (Bolton et al., 2017) that use the same box size, mass resolution and initial conditions as the other simulations used in this work. These two additional simulations use either the simplified scheme used in this study (QLyα) or the star formation and energy driven winds prescription of Puchwein & Springel (2013, PS13). The only difference between these two models is the incorporation of dense, star forming gas within the PS13 simulation.

In Fig. 3.4, we show the differential line number distribution obtained after applying the neutral fraction, gas kinetic and spin temperature from the patchy RT-late simulation to the native density and peculiar velocity fields from the QLyα and PS13 models. As in the previous section, we consider three different X-ray efficiencies, particularly $f_{\rm X} = 0.01$ (blue curves), 0.1 (fuchsia curves) and 1 (orange curves). We observe little to no difference in the statistics of the 21-cm forest computed from these two simulations. This is because the highest density gas is usually located close to ionizing sources, and so is often too hot, ionized or rare to exhibit significant amounts of strong absorption in the hyperfine line. This is further illustrated by the cyan curves in Fig. 3.4, where the mock 21-cm forest spectra are instead computed assuming a fully neutral, isothermal gas with $T_{\rm S} = T_{\rm K} = T_{\rm ad,0}$, where $T_{\rm ad,0} = 2.73\,{\rm K}(1+z)^2/148.8$ is the gas temperature assuming adiabatic cooling at the mean density. Small differences due to the presence of the high density gas in the PS13 simulation are now apparent in the tail of the distribution at $\tau_{21} \gtrsim 10$. However, if we also include the adiabatic heating of the gas by compression, such that

$T_{\rm ad} = T_{\rm ad,0}(1+\delta)^{2/3}$, these models become almost identical. We conclude that the approximate treatment of dense, star forming gas we adopt in this work should not significantly change our key results. The relative rarity of 21-cm absorption from cold gas within massive haloes suggests this population will in any case be completely dominated by 21-cm absorbers from the diffuse IGM and/or minihaloes during reionization.

Now we will investigate the number density distributions for different model parameters at three different redshifts, $z = 9$, 7.5 and 6, for our fiducial model with $f_\alpha = 1$ in Fig. 3.5. We also illustrate the effect of these model parameter variations on individual absorbers in Fig. 3.6. Each column in Fig. 3.5 corresponds to a different model parameter choice, each row shows a different redshift, and in each panel we show the distribution for three X-ray efficiencies: $f_{\rm X} = 0.01$ (blue curves), $f_{\rm X} = 0.1$ (fuchsia curves) and $f_{\rm X} = 1$ (orange curves). The peak of the distribution is at $\tau_{21} \leq 0.1$, and it shifts to lower amplitudes and smaller optical depths as the IGM reionizes and the spin temperature of the X-ray heated gas increases. The distribution also has an extended tail toward higher optical depths. While strong 21-cm absorbers will be rare, this suggests that for $f_{\rm X} \sim 0.1$, features with a transmission of $F = e^{-\tau_{21}} \simeq 0.9$ should still be present at $z = 7.5$ in the late reionization model (see also Fig. 3.1).

In the first column of Fig. 3.5 we re-examine the effect of strong Lyα coupling on the distribution of 21-cm optical depths. As was the case for the volume averaged optical depth in Fig. 3.3, the impact is relatively modest for low X-ray efficiencies: for $f_{\rm X} = 0.01$ at $z = 6$, the two cases are almost identical. For $f_{\rm X} = 1$, however, the abundance of features with $\tau_{21} \geq 0.01$ for $T_{\rm S} = T_{\rm K}$ is more than 50 per cent smaller than the full calculation at

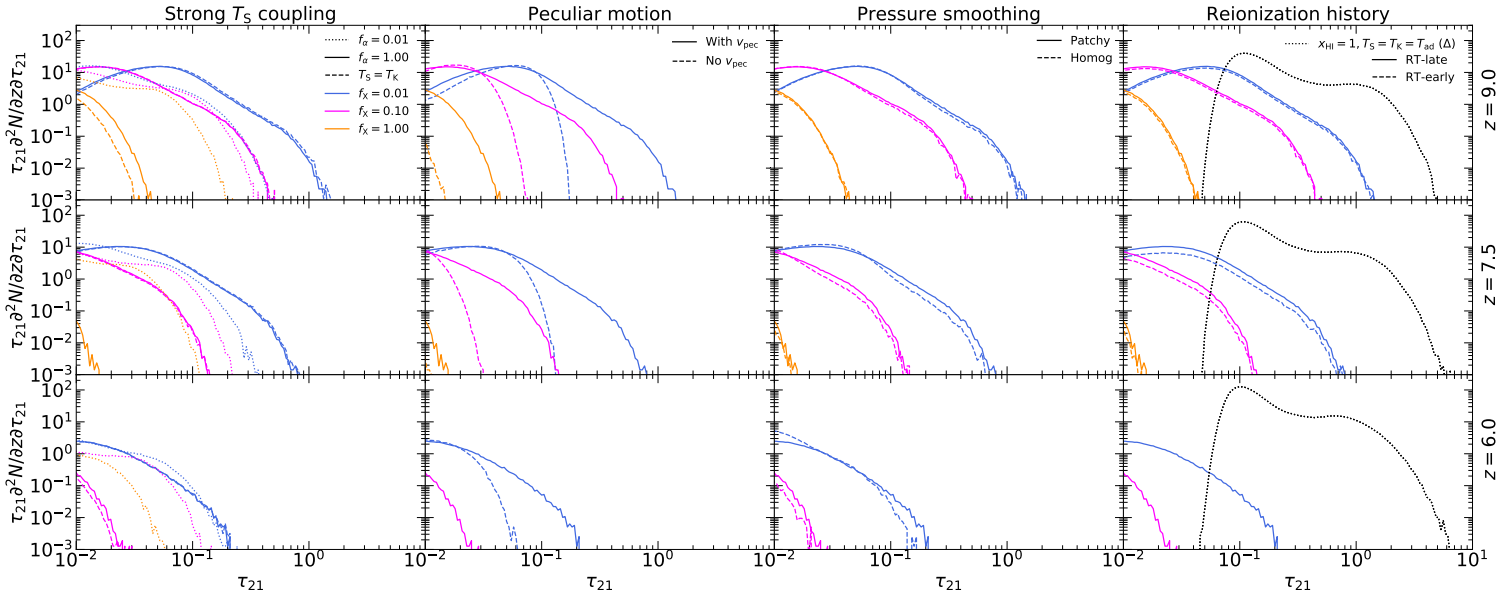

Figure 3.5: The differential number density of absorption lines in synthetic 21-cm forest spectra. Each row shows the distribution at redshift $z = 9$ (top row), 7.5 (middle row) and 6 (bottom row) for our fiducial model with Lyα efficiency $f_\alpha = 1$, and in each panel the distribution is shown for three X-ray efficiencies, $f_X = 0.01$ (blue curves),$f_X = 0.1$ (fuchsia curves) and $f_X = 1$ (orange curves). Each column displays the RT-late simulation (solid curves) compared to models where one of the parameter choices is varied (dashed curves). These parameters are, from left to right, the assumption of strong Lyα coupling (i.e. $T_S = T_K$), neglecting the effect of peculiar velocities (i.e $v_{pec} = 0$), pressure smoothing due to a uniform rather than patchy UV photo-heating rate (i.e the Homog-late model) and an earlier end to reionization (the RT-early model). In the first column, we also show the number density distribution for very weak Lyα coupling (i.e. $f_\alpha = 0.01$, dotted curves). The black dotted curves in the last column show the case of no reionization or X-ray heating (i.e. $T_S = T_K = T_{ad} = 2.73\,\mathrm{K}\ (1+\delta)^{2/3}(1+z)^2/(1+z_{dec})$, where $z_{dec} = 147.8$ (Furlanetto et al., 2006), and $x_{HI} = 1$).

$z = 9$. In either case, however, by $z = 7.5$ most gas in the $f_{\rm X} = 1$ model has $\tau_{21} < 10^{-2}$, and will therefore be challenging to detect directly. However, the dotted curves also demonstrate that if $f_\alpha = 0.01$, the weak coupling of $T_{\rm S}$ to $T_{\rm K}$ allows strong 21-cm absorbers to still be observable at $z = 6$, even for $f_{\rm X} = 1$.

We consider the effect of gas peculiar velocities on the 21-cm forest in the second column of Fig. 3.5. Redshift space distortions are well known to impact on the observability of the high redshift 21-cm signal (Bharadwaj & Ali, 2004; Mao et al., 2012; Majumdar et al., 2020). We do this by creating mock 21-cm spectra that ignore the effect of gas peculiar motions, such that $v_{\rm pec} = 0$ in Eq. (3.5). The results are shown by the dashed curves (see also the top panels of Fig. 3.6). While the position of the peak in the number density distribution is unchanged, the high optical depth tail is strongly affected, particularly for inefficient X-ray heating. Ignoring peculiar velocities within 21-cm forest models can therefore significantly reduce the incidence of the strongest absorbers, and this will have a negative impact on the predicted observability of the 21-cm forest. Qualitatively, this agrees with the assessment of Semelin (2016), who also included the effect of gas peculiar motions in their models.

As our hybrid simulations self-consistently model the hydrodynamical response of gas to photo-heating by the inhomogeneous UV radiation field, we may also estimate the effect of the lack of Jeans smoothing on the 21-cm forest. Inhomogeneous reionization introduces large scale gas temperature fluctuations in the IGM (Keating et al., 2018), and these lead to differences in the local gas pressure that smooth the structure of the IGM on different scales (e.g. Gnedin & Hui, 1998; Kulkarni et al., 2015; Nasir et al., 2016;

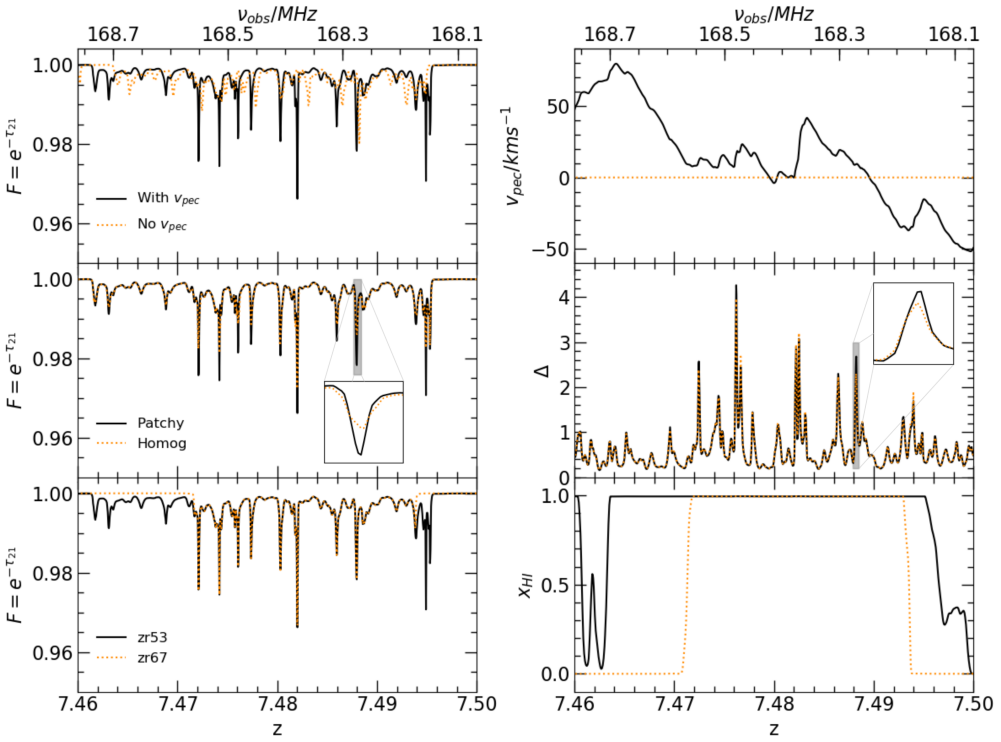

Figure 3.6: Left: An example line of sight drawn from our mock 21-cm forest spectra at $z \sim 7.5$ for an X-ray efficiency of $f_{\rm X} = 0.1$ and Lyα efficiency $f_\alpha = 1$. From top to bottom, we show the RT-late model with the solid black curve, and compare this to several model parameter variations (orange dotted curves): gas peculiar velocities set to zero (top), pressure smoothing under the assumption of homogeneous heating in the Homog-late simulation (middle) and an earlier end to reionization in the RT-early model (bottom). Right: The quantities responsible for the observed differences between the spectra displayed in the left column. From top to bottom, these are the gas peculiar velocity, $v_{\rm pec}$, normalised gas density $\Delta = (1 + \delta) = \rho/\langle\rho\rangle$, and hydrogen neutral fraction, $x_{\rm HI}$. In the middle panels we also present a zoomed-in view of an absorption feature (left) and the associated density peak (right), which has been broadened by pressure smoothing in the simulation with homogeneous heating.

D'Aloisio et al., 2020). In the absence of significant X-ray heating, the neutral gas responsible for the 21-cm forest should therefore experience minimal pressure smoothing compared to the photo-ionized IGM. We therefore compare the results of our RT-late model to the Homog-late simulation in the third column of Fig. 3.5. The latter model has exactly the same initial

conditions and volume averaged reionization history as RT-late, but all the gas in the simulation volume is instead heated simultaneously (i.e. we do not follow the radiative transfer for UV photons).

The dashed curves in the third column of Fig. 3.5 show the line density distribution obtained from the density and peculiar velocity fields in the Homog-late model (differences due to $x_{\rm HI}$, $T_{\rm K}$ and $T_{\rm S}$ in the two models have been removed). We observe that there is a small, redshift dependent difference between the two distributions, such that the simulation with the homogeneous UV background exhibits fewer strong absorption lines. This is because the gas responsible for the highest optical depths in the 21-cm forest (see Fig. 3.2) is still cold within the hybrid model, and hence has slightly higher density due to the smaller pressure smoothing scale (as shown in the middle panels of Fig. 3.6).

We caution, however, that this comparison will still not fully capture the effect of pressure smoothing on 21-cm forest absorbers. For reference, the comoving pressure smoothing scale in the IGM is (Gnedin & Hui, 1998; Garzilli et al., 2015)

$$\begin{aligned}\lambda_{\rm p} &= f_{\rm J}\lambda_{\rm J} = f_{\rm J}\left(\frac{40\pi^2 k_{\rm B}T_{\rm K}}{9\mu m_{\rm H}(1+\delta)H_0^2\Omega_{\rm m}(1+z)}\right)^{1/2}, \\ &= 9.8h^{-1}\,{\rm ckpc}\,f_{\rm J}\left[\left(\frac{10}{1+\delta}\right)\left(\frac{1.22}{\mu}\right)\left(\frac{T_{\rm K}}{10^2\,{\rm K}}\right)\left(\frac{10}{1+z}\right)\right]^{1/2}, \end{aligned} \tag{3.7}$$

where $\lambda_{\rm J}$ is the Jeans scale (see Eq. (1.5)), μ is the mean molecular weight of hydrogen and helium assuming primordial composition ($\mu = 1.22$ for fully neutral gas, $\mu = 0.59$ for fully ionized), and $f_{\rm J} = \lambda_{\rm p}/\lambda_{\rm J}$ is a factor of order unity that accounts for the finite time required for gas to dynamically respond to a change in pressure. For comparison, the mean

interparticle separation and gravitational softening length in our simulations are $19.5h^{-1}$ ckpc and $0.78h^{-1}$ ckpc, respectively. Eq. (3.7) thus implies that the pressure smoothing scale for typical 21-cm forest absorbers is not fully resolved in our simulations (see also Emberson et al., 2013). We furthermore do not capture the 21-cm absorption from minihaloes with $M < 2.5 \times 10^7\,M_\odot$ (Furlanetto, 2006a). Larger differences could then be observed in Fig. 3.5 for fully resolved gas. On the other hand, although we follow the dynamical response of gas to heating by UV photons, the X-ray heating of the neutral gas in our hybrid simulation is applied in post-processing. It is therefore decoupled from the hydrodynamics, and this may then underestimate the impact of pressure smoothing on cold gas for high X-ray efficiencies. Regardless of these modelling uncertainties, however, this suggests that the effect of the pressure smoothing scale on the 21-cm forest in the diffuse IGM remains small compared to the substantial impact of X-ray heating on the spin temperature at $z \leq 10$.

Finally, in the fourth column of Fig. 3.5 the effect of the reionization history is displayed for the RT-late (solid curves) and RT-early (dashed curves) simulations. For comparison, the dotted curves also show the line number density distribution under the assumption of no reionization or X-ray heating (i.e. $T_\mathrm{S} = T_\mathrm{K} = T_\mathrm{ad}$ and $x_\mathrm{HI} = 1$). As expected, the two reionization models are significantly different at $z = 6$; there are no strong absorption features with $\tau_{21} > 10^{-2}$ in RT-early model, as reionization has already completed by this time. At $z = 7.5$ one can see that there are also fewer absorption features in the RT-early model due to the larger volume of ionized gas. This is also apparent in the bottom panels of Fig. 3.6. However, the differences between the two models become smaller with increasing red-

shift. This again demonstrates that for reionization models that complete at $z < 6$, the 21-cm forest may remain observable if sufficiently bright radio sources exist at $6 < z < 7$. Alternatively, a null-detection could place an interesting limit on the very uncertain X-ray background (e.g. Mack & Wyithe, 2012). We now investigate this possibility further.

3.3.3 Detectability of strong 21-cm forest absorbers at redshift $z = 6$ for late reionization and X-ray heating

A detection of the 21-cm forest relies on the identification of objects at high redshift that are sufficiently radio bright to act as background sources. Based on a model for the radio galaxy luminosity function at $z > 6$, Saxena et al. (2017) predict around one radio source per 400 square degrees at a flux density limit of $S_{150\,\mathrm{MHz}} = 3.5\,\mathrm{mJy}$, and at least ~ 30 bright sources with $S_{150\,\mathrm{MHz}} > 15\,\mathrm{mJy}$ (see also Bolgar et al., 2018). Ongoing observational programmes such as the LOFAR Two-metre Sky Survey (LoTSS, Shimwell et al., 2017; Kondapally et al., 2021), the Giant Metrewave Radio Telescope (GMRT) all sky radio survey at 150 MHz (Intema et al., 2017), and the Galactic and Extragalactic All-sky Murchison Widefield Array survey (GLEAM, Wayth et al., 2015) should furthermore detect hundreds of bright $z > 6$ radio sources. Encouragingly, a small number of radio-loud sources have already been identified at $z > 5.5$ (e.g. Bañados et al., 2018b), including the $z = 6.1$ blazar PSO J0309+27 with a flux density $S_{147\,\mathrm{MHz}} = 64.2 \pm 6.2\,\mathrm{mJy}$ (Belladitta et al., 2020)

We now use our hydrodynamical simulations to assess the feasibility of detecting the 21-cm forest in late reionization models, assuming $f_\alpha = 1$.

We shall calculate the minimum redshift path length, $\Delta z_{\rm min}$, necessary for detecting a single, strong (i.e. $\tau_{21} > 0.01$) absorption line with a minimum transmission at some arbitrary threshold $F_{\rm th} = e^{-\tau_{21,\,\rm th}}$. For a signal-to-noise ratio S/N, the minimum flux density contrast, $\Delta S_{\rm min}$, detectable by an interferometric radio array is then (e.g. Ciardi et al., 2015a),

$$\Delta S_{\rm min} = S_{\rm min} - S_{\rm abs} = \frac{2k_{\rm B}T_{\rm sys}}{A_{\rm eff}\sqrt{\Delta\nu t_{\rm int}}}\,{\rm S/N}, \tag{3.8}$$

where $T_{\rm sys}$ is the system temperature, $\Delta\nu$ is the bandwidth, $A_{\rm eff}$ is the effective area of the telescope, $t_{\rm int}$ is the integration time, and $S_{\rm min}$ is the minimum intrinsic flux density a radio source must have to allow detection of a 21-cm absorption feature with a minimum at a flux density of $S_{\rm abs} = S_{\rm min}e^{-\tau_{21,\,\rm th}}$. Adopting some representative values in Eq. (3.8), the minimum flux density required to detect a 21-cm absorption feature with a minimum transmission $F_{\rm th}$ is therefore

$$\begin{aligned} S_{\rm min} = \; & 10.3\,{\rm mJy}\left(\frac{0.01}{1-F_{\rm th}}\right)\left(\frac{\rm S/N}{5}\right)\left(\frac{5\,{\rm kHz}}{\Delta\nu}\right)^{1/2}\left(\frac{1000\,{\rm hr}}{t_{\rm int}}\right)^{1/2} \\ & \times\left(\frac{1000\,{\rm m^2\,K^{-1}}}{A_{\rm eff}/T_{\rm sys}}\right). \end{aligned} \tag{3.9}$$

In what follows, we shall adopt values for the sensitivity, $A_{\rm eff}/T_{\rm sys}$, in Eq. (3.8) appropriate for LOFAR, SKA1-low and SKA2, where $A_{\rm eff}/T_{\rm sys} \simeq 80\,{\rm m^2\,K^{-1}}$, $600\,{\rm m^2\,K^{-1}}$ and $5500\,{\rm m^2\,K^{-1}}$, respectively[3] (Braun et al., 2019). Additionally, to approximately model the effect of spectral resolution on the data we convolve our mock spectra with a boxcar function. Following the bandwidths adopted in Ciardi et al. (2015b), we assume boxcar widths

[3]Note that in reality the sensitivity $A_{\rm eff}/T_{\rm sys}$ is frequency dependent. However, over the frequency range we consider, $142\,{\rm MHz} \leq \nu_{21}/(1+{\rm z}) \leq 203\,{\rm MHz}$, this dependence is reasonably weak. See fig. 8 in Braun et al. (2019) for further details.

of 10 kHz and 5 kHz for LOFAR and SKA1-low, respectively. For a more futuristic measurement with SKA2, we assume a smaller bandwidth and adopt a boxcar width of 1 kHz.

First, in Fig. 3.7, we show the minimum redshift path length $\Delta z_{\rm min}$ required to detect a single 21-cm absorption line in the minimum transmission threshold $F_{\rm th}$-redshift plane for three different X-ray efficiencies $f_{\rm X}$ (upper panels), or in the $f_{\rm X}$-redshift plane for three different transmission thresholds $F_{\rm th}$ (lower panels). Note that for now we assume a sufficient number of background radio sources exists for such a measurement; we consider the issue of detectability at $z = 6$ further in Fig. 3.8. The mock spectra used in Fig. 3.7 are drawn from the RT-late simulation and have been convolved with a boxcar of width 5 kHz (i.e. our assumed SKA1-low bandwidth). Unshaded white regions indicate where no absorbers are present over our total simulated path length of $200h^{-1}$ cGpc. Fig. 3.7 shows that no absorption features with $F_{\rm th} \leq 0.77$ should be present at $z \lesssim 8$ for even a very low X-ray efficiency of $f_{\rm X} = 0.01$ in the late reionization model. Similarly, almost no strong 21-cm absorption with $F_{\rm th} \lesssim 0.99$ will exist at $z < 7$ for $f_{\rm X} \geq 1$. This highlights the challenging nature of 21-cm forest measurements from the diffuse IGM, even if reionization ends very late, and also how sensitive the 21-cm forest absorption is to X-ray heating. Proposals to use the 21-cm forest as a sensitive probe for distinguishing between different cosmological or dark matter models using the diffuse IGM are therefore likely to be restricted to very high redshifts, prior to any substantial X-ray heating of the IGM.

As a reference, the black curves in Fig. 3.7 correspond to the redshift path length obtainable by a hypothetical observation of 1, 10 or 100 radio

sources of sufficient brightness in redshift bins of width $\Delta z = 0.2$ (i.e. an observation of N radio sources provides a total redshift path length of $0.2N$)[4]. A null-detection over this path length would provide a model-dependent lower limit on the X-ray background emissivity, such that $f_{\rm X} \geq f_{\rm X,max}$, where $f_{\rm X,max}$ is the maximum X-ray efficiency that retains at least one strong absorption feature with $F \leq F_{\rm th}$. From the lower middle panel in Fig. 3.7, the null-detection of a feature with $F_{\rm th} < 0.9$ at $z = 9$ in 1 radio source implies $f_{\rm X,max} \simeq 0.04$ while in 10 radio sources it increases to $f_{\rm X,max} \simeq 0.07$. The parameter space that lies below the black curves would then be disfavoured.

In practice, however, radio telescope sensitivity, spectral resolution and the availability of sufficiently bright background radio sources will impact upon the detectability of strong lines. We quantify this in Fig. 3.8, where similarly to Fig. 3.7 we show $\Delta z_{\rm min}$, but now in the $f_{\rm X}$–$F_{\rm th}$ plane at redshift $z = 6$. This is shown for our LOFAR (left), SKA1-low (middle) and SKA2 (right) model assumptions, where we have convolved the synthetic spectra with a boxcar of width 10 kHz, 5 kHz and 1 kHz, respectively. The minimum intrinsic source flux density, $S_{\rm min}$, required to detected a line with $F_{\rm th}$ has also been calculated using Eq. (3.8) and is displayed on the horizontal top axis. Here we assume a strong absorption line with minimum transmission $F_{\rm th}$ is detected with S/N = 5 for an integration time of $t_{\rm int} = 1000$ hrs with LOFAR and SKA1-low, and $t_{\rm int} = 100$ hrs with SKA2. First, one can see that if using a more sensitive telescope with higher spectral resolution

[4]The choice of $\Delta z = 0.2$ is somewhat arbitrary – we require a bin that is small enough that redshift evolution is not significant, but large enough to probe a reasonable path length. For reference, increasing the bin size to $\Delta z = 0.4$ would approximately halve the number of background sources required to detect a single absorber with $F_{\rm th}$, assuming minimal redshift evolution across the bin.

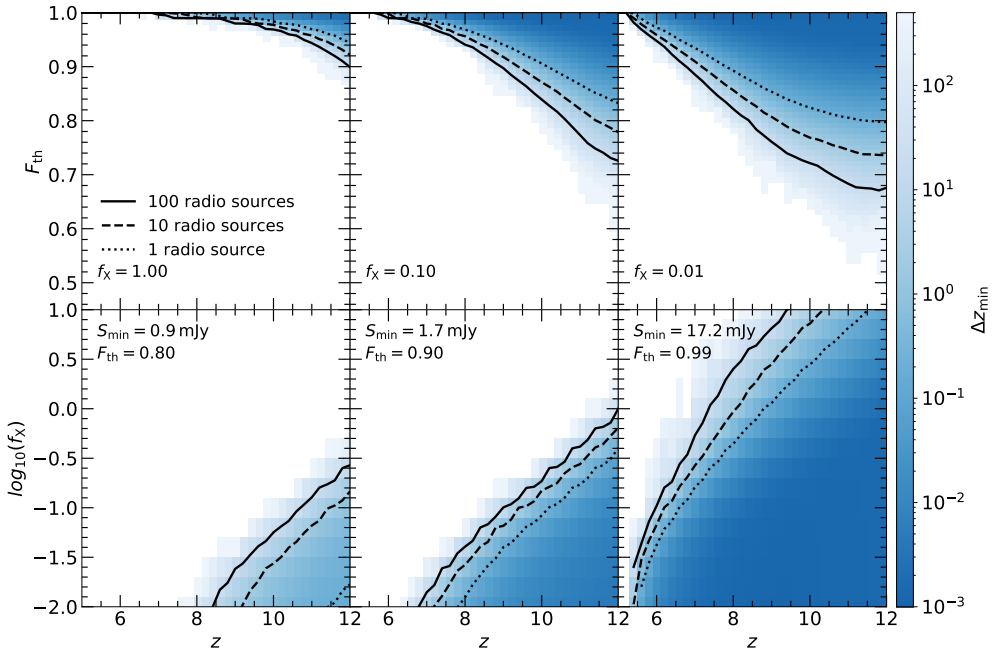

Figure 3.7: The minimum redshift path length, $\Delta z_{\rm min}$, required to observe a single 21-cm absorption feature in the RT-late simulation *assuming that a sufficient number of background radio sources exist.* The mock spectra have been convolved with a boxcar of width 5 kHz to approximately model the effect of spectral resolution on the lines. In the upper panels we show $\Delta z_{\rm min}$ in the $F_{\rm th}$–z plane for an X-ray efficiency factor of $f_{\rm X} = 1$ (left), 0.1 (middle) and 0.01 (right). In the lower panels we instead show $\Delta z_{\rm min}$ in the $f_{\rm X}$–z plane for a 21-cm absorption feature with minimum transmission $F \leq F_{\rm th} = 0.8$ (left), 0.9 (middle) and 0.99 (right). Here we also note the minimum intrinsic flux density, $S_{\rm min}$, that a background radio source must have such that an absorption line with a minimum at $F \leq F_{\rm th}$ is detectable with SKA1-low at a signal-to-noise of S/N = 5 and integration time of $t_{\rm int} = 1000$ hr (see Eq. 3.8). The unshaded white regions are where no absorbers are present over our total simulated path length of $200h^{-1}$ cGpc. The thick black curves in each panel track the redshift path length that would be covered by the observation of 1 (dotted), 10 (dashed) and 100 (solid) radio sources assuming redshift bins of width $\Delta z = 0.2$.

it is possible to detect deeper, narrower absorption features. Moreover, tighter constraints on the X-ray efficiency $f_{\rm X}$ may also be obtained. For example, at $z = 6$, there are no absorption features with $F \leq 0.95$ for $f_{\rm X} > 0.01$ if observed by LOFAR. However, this increases to $f_{\rm X} > 0.025$ for SKA1-low and $f_{\rm X} > 0.05$ for SKA2. The minimum source flux density

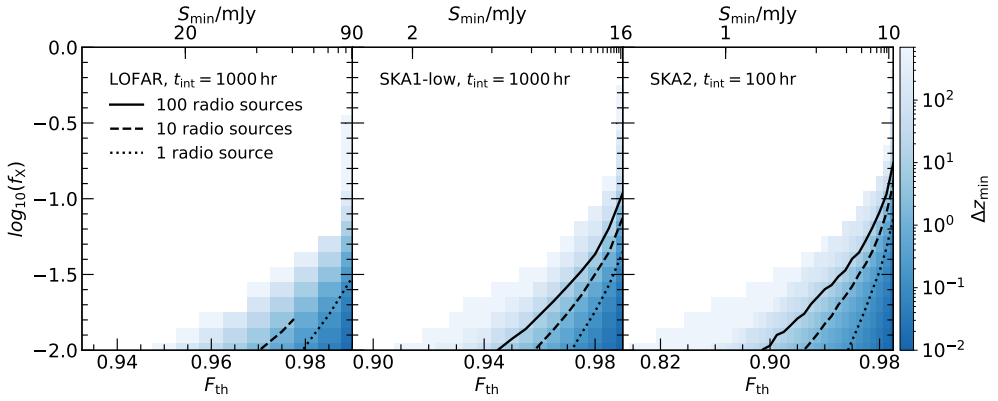

Figure 3.8: As for Fig. 3.7, but now the minimum redshift path length $\Delta z_{\rm min}$ is shown in the $f_{\rm X}$–$F_{\rm th}$ plane at redshift $z = 6$. The mock spectra have been convolved with a boxcar of width 10 kHz (left), 5 kHz (middle) and 1 kHz (right) to approximately model the effect of our assumed bandwidths for LOFAR, SKA1-low and SKA2, respectively. Note the scale on the horizontal axis is different in each panel. The upper horizontal axis now also shows the minimum intrinsic flux density, $S_{\rm min}$, required for a background radio source, such that a line with minimum transmission $F \leq F_{\rm th}$ is detectable at a signal-to-noise of S/N = 5 by LOFAR with an integration time of $t_{\rm int} = 1000$ hr (left), by SKA1-low with $t_{\rm int} = 1000$ hr (middle) and by SKA2 with $t_{\rm int} = 100$ hr (right). In the left panel (LOFAR) the thick dashed curve is truncated where the number of available background radio sources predicted by Saxena et al. (2017) with $S_{\rm min}$ at $z \simeq 6$ falls below 10. The curve for 100 sources (solid) is not shown, as this exceeds the expected radio source number from Saxena et al. (2017) at the required $S_{\rm min}$.

required to detect an absorption feature at fixed S/N = 5 also decreases significantly, thus increasing the number of potentially suitable background radio sources.

We quantify this in more detail in Tables 3.1, 3.2 and 3.3, where we list the maximum X-ray efficiency, $f_{\rm X,max}$, that retains at least one 21-cm absorption feature at $z = 6$ with a transmission minimum $F \leq F_{\rm th}$ over a path length of $\Delta z = 0.2$, $\Delta z = 2$ or $\Delta z = 20$ in the RT-late simulation. This corresponds to N = 1, 10 and 100 sources, respectively, for redshift bins of width $\Delta z = 0.2$. We also give the minimum flux density, $S_{\rm min}$, required to detect an absorption line with $F_{\rm th}$ at S/N = 5. Additionally, we give the ex-

Table 3.1: The maximum X-ray background efficiency, $f_{\rm X,max}$, that retains at least one strong 21-cm absorption feature with transmission $F \leq F_{\rm th}$ in our synthetic 21-cm forest spectra, for a redshift path length corresponding to N bright radio sources covering a redshift bin of width $\Delta z = 0.2$, centred at redshift $z = 6$. The mock spectra have been convolved with a boxcar of width 5kHz to approximately model the effect of observed bandwidth on the lines. The minimum intrinsic flux density of the background source, $S_{\rm min}$, required to detect a line with $F_{\rm th}$ at a signal-to-noise of S/N = 5 with SKA1-low is calculated using Eq. (3.8), assuming a bandwidth $\Delta\nu = 5\,$kHz, sensitivity $A_{\rm eff}/T_{\rm sys} = 600\,{\rm m^2\,K^{-1}}$ and integration time of $t_{\rm int} = 1000\,$hr. The expected number of radio sources in the sky with $S_{\rm min}$ at $z = 6$, $\rm N_{S17}$, are estimated from Saxena et al. (2017) (their fig. 11). In the event of a null-detection of an absorption feature with $F_{\rm th}$, the $f_{\rm X,max}$ values give a (model dependent) lower limit on the X-ray efficiency.

		$z = 6$	$f_{\rm X,max}, z = 6$		
$F_{\rm th} = e^{-\tau_{21,\rm th}}$	$S_{\rm min}$[mJy]	$\rm N_{S17}$	N=1	N=10	N=100
0.99	17.2	∼100	0.045	0.075	0.109
0.95	3.4	∼2400	$<10^{-3}$	0.007	0.012
0.9	1.7	∼6100	$<10^{-3}$	$<10^{-3}$	$<10^{-3}$

pected number of background sources in the sky at $z \simeq 6$ with $S_{\rm min}$ reported by Saxena et al. (2017) for an observing time of 100 hrs with the standard LOFAR configuration (see their fig. 11). As a quantitative example, using Table 3.1 (SKA1-low), for a ten background sources with $S_{203\,\rm MHz} = 3.4\,$mJy, on average we would expect to detect at least one 21-cm absorption line with $F < 0.95$ at $z = 6.0 \pm 0.1$ if $f_{\rm X} \leq 0.007$. A null-detection would instead imply a lower limit of $f_{\rm X} > 0.007$. Within our model, this X-ray efficiency may be converted to an estimate of the soft X-ray band emissivity at 0.5–2 keV, where $\epsilon_{\rm X,0.5-2\,keV} = 10^{38.3} f_{\rm X}\,{\rm erg\,s^{-1}\,cMpc^{-3}}$ at $z = 6$. Hence $f_{\rm X} > 0.007$ corresponds to $\epsilon_{\rm X,0.5-2\,keV} > 10^{36.1}\,{\rm erg\,s^{-1}\,cMpc^{-3}}$. Alternatively, from Table 3.2 (LOFAR), the null-detection of an absorption line with $F < 0.95$ at $z = 6.0 \pm 0.1$ in the spectra of 10 radio bright sources with $S_{203\,\rm MHz} = 18.2\,$mJy would imply a slightly weaker constraint of $f_{\rm X} > 0.001$ and $\epsilon_{\rm X,0.5-2\,keV} > 10^{35.3}\,{\rm erg\,s^{-1}\,cMpc^{-3}}$. This suggests that lower limits on

Table 3.2: As for Table 3.1, except the mock 21-cm forest spectra are now smoothed with a boxcar of width 10 kHz and the minimum source flux densities, $S_{\rm min}$, have been computed for LOFAR using a bandwidth $\Delta\nu = 10\,{\rm kHz}$, sensitivity $A_{\rm eff}/T_{\rm sys} = 80\,{\rm m^2\,K^{-1}}$ and integration time of $t_{\rm int} = 1000\,{\rm hr}$. Dashes mean that $f_{\rm X,max}$ is not measurable due to the lack of expected sources.

		$z=6$	$f_{\rm X,max}, z=6$		
$F_{\rm th} = e^{-\tau_{21,\rm th}}$	$S_{\rm min}$[mJy]	$\rm N_{S17}$	N=1	N=10	N=100
0.99	91.0	~ 1	0.030	—	—
0.95	18.2	$\sim$90	$<10^{-3}$	0.001	—
0.9	9.1	$\sim$420	$<10^{-3}$	$<10^{-3}$	$<10^{-3}$

Table 3.3: As for Table 3.1, except the mock 21-cm forest spectra are now smoothed with a boxcar of width 1 kHz and the minimum source flux densities, $S_{\rm min}$, have been computed for SKA2 using a bandwidth $\Delta\nu = 1\,{\rm kHz}$, sensitivity $A_{\rm eff}/T_{\rm sys} = 5500\,{\rm m^2\,K^{-1}}$ and integration time of $t_{\rm int} = 100\,{\rm hr}$.

		$z=6$	$f_{\rm X,max}, z=6$		
$F_{\rm th} = e^{-\tau_{21,\rm th}}$	$S_{\rm min}$[mJy]	$\rm N_{S17}$	N=1	N=10	N=100
0.99	13.2	$\sim$190	0.074	0.125	0.172
0.95	2.6	$\sim$3600	0.007	0.020	0.031
0.9	1.3	$\sim$8000	$<10^{-3}$	0.004	0.011
0.8	0.7	$\sim$5300	$<10^{-3}$	$<10^{-3}$	$<10^{-3}$

the soft X-ray background emissivity at high redshift from a null-detection of the 21-cm forest may complement existing constraints from upper limits on the 21-cm power spectrum (Greig et al., 2021a). We note, however, these results are highly model dependent. If the Lyα coupling is very weak (i.e. if $f_\alpha \ll 1$), or there is a significant contribution to the 21-cm forest absorption from unresolved small scale structure, the $f_{\rm X,max}$ values in Table 3.1–3.3 will translate to lower limits on $f_{\rm X}$ that are conservative.

3.4 Conclusions

We have used very high resolution hydrodynamical simulations combined with a novel approach for implementing patchy reionization to model the 21-cm forest during the epoch of reionization. Our simulations have been performed as part of the Sherwood-Relics simulation programme (Puchwein et al., 2022). In particular, we have considered the observability of strong ($\tau_{21} > 10^{-2}$) 21-cm absorbers in a late reionization model consistent with the large Lyα forest transmission fluctuations observed at $z = 5.5$ (Becker et al., 2015b), where large neutral islands of intergalactic gas persist until $z \simeq 6$ (Kulkarni et al., 2019; Keating et al., 2020). We also explore a wide range of assumptions for X-ray heating in the pre-reionization intergalactic medium (IGM), and have assessed the importance of several common modelling assumptions for the predicted incidence of strong 21-cm absorbers. Our key results are summarised as follows:

- In a model of late reionization ending at $z = 5.3$, for an X-ray efficiency parameter $f_{\rm X} \lesssim 0.1$ (i.e. for relatively modest X-ray preheating of neutral hydrogen gas, such that the gas kinetic temperature $T_{\rm K} \lesssim 10^2\,{\rm K}$) strong 21-cm absorption lines with optical depths $\tau_{21} \geq 0.01$ situated in neutral islands of intergalactic gas should persist until $z = 6$. In this case, the 21-cm absorbers with the largest optical depths should arise from cold, diffuse gas with overdensities $3 < \Delta < 10$ and kinetic temperatures $T_{\rm K} < 10^2\,{\rm K}$. A null-detection of 21-cm forest absorbers at $z = 6$ may therefore place a valuable lower limit on the high redshift soft X-ray background and/or the kinetic temperature of the diffuse pre-reionization IGM in the neutral

islands. With ~ 10 radio-loud active galactic nuclei now known at $5.5 < z < 6.5$ (e.g. Bañados et al., 2018b; Liu et al., 2021) and the prospect of more radio-loud sources being identified in the next few years, this possibility merits further investigation.

- By far the largest uncertainty in models of the 21-cm forest is the heating of the pre-reionization IGM by the soft X-ray background (see also Mack & Wyithe, 2012). In the absence of strong constraints on the soft X-ray background at $z \geq 6$, proposals to use the 21-cm forest to distinguish between cosmological models (where differences between competing models are small compared to the effect of X-ray heating) will likely be restricted to redshifts prior to the build-up of the soft X-ray background. Uncertainties in the strength of the Wouthuysen-Field coupling will also be important to consider if the Lyα background is significantly weaker than expected from extrapolating the observed star formation rate density to $z > 6$. By contrast, we find the effect of uncertain pressure/Jeans smoothing on the 21-cm absorption from the diffuse IGM should remain comparatively small.

- Models of the 21-cm forest must include the effect of gas peculiar motions on absorption line formation to accurately predict the incidence of strong absorption features (see also Semelin, 2016). Ignoring redshift space distortions reduces the incidence of the strongest 21-cm forest absorbers, and results in a maximum optical depth in the 21-cm forest that is up to a factor of ~ 10 smaller compared to a model that correctly incorporates gas peculiar velocities.

- We present model dependent estimates for the minimum redshift path

length required to detect a single, strong 21-cm forest absorption feature as a function of redshift and X-ray efficiency parameter, $f_{\rm X}$ within a late reionization model that ends at redshift $z = 5.3$. At $z = 6.0 \pm 0.1$ for an integration time of $t_{\rm int} = 1000\,{\rm hrs}$ per background radio source, a null-detection of 21-cm forest absorbers with $F < 0.95$ at a signal-to-noise of ${\rm S/N} = 5$ in the spectra of 10 radio sources with $S_{203\,{\rm MHz}} > 3.4\,{\rm mJy}$ ($> 18.2\,{\rm mJy}$) using SKA1-low (LOFAR) implies a soft X-ray background emissivity $\epsilon_{\rm X,0.5-2\,keV} > 10^{36.1(35.3)}\,{\rm erg\,s^{-1}\,cMpc^{-3}}$. As the soft X-ray background at high redshift is still largely unconstrained, this suggests lower limits on the X-ray emissivity from a null-detection of the 21-cm forest could provide a valuable alternative constraint that complements existing and forthcoming constraints from upper limits on the 21-cm power spectrum.

While the calculation we present in this work is illustrative, a more careful forward modelling of the 21-cm absorption data is still required. We have not considered how to recover absorption features from noisy data beyond the simple signal-to-noise calculation adopted here, or how an imperfect knowledge of the radio source continuum and/or radio background might impact upon the detectability of 21-cm absorbers. Uncertainties in other parameters such as the reionization history and the Lyα background emissivity should furthermore be marginalised over to obtain a robust lower limit on the soft X-ray background. Our simulations do not account for the absorption from unresolved minihaloes with masses $< 2.5 \times 10^7\,{\rm M_\odot}$, and will lack coherent regions of neutral gas on scales greater than our box size of $40h^{-1}\,{\rm cMpc}$. On the other hand, even a modest amount of feedback,

either in the form of photo-evaporation (Park et al., 2016; Nakatani et al., 2020) or feedback from star formation (Meiksin, 2011) will substantially reduce the absorption signature from minihaloes. These feedback effects may be particularly important during the final stages of reionization at $z \simeq 6$, where any remaining 21-cm absorption should arise from neutral islands in the diffuse IGM.

More detailed models of the 21-cm forest will require either radiation-hydrodynamical simulations that encompass a formidable dynamic range, and/or multi-scale, hybrid approaches that adopt sub-grid models for unresolved absorbers and their response to feedback. Both must furthermore cover a very large and uncertain parameter space. Nevertheless, we conclude that if reionization completes at $z < 6$, the prospects for using SKA1-low or possibly LOFAR to place an independent constraint on the soft X-ray background using strong absorbers in the 21-cm forest are encouraging.

Chapter 4

Probing quasar lifetimes with proximate 21-centimetre absorption in the diffuse intergalactic medium at redshifts $z \geq 6$

The work contained in this chapter is based on a manuscript submitted to Monthly Notices of Royal Astronomical Society. The appendices are included in the main body at appropriate places, and minor formatting modifications have been added.

4.1 Introduction

The intergalactic medium (IGM) becomes opaque to Lyα photons approaching the end stages of reionization at $z \gtrsim 5.5$, when the average neutral hydrogen fraction $\langle x_{\rm HI} \rangle \gtrsim 10^{-4}$ (for a review see Becker et al., 2015a). However, in close proximity to highly luminous quasars at $z \gtrsim 5.5$, local enhancements in the ionizing radiation field leave short windows of Lyα transmission blueward of the quasar Lyα emission line. These regions – referred to as Lyα near-zones or proximity zones – are typically 1–10 proper Mpc (pMpc) in extent (Fan et al., 2006; Carilli et al., 2010; Willott et al., 2010; Venemans et al., 2015; Reed et al., 2015; Eilers et al., 2017, 2021; Mazzucchelli et al., 2017; Ishimoto et al., 2020). Several near-zones at $z \simeq 7$ also exhibit evidence for Lyα damping wings that extend redward of the quasar systemic redshift (Mortlock et al., 2011; Bañados et al., 2018a; Wang et al., 2020; Yang et al., 2020a), which is expected if the surrounding IGM is substantially neutral (Miralda-Escudé & Rees, 1998). Early work suggested that Lyα near-zones may be tracing quasar H II regions embedded in an otherwise largely neutral IGM (e.g. Shapiro & Giroux, 1987; Cen & Haiman, 2000; Madau & Rees, 2000; Wyithe & Loeb, 2004a). Subsequent radiative transfer modelling (Bolton & Haehnelt, 2007; Maselli et al., 2007; Lidz et al., 2007; Wyithe et al., 2008) demonstrated a more complex picture, where the Lyα near-zones at $z \simeq 6$ may also be explained if the quasars are surrounded by a highly ionized IGM – analogous to the classical proximity effect at lower redshift (e.g. Murdoch et al., 1986; Bajtlik et al., 1988).

In the last decade the number of $z \gtrsim 6$ quasar spectra with well measured Lyα near-zone sizes has grown considerably. Over 280 quasars at

$z > 6$ have now been discovered (see e.g. Bosman, 2022). Submillimetre observations have provided improved measurements of quasar systemic redshifts, yielding better estimates of the Lyα near-zone sizes (Eilers et al., 2021). After correcting for differences in the intrinsic luminosity of the quasars, the scatter in the ~ 80 published Lyα near-zone sizes can be largely explained by a combination of cosmic variance (Keating et al., 2015), differences in the optically/UV bright lifetime of the quasars (Morey et al., 2021), and perhaps the occasional proximate high column density absorption system (Chen & Gnedin, 2021a). The observed Lyα near-zone size distribution is reasonably well reproduced if a highly ionized IGM surrounds the quasars at $z \simeq 6$ (Wyithe et al., 2008; Morey et al., 2021). However, the Lyα damping wings in the spectra of several $z > 7$ quasars are suggestive of a substantially more neutral IGM by $z \simeq 7$, such that $\langle x_{\rm HI} \rangle > 0.1$, (Bolton et al., 2011; Greig et al., 2017, 2022; Davies et al., 2018, but see also Bosman & Becker (2015)).

Several recent studies have focused on constraining optically/UV bright quasar lifetimes, $t_{\rm Q}$, from the Lyα near-zone data at $z \simeq 6$. Morey et al. (2021) find an average optically/UV bright lifetime of $t_{\rm Q} \sim 10^6\,{\rm yr}$ is consistent with the transmission profiles of most Lyα near-zones at $z \simeq 6$. Eilers et al. (2017, 2021) have furthermore presented several very small Lyα near-zones with luminosity corrected sizes of $\lesssim 1\,{\rm pMpc}$, consistent with optically/UV bright lifetimes of $t_{\rm Q} \lesssim 10^4$–$10^5\,{\rm yr}$. These small Lyα near-zones represent $\lesssim 10$ per cent of all quasar Lyα near-zones at $z \simeq 6$. However, if the black holes powering these quasars accrete most of their mass when the quasars are optically/UV bright, such a short average lifetime is in significant tension with the build up of $\sim 10^9\,{\rm M}_\odot$ supermassive

black holes by $z = 6$; the e-folding time for Eddington limited accretion is at least an order of magnitude larger. Possible solutions are radiatively inefficient, mildly super-Eddington accretion (Madau et al., 2014; Davies et al., 2019), black holes that grow primarily in an obscured, optically/UV faint phase (Hopkins et al., 2005; Ricci et al., 2017) or episodic accretion that produces "flickering" quasar light curves (Schawinski et al., 2015; Davies et al., 2020).

Observationally distinguishing between very young quasars and older quasars that have experienced episodic or obscured accretion with Lyα near-zones is challenging, however. Another possibility is detecting the 21-cm signal from neutral hydrogen around the quasars. In principle, if the foregrounds can be accurately removed, the sizes of quasar H II regions may be measured directly with 21-cm tomography; the neutral, X-ray heated hydrogen outside of the quasar H II region should appear in emission against the radio background (e.g. Wyithe & Loeb, 2004b; Kohler et al., 2005; Rhook & Haehnelt, 2006; Geil & Wyithe, 2008; Majumdar et al., 2012; Datta et al., 2012; Kakiichi et al., 2017; Ma et al., 2020; Davies et al., 2021). Assuming the recombination timescale $t_{\rm rec} \gg t_{\rm Q}$, 21-cm tomography measurements would enable a direct determination of the quasar age, because the H II region size $R_{\rm HII} \propto t_{\rm Q}^{1/3}$ (see e.g. Eq. (4.8) later). A related approach that has received less attention is to instead consider the forest of redshifted 21-cm absorption expected from the neutral IGM in the spectra of radio-loud background sources at $z \gtrsim 6$ (for recent examples of potential background sources, see e.g. Belladitta et al., 2020; Ighina et al., 2021; Bañados et al., 2021; Liu et al., 2021). Unlike tomography, observing the IGM in 21-cm absorption allows small-scale IGM structure to be resolved

and it is (in principle) a simpler observation that does not rely on the removal of challenging foregrounds (see e.g. Carilli et al., 2002; Furlanetto & Loeb, 2002; Furlanetto, 2006a; Meiksin, 2011; Xu et al., 2011; Ciardi et al., 2013; Semelin, 2016; Villanueva-Domingo & Ichiki, 2022).

In Chapter 3, we discussed the detectability of the 21-cm forest in the context of the late ($z \simeq 5.3$) reionization models (e.g. Kulkarni et al., 2019; Keating et al., 2020; Nasir & D'Aloisio, 2020; Qin et al., 2021; Choudhury et al., 2021) that appear to be favoured by the large variations found in the Lyα forest effective optical depth at $z > 5$ (Becker et al., 2015b; Eilers et al., 2018; Yang et al., 2020b; Bosman et al., 2018, 2022). We noted that, for modest X-ray pre-heating, such that the IGM spin temperature $T_{\rm S} \lesssim 10^2\,{\rm K}$, strong 21-cm forest absorption with optical depths $\tau_{21} \geq 10^{-2}$ will persist until $z = 6$ in late reionization models. A null detection of the 21-cm forest at $z = 6$ would also place useful limits on the soft X-ray background. Toward higher redshifts, $z > 7$, strong 21-cm forest absorbers will become significantly more abundant, particularly if the spin and kinetic temperatures are not tightly coupled (see e.g. Fig. 3.5).

In this context, Bañados et al. (2021) have recently reported the discovery of a radio-loud quasar PSO J172+18 at $z = 6.82$, with an absolute AB magnitude $M_{1450} = -25.81$ and an optical/near-infrared spectrum that exhibits a Lyα near-zone size $R_{{\rm Ly}\alpha} = 3.96 \pm 0.48\,{\rm pMpc}$. This raises the intriguing possibility of also obtaining a radio spectrum from this or similar objects with low frequency radio interferometry arrays. For spin temperatures of $T_{\rm S} \sim 10^2\,{\rm K}$ in the pre-reionization IGM, in late reionization scenarios there will be proximate 21-cm absorption from neutral islands in the diffuse IGM that will approximately trace the extent of the quasar

H II region. If this proximate 21-cm absorption is detected, either for an individual radio-loud quasar or within a population of objects, it would provide another possible route to constraining the lifetime of high redshift quasars. In particular, when combined with Lyα near-zone sizes, such a measurement could help distinguish between quasars that are very young (as is suggested if taking the Eilers et al. (2017, 2021) Lyα near-zone data at face value), or that are much older and have only recently transitioned to an optically/UV bright phase.

Our goal is to explore this possibility by modelling the properties of proximate 21-cm absorbers in the diffuse IGM around (radio-loud) quasars. We do this by building on the simulation framework presented in Chapter 2 and 3, who used the Sherwood-Relics simulations (see Puchwein et al., 2022) of inhomogeneous, late reionization to predict the properties of the 21-cm forest. In this chapter, we now additionally couple Sherwood-Relics with a line of sight radiative transfer code that simulates the photo-ionization and photo-heating around bright quasars (for similar approaches see e.g. Bolton & Haehnelt, 2007; Lidz et al., 2007; Davies et al., 2020; Chen & Gnedin, 2021a; Satyavolu et al., 2022).

We begin by describing our fiducial quasar spectral energy distribution and the effect of the quasar UV and soft X-ray radiation on proximate Lyα and 21-cm absorption using a simplified, homogeneous IGM model in Section 4.2. We then introduce a more realistic model by using the Sherwood-Relics simulations in Section 4.3, and validate our model by comparing the predicted Lyα near-zone sizes in our simulations to observational data. Our predictions for the extent of the proximate 21-cm absorption around $z \geq 6$ quasars for a constant "light bulb" quasar emission model are presented in

Section 4.4. In Section 4.5 we then extend this model to include "flickering" quasar light curves that may be appropriate for episodic black hole accretion, and discuss the implications for constraining quasar lifetimes and black hole growth. Finally, we summarise and conclude in Section 4.6.

4.2 Quasar radiative transfer model

4.2.1 The quasar spectral energy distribution

The effect of UV and X-ray ionizing photons emitted by quasars on the high redshift IGM is simulated using the 1D multi-frequency radiative transfer (RT) calculation first described by Bolton & Haehnelt (2007), and subsequently updated in Knevitt et al. (2014) to include X-rays and secondary ionizations by fast photo-electrons (Furlanetto & Stoever, 2010). In brief, as an input this model takes the gas overdensity Δ, peculiar velocity $v_{\rm pec}$, neutral hydrogen fraction $x_{\rm HI}$, gas kinetic temperature $T_{\rm K}$, and background photo-ionization rate $\Gamma_{\rm HI}$, from sight lines drawn through a hydrodynamical simulation (see Section 4.3.1 for further details). We assume a spectral energy distribution (SED) for the quasar, and follow the RT of ionizing photons through hydrogen and helium gas along a large number of individual sight lines, all of which start at the position of a halo. Our RT simulations track ionizing photons emitted by the quasar at energies between 13.6 eV and 30 keV, using 80 logarithmically spaced photon energy bins.

We model the quasar SED as a broken power law, $f_\nu \propto \nu^\alpha$, as shown in Fig. 4.1 (blue solid curve). Our choice of SED is similar to the template from Shen et al. (2020) (dashed fuchsia curve). To construct the UV part of

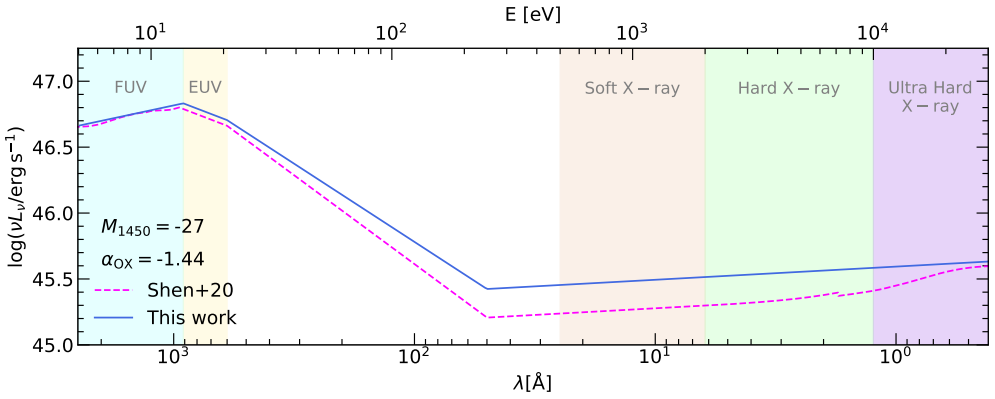

Figure 4.1: The fiducial power-law quasar SED used in this chapter (solid blue curve) compared to the SED template from Shen et al. (2020) (dashed fuchsia curve). Both SEDs are normalised at 1450 Å to correspond to an absolute AB magnitude $M_{1450} = -27$. The SED is modelled as a broken power law, $f_\nu \propto \nu^\alpha$, with spectral index $\alpha_{\rm FUV} = -0.61$ between $\lambda = 912\,\text{Å} - 2500\,\text{Å}$ (far UV), $\alpha_{\rm EUV} = -1.70$ between $\lambda = 600\,\text{Å} - 912\,\text{Å}$ (extreme UV) and $\alpha_{\rm Xray} = -0.9$ at $\lambda \leq 50\,\text{Å}$ (X-ray). The X-ray part of the spectrum is normalized with an optical-to-X-ray spectral index of $\alpha_{\rm OX} = -1.44$. The SED between $\lambda = 50\,\text{Å} - 600\,\text{Å}$ connects the UV and X-ray sections of the spectrum. The shaded regions indicate common wavelength bands. Our fiducial model corresponds to an ionizing photon emission rate of $\dot{N} = 1.64 \times 10^{57}\,\mathrm{s^{-1}}$.

the SED, we follow Lusso et al. (2015) and assume a spectral index $\alpha_{\rm FUV} = -0.61$ at $912\,\text{Å} \leq \lambda \leq 2500\,\text{Å}$ and $\alpha_{\rm EUV} = -1.70$ at $600\,\text{Å} \leq \lambda \leq 912\,\text{Å}$. We choose the spectral index at X-ray energies ($\lambda \leq 50\,\text{Å}$) to be $\alpha_{\rm Xray} = -0.9$, to approximately match the shape of the Shen et al. (2020) SED. The X-ray part of the SED is normalised using the observed correlation between the specific luminosities $L_\nu(2500\,\text{Å})$ and $L_\nu(2\,\text{keV})$, typically parameterised by the optical-to-X-ray spectral index, $\alpha_{\rm OX}$ (Steffen et al., 2006; Lusso et al., 2010). We assume a fiducial value of $\alpha_{\rm OX} = -1.44$ in this chapter, but vary this by $\Delta\alpha_{\rm OX} = 0.3$ to account for a range of $L_\nu(2500\,\text{Å})$ values. Our fiducial $\alpha_{\rm OX}$ is similar to the best fit value of $\alpha_{\rm OX} = -1.45 \pm 0.11$ recently inferred by Connor et al. (2021) for a radio-loud quasar at $z = 5.831$. Finally, the spectral shape at $\lambda = 50\,\text{Å} - 600\,\text{Å}$ is obtained by connecting

the UV and X-ray parts of the SED.

For ease of comparison with previous literature (Eilers et al., 2017; Davies et al., 2020), we adopt a normalisation for the quasar SED corresponding to an absolute AB magnitude at 1450 Å of $M_{1450} = -27$ and a specific luminosity $L_\nu(2500\,\text{Å}) = 3.8 \times 10^{31}\,\text{ergs}^{-1}\text{Hz}^{-1}$. For $\alpha_{\text{OX}} = -1.44$, this results in an ionizing photon ($E > 13.6\,\text{eV}$) emission rate of $\dot{N} = 1.64 \times 10^{57}\,\text{s}^{-1}$. For most of this study we will furthermore assume a constant luminosity "light bulb" model for the quasar light curve (e.g. Bolton & Haehnelt, 2007). However, in Section 4.5 we will also consider a model where the quasar luminosity varies with time (cf. Davies et al., 2020).

4.2.2 Lyα and 21-cm absorption in a homogeneous medium

We examine the Lyα and 21-cm absorption in the vicinity of bright quasars by constructing mock absorption spectra from the sight lines extracted from our RT simulations. We calculate the Lyα optical depth, $\tau_{\text{Ly}\alpha}$, along each quasar sight line following Bolton & Haehnelt (2007) (see their eq. (15)), where we use the Tepper-García (2006) approximation for the Voigt line profile. To compute the 21-cm forest optical depth, τ_{21}, we follow the approach described in Section 3.2 and assume a Gaussian line profile (see Eq. 3.5). Strong 21-cm absorption will arise from dense, cold and significantly neutral hydrogen gas. Note also that because we consider gas in the vicinity of luminous quasars, we shall assume strong Lyα coupling when calculating the 21-cm optical depths, such that the hydrogen spin temperature, T_{S}, is equal to the gas kinetic temperature, T_{K}.

First, to develop intuition, we shall consider the propagation of ionizing

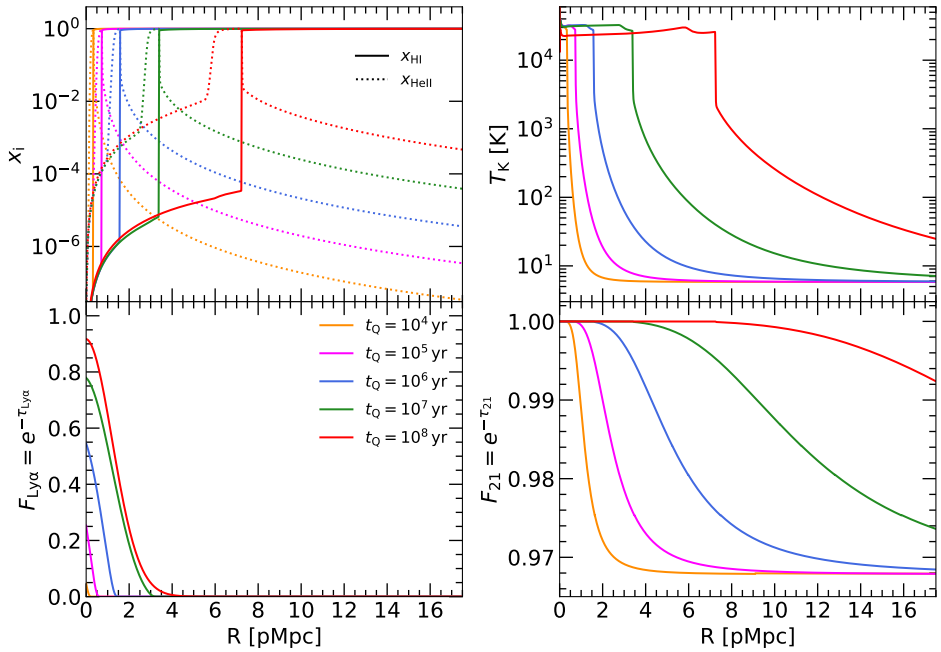

Figure 4.2: Radiative transfer simulation of UV and X-ray photons emitted by a quasar into a uniform density field with $\Delta = \rho/\langle\rho\rangle = 1$ at $z = 7$. The hydrogen and helium gas is assumed to be initially cold and neutral, and the quasar has an absolute AB magnitude $M_{1450} = -27$ (corresponding to an ionizing photon emissivity of $\dot{N} = 1.64 \times 10^{57}\,{\rm s}^{-1}$ for our fiducial SED in Fig. 4.1). Curves with different colours show different values for the optically/UV bright lifetime of the quasar, $t_{\rm Q}$, as indicated in the lower left panel. *Upper left:* the H I fraction (solid curves, $x_{\rm HI} = n_{\rm HI}/n_{\rm H}$) and He II fraction (dotted curves, $x_{\rm HeII} = n_{\rm HeII}/n_{\rm He}$). *Upper right:* the gas kinetic temperature $T_{\rm K}$. We assume strong coupling of the spin temperature in the vicinity of the quasar, such that the spin temperature $T_{\rm S} = T_{\rm K}$. *Lower left:* the Lyα transmission, $F_{\rm Ly\alpha} = e^{-\tau_{\rm Ly\alpha}}$. *Lower right:* the 21-cm transmission, $F_{21} = e^{-\tau_{21}}$.

radiation from a quasar into a homogeneous medium. We assume $\Delta = \rho/\langle\rho\rangle = 1$, ignore peculiar velocities, and assume the gas is initially cold and neutral. Fig. 4.2 shows the results from an RT simulation for a quasar at $z = 7$ with $M_{\rm AB} = -27$, assuming our fiducial SED. The outputs for different optically/UV bright lifetimes, $t_{\rm Q}$, for the quasar are shown by the coloured curves and are labelled in the lower left panel.

The top left panel in Fig. 4.2 shows the neutral hydrogen ($x_{\rm HI}$, solid

curves) and singly-ionized helium ($x_{\rm HeII}$, dotted curves) fractions around the quasar. One can see the H II and He III ionization fronts expanding with time. The hydrogen within the quasar H II region is highly ionized ($x_{\rm HI} < 10^{-4}$), and the gas is optically thin to Lyα photons. This is demonstrated in the bottom left panel of Fig. 4.2 where we show the Lyα transmission, $F_{\rm Ly\alpha} = e^{-\tau_{\rm Ly\alpha}}$. Note, however, that the Lyα transmission does not saturate at the position of the H II ionization front. This is particularly apparent for larger optically/UV bright lifetimes, $t_{\rm Q} > 10^7\,{\rm yr}$. This is in part due to the IGM Lyα damping wing from the neutral IGM that is evident in the Lyα transmission profile (Miralda-Escudé & Rees, 1998; Mesinger & Furlanetto, 2008; Bolton et al., 2011), but also because the residual neutral hydrogen density close to the H II ionization front has already risen above the threshold required for saturated Lyα absorption (see e.g. Bolton & Haehnelt, 2007; Lidz et al., 2007; Maselli et al., 2007; Keating et al., 2015; Eilers et al., 2017; Davies et al., 2020; Chen & Gnedin, 2021a).

The gas temperature around the quasar, displayed in the top right panel of Fig. 4.2, is $T_{\rm K} \sim 2$–$3 \times 10^4\,{\rm K}$ behind the H II and He III ionization fronts (e.g. D'Aloisio et al., 2019). However, there is also heating of the neutral gas *ahead* of the H II ionization front. For example, for $t_{\rm Q} = 10^7\,{\rm yr}$ (green curve), the average gas temperature ahead of the H II ionization front position at $R = 3.5\,{\rm pMpc}$ is $\langle T \rangle \sim 100\,{\rm K}$. This heating is due to soft X-ray photons with long mean free paths, $\lambda_{\rm X}$, that can penetrate into the neutral IGM. By converting $\lambda_{\rm X}$ from Eq. (2.26) to proper distance and adopting fiducial values we obtain

$$\lambda_{\rm X} = \frac{1}{n_{\rm HI}\sigma_{\rm HI}} \simeq 1.0\,{\rm pMpc}\, x_{\rm HI}^{-1}\Delta^{-1}\left(\frac{E}{0.2\,{\rm keV}}\right)^{2.8}\left(\frac{1+z}{8}\right)^{-3}. \qquad (4.1)$$

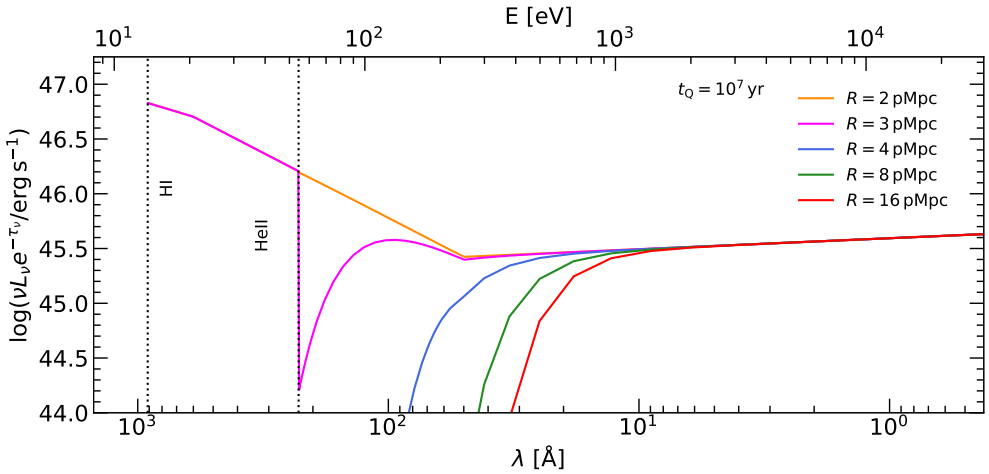

Figure 4.3: Ionizing spectrum (i.e. photon energies $E > 13.6\,\mathrm{eV}$) at different distances from a $M_{1450} = -27$ quasar after following the radiative transfer of the intrinsic quasar SED displayed in Fig. 4.1 through a uniform, neutral IGM with density $\Delta = 1$ at $z = 7$. The spectrum corresponds to the model shown by the green curves in Fig. 4.2 for an optically/UV bright lifetime of $t_Q = 10^7$ yr. The ionization thresholds for H I and He II are displayed as dotted vertical lines. Note that only X-ray photons propagate unimpeded beyond the H II ionization front, which is located at $R = 3.5\,\mathrm{pMpc}$ in Fig. 4.2.

The role of X-rays is further evident from Fig. 4.3, which shows the IGM attenuated quasar luminosity, $L_\nu e^{-\tau_\nu}$, at different distances, R, from the quasar assuming an optically/UV bright lifetime of $t_Q = 10^7$ yr (the green curves in Fig. 4.2). Beyond the H II ionization front (i.e. $R \geq 3.5\,\mathrm{pMpc}$) only X-ray photons penetrate into the neutral IGM surrounding the quasar H II region. This long range X-ray heating acts to suppress the 21-cm absorption from neutral gas by increasing the H I spin temperature (see e.g. Xu et al., 2011; Mack & Wyithe, 2012, and Chapter 3) and thus lowering the 21-cm optical depth. Note also that at $R = 2\,\mathrm{pMpc}$ (orange curve in Fig. 4.3) the IGM is optically thin and the quasar spectrum matches the intrinsic SED in Fig. 4.1, while the spectrum at $R = 3\,\mathrm{pMpc}$ (fuchsia curve) lies between the H II and He III ionization front and therefore exhibits

a strong absorption edge at the He II ionization potential, $E = 54.4\,\mathrm{eV}$.

The lower right panel of Fig. 4.2 shows the resulting 21-cm transmission, $F_{21} = e^{-\tau_{21}}$, around the quasar. Here $\tau_{21} \ll 1$ behind the H II ionization front because the gas is hot and ionized, but where the gas (and spin) temperature decrease to $T_{\rm K} = T_{\rm S} < 100\,\mathrm{K}$, some 21-cm absorption (i.e. $F_{21} < 1$) is apparent. For longer optically/UV bright lifetimes the quasar H II region expands and X-ray heating extends further into the neutral IGM. The 21-cm absorption close to the quasar then becomes partially or completely suppressed even if the gas ahead of the H II ionization front remains largely neutral.

In summary, we expect the Lyα transmission arising from the highly ionized hydrogen around quasars to be influenced by UV photons, but for neutral hydrogen, the 21-cm forest absorption will be very sensitive to long range heating by the X-ray photons emitted by the quasar. We now turn to consider more detailed simulations of Lyα and 21-cm absorption around quasars using realistic density, peculiar velocity and ionization fields extracted from the Sherwood-Relics simulations.

4.3 Near-zones in inhomogeneous reionization simulations

4.3.1 Hydrodynamical simulations

We use a subset of simulations drawn from the Sherwood-Relics project (Puchwein et al., 2022) to generate realistic Lyα and 21-cm forest spectra

Table 4.1: The volume averaged H I fraction in the IGM, $\langle x_{\rm HI} \rangle$, at redshift $z = 6$, 7 and 8 for the three Sherwood-Relics simulations used in this chapter: RT-late, RT-mid and RT-early (see Molaro et al., 2022, for further details).

Model	$\langle x_{\rm HI} \rangle$, $z = 6$	$\langle x_{\rm HI} \rangle$, $z = 7$	$\langle x_{\rm HI} \rangle$, $z = 8$
RT-late	1.42×10^{-1}	4.75×10^{-1}	7.07×10^{-1}
RT-mid	2.39×10^{-3}	4.44×10^{-1}	7.12×10^{-1}
RT-early	7.70×10^{-6}	1.56×10^{-1}	5.49×10^{-1}

around bright quasars. These simulations are described in Section 2.1. The main advantage that Sherwood-Relics offers for the work in this chapter is it provides a model for the spatial variations expected in the H I fraction and photo-ionization rates around the dark matter haloes hosting bright quasars at $z \geq 6$ (see also Lidz et al., 2007; Satyavolu et al., 2022).

In this chapter we analyse Sherwood-Relics runs that use the three reionization histories first described by Molaro et al. (2022) (see their fig. 2), in which reionization completes at $z_{\rm R} = 5.3$, $z_{\rm R} = 6.0$ and $z_{\rm R} = 6.6$ (labelled RT-late, RT-mid and RT-early, respectively). Here we define $z_{\rm R}$ as the redshift where the volume averaged neutral fraction first falls below $\langle x_{\rm HI} \rangle \sim 10^{-3}$. The volume averaged H I fractions in the simulations at $z = 6$, 7 and 8 are listed in Table 4.1. All three models are consistent with existing constraints on $\langle x_{\rm HI} \rangle$ at $z > 6$ and the CMB electron scattering optical depth, but the RT-late model in particular is chosen to match the $z_{\rm R}$ required by the large scale fluctuations observed in the Lyα forest effective optical depth at $z \gtrsim 5$ (Becker et al., 2015b; Kulkarni et al., 2019; Keating et al., 2020; Bosman et al., 2022; Zhu et al., 2022). We use RT-late for our fiducial reionization model in this chapter.

In order to construct realistic quasar sight-lines from Sherwood-Relics simulations, we first use a friends-of-friends halo finder to identify dark

matter haloes in the simulations. We select haloes with mass $> 10^{10}\,\mathrm{M}_{\odot}$ and extract sight lines in three orthogonal directions around them. The mass of the dark matter haloes that host supermassive black holes is uncertain, although clustering analyses at lower redshift suggest $\sim 10^{12}\,\mathrm{M}_{\odot}$ (e.g. Shen et al., 2007), which is significantly larger than our minimum halo mass. However, as discussed by Keating et al. (2015) and Satyavolu et al. (2022), the choice of halo mass has a very limited impact on the sizes of quasar Lyα near-zones. This is because the halo bias at $\gtrsim 2\,\mathrm{pMpc}$ from a halo at $z \gtrsim 6$ is very small (see also Calverley et al., 2011; Chen et al., 2022b). We have confirmed this is also true for the 21-cm absorption from the diffuse IGM we consider in this chapter. Next, we splice these halo sight lines (consisting of the gas overdensity Δ, gas peculiar velocity v_{pec}, gas temperature T_{K}, neutral hydrogen fraction x_{HI}, and UV background photo-ionization rate Γ_{HI}) with skewers drawn randomly through the simulation volume to give a total sight line length of $100h^{-1}\,\mathrm{cMpc}$. Each of the randomly drawn skewers is taken from simulation outputs sampled every $\Delta z = 0.1$ to account for the redshift evolution along the quasar line of sight. Individual skewers are connected at pixels where Δ, T_{K}, x_{HI} and v_{pec} agree within < 10 per cent. For every model parameter variation, we then construct 2000 unique sight lines for performing the 1D quasar RT calculations.

Finally although our hydrodynamical simulations follow heating from adiabatic compression, shocks and photo-ionization by an inhomogeneous UV radiation field, they do not model neutral gas heated and ionized by the high redshift X-ray background. We follow Section 2.2 and include the pre-heating of the neutral IGM by assuming a uniform X-ray background emissivity (see Eq. 2.2). We consider $0.01 \leq f_{\mathrm{X}} \leq 0.1$ in this chapter, which

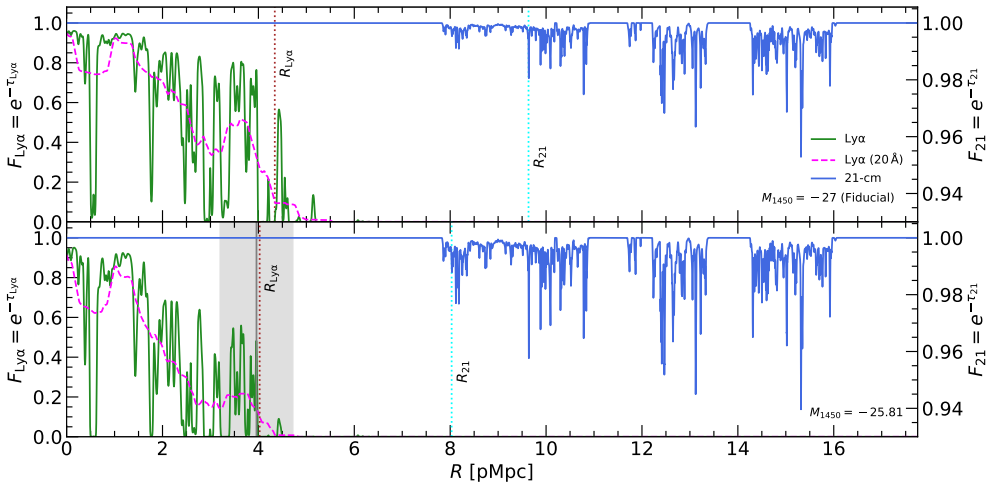

Figure 4.4: An example of simulated Lyα and 21-cm absorption in the vicinity of a bright quasar at $z = 7$, obtained from the RT-late Sherwood-Relics simulation with $\langle x_{\rm HI} \rangle = 0.48$ combined with a 1D RT calculation for the quasar radiation. The quasar has an optically/UV bright lifetime of $t_{\rm Q} = 10^7$ yr and an X-ray background efficiency of $f_{\rm X} = 0.01$ is assumed. *Top panel:* The Lyα (green curves) and 21-cm (blue curves) transmission for our fiducial quasar SED with $M_{1450} = -27$. Note the scale for F_{21} is shown on the right vertical axis. The dashed fuchsia curve shows the Lyα transmission after smoothing by a boxcar of width 20 Å, with the Lyα near-zone size, $R_{\rm Ly\alpha}$, shown by the vertical brown dotted line. The 21-cm forest spectrum is smoothed by a boxcar of width 5 kHz and the cyan vertical line, labelled with R_{21}, shows the distance from the quasar where the 21-cm absorption first reaches $F_{21} = 0.99$. *Bottom panel:* As for the top panel, but for a fainter quasar absolute magnitude of $M_{1450} = -25.81$, matching the $z = 6.82$ radio-loud quasar PSO J172+18 (Bañados et al., 2021). The grey band shows the observed $R_{\rm Ly\alpha}$ for PSO J172+18.

is equivalent to $10^{36.2}\,{\rm erg\,s^{-1}\,cMpc^{-3}} \leq \epsilon_{\rm X,0.5-2\,keV} \leq 10^{37.2}\,{\rm erg\,s^{-1}\,cMpc^{-3}}$ at $z = 7$.

4.3.2 Example Lyα and 21-cm absorption spectrum

A simulated quasar spectrum at $z = 7$ constructed from the RT-late simulation is displayed in Fig. 4.4. The panels show the Lyα (solid green curves) and 21-cm absorption (solid blue curves) for our fiducial SED with

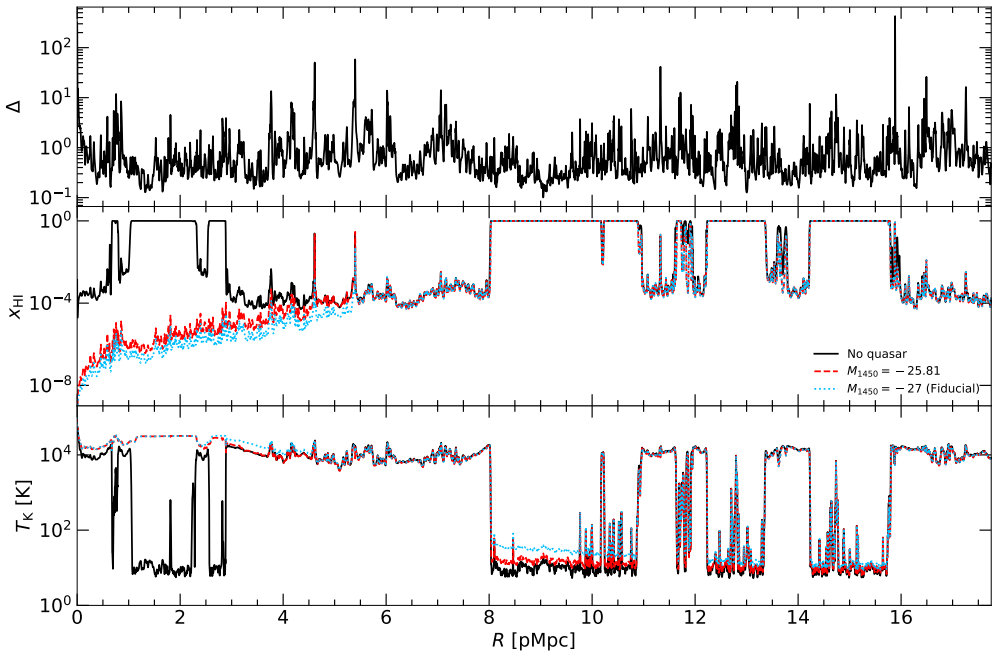

Figure 4.5: Properties of an inhomogeneous IGM in the proximity of a quasar. *Top panel:* Gas overdensity, $\Delta = \rho/\langle\rho\rangle$, along the sight line. *Middle panel:* Neutral hydrogen fraction, $x_{\rm HI}$, for the case of no quasar (black curve), the fiducial quasar model (cyan dotted curve) and for the fainter quasar that mimics PSO J172+18 (red dashed curve). *Bottom panel:* Gas temperature, where the line styles match those in the panel above.

$M_{1450} = -27$, and for a fainter quasar with $M_{1450} = -25.81$, corresponding to an ionizing photon emissivity of $\dot{N} = 5.48 \times 10^{56}\,{\rm s}^{-1}$. Both models assume an optically/UV bright quasar lifetime of $t_{\rm Q} = 10^7\,{\rm yr}$ and an X-ray background efficiency $f_{\rm X} = 0.01$. The fainter absolute magnitude is chosen to match the radio-loud quasar PSO J172+18 at $z = 6.82$, recently presented by Bañados et al. (2021). From top to bottom, Fig. 4.5 displays the gas overdensity, $\Delta = \rho/\langle\rho\rangle$, neutral hydrogen fraction, $x_{\rm HI}$, and gas temperature, $T_{\rm K}$, for the case of no quasar (black curves), the fiducial quasar model (cyan dotted curves) and for the fainter quasar that mimics PSO J172+18 (red dashed curves). Note the pre-existing neutral and ionized regions associated with patchy reionization, and the heating of neutral gas

ahead of the large ionized region at $R > 8\,\mathrm{pMpc}$ by the X-ray emission from the quasar. The 21-cm absorption is only present where the gas is neutral, and it is stronger for the $M_{1450} = -25.81$ quasar due to the lower gas (and H I spin) temperature at $R > 8\,\mathrm{pMpc}$. There is also a proximate Lyman limit system at $R \sim 5.4\,\mathrm{pMpc}$ that terminates the quasar H II ionization front, beyond which the neutral hydrogen fractions are very similar for all the three cases (see also Chen & Gnedin, 2021a).

We obtain the size of the simulated Lyα near-zones, $R_{\mathrm{Ly}\alpha}$, following the definition introduced by Fan et al. (2006). This is the point where the normalised transmission first drops below $F_{\mathrm{Ly}\alpha} = 0.1$ after smoothing the Lyα spectrum with a boxcar of width 20 Å. The smoothed spectrum is shown by the fuchsia dashed curves in Fig. 4.4. For our fiducial quasar SED we obtain $R_{\mathrm{Ly}\alpha} = 4.34\,\mathrm{pMpc}$ (shown by the vertical brown dotted line in Fig. 4.4), and for the fainter quasar with $M_{1450} = -25.81$ we find $R_{\mathrm{Ly}\alpha} = 4.03\,\mathrm{pMpc}$.[1] In this case we have deliberately chosen a simulated quasar sight line that matches the observed Lyα near-zone size of $R_{\mathrm{Ly}\alpha} = 3.96 \pm 0.48\,\mathrm{pMpc}$ for PSO J172+18 (Bañados et al., 2021), shown by the grey band in the second panel of Fig. 4.4. As noted by Bañados et al. (2021), after correcting for the quasar luminosity, the Lyα near-zone size for PSO J172+18 is in the top quintile of $R_{\mathrm{Ly}\alpha}$ for quasars at $z \gtrsim 6$. Our modelling suggests a possible explanation is that PSO J172+18 is surrounded by an IGM that is (locally) highly ionized due to UV emission from galaxies, despite the *average* H I fraction in the IGM being much larger. For example, for the model displayed in Fig. 4.4, the average IGM

[1] Note that the dependence of $R_{\mathrm{Ly}\alpha}$ on $\dot{N}$ for this example is much weaker than the expected scaling of between $R_{\mathrm{Ly}\alpha} \propto \dot{N}^{1/3}$ and $R_{\mathrm{Ly}\alpha} \propto \dot{N}^{1/2}$ (Bolton & Haehnelt, 2007; Eilers et al., 2017). This is due to the effect of the proximate Lyman limit system.

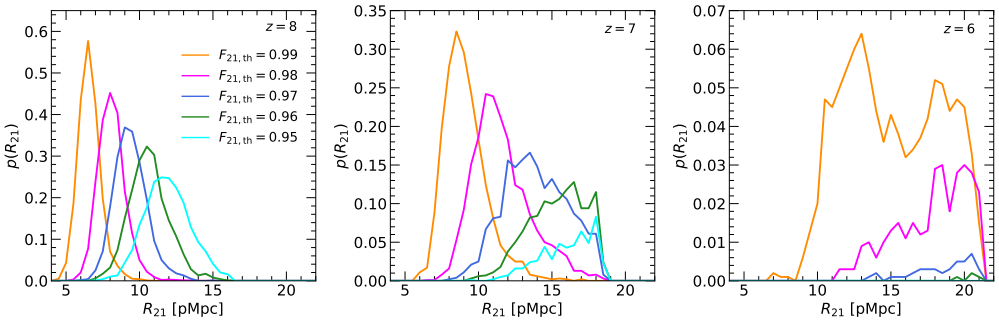

Figure 4.6: The probability distribution of R_{21} assuming different values for distance from the quasar at which the 21-cm transmission first drops below $F_{21,\mathrm{th}}$, after smoothing the 21-cm spectrum with a boxcar filter of width 5 kHz. The results are shown for our fiducial model for 2000 sight lines at $z = 8$, 7 and 6. Note the different scale on the vertical axes of each panel; many sight lines at $z = 6$ show no 21-cm absorption with $F < F_{21,\mathrm{th}}$. Additionally, the length of the simulated sight-lines is $100h^{-1}$ cMpc, so there is an artificial cut-off in the distributions at $R_{21} = [16.4, 18.4, 21.1]$ pMpc at $z = [8, 7, 6]$.

neutral fraction is $\langle x_{\mathrm{HI}} \rangle = 0.48$, but there is a pre-existing highly ionized region with $x_{\mathrm{HI}} \sim 10^{-4}$ close to the quasar halo at $R \sim 3$–8 pMpc.

In Fig. 4.4 we have also marked the distance from the quasar, R_{21}, where the proximate 21-cm absorption first reaches a threshold of $F_{21,\mathrm{th}} = e^{-\tau_{21}} = 0.99$ after smoothing the spectrum with a boxcar of width 5 kHz (vertical cyan dotted lines). This occurs at $R_{21} = 9.63$ pMpc for the $M_{\mathrm{AB}} = -27$ quasar and at $R_{21} = 8.03$ pMpc for the $M_{\mathrm{AB}} = -25.81$ quasar. By what follows, we will use this as our working definition of what we term the "21-cm near-zone" size. In analogy to the widely used definition for $R_{\mathrm{Ly}\alpha}$ (e.g. Fan et al., 2006), our definition of R_{21} is practical rather than physically motivated. The choice of $F_{21,\mathrm{th}} = 0.99$ as the transmission threshold where we define R_{21} is somewhat arbitrary. Here we show how a different choice of $F_{21,\mathrm{th}}$ affects our results. Fig. 4.6 shows the distribution of R_{21} in our fiducial RT-late reionization model at redshift $z = 8$, 7 and 6, assuming a range of $F_{21,\mathrm{th}}$ values. We have assumed $M_{1450} = -27$, $f_{\mathrm{X}} = 0.01$,

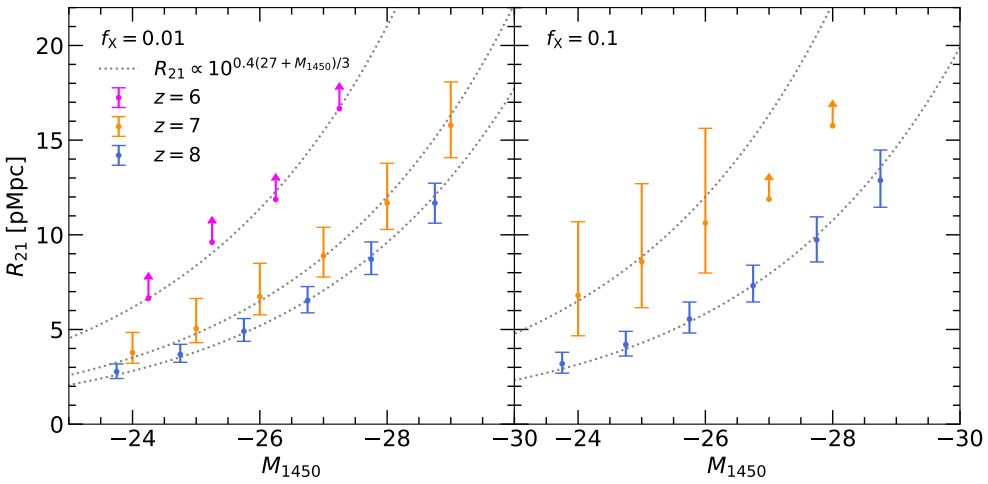

Figure 4.7: The 21-cm near-zone size, R_{21}, as a function of the quasar magnitude, M_{1450}, at z = 6 (fuchsia points), $z = 7$ (orange points) and $z = 8$ (blue points) in the RT-late model. The fiducial SED and optically/UV bright lifetime of $t_Q = 10^7$ yr are assumed, for an X-ray background efficiency $f_X = 0.01$ (left panel) and $f_X = 0.1$ (right panel). The data points correspond to the median and 68 per cent range for 2000 simulated quasar sight-lines. Arrows indicate the 68 per cent lower limit for R_{21} when multiple sight-lines have no pixels with $F_{21,th} < 0.99$. The points are slightly offset on the horizontal axes for presentation purposes. The grey dotted curves show $R_{21} \propto 10^{0.4(27+M_{1450})/3}$, which is the expected scaling for an H II region (i.e. $R_{21} \propto \dot{N}^{1/3}$). Note also there are no sight lines with $F_{21,th} < 0.99$ for $f_X = 0.1$ at $z = 6$.

$t_Q = 10^7$ yr and our fiducial quasar SED in the models. Decreasing $F_{21,th}$ shifts the R_{21} distribution to larger values, consistent with the expectation that stronger 21-cm absorption features should appear further from the quasar due to the lower spin temperatures (see e.g. Fig. 4.2). In addition, note that while we find absorption features with $F_{21,th} \geq 0.98$ in almost all sight lines at $z = 7$, only 62 per cent contain features with $F_{21,th} = 0.96$, and this further decreases to 26 per cent for $F_{21,th} = 0.95$.

The dependence of $R_{Ly\alpha}$ on the quasar magnitude, M_{1450} (or equivalently the ionizing photon emission rate, $\dot{N}$) has been discussed extensively elsewhere (e.g. Bolton & Haehnelt, 2007; Davies et al., 2020; Ishimoto et al.,

2020; Satyavolu et al., 2022). In particular, Eilers et al. (2017) derived the scaling relation using their radiative transfer simulations (see Eq. (4.3)). Analogously, we present the dependence of R_{21} on M_{1450} in Fig. 4.7 for $f_{\rm X} = 0.01$ (top panel) and $f_{\rm X} = 0.1$ (bottom panel) at $z = 6$ (fuchsia points), $z = 7$ (orange points) and $z = 8$ (blue points) for a quasar with an optically/UV bright lifetime of $t_{\rm Q} = 10^7$ yr. The error bars show the 68 per cent scatter around the median obtained from 2000 simulated sight lines, and the arrows show 68 per cent lower limits.

We find $R_{21} \propto 10^{0.4(27+M_{1450})/3} \propto \dot{N}^{1/3}$ (dashed grey curves) is consistent with the simulations, in agreement with the expected scaling for the expansion of a quasar H II region (see Eq. (4.8)). Although note, because of X-ray heating beyond the ionization front and the patchy ionization state of the IGM, R_{21} does not always correspond to the position of the quasar H II ionization front. It instead roughly corresponds to the size of the region heated to $T_{\rm S} \gtrsim 100\,{\rm K}$ by the quasar. The only exception is for $f_{\rm X} = 0.1$ at $z = 6$, where proximate 21-cm absorption is very rare due to the heating of the remaining neutral gas in the IGM to spin temperatures $T_{\rm S} \gtrsim 10^2\,{\rm K}$. In this case only ~ 0.2 per cent of our 2000 synthetic spectra have $R_{21} < 21\,{\rm pMpc}$ for $M_{1450} > -27$, and even fewer for more luminous quasars. For comparison, in Chapter 3 we infer a lower limit of $f_{\rm X} > 0.109$ assuming a null detection of 21-cm absorption with $F_{21} \leq 0.99$ over a redshift path length of $\Delta z = 20$ at $z = 6$ (see Table 3.1). However, these numbers are for the general IGM, and exclude the effect of localised ionization and heating in close proximity to bright sources. Here, over our simulated path length of 2000 sight-lines of length $100h^{-1}\,{\rm cMpc}$ at $z = 6$ (corresponding to $\Delta z = 687.9$), from Chapter 3 we would naively expect

Table 4.2: The minimum flux density required to detect a 21-cm forest absorption feature with $F_{21,\rm th}$ with S/N = 5 using SKA1-low (middle column) or SKA2 (right column). This has been calculated from Eq. (4.2) assuming a bandwidth of $\Delta\nu = 5\,\rm kHz$, sensitivity $A_{\rm eff}/T_{\rm sys} = 600\,\rm m^2\,K^{-1}$ ($5500\,\rm m^2\,K^{-1}$) (Braun et al., 2019) and an integration time of $t_{\rm int} = 1000\,\rm hr$ ($100\,\rm hr$) for SKA1-low (SKA2).

$F_{21,\rm th}$	$S_{\rm min}/\,\rm mJy$, SKA1 − low	$S_{\rm min}/\,\rm mJy$, SKA2
0.99	17.2	5.9
0.98	8.6	3.0
0.97	5.7	2.0
0.96	4.3	1.5
0.95	3.4	1.2

~ 34 21-cm absorbers with $F_{21} < 0.99$. Instead, we find only 3 absorbers. This difference is largely due to the soft X-ray heating by the quasars reducing the incidence of the proximate 21-cm absorbers, and the rapid redshift evolution of the average IGM neutral fraction along our $100h^{-1}\,\rm cMpc$ sight lines.

Lastly, given our definition for R_{21}, we may also estimate the minimum radio source flux density, $S_{\rm min}$, required to detect an absorption feature with $F_{21,\rm th} = 0.99$ for a signal-to-noise ratio, S/N. Using Eq. 3.9 and adopting values representative for SKA1-low (Braun et al., 2019), we find

$$S_{\rm min} = 17.2\,\rm mJy \left(\frac{0.01}{1-F_{21,\rm th}}\right)\left(\frac{\rm S/N}{5}\right)\left(\frac{5\,\rm kHz}{\Delta\nu}\right)^{1/2}\left(\frac{1000\,\rm hr}{t_{\rm int}}\right)^{1/2} \times \left(\frac{600\,\rm m^2\,K^{-1}}{A_{\rm eff}/T_{\rm sys}}\right), \quad (4.2)$$

where $T_{\rm sys}$ is the system temperature, $\Delta\nu$ is the bandwidth, $A_{\rm eff}$ is the effective area of the telescope and $t_{\rm int}$ is the integration time. For a sensitivity appropriate for SKA1-low, $A_{\rm eff}/T_{\rm sys} \simeq 600\,\rm m^2\,K^{-1}$ (Braun et al., 2019), an integration time of $t_{\rm int} = 1000\,\rm hr$ and S/N = 5, we obtain $S_{\rm min} = 17.2\,\rm mJy$. Instead, for SKA2 with $A_{\rm eff}/T_{\rm sys} \simeq 5500\,\rm m^2\,K^{-1}$ (Braun

et al., 2019) and $t_{\rm int} = 100\,{\rm hr}$ a detection of an absorption feature of $F_{21,\rm th} = 0.99$ would require a radio-loud quasar with $S_{\rm min} = 5.9\,{\rm mJy}$. For comparison, PSO J172+18 has a 3σ upper limit on the flux density at 147.5 MHz of $S_{147.5\,{\rm MHz}} < 8.5\,{\rm mJy}$ (Bañados et al., 2021). The brightest known radio-loud blazar at $z > 6$, PSO J0309+27 at $z = 6.1$ with $M_{1450} = -25.1$, instead has a flux density $S_{147\,{\rm MHz}} = 64.2 \pm 6.2\,{\rm mJy}$ (Belladitta et al., 2020). Both objects are therefore potential targets for detecting proximate 21-cm absorption from the diffuse IGM, although note the shape of their SEDs will be rather different. Also, we list the $S_{\rm min}$ that a radio source must have for SKA1-low or SKA2 to detect a 21-cm forest absorber with $F_{21,\rm th}$ in Table 4.2.

4.3.3 Comparison to observed Lyα near-zone sizes

Next, as a consistency check of our model, we compare the Lyα near-zone sizes predicted in our simulations to the observed distribution in Fig. 4.8. We have compiled a sample of Lyα near-zone sizes measured from the spectra of 76 $z > 5.77$ quasars (Carilli et al., 2010; Reed et al., 2015; Eilers et al., 2017, 2020, 2021; Mazzucchelli et al., 2017; Bañados et al., 2018a, 2021; Ishimoto et al., 2020; Greig et al., 2022) which is presented in Table 4.3. We use the (model dependent) $R_{\rm Ly\alpha}$–M_{1450} scaling relation derived by Eilers et al. (2017) to approximately correct for differences in the quasar absolute magnitudes. For an observed absolute magnitude of $M_{1450,\rm obs}$, this gives a corrected Lyα near-zone size of

$$R_{\rm Ly\alpha,corr} = R_{\rm Ly\alpha,obs} \times 10^{0.4\left(27+M_{1450,\rm obs}\right)/2.35} \propto \dot{N}^{0.43}. \tag{4.3}$$

Table 4.3: Overview of the measurements of the Lyα near-zone sizes. The columns show the name of the source, its redshift, AB magnitude at 1450Å, the measured Lyα near-zone size and its corrected value scaled to $M_{1450} = -27$ luminosity according to Eq. 4.3. The redshifts were measured using [C II] (*a*), Mg II (*b*), CO (*c*), Lyα (*d*) and Lyα+NV (*e*) lines. References: (1) Carilli et al. (2010), (2) Reed et al. (2015), (3) Eilers et al. (2017), (4) Mazzucchelli et al. (2017), (5) Bañados et al. (2018a), (6) Eilers et al. (2020), (7) Ishimoto et al. (2020), (8) Bañados et al. (2021), (9) Eilers et al. (2021), (10) Greig et al. (2022).

Object	z	M_{1450}	$R_{\mathrm{Ly}\alpha,\mathrm{obs}}$ [cMpc]	$R_{\mathrm{Ly}\alpha,\mathrm{corr}}$ [cMpc]	Ref.
ULAS J1342+0928	7.541^{a}	-26.76	1.3	1.43	5
J1007+2115	7.515^{a}	-26.66	1.5	1.71	10
ULAS J1120+0641	7.084^{a}	-26.58	2.1 ± 0.02	2.48 ± 0.02	4
DES J0252+0503	7.020^{e}	-26.50	1.7	2.07	10
VIK J2348–3054	6.902^{a}	-25.74	2.64 ± 0.03	4.33 ± 0.05	4
PSO J172+18	6.823^{b}	-25.81	3.96 ± 0.48	6.31 ± 0.77	8
VIK J0109–3047	6.791^{a}	-25.58	1.59 ± 0.02	2.77 ± 0.03	4
PSO J338+29	6.666^{a}	-26.08	5.35 ± 0.17	7.67 ± 0.25	4
PSO J006+39	6.621^{a}	-25.94	4.47 ± 0.06	6.77 ± 0.09	4
VIK J0305–3150	6.615^{a}	-26.13	3.417 ± 0.004	4.81 ± 0.006	4
PSO J323+12	6.588^{a}	-27.06	6.23 ± 0.01	6.09 ± 0.01	4
PSO J231–20	6.586^{a}	-27.14	4.28 ± 0.03	4.05 ± 0.03	4
SHELLQs J0921+0007	6.563^{b}	-26.16	3.05 ± 0.45	4.24 ± 0.63	7
PSO J0226+0302	6.541^{a}	-27.33	3.66 ± 0.09	3.22 ± 0.08	7
PSO J167–13	6.515^{a}	-25.57	2.02 ± 0.02	3.54 ± 0.03	4
SHELLQs J1545+4232	6.511^{b}	-24.76	2.14 ± 0.18	5.15 ± 0.43	7
PSO J261+19	6.494^{b}	-25.69	$3.36^{+0.59}_{-0.33}$	$5.61^{+0.99}_{-0.55}$	9
PSO J247+24	6.476^{b}	-26.53	2.46 ± 0.2	2.96 ± 0.24	4
PSO J011+09	6.470^{a}	-26.85	2.42 ± 0.13	2.57 ± 0.14	9
CFHQS J0210–0456	6.432^{a}	-24.53	1.38 ± 0.03	3.63 ± 0.08	7
SDSS J1148+5251	6.419^{a}	-27.62	4.7 ± 0.03	3.69 ± 0.02	7
CFHQS J2329-0301	6.416^{a}	-25.25	2.73 ± 0.04	5.42 ± 0.08	7
SHELLQs J0859+0022	6.390^{a}	-23.10	1.14 ± 0.03	5.26 ± 0.14	7
SHELLQs J1152+0055	6.364^{a}	-25.08	2.67 ± 0.03	5.67 ± 0.06	7
SHELLQs J2304+0045	6.350^{a}	-24.28	1.15 ± 0.01	3.34 ± 0.03	7
SDSS J0100+2802	6.326^{a}	-29.14	7.12 ± 0.13	3.08 ± 0.06	3
SDSS J1030+0524	6.309^{b}	-26.99	6.00 ± 0.51	6.02 ± 0.51	7
SHELLQs J1406–0116	6.292^{b}	-24.76	0.14 ± 0.05	0.34 ± 0.12	7
SDSS J1623+3112	6.257^{a}	-26.55	5.05 ± 0.14	6.02 ± 0.17	7
CFHQS J0050+3445	6.253^{b}	-26.70	3.96 ± 0.17	4.45 ± 0.19	7
VDES J0323-4701	6.250^{b}	-26.02	$2.26^{+0.62}_{-0.35}$	$3.32^{+0.91}_{-0.51}$	9

Table 4.3 (cont.)

Object	z	M_{1450}	$R_{\mathrm{Ly}\alpha,\mathrm{obs}}$ [cMpc]	$R_{\mathrm{Ly}\alpha,\mathrm{corr}}$ [cMpc]	Ref.
SHELLQs J2239+0207	6.250^{a}	-24.60	1.65 ± 0.02	4.23 ± 0.05	7
VDES J0330-4025	6.249^{b}	-26.42	$1.69^{+0.62}_{-0.35}$	$2.12^{+0.78}_{-0.44}$	9
SDSS J1048+4637	6.228^{c}	-27.55	4 ± 0.6	3.22 ± 0.48	1
CFHQS J0227–0605	6.212^{d}	-25.28	2.27 ± 0.4	4.45 ± 0.78	7
PSO J0402+2452	6.180^{d}	-26.95	4.17 ± 1.38	4.25 ± 1.41	3
PSO J359-06	6.172^{a}	-26.79	2.83 ± 0.14	3.07 ± 0.15	9
CFHQS J2229+1457	6.152^{a}	-24.78	0.47 ± 0.14	1.12 ± 0.33	9
SDSS J1250+3130	6.138^{b}	-26.53	4.91 ± 0.29	5.9 ± 0.35	7
ULAS J1319+0950	6.133^{a}	-27.05	4.99 ± 0.04	4.89 ± 0.04	7
CFHQS J1509–1749	6.118^{b}	-26.98	4.3 ± 0.72	4.33 ± 0.73	1
SDSS J2315–0023	6.117^{d}	-25.66	3.7 ± 1.39	6.26 ± 2.35	3
SHELLQs J1208–0200	6.117^{a}	-24.36	0.62 ± 0.01	1.74 ± 0.03	7
PSO J239–07	6.110^{a}	-27.46	1.32 ± 0.14	1.1 ± 0.12	9
SHELLQs J2216–0016	6.096^{a}	-23.65	0.66 ± 0.02	2.45 ± 0.07	7
DES J0454–4448	6.090^{d}	-26.50	4.1 ± 1.1	4.99 ± 1.34	2
SDSS J1602+4228	6.083^{b}	-26.94	6.82 ± 0.29	6.98 ± 0.30	7
CFHQS J2100-1715	6.081^{a}	-25.55	0.37 ± 0.14	0.65 ± 0.25	9
SHELLQs J2228+0152	6.081^{a}	-24.00	2.11 ± 0.02	6.84 ± 0.06	7
SDSS J0303-0019	6.078^{b}	-25.56	2.28 ± 0.44	4.01 ± 0.77	7
SDSS J0842+1218	6.076^{a}	-26.91	6.95 ± 0.04	7.2 ± 0.04	7
PSO J158-14	6.069^{a}	-27.41	1.95 ± 0.14	1.66 ± 0.12	9
SDSS J1630+4012	6.065^{b}	-26.19	5.25 ± 1.03	7.21 ± 1.41	7
SDSS J0353+0104	6.049^{e}	-26.53	1.8 ± 1.34	2.16 ± 1.61	1
CFHQS J1641+3755	6.047^{b}	-25.67	4.00 ± 0.18	6.74 ± 0.3	7
SDSS J2054–0005	6.039^{a}	-26.21	3.12 ± 0.01	4.25 ± 0.01	7
SDSS J1306+0356	6.034^{a}	-26.81	6.51 ± 0.02	7.01 ± 0.02	7
PSO J265+41	6.026^{a}	-25.56	1.04 ± 0.14	1.83 ± 0.25	6
SDSS J0818+1723	6.020^{d}	-27.52	5.89 ± 1.42	4.8 ± 1.16	3
SDSS J1137+3549	6.009^{b}	-27.36	5.81 ± 0.62	5.05 ± 0.54	7
SDSS J0841+2905	5.980^{e}	-27.12	10.9 ± 1.34	10.4 ± 1.28	1
ULAS J0148+0600	5.980^{b}	-27.39	6.11 ± 0.64	5.24 ± 0.55	7
PSO J056–16	5.968^{a}	-26.72	0.79 ± 0.14	0.88 ± 0.16	9
SHELLQs J1202–0057	5.929^{a}	-22.83	0.74 ± 0.01	3.79 ± 0.05	7
SDSS J1411+1217	5.904^{b}	-26.69	4.61 ± 0.13	5.21 ± 0.15	7
SDSS J1335+3533	5.901^{c}	-26.67	0.7 ± 0.1	0.8 ± 0.11	7
NDFWS J1425+3254	5.892^{c}	-26.09	8.8 ± 0.6	12.57 ± 0.86	1
SDSS J1436+5007	5.850^{e}	-26.54	8.7 ± 1.34	10.42 ± 1.6	1
SDSS J0840+5624	5.844^{c}	-27.24	0.88 ± 0.15	0.8 ± 0.14	3
SDSS J0005–0006	5.844^{b}	-25.73	2.91 ± 0.06	4.79 ± 0.10	7

Table 4.3 (cont.)

Object	z	M_{1450}	$R_{\mathrm{Ly}\alpha,\mathrm{obs}}$ [cMpc]	$R_{\mathrm{Ly}\alpha,\mathrm{corr}}$ [cMpc]	Ref.
SDSS J1143+3808	5.837^{c}	-26.69	3.93 ± 0.63	4.44 ± 0.71	9
SDSS J0002+2550	5.818^{b}	-27.31	8.83 ± 0.46	7.82 ± 0.41	7
PSO J004+17	5.817^{a}	-26.01	1.16 ± 0.15	1.71 ± 0.22	9
SDSS J0836+0054	5.810^{b}	-27.75	5.16 ± 0.2	3.85 ± 0.15	7
SDSS J1044–0125	5.782^{c}	-27.47	5.7 ± 0.6	4.74 ± 0.5	1
SDSS J0927+2001	5.772^{c}	-26.76	4.69 ± 0.05	5.15 ± 0.05	7

In this work we rescale the observed sizes, $R_{\mathrm{Ly}\alpha,\mathrm{obs}}$, to obtain a corrected size, $R_{\mathrm{Ly}\alpha,\mathrm{corr}}$, at our fiducial absolute magnitude $M_{1450} = -27$.

In each panel of Fig. 4.8 we vary one parameter around our fiducial model values and compare the simulated Lyα near-zone sizes at $z = 6$, 7 and 8 to the observed $R_{\mathrm{Ly}\alpha,\mathrm{corr}}$. Clockwise from the upper left, the parameters varied are: the reionization history of the Sherwood-Relics model (and hence the initial volume averaged H I fraction in the IGM, see Table 4.1), the efficiency parameter for the X-ray background, f_{X}, the optical-to-X-ray spectral index of the quasar, α_{OX}, and the optically/UV bright lifetime of the quasar, t_{Q}, assuming a "light bulb" model for the quasar light curve. At each redshift, we show the median $R_{\mathrm{Ly}\alpha}$ and the 68 per cent distribution from 2000 simulated sight lines. For comparison, in the lower left panel we also show the results from the 1D RT simulations performed by Eilers et al. (2017) for an optically/UV bright lifetime of $t_{\mathrm{Q}} = 10^{7.5}\,\mathrm{yr}$, assuming either a highly ionized IGM (dashed green line) or fully neutral IGM (dashed cyan line). The results for our fiducial parameters (i.e. RT-late, $f_{\mathrm{X}} = 0.01$, $\alpha_{\mathrm{OX}} = -1.44$ and $t_{\mathrm{Q}} = 10^{7}\,\mathrm{yr}$) are consistent with the Eilers et al. (2017) models within the 68 per cent scatter. Similarly, the dashed purple curve shows the 1D RT simulations from Chen & Gnedin (2021a)

for $t_{\rm Q} = 10^6\,{\rm yr}$, which – allowing for the somewhat larger $\langle x_{\rm HI} \rangle$ we have assumed in the RT-late reionization model – are again similar to this work if using the same optically/UV bright quasar lifetime.

In general, the simulated $R_{{\rm Ly}\alpha}$ decreases with increasing redshift (e.g. Fan et al., 2006; Wyithe, 2008; Carilli et al., 2010) and, as shown in the upper left panel of Fig. 4.8, models with a larger initial IGM H I fraction produce slightly smaller Lyα near-zone sizes. Note, however, that any inferences regarding $\langle x_{\rm HI} \rangle$ from $R_{{\rm Ly}\alpha}$ will be correlated with the assumed optically/UV bright lifetime (e.g. Bolton et al., 2011; Keating et al., 2015). Furthermore, at $z = 6$ the $R_{{\rm Ly}\alpha}$ for RT-early (blue data points), which has a volume averaged H I fraction of $\langle x_{\rm HI} \rangle = 7.7 \times 10^{-6}$ at this redshift, is outside the range displayed. This is because many sight lines in this model are highly ionized and do not have (20 Å smoothed) Lyα transmission that falls below $F_{{\rm Ly}\alpha} = 0.1$. For RT-early at $z = 6$, we instead obtain a 68 per cent lower limit of $R_{{\rm Ly}\alpha} > 18.33\,{\rm pMpc}$, suggesting that the UV background at $z \simeq 6$ is significantly overproduced by the RT-early model. In contrast, varying the X-ray heating of the IGM, either by changing $f_{\rm X}$ or $\alpha_{\rm OX}$ (upper and lower right panels, respectively), has very little effect on the Lyα near-zone sizes. As already discussed in Section 4.2.2, this is because the ionization and heating by X-rays is important only for the cold, neutral IGM, and not the ionized gas observed in Lyα transmission.

Finally, in the lower left panel of Fig. 4.8, we observe that some of the scatter in the observational data may be reproduced by varying the optically/UV bright lifetime of the quasar. Indeed, Morey et al. (2021) have recently demonstrated that the majority of $R_{{\rm Ly}\alpha,{\rm corr}}$ measurements at $z \simeq 6$ are reproduced assuming a median optically/UV bright lifetime of

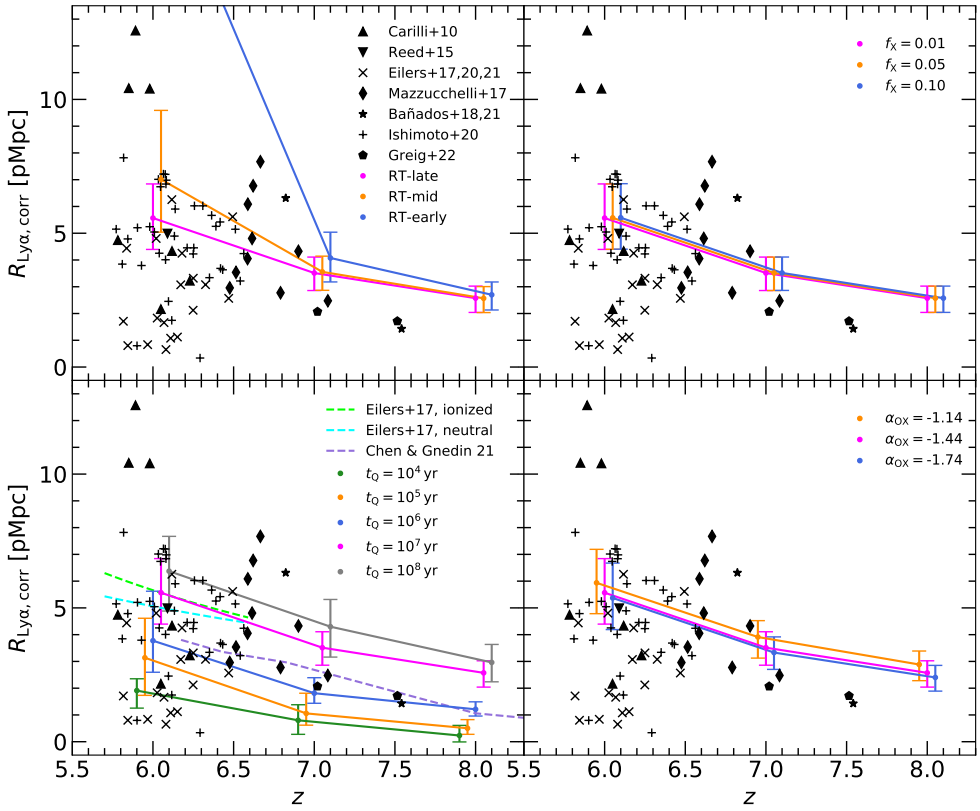

Figure 4.8: The redshift evolution of observed and simulated Lyα near-zone sizes. The filled circles at $z = 6$, 7 and 8 connected by solid lines show the median $R_{\mathrm{Ly}\alpha}$ and 68 per cent scatter from 2000 simulated quasar sight lines. Clockwise from the top left, each panel shows the effect of varying one parameter around our fiducial model value: the reionization history of the Sherwood-Relics model (and hence the initial volume averaged H I fraction in the IGM, see Table 4.1), the efficiency parameter for the X-ray background, f_{X}, the optical-to-X-ray spectral index of the quasar, α_{OX}, and the optically/UV bright lifetime of the quasar, t_{Q}, assuming a "light bulb" model for the quasar light curve. Note that the data point at $z = 6$ for the RT-early model (blue, top left panel) is outside the range shown here. Results from the 1D RT simulations performed by Eilers et al. (2017) for an optically/UV bright lifetime of $t_{\mathrm{Q}} = 10^{7.5}$ yr are also shown for an initially highly ionized IGM (dashed green line) or fully neutral IGM (dashed cyan line) in the bottom left panel. In this panel we also show results from the 1D RT simulations from Chen & Gnedin (2021a) for $t_{\mathrm{Q}} = 10^6$ yr and an inhomogeneously reionized IGM (dashed purple curve). The observed $R_{\mathrm{Ly}\alpha}$ (black data points, Carilli et al., 2010; Reed et al., 2015; Eilers et al., 2017, 2020, 2021; Mazzucchelli et al., 2017; Bañados et al., 2018a, 2021; Ishimoto et al., 2020; Greig et al., 2022) have been rescaled to correspond to an absolute magnitude of $M_{1450} = -27$ (see Eq. 4.3).

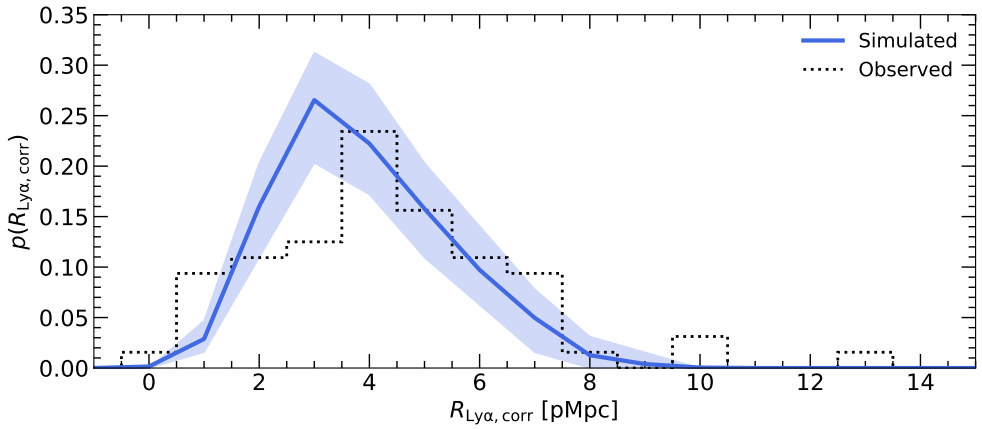

Figure 4.9: The probability distribution for (luminosity corrected) Lyα near-zone sizes (blue solid curve) at $z = 6$ from radiative transfer simulations using our fiducial model the quasar lifetime distribution from Morey et al. (2021). The shaded region shows the 1σ uncertainty obtained by bootstrapping. For comparison, the $R_{\mathrm{Ly}\alpha,\mathrm{corr}}$ distribution from observed quasars in the redshift range $5.8 \leq z \leq 6.6$ is shown by the dotted histogram.

$t_{\mathrm{Q}} = 10^{5.7}$ yr with a 95 per cent confidence interval $t_{\mathrm{Q}} = 10^{5.3}$–$10^{6.5}$ yr (see their fig. 6).[2] We test this in Fig. 4.9, where instead of using a single value for t_{Q} in our simulations, we adopt values using the posterior probability distribution for the quasar lifetimes inferred by Morey et al. (2021). We select 2000 quasar lifetime values from their distribution using a Monte Carlo rejection method. Each simulated sight line was then randomly assigned a different t_{Q} from this sample. We then performed 2000 radiative transfer simulations of our fiducial model at $z = 6$, and bootstrapped 10^4 sets of sight lines from these simulations to obtain a 1σ uncertainty. Each bootstrapped set contains 64 synthetic sight lines, corresponding to the number of quasars in the compiled observational sample we use for quasars at $5.8 \leq z \leq 6.6$.

The dotted black curve in Fig. 4.9 shows the observed distribution of

[2]See also Khrykin et al. (2019, 2021) and Worseck et al. (2021) for closely related results obtained with the He II proximity effect at $z \simeq 3$–4.

luminosity corrected Lyα near-zone sizes at $5.8 \leq z \leq 6.6$. The solid blue curve corresponds to the median and 1σ uncertainty obtained by bootstrapping our simulations. A two-sided Kolmogorov-Smirnov test yields a p-value of 0.055, which remains consistent ($p > 0.05$) with the null-hypothesis that the samples are drawn from the same distribution. There is a hint that the simulated near-zone sizes are slightly smaller than the observational data, which may be a result of applying the Morey et al. (2021) $t_{\rm Q}$ distribution to our late reionization model (see also Satyavolu et al., 2022). Our RT-late simulation has a larger average IGM neutral fraction at $z = 6$ compared to the models used by Morey et al. (2021), which assumes a fully ionized IGM. However, this difference is not highly significant.

On the other hand, the largest Lyα near-zones with $R_{\rm Ly\alpha,corr} \geq 10\,$pMpc reported by Carilli et al. (2010) are not reproduced by the RT-late simulation even for $t_{\rm Q} = 10^8\,$yr, suggesting the IGM along these sight lines may be more ionized than assumed in the RT-late model. It is also possible our small box size of $40h^{-1}\,$cMpc fails to correctly capture large ionized regions near the quasar host haloes at the tail-end of reionization (cf. Iliev et al., 2014; Kaur et al., 2020), and may therefore miss sight lines with the largest $R_{\rm Ly\alpha}$. Of particular interest here, however, are the quasars with $R_{\rm Ly\alpha,corr} \lesssim 2\,$pMpc (Eilers et al., 2020, 2021), which correspond to $\lesssim 10$ per cent of the observational data at $z \simeq 6$. As noted by Eilers et al. (2021), a very short optically/UV bright quasar lifetime of $t_{\rm Q} \lesssim 10^4$–$10^5\,$yr is required to reproduce these Lyα near-zone sizes. The implied average optically/UV bright lifetime of $t_{\rm Q} \sim 10^6\,$yr, consistent with Morey et al. (2021), therefore presents an apparent challenge for black hole growth at

$z \geq 6$. We discuss this further in Section 4.5.1.

In summary, the Lyα forest near-zone sizes predicted by our simulations assuming a late end to reionization at $z \simeq 5.3$ are consistent with both independent modelling and the observational data if we allow for a distribution of optically/UV bright quasar lifetimes (e.g. Morey et al., 2021). We now use this model to explore the expected proximate 21-cm forest absorption around (radio-loud) quasars at $z \geq 6$.

4.4 Predicted extent of proximate 21-cm absorption

4.4.1 The effect of X-ray heating and IGM neutral fraction

The effect of X-ray heating and the IGM neutral fraction on the distribution of "21-cm near zone" sizes, R_{21}, predicted by our simulations is displayed in Fig. 4.10 (solid curves). In all cases we assume $M_{1450} = -27$ and a light bulb quasar model with an optically/UV bright lifetime of $t_{\rm Q} = 10^7\,{\rm yr}$. For comparison, the $R_{{\rm Ly}\alpha}$ distributions from the same models are given by the dashed curves. The top left panel shows the effect of varying the reionization model, and hence the initial volume averaged neutral fraction in the IGM, $\langle x_{\rm HI} \rangle$. At $z = 7$, the $\langle x_{\rm HI} \rangle$ values for RT-late (fuchsia curves) and RT-mid (orange curves) are very similar, and we find little difference between these models for R_{21} or $R_{{\rm Ly}\alpha}$. For the more highly ionized RT-early simulation, the near-zone sizes are slightly larger, although note almost half of the 2000 quasar spectra do not have any pixels with $F_{21} < 0.99$ at $z = 7$. In the bottom left panel, we instead show results from the RT-late

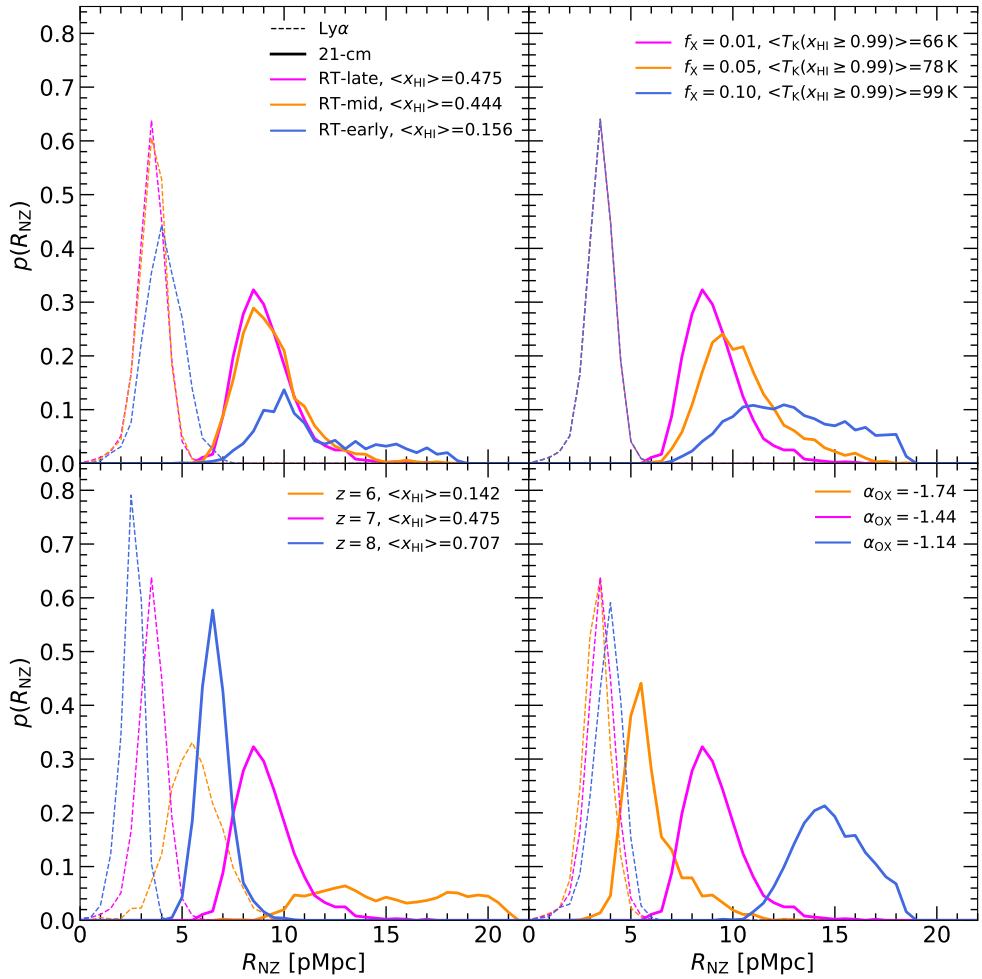

Figure 4.10: Probability distributions for Lyα (dashed thin curves) and 21-cm (solid thick curves) near-zone sizes obtained from 2000 simulated quasar sight lines (see Section 4.3.2 for the definition of $R_{\mathrm{Ly}\alpha}$ and R_{21}). The distributions show the effect of varying parameters around our fiducial model. Clockwise from the top left, these parameters are: the reionization history, the X-ray background efficiency f_{X}, the quasar optical-to-X-ray spectral index α_{OX}, and the redshift of the quasar. We also list the mean neutral hydrogen fraction (left panels) and the mean temperature in pixels with $x_{\mathrm{HI}} \geq 0.99$ (top right panel) prior to any quasar heating. The fiducial values at $z = 7$ are RT-late with $\langle x_{\mathrm{HI}} \rangle = 0.48$, $f_{\mathrm{X}} = 0.01$ and $\alpha_{\mathrm{OX}} = -1.44$. All models furthermore assume an absolute magnitude of $M_{1450} = -27$ and an optically/UV bright lifetime of $t_{\mathrm{Q}} = 10^7$ yr. Note that while $R_{\mathrm{Ly}\alpha}$ is insensitive to f_{X} or α_{OX}, R_{21} has a strong dependence on the X-ray heating around the quasar. Both $R_{\mathrm{Ly}\alpha}$ and R_{21} are sensitive to the IGM neutral fraction. The solid curves in the bottom left panel are the same as the orange curves shown in Fig. 4.6.

simulation at three different redshifts, $z = 6$, 7 and 8. The Lyα and 21-cm near-zone sizes are larger toward lower redshift, again due to the smaller H I fraction in the IGM, but also now because of the decrease in the proper gas density (i.e. $n_{\rm H} \propto (1+z)^3$). However, once again, at $z = 6$ (fuchsia curves) around half the quasar sight-lines do not exhibit 21-cm absorption with $F_{21} < 0.99$. This suggests that observing 21-cm absorption from the diffuse IGM in close proximity to radio-loud quasars will be more likely if reionization is late ($z_{\rm R} \simeq 5.3$) as suggested by Kulkarni et al. (2019), and if suitably bright radio-loud quasars can be identified at $z \gtrsim 7$.

The effect of X-ray heating on the near-zone sizes is displayed in the right panels of Fig. 4.10. The top right panel shows the heating by the X-ray background, while the bottom right panel shows the effect of quasar X-ray heating when varying the optical-to-X-ray spectral index, $\alpha_{\rm OX}$. As noted earlier, $R_{{\rm Ly}\alpha}$ is insensitive to $f_{\rm X}$ and $\alpha_{\rm OX}$, but R_{21} is sensitive to both; the average 21-cm near-zone size increases as the spin temperature of the neutral gas is raised by X-ray photo-heating. For example, for $f_{\rm X} = 0.01$ the average temperature of hydrogen with $x_{\rm HI} > 0.99$ (i.e. neutral gas ahead of the H II ionization front) is $T_{\rm K} = 66\,{\rm K}$, but this increases to $T_{\rm K} = 99\,{\rm K}$ for $f_{\rm X} = 0.1$. For $T_{\rm K} \gg 10^2\,{\rm K}$ (or equivalently, $f_{\rm X} \gg 0.1$), we expect very little 21-cm absorption will be detectable at all (see Chapter 3). A similar situation holds for $\alpha_{\rm OX}$, with a harder quasar X-ray spectrum producing larger R_{21}. Deep X-ray observations may be used to constrain $\alpha_{\rm OX}$ for at least some $z \gtrsim 6$ radio-loud quasars (Connor et al., 2021). Prior knowledge of the quasar X-ray spectrum could therefore help break some of the degeneracy between R_{21} and the X-ray heating parameters $f_{\rm X}$ and $\alpha_{\rm OX}$. As already discussed, however, the location of the expanding

quasar H II region and the spin temperature beyond the H II ionization front determine the optical depth of neutral gas, where $\tau_{21} \propto x_{\rm HI}/T_{\rm S} \sim T_{\rm S}^{-1}$. This means R_{21} is also sensitive to the optically/UV bright lifetime of the quasar, $t_{\rm Q}$.

4.4.2 The effect of the optically/UV bright lifetime

In Fig. 4.11, for our fiducial model we examine how $R_{\rm Ly\alpha}$ and R_{21} evolve with the optically/UV bright lifetime of the quasar at redshift $z = 6$ (orange curves), $z = 7$ (fuchsia curves) and $z = 8$ (blue curves). The shaded regions bound 68 per cent of the data around the median for 2000 simulated sight lines. The behaviour of $R_{\rm Ly\alpha}$ at $z = 6$, displayed in the left panel, is qualitatively similar to the results of other recent work (e.g. Eilers et al., 2018, 2021; Davies et al., 2020; Satyavolu et al., 2022). There are three distinct phases in the evolution of $R_{\rm Ly\alpha}$ at $z = 6$. For a highly ionized IGM, when the optically/UV bright lifetime of the quasar is shorter than the equilibriation timescale, $t_{\rm Q} < t_{\rm eq}$, we expect $R_{\rm Ly\alpha}$ to increase with $t_{\rm Q}$. The equilibriation timescale is approximately

$$t_{\rm eq} = \frac{x_{\rm HI,\,eq}}{n_{\rm e}\alpha_A(T)} \simeq \frac{10^{5.0}\,{\rm yr}}{\Delta}\left(\frac{x_{\rm HI,\,eq}}{10^{-4}}\right)\left(\frac{T}{10^4\,{\rm K}}\right)^{0.72}\left(\frac{1+z}{7}\right)^{-3}, \qquad (4.4)$$

where $x_{\rm HI,\,eq}$ is the H I fraction in ionization equilibrium, we have used a case-A recombination coefficient $\alpha_{\rm A} = 4.06 \times 10^{-13}\,{\rm cm^3\,s^{-1}}(T/10^4\,{\rm K})^{-0.72}$ and assumed $n_{\rm e} = 1.158 n_{\rm H}$ for a fully ionized hydrogen and helium IGM. For $t_{\rm Q} > t_{\rm eq}$, the growth of the Lyα near-zone size slows and becomes largely insensitive to $t_{\rm Q}$ (see e.g. Bolton & Haehnelt, 2007). In this regime the near-zone size is set by the Lyα absorption from the residual H I in the

IGM, rather than the growth of the H II region around the quasar. Finally, at $t_{\rm Q} \gtrsim 10^{6.5}\,{\rm yr}$, the Ly$\alpha$ near-zone starts to grow again. As noted by Eilers et al. (2018), the late growth of $R_{\rm Ly\alpha}$ is due to the propagation of the He III ionization front into the IGM. The associated He II photo-heating raises the IGM temperature and hence further lowers the H I fraction in the IGM (see also Bolton et al., 2012). We also point out that the median $R_{\rm Ly\alpha}$ we obtain at $z = 6$ for $10^5\,{\rm yr} < t_{\rm Q} < 10^{6.5}\,{\rm yr}$ are slightly smaller than those reported in fig. 2 of Davies et al. (2020). This is because we use our RT-late simulation with $\langle x_{\rm HI} \rangle = 0.14$ at $z = 6$, instead of assuming a highly ionized IGM as Davies et al. (2020) do. In the RT-late model, neutral islands will persist in underdense regions at $z = 6$ and hence slow the growth of the near-zones. Further discussion of this point can also be found in Satyavolu et al. (2022).

For reference, we also show the distribution of observed $R_{\rm Ly\alpha,corr}$ in the left panel of Fig. 4.11, which has a mean quasar redshift of $z = 6.26$. Once again, note that reproducing the Lyα near-zones with $R_{\rm Ly\alpha,corr} < 2\,{\rm pMpc}$ at $z \simeq 6$ requires $t_{\rm Q} \lesssim 10^4$–$10^5\,{\rm yr}$. As expected, at $z = 7$ and $z = 8$, the Lyα near-zones are smaller. Here the initial H I fractions in the IGM for RT-late are $\langle x_{\rm HI} \rangle = 0.48$ and $\langle x_{\rm HI} \rangle = 0.71$, respectively. The large IGM H I fractions also produce a strong Lyα damping wing that suppresses Lyα near-zone sizes. For reference, the $z = 7.54$ quasar ULAS J1342+0928 has $R_{\rm Ly\alpha,corr} = 1.43\,{\rm pMpc}$ (Bañados et al., 2018a), whereas the $z = 7.08$ quasar ULAS J1120+0641 has $R_{\rm Ly\alpha,corr} = 2.48 \pm 0.2\,{\rm pMpc}$ (Mortlock et al., 2011; Mazzucchelli et al., 2017). We find our simulations are consistent with these sizes for optically/UV bright lifetimes in the range $10^4\,{\rm yr} \leq t_{\rm Q} \leq 10^{6.8}\,{\rm yr}$.

In the right panel of Fig. 4.11 we show the dependence of the 21-cm near-

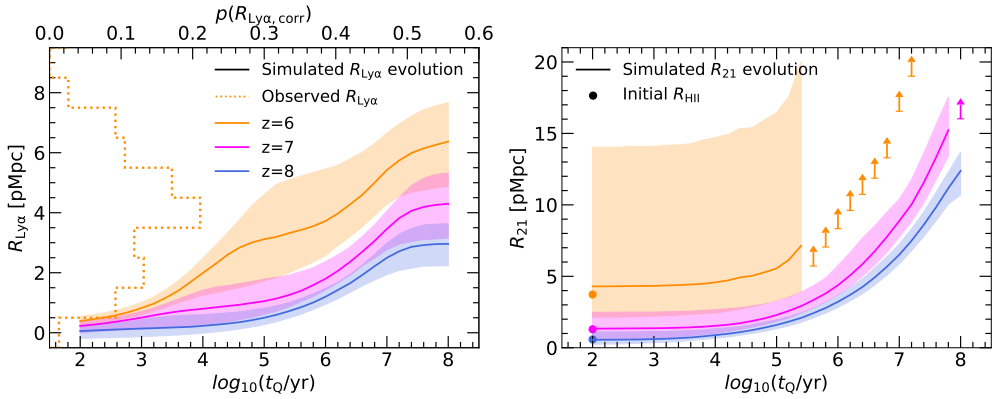

Figure 4.11: The dependence of the Lyα (left panel) and 21-cm (right panel) near-zone sizes on the optically/UV bright quasar lifetime, t_{Q}, at $z = 6$ (orange), $z = 7$ (fuchsia) and $z = 8$ (blue). Note the different scales on the vertical axes of the panels. The curves show the median value obtained from 2000 mock spectra, while the shaded regions mark the 68 per cent range around the median. Upward pointing arrows give the lower 68 per cent bound on R_{21} in the cases where some of the sight-lines have no pixels with $F_{21} < 0.99$. The dotted orange histogram in the left panel shows the observed distribution of $R_{\mathrm{Ly}\alpha,\mathrm{corr}}$, with a mean quasar redshift of $z = 6.26$. The filled circles at $t_{\mathrm{Q}} = 10^2\,\mathrm{yr}$ in the right panel show the median size, R_{HII}, of the pre-existing H II region surrounding the quasar host halo. All models are drawn from the RT-late simulation and assume $M_{1450} = -27$, $f_{\mathrm{X}} = 0.01$ and $\alpha_{\mathrm{OX}} = -1.44$.

zone size on the optically/UV bright lifetime, t_{Q}. Note in particular the filled circles in Fig. 4.11 at $t_{\mathrm{Q}} = 10^2\,\mathrm{yr}$, which show the median size, R_{HII}, of the pre-existing H II regions created by the galaxies surrounding the quasar host haloes.[3] The initial value of R_{21} is very similar to R_{HII}, suggesting the typical size of these pre-existing H II regions will set the 21-cm near-zone sizes for short optically/UV bright lifetimes. We find $R_{21} \sim R_{\mathrm{HII}}$ for $t_{\mathrm{Q}} \lesssim 10^4\,\mathrm{yr}$. However, for $t_{\mathrm{Q}} \gtrsim 10^4\,\mathrm{yr}$ (i.e. exceeding the local photo-ionization timescale at R_{HII}, where $t_{\mathrm{ion}} = \Gamma_{\mathrm{HI}}^{-1} \sim 10^4$–$10^5\,\mathrm{yr}$), the quasar starts to expand the pre-existing H II region and X-rays begin to photo-heat

[3]We define R_{HII} as the distance from the quasar host halo where $x_{\mathrm{HI}} = 0.9$ is first exceeded, and have verified that choosing larger values of x_{HI} up to 0.999 does not change R_{HII} significantly.

the neutral gas ahead of the quasar H II ionization front to $T_{\rm K} > 10^2$ K. The 21-cm near-zone then grows. Note also that at $z = 6$, there is a large 68 per cent scatter around the median R_{21}, and for $t_{\rm Q} > 10^{5.5}$ yr, many of the simulated sight-lines at $z = 6$ have no pixels with $F_{21} < 0.99$. In this case we instead show lower limits for R_{21} that bound 68 per cent of the simulated sight-lines. At $z = 7$ and $z = 8$, the median R_{21} is smaller with significantly less scatter, which (as for the case for the Lyα near-zones) is primarily because the average H I fraction in the IGM is larger at these redshifts.

In summary, our results suggest two intriguing possibilities. First, if there is a population of very young quasars at $z \geq 6$, as observed Lyα near-zones with $R_{{\rm Ly}\alpha} < 2$ pMpc imply (e.g. Eilers et al., 2017), then if $f_{\rm X} \lesssim 0.01$, a measurement of R_{21} around these objects should constrain the size of the H II region created by the galaxies clustered around the quasar host halo. Such a measurement would be complimentary to similar proposed measurements of $R_{\rm HII}$ from 21-cm tomography (e.g. Furlanetto et al., 2004b; Wyithe & Loeb, 2004b; Geil & Wyithe, 2008; Datta et al., 2012; Kakiichi et al., 2017; Ma et al., 2020; Davies et al., 2021), and would provide a strong constraint on the reionization sources. Second, once the quasar begins to heat the IGM ahead of the H II ionization front to $T_{\rm K} \gtrsim 10^2$ K, the 21-cm absorption is suppressed and R_{21} increases monotonically. In the absence of significant ionization, the cooling timescale for this gas is the adiabatic cooling timescale, where

$$t_{\rm ad} = \frac{1}{2H(z)} \simeq 10^{8.8}\,{\rm yr}\left(\frac{1+z}{8}\right)^{-3/2}, \tag{4.5}$$

and $H(z) \simeq H_0 \Omega_{\rm m}^{1/2}(1+z)^{3/2}$ is the Hubble parameter. Hence, in general R_{21} should always increase and it will be sensitive to the integrated lifetime of the quasar, because we typically expect $t_{\rm Q} \lesssim t_{\rm ad}$ (e.g Haehnelt et al., 1998; Yu & Tremaine, 2002; Martini, 2004). We now turn to explore the consequence of this for variable quasar emission, with particular emphasis on the possible implications for black hole growth at $z \gtrsim 6$ (cf. Eilers et al., 2018, 2021).

4.5 Probing integrated quasar lifetimes with proximate 21-cm absorption

4.5.1 A simple model for flickering quasar emission

Morey et al. (2021) have recently pointed out that the typical optically/UV bright lifetime of $t_{\rm Q} \sim 10^6\,{\rm yr}$ implied by the observed $R_{{\rm Ly}\alpha}$ is a challenge for the growth of $\sim 10^9\,{\rm M}_\odot$ black holes observed at $z \gtrsim 6$ (Mortlock et al., 2011; Bañados et al., 2018a; Yang et al., 2020a; Wang et al., 2020; Farina et al., 2022). Further discussion of this point in the context of Lyα near-zones can be found in Eilers et al. (2018) and Eilers et al. (2021), but we briefly repeat the argument here. For a quasar with bolometric luminosity L, the Salpeter (1964) (or e-folding) timescale if the black hole is accreting at the Eddington limit is

$$t_{\rm S} = \frac{\epsilon}{1-\eta}\frac{c\sigma_{\rm T}}{4\pi G \mu m_{\rm p}} = 4.33\times10^7\,{\rm yr}\left(\frac{L}{L_{\rm E}}\right)^{-1}\left(\frac{\epsilon}{0.1}\right)\left(\frac{1-\eta}{0.9}\right)^{-1}, \quad (4.6)$$

where $L_{\rm E}$ is the Eddington luminosity, $\sigma_{\rm T}$ is the Thomson cross-section,

$\mu = 1.158$ is the mean molecular weight for fully ionized hydrogen and helium with $Y_{\rm p} = 0.24$, η is the accretion efficiency, and ϵ is the radiative efficiency (e.g. Shakura & Sunyaev, 1973) where we assume $\epsilon = \eta$. For a black hole seed of mass $M_{\rm seed}$ and a constant accretion rate, the black hole mass, $M_{\rm BH}$, after $t_{\rm Q} = [10^6,\, 10^7,\, 10^8]\,{\rm yr}$ is then

$$M_{\rm BH} = M_{\rm seed} \exp\left(\frac{t_{\rm Q}}{t_{\rm S}}\right) = [1.0,\, 1.3,\, 10.1] M_{\rm seed}. \tag{4.7}$$

If $t_{\rm Q} \sim 10^6\,{\rm yr}$ there is insufficient time for the black hole to grow; Eq. (4.7) requires $M_{\rm BH} \sim M_{\rm seed} \sim 10^9\,{\rm M}_\odot$, yet the largest theoretically plausible seed mass is $M_{\rm seed} \sim 10^5$–$10^6\,{\rm M}_\odot$ (e.g. from the direct collapse of atomically cooled halo gas, Loeb & Rasio, 1994; Dijkstra et al., 2008; Regan et al., 2017; Inayoshi et al., 2020).

As discussed by Eilers et al. (2021), there are two possible solutions to this apparent dilemma; the $z \gtrsim 6$ quasars are indeed very young and have grown rapidly from massive seeds by radiatively inefficient ($\epsilon \sim 0.01$), mildly super-Eddington accretion (e.g. Madau et al., 2014; Volonteri et al., 2015; Davies et al., 2019) or the quasars are much older than the $R_{\rm Ly\alpha}$ measurements imply, such that $t_{\rm Q} \gtrsim 10^7\,{\rm yr}$. This is possible if the black holes have grown primarily in an optically/UV obscured phase and the quasars have only recently started to ionize their vicinity, perhaps due to the evacuation of obscuring material by feedback processes (Hopkins et al., 2005). Alternatively, quasar luminosity may vary between optically/UV bright and faint phases over an episodic lifetime of $t_{\rm ep} \sim 10^4$–$10^6\,{\rm yr}$, likely as a result of variable accretion onto the black hole (Schawinski et al., 2015; King & Nixon, 2015; Anglés-Alcázar et al., 2017; Shen, 2021). In this

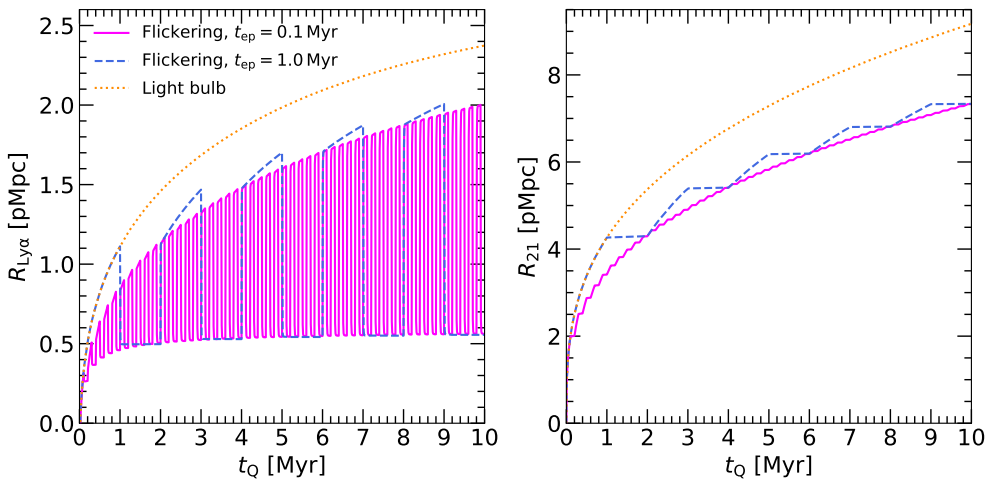

Figure 4.12: The dependence of $R_{\mathrm{Ly}\alpha}$ (left panel) and R_{21} (right panel) on the integrated quasar lifetime, t_{Q}, for a quasar at $z = 7$ that varies between a bright phase with $M_{1450} = -27$ and faint phase with $M_{1450} = -23$. We assume an optically/UV bright duty cycle of $f_{\mathrm{duty}} = 0.5$ and consider episodic lifetimes of $t_{\mathrm{ep}} = 10^5\,\mathrm{yr}$ (fuchsia solid curves) and $t_{\mathrm{ep}} = 10^6\,\mathrm{yr}$ (blue dashed curves). The IGM surrounding the quasar is initially cold and neutral. The near-zone size for a light bulb quasar emission model (dotted orange curves) is shown for comparison. Note in particular that while $R_{\mathrm{Ly}\alpha}$ decreases on the equilibriation timescale during the faint phase, t_{eq}, R_{21} remains almost constant due to the much longer adiabatic cooling timescale for the neutral gas, where the 21-cm optical depth $\tau_{21} \propto x_{\mathrm{HI}}/T_{\mathrm{S}}$.

scenario, when the quasars are faint the ionized hydrogen in their vicinity recombines on the equilibriation timescale (see Eq. 4.4). This produces an initially small Lyα near-zone size that regrows over a timescale $t_{\mathrm{ion}} = \Gamma_{\mathrm{HI}}^{-1} \sim 10^4$–$10^5\,\mathrm{yr}$ once the quasars re-enter the optically/UV bright phase (Davies et al., 2020; Satyavolu et al., 2022). Furthermore, for $t_{\mathrm{ep}} \lesssim t_{\mathrm{eq}}$ the H I surrounding the quasars never fully equilibriates, and $R_{\mathrm{Ly}\alpha}$ remains smaller than predicted for a light bulb light curve with the same *integrated* quasar lifetime.

However, it is difficult to distinguish between these possibilities using $R_{\mathrm{Ly}\alpha}$ alone. We suggest the proximate 21-cm absorption around sufficiently radio-bright quasars may provide some further insight. The long adiabatic

cooling timescale for neutral gas in the IGM means that, unlike $R_{\mathrm{Ly}\alpha}$, R_{21} will be sensitive to the integrated lifetime of the quasars. To illustrate this point further consider Fig. 4.12, where we use the simplified neutral, homogeneous IGM model discussed in Section 4.2.2 and Fig. 4.2 to explore the effect of variable quasar emission on the evolution of $R_{\mathrm{Ly}\alpha}$ (left panel) and R_{21} (right panel). In both panels the orange dotted curves show $R_{\mathrm{Ly}\alpha}$ and R_{21} for a light bulb emission model with $M_{1450} = -27$ and the fiducial SED. For the variable emission model, we instead follow a similar approach to Davies et al. (2020) and Satyavolu et al. (2022) and assume the quasar periodically flickers between a bright phase with $M_{1450} = -27$ and faint phase with $M_{1450} = -23$, while keeping the shape of the quasar SED fixed. We assume an optically/UV bright duty cycle of $f_{\mathrm{duty}} = 0.5$ and consider episodic lifetimes of $t_{\mathrm{ep}} = 10^5\,\mathrm{yr}$ (fuchsia solid curves) and $t_{\mathrm{ep}} = 10^6\,\mathrm{yr}$ (blue dashed curves). Shorter episodic lifetimes, $t_{\mathrm{ep}} \ll 10^5\,\mathrm{yr}$ may also be appropriate for some of the smallest observed near-zones at $z \simeq 6$ with $R_{\mathrm{Ly}\alpha,\mathrm{corr}} < 2\,\mathrm{pMpc}$, but the good agreement between the majority of the $R_{\mathrm{Ly}\alpha,\mathrm{corr}}$ measurements and simple light bulb models with $t_{\mathrm{Q}} \sim 10^6\,\mathrm{yr}$ suggest such short episodic lifetimes are unusual (Morey et al., 2021; Eilers et al., 2021). While we find that, as expected, $R_{\mathrm{Ly}\alpha}$ varies on timescales $t \simeq t_{\mathrm{eq}}$ and can potentially have $R_{\mathrm{Ly}\alpha} < 1\,\mathrm{pMpc}$ for $t_{\mathrm{Q}} \sim 10^7\,\mathrm{yr}$ if the quasar has just re-entered the bright phase, R_{21} instead increases monotonically with t_{Q}. Furthermore, in this example we have assumed the optical/UV and X-ray emission from the quasar become fainter simultaneously. If instead only the optical/UV emission is reduced – perhaps due to obscuring material that remains optically thin to X-rays – the X-ray heating will continue and R_{21} will evolve similarly to the light bulb model.

Note also that for a homogeneous medium for $t_{\rm Q} \ll t_{\rm rec}$, where $t_{\rm rec} = (\alpha_{\rm A}(T_{\rm K})\langle n_{\rm e}\rangle)^{-1} \equiv t_{\rm eq}/x_{\rm HI}$ is the recombination timescale, the quasar H II region will have size $R_{\rm HII} = [3\dot{N} f_{\rm duty} t_{\rm Q}/(4\pi\langle n_{\rm H}\rangle)]^{1/3}$, where

$$R_{\rm HII} \simeq 3.5\,{\rm pMpc} \left(\frac{f_{\rm duty}}{x_{\rm HI}}\right)^{1/3} \left(\frac{\dot{N}}{1.64\times10^{57}\,{\rm s}^{-1}}\right)^{1/3} \left(\frac{t_{\rm Q}}{10^7\,{\rm yr}}\right)^{1/3} \times \left(\frac{1+z}{8}\right)^{-1}. \tag{4.8}$$

Hence, for the example displayed in Fig. 4.12, $R_{{\rm Ly}\alpha} < R_{\rm HII}$ due to the IGM damping wing, but $R_{21} > R_{\rm HII}$ due to heating by X-rays ahead of the H II ionization front. We also expect the ratio $R_{21}/R_{{\rm Ly}\alpha}$ will typically be larger for flickering quasars with longer integrated lifetimes, $t_{\rm Q} \sim 10^7\,{\rm yr}$, that have just re-entered their bright phase. As R_{21} is sensitive to the integrated lifetime of the quasar, this suggests a combination of R_{21} and $R_{{\rm Ly}\alpha}$ – either for an individual radio-loud quasar or for a population of objects – could sharpen existing constraints on quasar lifetimes if the uncertainty in the X-ray background efficiency, $f_{\rm X}$, and the optical-to-X-ray spectral index, $\alpha_{\rm OX}$, can be marginalised over. Evidence for strong 21-cm absorption within a few proper Mpc of a radio-loud quasar would then hint at a short integrated quasar lifetime.

4.5.2 Time evolution of Lyα and 21-cm near-zones for flickering emission

We further consider the flickering quasar emission model using the RT-late Sherwood-Relics simulation for $f_{\rm X} = 0.01$ and our fiducial SED. In Fig. 4.13 we show the dependence of the median $R_{{\rm Ly}\alpha}$ (left panels) and R_{21} (right

panels) at $z = 7$ on the current episodic lifetime, $T_{\rm ep}$. This is just the duration of the most recent optically/UV bright phase with $M_{1450} = -27$ for a quasar that already has an integrated age $t_{\rm Q}$, with $f_{\rm duty} = 0.5$ and $t_{\rm ep} = 10^6\,{\rm yr}$. Three different integrated quasar ages are displayed, where $t_{\rm Q} = 0\,{\rm yr}$ (blue curves), $t_{\rm Q} = 2 \times 10^6\,{\rm yr}$ (fuchsia curves) and $t_{\rm Q} = 10^7\,{\rm yr}$ (orange curves), as measured from the start of the most recent optically/UV bright phase (i.e. for 0, 1 and 5 earlier episodic cycles with $t_{\rm ep} = 10^6\,{\rm yr}$, respectively). The shaded regions show the 68 per cent scatter around the median.

First, note the $R_{{\rm Ly}\alpha}$ and R_{21} values for $t_{\rm Q} = 0\,{\rm yr}$ are almost identical to the light bulb model in Fig. 4.11 (fuchsia curves) for $t_{\rm Q} \leq 10^6\,{\rm yr}$, as should be expected. However, in the case of older quasars with $t_{\rm Q} > t_{\rm ep}$ that have experienced at least one episodic cycle, we find (within the 68 per cent scatter) that $R_{{\rm Ly}\alpha} \lesssim 2\,{\rm pMpc}$ for $T_{\rm ep} \sim t_{\rm ion} < 10^{4.5}\,{\rm yr}$, and that $R_{{\rm Ly}\alpha}$ is *insensitive* to the integrated quasar age. As already discussed, this is a consequence of the re-equilibriation of the neutral hydrogen behind the quasar H II ionization front during the quasar faint phase. For an episodic lifetime of $t_{\rm ep} = 10^6\,{\rm yr}$, we would therefore expect $R_{{\rm Ly}\alpha,{\rm corr}} \lesssim 2\,{\rm pMpc}$ for ~ 3 per cent of $z = 7$ quasars, even if the integrated quasar age $t_{\rm Q} > t_{\rm ep}$. Similar results have been pointed out elsewhere (e.g. Davies et al., 2020)

On the other hand, as a result of the long cooling timescale for neutral gas ahead of the H II ionization front, R_{21} is ~ 2–5.5 times larger for $t_{\rm Q} = 10^7\,{\rm yr}$ (orange curve) compared to R_{21} for a quasar that has just turned on for the first time (blue curve). Hence, if invoking flickering quasar emission to reconcile the apparent short optically/UV bright lifetimes of quasars at $z \gtrsim 6$ with the build-up of $\sim 10^9\,{\rm M}_\odot$ black holes, we expect

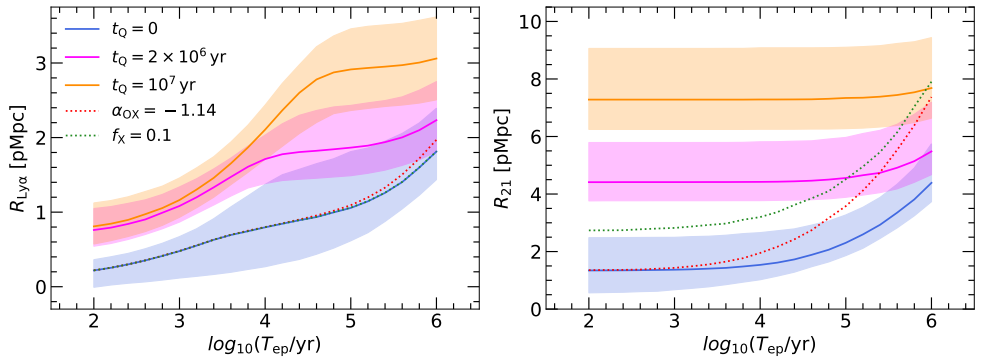

Figure 4.13: The dependence of $R_{\mathrm{Ly}\alpha}$ and R_{21} at $z = 7$ on the *current* episodic lifetime, T_{ep}, in a flickering quasar emission model. Results are shown for young quasars in their first bright phase ($t_{\mathrm{Q}} = 0\,\mathrm{yr}$, blue curves), for an intermediate case similar to the lifetime inferred by Morey et al. (2021) ($t_{\mathrm{Q}} = 10^{6.3}\,\mathrm{yr}$, fuchsia curves) and for our fiducial optically/UV bright quasar lifetime ($t_{\mathrm{Q}} = 10^{7}\,\mathrm{yr}$, orange curves). The shading corresponds to the 68 per cent scatter around the median from 2000 simulated sight lines. Note that while Lyα near-zones can be small ($R_{\mathrm{Ly}\alpha} < 1\,\mathrm{pMpc}$) for all t_{Q} when the quasar has recently entered the bright phase, R_{21} increases monotonically and will be considerably larger than $R_{\mathrm{Ly}\alpha}$ for $t_{\mathrm{Q}} = 10^{7}\,\mathrm{yr}$. We also show two additional models in which we boost the X-ray heating in the pre-reionization IGM by setting $f_{\mathrm{X}} = 0.1$ (dotted green curves) and $\alpha_{\mathrm{OX}} = -1.14$ (dotted red curves). Note these curves are almost indistinguishable in the left panel.

$R_{21} > R_{\mathrm{Ly}\alpha}$. Only for the case of a very young quasar do we find proximate 21-cm absorption with $R_{21} \sim 2\,\mathrm{pMpc}$. An important caveat here, however, is the level of X-ray heating in the neutral IGM. The dotted curves show results for $f_{\mathrm{X}} = 0.1$ or $\alpha_{\mathrm{OX}} = -1.14$ for the case of a $t_{\mathrm{Q}} = 0\,\mathrm{yr}$ (i.e. the blue curves for the fiducial model). While $R_{\mathrm{Ly}\alpha}$ remains unaffected by X-ray heating, R_{21} increases. Raising the X-ray background efficiency, f_{X}, results in a larger initial R_{21}, while a harder optical-to-X-ray spectral index, α_{OX}, increases R_{21} on timescales $T_{\mathrm{ep}} \gtrsim t_{\mathrm{ion}}$. Nevertheless, for $t_{\mathrm{Q}} \lesssim 10^{4}\,\mathrm{yr}$ we still expect $R_{21} \lesssim 3\,\mathrm{pMpc}$ if the quasar has not undergone earlier episodic cycles for $M_{\mathrm{AB}} = -27$, where the magnitude corrected size scales as $R_{21,\mathrm{corr}} \propto 10^{0.4(27+M_{1450})/3}$ (see Fig. 4.7). Finally, we point out that a

null detection of proximate 21-cm absorption with $F_{21} < 0.99$ would be indicative of an X-ray background with $f_{\rm X} \gtrsim 1$ at $z = 7$ (see Fig. 3.7).

In summary, we suggest that a measurement of R_{21} along the line of sight to radio-loud quasars could complement existing constraints on the lifetime of quasars obtained from Lyα transmission. Furthermore, a detection of proximate 21-cm absorption from the diffuse IGM within a few proper Mpc of a bright quasar at $z \simeq 7$ would present yet another challenge for the growth of $\sim 10^9\,{\rm M}_\odot$ black holes during the reionization epoch. Our modelling indicates that long range heating by X-ray photons means that for $f_{\rm X} \lesssim 0.1$, $R_{21} \lesssim$ 2–3pMpc should only occur for radio-loud quasars that have recently initiated accretion. Larger values of R_{21} coupled with $R_{{\rm Ly}\alpha,{\rm corr}} < 2\,{\rm pMpc}$ would instead hint at black hole growth progressing over timescales much longer than the optically/UV bright lifetimes of $t_{\rm Q} \sim 10^4\,{\rm yr}$ implied by the smallest Lyα near-zone sizes of the quasar population at $z \gtrsim 6$ (Morey et al., 2021).

4.6 Conclusions

Recent studies have suggested that observed Lyα near-zone sizes at $z \gtrsim 6$ (Fan et al., 2006; Carilli et al., 2010; Willott et al., 2010; Venemans et al., 2015; Reed et al., 2015; Eilers et al., 2017, 2021; Mazzucchelli et al., 2017; Ishimoto et al., 2020) are consistent with an average quasar optically/UV bright lifetime of $t_{\rm Q} \sim 10^6\,{\rm yr}$, with lifetimes as short as $t_{\rm Q} \lesssim 10^4$–$10^5\,{\rm yr}$ preferred by the smallest Lyα near-zones at $z \simeq 6$ (Eilers et al., 2017, 2021; Morey et al., 2021). If correct, this presents an apparent challenge for the build-up of $\sim 10^9\,{\rm M}_\odot$ supermassive black holes at $z \gtrsim 6$, as the black hole

growth e-folding time is at least an order of magnitude larger than $t_{\rm Q}$ if assuming Eddington limited accretion. These very young quasars would need to have grown from very massive seeds through radiatively inefficient, super Eddington accretion (Madau et al., 2014; Davies et al., 2019). Note, however, that because the number of black holes implied by the detected optically/UV bright quasars scales inversely with the optically/UV bright lifetime (e.g. Haehnelt et al., 1998), this would also push the quasars into rather low mass haloes. Alternatively, the quasars could be much older and have only recently entered an optically/UV bright phase. This is possible if most quasars at $z \gtrsim 6$ grow primarily in an optical/UV obscured phase (Hopkins et al., 2005; Ricci et al., 2017), or variable accretion causes them to "flicker" between optically/UV bright and faint states on episodic timescales $t_{\rm ep} \sim 10^5$–$10^6\,{\rm yr}$ (Schawinski et al., 2015; Shen, 2021). Distinguishing between these possibilities with Lyα near-zones is difficult, however, due to the relatively short equilibriation timescale, $t_{\rm eq} \sim 10^5\,{\rm yr}$, for the residual neutral hydrogen surrounding the quasar (Davies et al., 2020).

In this chapter, we have therefore used the Sherwood-Relics simulations of inhomogeneous reionization (Puchwein et al., 2022), coupled with line of sight radiative transfer calculations, to model the Lyα and 21-cm absorption in close proximity to $z \gtrsim 6$ quasars. The empirically calibrated reionization histories available in the Sherwood-Relics simulation suite and the flexibility of our line of sight radiative transfer algorithm allows us to explore a large parameter space, including variations in the IGM neutral fraction, the X-ray background intensity, and the quasar age and spectral shape. We suggest that the observation of proximate 21-cm absorption in the spectra of radio-loud quasars at $z \gtrsim 6$ (with e.g. SKA1-low or SKA2)

could provide a route for probing the lifetimes of $z \gtrsim 6$ quasars that is complementary to Lyα near-zones and proposed analyses of quasar H II regions using 21-cm tomography (e.g. Wyithe & Loeb, 2004b; Kohler et al., 2005; Rhook & Haehnelt, 2006; Geil & Wyithe, 2008; Majumdar et al., 2012; Datta et al., 2012; Kakiichi et al., 2017; Ma et al., 2020; Davies et al., 2021). Our main conclusions are as follows:

- If allowing for a distribution of optically/UV bright lifetimes with a median of $t_{\rm Q} \simeq 10^6\,{\rm yr}$ (Morey et al., 2021), the luminosity corrected sizes of Lyα near-zones, $R_{{\rm Ly}\alpha,{\rm corr}}$, are reasonably well reproduced within the Sherwood-Relics simulations for a model with late reionization ending at $z = 5.3$. Slightly larger average lifetimes may be allowable within late reionization models (e.g. Satyavolu et al., 2022), although in the models presented here the effect is modest and differences are within the 68 per cent scatter around the predicted median $R_{{\rm Ly}\alpha}$ (compare e.g. RT-late and RT-mid in Fig. 4.8). We also confirm that the smallest Lyα near-zones at $z \simeq 6$, with quasar luminosity corrected sizes of $R_{{\rm Ly}\alpha,{\rm corr}} \lesssim 2\,{\rm pMpc}$, are consistent with optically/UV bright quasar lifetimes of $t_{\rm Q} \lesssim 10^4$–$10^5\,{\rm yr}$ in late reionization models (Eilers et al., 2017, 2021).

- We define the "21-cm near-zone" size, R_{21}, as the distance from a (radio-loud) quasar where the normalised 21-cm forest spectrum first drops below the threshold $F_{21,{\rm th}} = 0.99$ (i.e $\tau_{21} \gtrsim 10^{-2}$), after smoothing the radio spectrum with a 5 kHz boxcar filter. Detecting a strong proximate 21-cm absorber with $\tau_{21} \geq 10^{-2}$ requires a minimum source flux density of 17.2 mJy for a 1000 hour integration with SKA1-low, assuming a signal-to-noise ratio of S/N = 5 and bandwidth of

5 kHz. This decreases to 5.9 mJy for a 100 hour integration with SKA2. For comparison, the recently discovered radio-loud quasar PSO J172+18 has a 3σ upper limit on the flux density at 147.5 MHz of $S_{147.5\,\mathrm{MHz}} < 8.5\,\mathrm{mJy}$ (Bañados et al., 2021), and the blazar PSO J0309+27 at $z = 6.1$ has $S_{147\,\mathrm{MHz}} = 64.2 \pm 6.2\,\mathrm{mJy}$ (Belladitta et al., 2020). Proximate 21-cm absorption around these or similar radio-loud sources should therefore be within reach of the SKA.

- We show that for modest pre-heating of the IGM by the X-ray background, such that the IGM spin temperature $T_\mathrm{S} \lesssim 10^2\,\mathrm{K}$, strong proximate 21-cm absorption from the diffuse IGM should be present in the spectra of radio-loud quasars (see also Chapter 3). We demonstrate that R_{21} will depend on the quasar optical-to-X-ray spectral index, α_OX, and the *integrated* quasar lifetime, t_Q. In contrast, the Lyα near-zone size remains insensitive to the level of X-ray heating in the IGM. For very young quasars, R_{21} should trace the extent of the pre-existing H II regions created by galaxies clustered around the quasar host halo.

- Unlike the Lyα near-zone size – which can vary over the equilibriation timescale, $t_\mathrm{eq} \sim 10^5\,\mathrm{yr}$, for neutral hydrogen in a highly ionized IGM (e.g. Davies et al., 2020) – R_{21} is sensitive to the integrated lifetime of the quasar and will increase monotonically with quasar age. This is because the 21-cm optical depth is inversely proportional to the spin temperature of neutral hydrogen, $\tau_{21} \propto T_\mathrm{S}^{-1}$, and the neutral hydrogen will cool adiabatically on a timescale $t_\mathrm{H}/2$, where $t_\mathrm{H} \gg t_\mathrm{Q}$ is the Hubble time. A combination of R_{21} and $R_{\mathrm{Ly}\alpha}$ may therefore help sharpen constraints on quasar lifetimes if the uncertain heating

by X-rays from the quasar and X-ray background can be marginalised over.

- For quasars that exhibit unusually small luminosity corrected Lyα near-zone sizes (where evidence for a Lyα damping wing from a large neutral column in the IGM may also be limited), proximate 21-cm absorption could help distinguish between very young quasars with $t_{\rm Q} < 10^4$–$10^5\,{\rm yr}$, or older quasars that have experienced episodic accretion. We find that proximate 21-cm absorption from the diffuse IGM is only expected within a few proper Mpc of the quasar systemic redshift for very young objects. Such short lifetimes may point toward massive black hole seeds (e.g. Loeb & Rasio, 1994; Dijkstra et al., 2008; Regan et al., 2017) and radiatively inefficient, mildly super-Eddington accretion (Madau et al., 2014; Davies et al., 2019). Larger values of R_{21} coupled with small Lyα near-zones with $R_{{\rm Ly}\alpha,{\rm corr}} \lesssim 2\,{\rm pMpc}$ would instead be consistent with time-variable black hole growth occurring over longer periods.

Our results provide further impetus for searching for 21-cm absorption from the diffuse IGM at high redshift. However, the caveats discussed in Chapter 3, where we focused on 21-cm absorption from the general IGM, also apply here. We have not considered any of the practical issues regarding the recovery of 21-cm absorption features from noisy data. The role of 21-cm absorption from any minihaloes that are unresolved in our simulations (i.e. minihaloes with masses $< 2.5 \times 10^7\,{\rm M}_\odot$) also remains uncertain (Meiksin, 2011; Park et al., 2016; Nakatani et al., 2020). Soft X-ray heating of the IGM by the transverse quasar proximity effect may also be an important uncertainty, particularly for the large population of faint

or obscured quasars that would be implied by short optically/UV bright quasar lifetimes and/or duty cycles. Finally, note that if the neutral IGM is already pre-heated to temperatures $T_{\rm K} \gg 10^2\,{\rm K}$ at $z \gtrsim 6$, there will be very little or no detectable 21-cm absorption from the diffuse IGM at all. Although constraints on the X-ray background and spin temperature in the IGM are still weak (Greig et al., 2021a; The HERA Collaboration, 2022a), further progress toward placing limits and/or detecting the 21-cm power spectrum should help narrow parameter space over the next decade.

Chapter 5

The effect of intergalactic medium density fluctuations on the global 21-cm signal at Cosmic Dawn

5.1 Introduction

The global 21-cm signal is usually quantified as the sky-averaged 21-cm differential brightness temperature, $\delta T_{\rm b}$. This signal contains information on structure formation and the sources of radiation throughout cosmological history, from the Dark Ages to the Epoch of Reionization (see e.g. Furlanetto et al., 2006; Pritchard & Loeb, 2012, for a review). Motivated by this, many experiments such as ASSASSIN (McKinley et al., 2020), BIGHORNS (Sokolowski et al., 2015), DAPPER (Burns et al., 2021), DSL (Chen et al., 2021), HERA (Neben et al., 2016), LEDA (Price et al., 2018), LOFAR (van Haarlem et al., 2013), PRIZM (Philip et al., 2019), SARAS 3 (Nambissan T. et al., 2021), SCI-HI (Voytek et al., 2014) and SKA (Dewdney et al.,

2009) aim to detect it at various redshifts. In addition, EDGES has reported the first measurement of the global 21-cm signal from the Cosmic Dawn at 78 MHz, corresponding to $z \approx 17$ (Bowman et al., 2018).

However, the measured shape and amplitude of the EDGES signal differs significantly from theoretical expectations. The EDGES absorption signal shows a flat bottom and sharp edges, rather than a Gaussian-like shape. The sharp edges suggest a rapid coupling of the spin temperature to the gas kinetic temperature caused by UV photons from rare massive halos (Kaurov et al., 2018). The flat bottom of the signal can be obtained from the Lyα and X-ray radiation produced by popIII stars (Mittal & Kulkarni, 2022b). Furthermore, the signal amplitude of $\delta T_{\rm b} = 500^{+200}_{-500}$ mK is 2-3 times larger than predicted (e.g. Pritchard & Loeb, 2010a; Fialkov & Loeb, 2016; Cohen et al., 2017). Various studies have proposed new physics to explain this large amplitude, namely an excess radio background (e.g. Feng & Holder, 2018; Fraser et al., 2018; Ewall-Wice et al., 2018; Fialkov & Barkana, 2019; Mittal et al., 2022) or extra cooling of the IGM driven by dark matter (e.g. Muñoz & Loeb, 2018; Fialkov et al., 2018; Houston et al., 2018; Barkana et al., 2018), both of which would increase the contrast between the 21-cm brightness temperature and the radio background temperature, and hence increase the amplitude of $\delta T_{\rm b}$.

Rather than exploring these new physics models, in this chapter we will implement a standard model where the CMB is the only source of the radio background, and only consider standard adiabatic cooling. We implement CMB heating following Venumadhav et al. (2018) and Lyα heating following Chen & Miralda-Escudé (2004) and Furlanetto & Pritchard (2006), but see also Chuzhoy & Shapiro (2007), Ghara & Mellema (2020) and Meiksin

(2021) for different implementations. We will pay particular attention to common assumptions such as the strong Lyα coupling of the spin temperature to the gas kinetic temperature. This approximation is appropriate only at later stages of reionization when there are enough Lyα photons. However, this fails at earlier times, as has been investigated in Section 3.3 for the 21-cm forest, and by Santos et al. (2008), Baek et al. (2010) and Ghara et al. (2015) for the global 21-cm signal.

In this chapter we will mainly focus on the effect of IGM density fluctuations on $\delta T_{\rm b}$. Xu et al. (2018) performed an analytical calculation of the global 21-cm signal that includes IGM density fluctuations and find a 40% reduction of the signal relative to a homogeneous IGM model. However, they assume saturated coupling of the $T_{\rm S}$ and do not model the halo clustering which would affect the density distribution of the gas. To account for the latter they use a hydrodynamical simulation tracking 2×800^3 dark matter and gas particles in $4h^{-1}$ cMpc volume (Xu et al., 2021). This decreases the discrepancy between the $\delta T_{\rm b}$ in the model with a homogeneous IGM to $\approx 15\%$. However, this work also uses the approximation of $T_{\rm S} = T_{\rm K}$. Villanueva-Domingo et al. (2020) do not use this approximation, and instead calculate the $T_{\rm S}$ considering Lyα and collisional coupling. They also use the density distribution extracted from a hydrodynamical simulation (Miralda-Escudé et al., 1996, 2000). Similarly to Xu et al. (2021), they find a decrease of the global 21-cm absorption feature amplitude of $\approx 15\%$ when including the density fluctuations when compared to the case of neglecting them. However, the simulation used in their work is based on a now disfavoured cosmology (Miralda-Escudé et al., 1996).

In this chapter we follow the $\delta T_{\rm b}$ calculation from Villanueva-Domingo

et al. (2020), but using density distributions from up to date cosmological hydrodynamical simulations drawn from Sherwood-Relics simulation suite (Puchwein et al., 2022). We present the density distributions used in this work and examine how they affect the global 21-cm signal in Section 5.2 and 5.3, respectively. We conclude in Section 5.4.

5.2 Density distribution of the intergalactic medium at Cosmic Dawn

Following Villanueva-Domingo et al. (2020) We use a probability density function (PDF) for the density distributions of the form

$$P(\Delta) = A\Delta^{-\beta}\exp\left(-\frac{\left(\Delta^{-2/3} - \mathrm{C}_0\right)^2}{2\left(2\delta_0/3\right)^2}\right), \tag{5.1}$$

which fits well with the L10 simulation in Miralda-Escudé et al. (1996), as discussed by Miralda-Escudé et al. (2000). For consistency with the literature, we will refer to this simulation as MHR00.

The combination of A and C_0 are found by using the probability normalization

$$\int_0^\infty d\Delta P(\Delta) = 1, \tag{5.2}$$

and mass normalization

$$\int_0^\infty d\Delta\Delta P(\Delta) = 1. \tag{5.3}$$

Table 5.1: Hydrodynamical simulation with different mass resolution used in this chapter. All simulation volumes are $40h^{-1}$ cMpc on a side and follow the RT-mid model which is described in Section 2.1. From left to right, the columns give the number of dark matter and baryonic particles in the simulation, and the gas and dark matter particle masses.

$N_{\rm p}$	$M_{\rm gas}$ [$\rm M_\odot$]	$M_{\rm dm}$ [$\rm M_\odot$]
2×2048^3	1.47×10^5	7.92×10^5
2×1024^3	1.18×10^6	6.34×10^6
2×512^3	9.41×10^6	5.07×10^7

For MHR00 we set $\beta = 5/2$ as was done in Villanueva-Domingo et al. (2020), and find δ_0 that fits best the distributions at $z = 10$ and 30 given in their fig. 1. Then we interpolate between these values to acquire δ_0 at $10 \leq z \leq 24$, and hence obtain $P(\Delta)$ at these redshifts. Note however, the MHR00 is based on a now disfavoured cosmology which assumes $\Omega_\Lambda = 0.6$, $\Omega_{\rm m} = 0.4$, $\Omega_{\rm b} = 0.0355$, $\sigma_8 = 0.79$, $n_{\rm s} = 0.96$ and $h = 0.65$.

Therefore, we also apply the analyses described in Villanueva-Domingo et al. (2020) using simulations with more up to date cosmology drawn from the Sherwood-Relics simulation suite (Puchwein et al., 2022). Particularly, we use the RT-mid simulation which incorporates cosmology consistent with Planck Collaboration (2014), i.e. $\Omega_\Lambda = 0.692$, $\Omega_{\rm m} = 0.308$, $\Omega_{\rm b} = 0.0482$, $\sigma_8 = 0.829$, $n_{\rm s} = 0.961$ and $h = 0.678$. We would expect that the reionization history should have no effect on the results in this chapter given that we explore the pre-reionization era. This simulation has a $(40h^{-1}\,\text{cMpc})^3$ volume, a cell size of $\approx 19.5h^{-1}$ ckpc and tracks 2×2048^3 dark matter and baryon particles (see Section 2.1 for more details). We also use identical simulations except they track 2×1024^3 and 2×512^3 particles. These configurations result in a gas particle mass of $M_{\rm gas} = 1.47 \times 10^5\,\rm M_\odot$, $1.18 \times 10^6\,\rm M_\odot$ and $9.41 \times 10^6\,\rm M_\odot$ and a dark matter

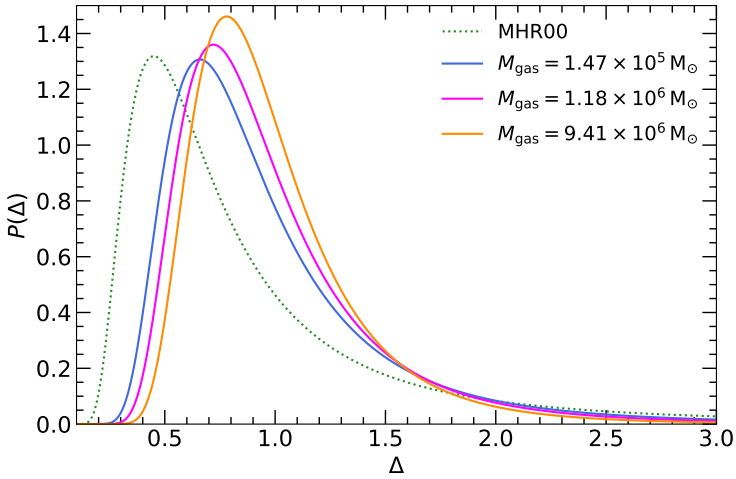

Figure 5.1: Density PDF defined by Eq. (5.1) at $z = 17$ for the MHR00 simulation (dotted green curve) and Sherwood-Relics simulations (solid curves) with different mass resolutions. All of the Sherwood-Relics simulations have a box size of $(40h^{-1}\,{\rm cMpc})^3$ but track different number of particles which results in different gas mass resolution, where $M_{\rm gas} = 1.47 \times 10^5\,{\rm M}_\odot$ (blue curve), $1.18 \times 10^6\,{\rm M}_\odot$ (fuchsia curve) and $9.41 \times 10^6\,{\rm M}_\odot$ (orange curve).

particle mass of $M_{\rm dm} = 7.92 \times 10^5\,{\rm M}_\odot$, $6.34 \times 10^6\,{\rm M}_\odot$ and $5.07 \times 10^7\,{\rm M}_\odot$, respectively. These simulations are summarized in Table 5.1. The MHR00 simulation was run with an Eulerian code in a $10h^{-1}\,{\rm cMpc}$ box with 288^3 cells, corresponding to $\approx 35h^{-1}\,{\rm ckpc}$ cell size and $6.3 \times 10^5\,{\rm M}_\odot$ average baryonic mass per cell. Therefore, in addition to a more realistic cosmology model, the Sherwood-Relics simulations used in this work are 64 times larger in volume and have better mass resolution compared to MHR00.

We vary both β and δ_0 to extract the best fit $P(\Delta)$ from the Sherwood-Relics simulations. Fig. 5.1 shows the extracted density PDFs for all 4 simulations at $z = 17$ (i.e. around the maximum of the EDGES signal (Bowman et al., 2018)). The majority of the volume of the hydrogen is in underdense regions in all 4 cases. The MHR00 (dotted green curve) density distribution peaks at $30 - 45\%$ lower density, but yields more gas

at $\Delta \gtrsim 1.9$ than Sherwood-Relics. These differences arise from changes in the cosmology and resolution. The differences between the Sherwood-Relics simulations used here are due to different mass resolution. If the simulation tracks more particles, it resolves both lower and higher density regions better which results in a broader density distribution. We have also extracted the density PDF from a $(160h^{-1}\,\mathrm{cMpc})^3$ simulation with 2×2048^3 dark matter and baryon particles. The $P(\Delta)$ from this larger volume simulation was almost identical to the $(40h^{-1}\,\mathrm{cMpc})^3$ and 2×512^3 particles simulation (orange curve in Fig. 5.1) which has the same mass resolution, and hence is not used in this study.

5.3 The global 21-cm signal at Cosmic Dawn for different density distributions

The global 21-cm signal, quantified as the differential brightness temperature, δT_b, measures the contrast between the 21-cm radiation and radio background. Neglecting redshift space distortions, one can infer δT_b at a particular gas density to be (Furlanetto et al., 2006; Pritchard & Loeb, 2012; Villanueva-Domingo et al., 2020)

$$\delta T_\mathrm{b}(\Delta) = 27 x_\mathrm{HI} \Delta \sqrt{\frac{1+z}{10}} \left(1 - \frac{T_\gamma}{T_\mathrm{S}(\Delta)}\right) \mathrm{mK}, \tag{5.4}$$

where the factor of 27 depends on cosmology, as in the case of Eq. (3.1). Given that in this chapter we focus on the pre-reionization era, we assume $x_\mathrm{HI} \simeq 1$. Also, we will consider the only source of the radio background to be the CMB, and hence $T_\gamma = T_\mathrm{CMB} = 2.73\,\mathrm{K}(1+z)$ (Fixsen, 2009).

In various studies the global 21-cm signal is calculated at the mean cosmic density (i.e. $\Delta = 1$), thus neglecting the density distribution (e.g. Mirocha, 2014; Feng & Holder, 2018; Houston et al., 2018). To include the effect of density fluctuations on the global 21-cm signal, we average Eq. (5.4) over the density which results in

$$\langle \delta T_{\rm b} \rangle = 27 x_{\rm HI} \sqrt{\frac{1+z}{10}} \left(1 - \left\langle \Delta \frac{T_\gamma}{T_{\rm S}(\Delta)} \right\rangle \right) \ {\rm mK}. \tag{5.5}$$

We see that the signal at a given redshift depends only on $\langle \Delta / T_{\rm S}(\Delta) \rangle$. If $T_{\rm S} < T_\gamma$, as is expected during the Cosmic Dawn in the case of not too strong heating, a higher density results in an enhanced signal (i.e. makes it more negative) while a higher temperature reduces it. For simplicity let us assume a power-law dependence of the spin temperature on the density, i.e. $T_{\rm S} \propto \Delta^{K_{\rm T}}$, where $K_{\rm T}$ is a constant. Hence, $\langle \delta T_{\rm b} \rangle \propto \langle \Delta / T_{\rm S}(\Delta) \rangle \propto \left\langle \Delta^{1-K_{\rm T}} \right\rangle$. If $K_{\rm T} < 1$, the signal will be stronger at higher density and vice versa. In the special cases of $K_{\rm T} = 1$ and 0 we expect the signal to be independent of the gas density due to the probability and mass normalization of $P(\Delta)$.

We start by assuming strong Lyα coupling of the spin temperature to the gas kinetic temperature and adiabatic cooling for the gas. In this scenario $T_{\rm S}(\Delta) = T_{\rm K}(\Delta) = T_{\rm ad}(\Delta) = 2.73\,{\rm K} \Delta^{2/3} \left(1+z\right)^2 / \left(1+z_{\rm dec}\right)$ where $z_{\rm dec} = 147.8$ is the redshift at which we assume the gas thermally decouples from the CMB (Furlanetto et al., 2006). We show the $T_{\rm ad}$ at cosmic mean density (dotted curve) in the right panel of Fig. 5.2. For comparison we show the CMB temperature with a dash-dotted black curve. In this scenario $K_{\rm T} = 2/3$. If the gas distribution is weighted more towards the underdense gas, the global 21-cm signal will be reduced.

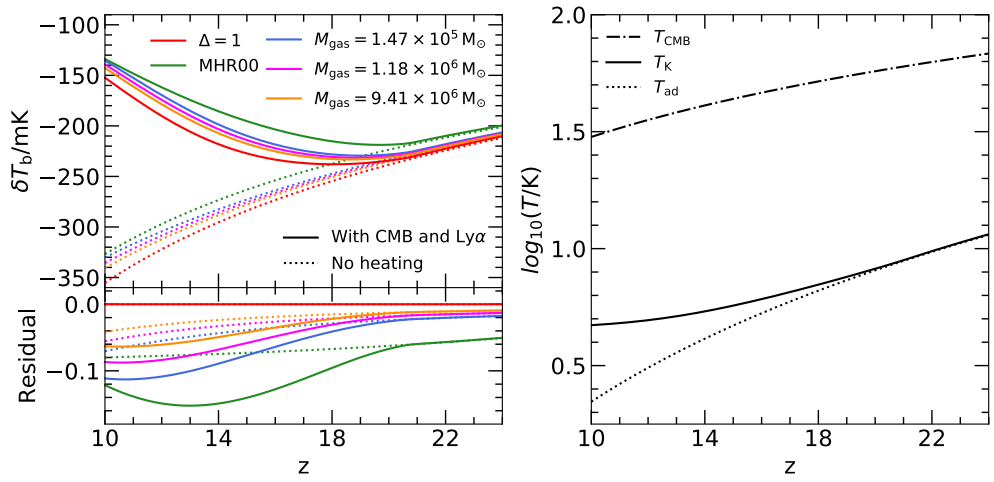

Figure 5.2: The 21-cm differential brightness temperature as a function of redshift (top left panel) in the case of no heating (dotted curves) and CMB and Lyα heating (solid curves). Red curves represent the calculation neglecting the density fluctuations. The rest of the curves assume a density PDF, with colours corresponding to Fig. 5.1. The residuals in the bottom left panel show the fractional difference between models relative to the case of neglecting the density fluctuations, i.e. $\left(\delta T_{\rm b,i} - \delta T_{\rm b}\left(\Delta = 1\right)\right)/\delta T_{\rm b}\left(\Delta = 1\right)$. We also plot the CMB temperature (dot-dashed black curve), kinetic temperature including CMB and Lyα heating (solid curve) and adiabatic temperature of the gas (dotted curve) in the right panel. The latter two are shown at the mean density.

Indeed, the signal has lower amplitude in all cases when incorporating the density fluctuations relative to the case at the cosmic mean density only (dotted red curve), as one can see in the top left panel of Fig. 5.2. We quantify this discrepancy using residuals defined as $\left(\delta T_{\rm b,i} - \delta T_{\rm b}\left(\Delta = 1\right)\right)/\delta T_{\rm b}\left(\Delta = 1\right)$ where i corresponds to the model of interest. Note that by this definition, negative residuals quantify the fractional amount of suppression of the signal in absorption relative to the model neglecting the density fluctuations. These residuals are shown in the bottom left panel of Fig. 5.2. The amplitude of the signal when including the density distribution from the $M_{\rm gas} = 9.41 \times 10^6\,{\rm M}_\odot$ simulation (dotted orange curve) is suppressed by 0.9% at $z = 24$ relative to the $\Delta = 1$

calculation, as shown in the bottom left panel of Fig. 5.2. At $z = 10$ this increases to 4.1%. This increases with the density distribution being shifted towards lower values as the mass resolution increases. For example, the simulation with 8 times more particles (dotted fuchsia curve) results in 1.3% and 5.5% suppression at $z = 24$ and 10, respectively. This further increases to 1.7% and 7.0% suppression at $z = 24$ and 10, respectively, for our highest resolution simulation with $M_{\rm gas} = 1.47 \times 10^5\,{\rm M}_\odot$ (dotted blue curve). For completeness, we also show $\delta T_{\rm b}$ using the MHR00 simulation (dotted green curve). This reaches a suppression of 8% while Villanueva-Domingo et al. (2020) reports a difference of $\sim 10\%$. This is caused by the fact that they assume $T_{\rm ad} \simeq 8\,{\rm K}\,((1+{\rm z})/20)^2\,\Delta^{2/3}$, which results in a slightly higher value which in turn decreases the amplitude of the $\delta T_{\rm b}$.

5.3.1 Including heating by CMB and Lyα radiation

In addition to the $T_{\rm S}$ coupling to the Lyα colour temperature by Lyα photons, these photons also heat the IGM. Here we include two heating mechanisms following Venumadhav et al. (2018) for the CMB and Chen & Miralda-Escudé (2004) for the Lyα radiation, as in Chapter 2. However, in this chapter we set the redshift at which the sources turn on to $z_* = 21$ to tune my model such that the lower frequency edge of the global 21-cm absorption feature is located approximately at the same redshift as the EDGES signal, which is at $z \approx 19.5 - 22$ (Bowman et al., 2018). The right panel of Fig. 5.2 shows the evolution of the gas kinetic temperature at the mean density including these two heating mechanisms (solid black curve).

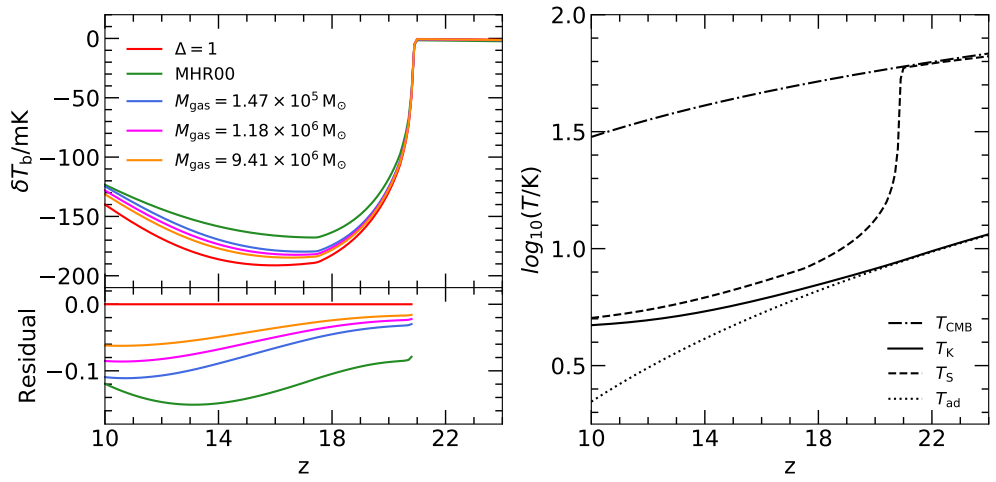

Figure 5.3: Same as Fig. 5.2 with the CMB and Lyα heating, but now applying a full calculation of T_S (added in the right panel, dashed line) instead of assuming strong Lyα coupling.

As the T_K deviates more from the T_{ad} and gets closer to the T_{CMB} over time, the signal becomes weaker relative to the no heating case displayed in the top left panel of Fig. 5.2. Including these two heating mechanisms boosts the difference between the calculation where density fluctuations are neglected by up to 15.2% for the MHR00 simulation (solid green curve) and [6.4%, 8.6%, 11.3%] for our $M_{gas} = [9.41 \times 10^6,\ 1.18 \times 10^6,\ 1.47 \times 10^5]$ $M_\odot$ simulations (solid [orange, fuchsia, blue] curve). Even though in this scenario the temperature dependence on density is nontrivial and cannot be expressed as a single power-law, T_K monotonically rises with Δ slower than it would with $K_T = 1$. Therefore, the absorption signal is stronger for a density distribution which is weighted more towards higher values as, discussed in detail in Section 5.2.

Now we will perform the full calculation of T_S as described in Section 3.2 including both the collisional and Lyα coupling. We show this evolution of T_S in the right panel of Fig. 5.3 (dashed curve). $T_S \approx T_{CMB}$ until the

Lyα background is generated at $z_* = 21$. Afterwards, T_S decouples from the CMB temperature and gradually couples to T_K via the Lyα photons. Even at later times T_S is slightly larger than T_K as the spin temperature partially couples to T_CMB.

As a result, δT_b is suppressed even more than in the saturated Lyα coupling case as seen in the top left panel of Fig. 5.3. However, the fractional difference between the models does not change significantly with the inclusion of the full T_S calculation, as seen in the bottom left panel. Note that at $z \gtrsim 21$, $\delta T_\mathrm{b} \approx 0$ and the residuals tend to infinity. Therefore, we exclude the residuals where $\delta T_\mathrm{b}(\Delta = 1) \geq -20\,\mathrm{mK}$ because at these values the absolute difference between the models is comparable to the δT_b.

5.3.2 Including heating by X-ray radiation

Finally, we include photo-heating by the soft X-ray background. We follow the modelling in Section 2.2 to do so. The top right panel of Fig. 5.4 shows the T_K (solid curves) and T_S (dashed curves) redshift evolution for three different X-ray efficiencies, specifically $f_\mathrm{X} = 0.1$ (brown curves), 1 (indigo curves) and 10 (cyan curves). We show the signal and corresponding residuals for these three X-ray efficiencies in the top left, bottom left and bottom right panel, respectively. Including the X-ray background causes the gas temperature to increase earlier. Hence, the gas does not reach as low temperatures as in the case of no X-ray background radiation, resulting in a shallower absorption feature. In addition, the bottom of the absorption feature is shifted to higher redshift due to this additional heating decreasing the difference between T_CMB and T_S earlier. The timing of the first drop in

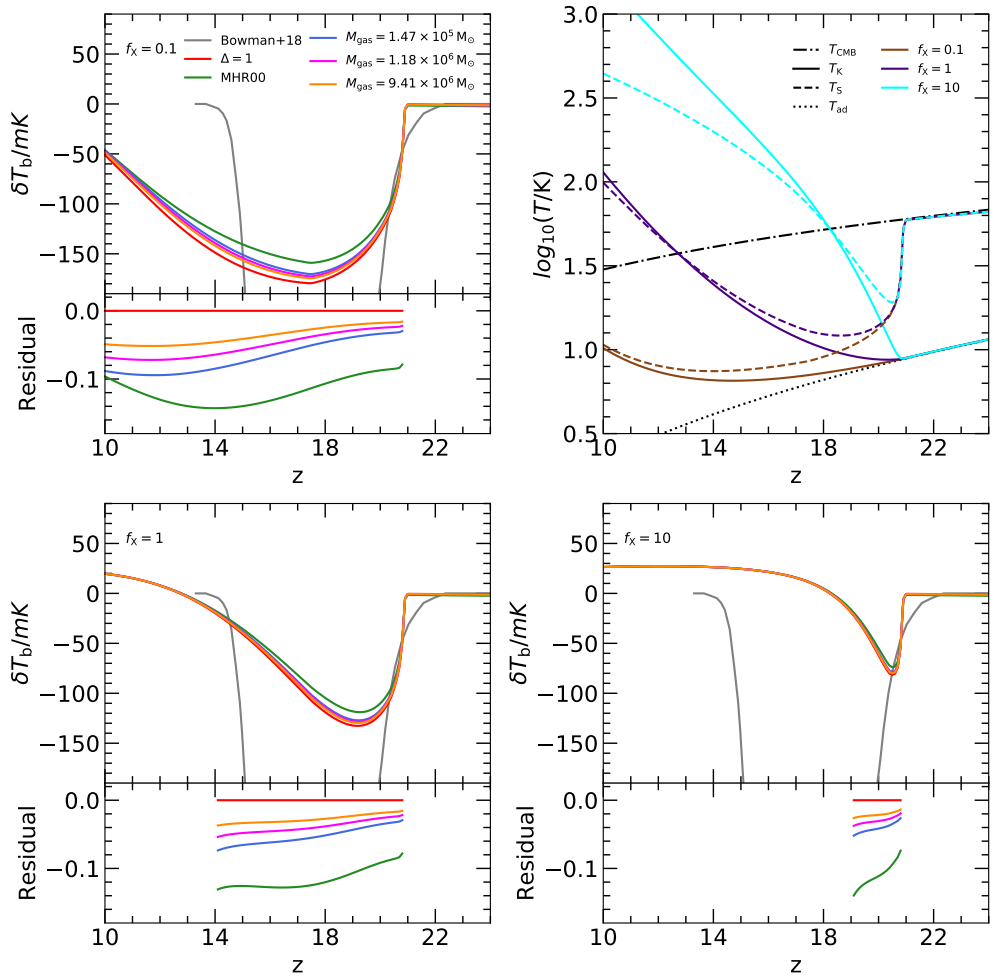

Figure 5.4: Same as Fig. 5.3 but including soft X-ray background radiation with $f_X = 0.1$ (top left panel), 1 (bottom left panel) and 10 (bottom right panel). We also include the best fit model to the measurement by EDGES (Bowman et al., 2018) shown as the grey curve. In addition to the CMB temperature (dash-dotted black curve) and the adiabatic temperature at $\Delta = 1$ (dotted black curve), the top right panel shows the gas kinetic (solid curves) and spin (dashed curves) temperature at cosmic mean density for $f_X = 0.1$ (brown curves), 1 (indigo curves) and 10 (cyan curves).

the δT_b in our models broadly agrees with the model profile recovered from the EDGES observations (Bowman et al., 2018) by design, which is shown as the solid grey line. However, the amplitude and shape of the signal is not reproduced by these models. The inclusion of extra cooling (e.g. Muñoz &

Loeb, 2018; Fialkov et al., 2018), and excess radio background (e.g. Feng & Holder, 2018; Mittal et al., 2022) or star formation densities for popIII stars (Mittal & Kulkarni, 2022b) could alleviate this issue, but we leave this analysis for future work.

The discrepancies between the $\Delta = 1$ case and the cases incorporating density fluctuations decrease only by $\approx 1 - 2\%$ if we include the $f_{\rm X} = 0.1$ X-ray background. In the cases of higher $f_{\rm X}$ the gas kinetic temperature and spin temperature rise above the CMB temperature in the redshift range studied here, as seen in the top right panel of Fig. 5.4. At this point the signal switches from absorption to emission and hence the residuals are high due to $\delta T_{\rm b}$ being very small. Therefore, similarly to Fig. 5.3, we truncate the residuals at $z \approx 14$ and 19 for $f_{\rm X} = 1$ and 10, respectively.

When the global 21-cm signal is in emission, the $T_{\rm S}$ dependence on Δ becomes much weaker and hence the expected value in the negative term in the right hand side of Eq. (5.5) will be almost the same for any $P(\Delta)$ due to the mass normalization. This results in negligible differences between the density distribution models in the emission part of the $\delta T_{\rm b}$ evolution.

5.4 Conclusions

In this chapter we have investigated how density fluctuations affect the global 21-cm signal at Cosmic Dawn. We followed the approach of Villanueva-Domingo et al. (2020) but used the density distributions from the cosmological hybrid RT/hydrodynamical simulations drawn from the Sherwood-Relics simulation suite (Puchwein et al., 2022). These use a more up-to-date cosmology compared to the Miralda-Escudé et al. (1996)

simulation used in Villanueva-Domingo et al. (2020), and have higher mass resolution.

We show that as long as the signal is in absorption and the spin temperature rises slower than linearly with the gas density, the signal will be suppressed because underdense gas occupies most of the IGM volume. This is the case for all 3 of our simulations where we found the signal reduced more as we increase the mass resolution of the simulation. This is in agreement with Xu et al. (2021). If we include CMB and Lyα heating, and perform the full calculation of $T_{\rm S}$ considering unsaturated Lyα coupling, the signal is suppressed by $6.4 - 11.3\%$ when including the density fluctuations. This is a few per cent less than the $\approx 15\%$ difference found by Villanueva-Domingo et al. (2020) and Xu et al. (2021).

These findings make the EDGES measurement of the global 21-cm signal at Cosmic Dawn even harder to explain. However, the aim of this chapter is not to reproduce this measurement, but to emphasize that the inclusion of density fluctuations is required to avoid misinterpretation of such measurements.

In this context, an obvious improvement of this work would be to include modelling of the excess radio background (e.g. Feng & Holder, 2018; Mittal et al., 2022) such that we could compare our models to the EDGES measurement. Furthermore, Xu et al. (2021) find that shock heating has a non-negligible impact on reducing the signal further. To include this effect we could use temperatures directly from our simulations instead of only extracting the density distribution from them. In addition, given the different density distributions arising from different simulation resolution, a simulation with a larger dynamic range is desirable.

Chapter 6

Conclusions and outlook

6.1 Summary of main results

In this thesis, I have used cosmological hydrodynamical and radiative transfer simulations drawn from the Sherwood-Relics simulation programme (Puchwein et al., 2022) to model the 21-cm forest and sky-averaged 21-cm spectrum signal. The main focus of this thesis is to explore how the 21-cm signal could be affected by a novel patchy reionization model in which reionization ends late (i.e. $z_{\rm R} = 5.3$). Such a model is supported by recent Lyα absorption observations (e.g. Becker et al., 2015b; Kulkarni et al., 2019; Bosman et al., 2022). I post-process the Sherwood-Relics simulations to include Lyα and X-ray background heating. This allows me to explore a wide parameter space. While current measurements of the high redshift 21-cm signal are limited to upper limits on the 21-cm power spectrum (e.g. The HERA Collaboration, 2022b) and a single global 21-cm signal detection (Bowman et al., 2018), many more observations are expected in the near future from facilities such as LOFAR (van Haarlem

et al., 2013) and SKA (Dewdney et al., 2009), to name two. Therefore, theoretical modelling of various probes based on the 21-cm line are vital to guide the observational strategies of these telescopes and the interpretation of the data they collect.

The main questions which I address in this thesis and my key findings are summarized below:

Q1: What are the prospects of detecting the 21-cm forest signal if reionization ends late?

If reionization is completed at $z_{\rm R} = 5.3$, large islands of neutral hydrogen are expected at $z \sim 6$. I explore the possibility of detecting strong 21-cm forest absorption ($\tau_{21} \gtrsim 10^{-2}$) arising from these neutral regions in Chapter 3. The strongest 21-cm absorbers, while rare relative to the bulk of the IGM, originate from cold, diffuse gas with densities $3 < \Delta < 10$. Furthermore, I find that the pressure smoothing caused by the patchiness of reionization has a modest effect on the observability of the 21-cm forest absorbers. The spin temperature coupling via Lyα photons and redshift space distortions have a more significant effect (Semelin, 2016) with the latter boosting the maximum τ_{21} by up to a factor of ~ 10. However, the biggest impact on the observability of the 21-cm forest signal is the heating of the pre-reionization IGM by the soft X-ray background (Xu et al., 2011; Mack & Wyithe, 2012). I find that strong 21-cm absorption features are detectable by SKA and (potentially) LOFAR at $z = 6$ if reionization ends late and the gas is pre-heated only modestly (i.e. $T_{\rm K} < 10^2\,{\rm K}$). On the other hand, I suggest that a null-detection of 21-cm forest absorbers of a specific strength can be used to place model-dependent constraints on the high redshift soft X-ray background radiation, which is still largely

unconstrained.

Q2: Can the 21-cm forest signal be used to constrain quasar lifetimes? Supermassive black holes (SMBH) with masses of $\sim 10^8 - 10^9\,\mathrm{M}_\odot$ have been detected at $z > 6$ (e.g. Mortlock et al., 2011; Bañados et al., 2018a, 2021). However, recent Lyα forest near-zone sizes, $R_{\mathrm{Ly}\alpha}$, around quasars hosting SMBH, imply optically/UV bright quasar lifetimes of $\sim 10^6\,\mathrm{yr}$ on average (Morey et al., 2021) with the smallest ones ($\lesssim 2\,\mathrm{pMpc}$) implying lifetimes of $\sim 10^4 - 10^5\,\mathrm{yr}$ (e.g. Eilers et al., 2017, 2021). If SMBHs accrete the bulk of their mass at an Eddington limited rate during these optically/UV bright phases, there is not enough time for them to build up so much mass. This tension between the SMBH mass and quasar lifetime measurements can be alleviated by flickering quasar models (e.g Davies et al., 2020; Satyavolu et al., 2022). However, it is challenging to distinguish between a very young quasar and an older flickering quasar with only $R_{\mathrm{Ly}\alpha}$ measurements. In Chapter 4 I study how one can use the 21-cm forest signal in proximity to quasars as a complementary probe of quasar lifetimes. I post-process the Sherwood-Relics simulations with 1D multifrequency radiative transfer (Bolton & Haehnelt, 2007; Knevitt et al., 2014) to model the effect of quasar radiation on the IGM. I show that the 21-cm near-zone size, R_{21}, which I define as the closest point from the host quasar at which the normalized 21-cm forest spectrum, smoothed by 5 kHz, reaches $F_{21} < 0.99$, is sensitive to the quasar X-ray radiation. This is caused by the fact that R_{21} is dictated by the temperature of the IGM as opposed to $R_{\mathrm{Ly}\alpha}$, which is sensitive to the ionization state of the gas and hence UV photons. Since neutral hydrogen cools adiabatically over a scale of the Hubble time, R_{21} is also sensitive to the integrated quasar lifetime. Therefore, I show

that R_{21} in combination with $R_{\mathrm{Ly}\alpha}$ could provide new insights into quasar lifetimes, especially if heating by the quasar and background X-rays can be marginalised over. For example, a quasar that exhibits a large R_{21} coupled with a small $R_{\mathrm{Ly}\alpha}$ would suggest that the quasar is relatively old and flickering while a small R_{21} would suggest a very young quasar. Furthermore, I suggest that the measurement of R_{21} for a quasar not older than $\sim 10^4$ yr would provide information on the size of pre-existing H II region.

Q3: How do density fluctuations of the intergalactic medium affect the global 21-cm signal at cosmic dawn?

EDGES presented the first (and currently the only) detection of the sky-averaged 21-cm spectrum which was observed at the frequency corresponding to cosmic dawn (Bowman et al., 2018). The discrepancy between this observation and the prediction from standard models, particularly the larger magnitude of the observed signal relative to theoretical models, may imply shortcomings in the theoretical modelling of this signal. Villanueva-Domingo et al. (2020) showed that including density perturbations in the calculation of global 21-cm differential brightness temperature reduces the amplitude of the cosmic dawn signal. In Chapter 5 I extend their work by using density distributions extracted from the Sherwood-Relics simulations. I find that the signal amplitude is reduced as the mass resolution of simulation is increased (Xu et al., 2021). For Sherwood-Relics, the signal is suppressed by $6.4 - 11.3\%$, which is a slightly less than previously found ($\approx 15\%$, Villanueva-Domingo et al., 2020; Xu et al., 2021). This means that the discrepancy between the EDGES measurement and standard theoretical predictions is even larger if realistic density fluctuations are taken into account.

6.2 Outlook

The observations of the 21-cm forest rely on the presence of high redshift radio-loud sources. This issue has been discussed briefly in Chapter 3, and the number density of radio-loud quasars has been estimated by Saxena et al. (2017) and Bolgar et al. (2018). Recently, 9 radio-loud quasars at $z > 6$ have been detected (Belladitta et al., 2020; Ighina et al., 2021; Liu et al., 2021; Bañados et al., 2021; Endsley et al., 2022; Gloudemans et al., 2022). Encouragingly, hundreds of bright radio sources at $z > 6$ are expected to be detected by surveys including LoTSS (Shimwell et al., 2017), the GMRT all-sky radio survey at 150 MHz (Intema et al., 2017) and GLEAM (Wayth et al., 2015). In addition, WEAVE will provide spectroscopic redshift measurements for LOFAR quasars (Smith et al., 2016). With WEAVE starting measurements at the time this thesis is submitted, we can expect that the space density of extremely radio-bright quasars up to $z = 6.7$ will be known in 5 years.

Furthermore, there are more than 400 quasars identified at $z > 5.7$ (Bosman, 2022) and this number is increasing (e.g. 162 quasars recently discovered by SHELLQs (Matsuoka et al., 2022)). Both the redshift at which quasars are expected to be detected and their number will increase with surveys in the next decade. For instance, more than 100 quasars at $z > 7$ are expected to be observed by the Euclid wide survey (Euclid Collaboration, 2019) and more than 2600 quasars by the Nancy Grace Roman Space Telescope[1] at $z > 7$. Follow-up spectroscopic surveys performed by telescopes such as E-ELT (Maiolino et al., 2013) will provide high-resolution Lyα forest spectra which can lead to new findings about the

[1] https://roman.gsfc.nasa.gov, accessed 12.10.2022

epoch of reionization and high redshift quasars. Recently, high-resolution Lyα forest spectra from XQR-30[2] were used to support the late end reionization scenario (Bosman et al., 2022) and probe density fields around high redshift quasars (Chen et al., 2022b).

The first 21-cm forest observations in the spectra of high redshift radio-loud sources will be possible with observatories such as LOFAR (Ciardi et al., 2013) and SKA (Ciardi et al., 2015a). As shown in Chapter 3, the detection of strong 21-cm forest absorbers at $z \simeq 6$ would be consistent with reionization ending late and an IGM that is not pre-heated above $T_{\rm S} \sim 10^2\,{\rm K}$. LOFAR and other interferometers including GMRT, HERA and MWA are gradually decreasing the upper limits on the 21-cm power spectrum (Paciga et al., 2013; Mertens et al., 2020; Trott et al., 2020; The HERA Collaboration, 2022b), which were already used to disfavour cold reionization models (no IGM pre-heating by the X-ray background) (Greig et al., 2021a,b; The HERA Collaboration, 2022a). The upcoming SKA will have substantially larger collecting area, and hence it will provide tighter constraints and possibly a detection of the 21-cm power spectrum (Mellema et al., 2013). The future measurements of the sky-averaged 21-cm spectrum obtained by BIGHORNS (Sokolowski et al., 2015), LEDA (Price et al., 2018), NenuFAR (Mertens et al., 2021), PRIZM (Philip et al., 2019), SCI-HI (Voytek et al., 2014) and the above mentioned interferometers will decrease the systematic uncertainties inherent to single experiments and so can either confirm or disprove the EDGES measurement (Bowman et al., 2018). Singh et al. (2022) already showed that their measurement with SARAS 3 are in tension with the EDGES results. Meanwhile, new global

[2] https://xqr30.inaf.it/

21-cm signal experiments, both ground-based (e.g. ASSASSIN (McKinley et al., 2020), SITARA (Nambissan T. et al., 2022), REACH (de Lera Acedo et al., 2022)) and space-based (e.g. DAPPER (Burns et al., 2021), DARE (Burns et al., 2012), DSL (Chen et al., 2021)), are being developed.

On the theoretical modelling front, the CoDaIII (Lewis et al., 2022) and THESAN (Kannan et al., 2022) simulations incorporate models in which reionization ends at $z < 6$ and use box sizes required to sample cosmic variance ($\sim 100h^{-1}$ cMpc), as suggested by Iliev et al. (2014). Simulations with a similar box size are able to capture the rarest objects in the Universe, and hence can be used to acquire a more complete distribution of 21-cm forest absorbers. Even though these simulations reach mass resolutions of 5.1×10^4 $M_\odot$ for dark matter and 9.4×10^3 $M_\odot$ for gas, minihaloes below the atomic cooling threshold are still not resolved in simulations with such large volumes. If this technical challenge is solved, a different type of 21-cm forest absorber can be potentially studied in addition to the diffuse IGM which was explored in Chapters 3 and 4. However, photo-evaporation or star formation feedback could also substantially suppress this (Meiksin, 2011; Park et al., 2016; Nakatani et al., 2020). Perhaps the excellent scaling of the GADGET-4 code (Springel et al., 2021) could help increase the dynamic range of cosmological simulations and decrease the computational cost.

The development of new numerical models will be also driven by observations. For instance, the CoDaIII simulation has already reproduced the short mean free path of ionizing photons measured by Becker et al. (2021). Models of ionizing radiation sources can be updated in the future to better fit measurements of the ionizing photons escape fraction (e.g. Begley et al., 2022). JWST will provide information on sources of ionizing photons too.

For example, the UV luminosity function might constrain reionization models, and the UV spectral shape of the sources might aid in the modelling of the Lyα coupling of the spin temperature. A more complex forward modelling of the data (e.g. Ciardi et al., 2013; Ciardi et al., 2015b) would also be beneficial for aiding the observational strategies of the upcoming surveys.

Another direction that the simulation work can take is to go beyond the ΛCDM model. For example, various studies used analytical and numerical approaches to predict the signatures of warm dark matter on 21-cm line probes (e.g. Sitwell et al., 2014; Shimabukuro et al., 2014; Carucci et al., 2015). This work can be improved by running hydrodynamical simulations coupled to radiative transfer to model reionization in a universe with warm dark matter. Furthermore, there have been efforts to model the patchy reionization of helium in cosmological simulations (e.g. La Plante et al., 2017; Upton Sanderbeck & Bird, 2020; Eide et al., 2020; Kannan et al., 2022). Even though helium reionization takes place at lower redshifts than hydrogen reionization, it is important to understand it as it shapes the thermal evolution of the IGM at $2 \lesssim z \lesssim 5$ (Tittley & Meiksin, 2007; Puchwein et al., 2015). It can also be used as a probe of the IGM after hydrogen reionization (La Plante et al., 2018; Villasenor et al., 2022) complementary to the Lyα forest signal. Incorporating the metal enrichment of the IGM during the EoR (e.g. Madau et al., 2001; Pallottini et al., 2014; Kirihara et al., 2020) could open windows for other probes of the high redshift IGM. Promising probes of reionization complementary to the 21-cm forest are C II, C IV, O I, Mg II, Si II, Si IV and Fe II lines (e.g. Oh, 2002; Keating et al., 2014; Doughty et al., 2018; Hennawi et al., 2021; Bhagwat et al., 2022).

In conclusion, the results presented in this thesis are timely because they aid and motivate ongoing efforts to study the high-redshift 21-cm line with radio telescopes such as LOFAR and next generation observatories such as SKA. The outlook for the next decade is bright and encouraging.

Bibliography

Abareshi B., et al., 2022, arXiv e-prints, p. arXiv:2205.10939

Abbott T. M. C., et al., 2022, Phys. Rev. D, 105, 023520

Abdalla E., et al., 2022, Journal of High Energy Astrophysics, 34, 49

Abel T., Bryan G. L., Norman M. L., 2002, Science, 295, 93

Adams N. J., et al., 2022, arXiv e-prints, p. arXiv:2207.11217

Adshead P., Easther R., Pritchard J., Loeb A., 2011, J. Cosmology Astropart. Phys., 2011, 021

Aldrovandi S. M. V., Pequignot D., 1973, A&A, 25, 137

Allen S. W., Rapetti D. A., Schmidt R. W., Ebeling H., Morris R. G., Fabian A. C., 2008, MNRAS, 383, 879

Almgren A. S., Bell J. B., Lijewski M. J., Lukić Z., Van Andel E., 2013, ApJ, 765, 39

Alpher R. A., Bethe H., Gamow G., 1948, Physical Review, 73, 803

Anderson L., et al., 2012, MNRAS, 427, 3435

Anglés-Alcázar D., Faucher-Giguère C.-A., Quataert E., Hopkins P. F., Feldmann R., Torrey P., Wetzel A., Kereš D., 2017, MNRAS, 472, L109

Angulo R. E., Hahn O., 2022, Living Reviews in Computational Astrophysics, 8, 1

Arons J., McCray R., 1970, Astrophys. Lett., 5, 123

Arons J., Wingert D. W., 1972, ApJ, 177, 1

Aubert D., Teyssier R., 2008, MNRAS, 387, 295

Bañados E., et al., 2018a, Nature, 553, 473

Bañados E., Carilli C., Walter F., Momjian E., Decarli R., Farina E. P., Mazzucchelli C., Venemans B. P., 2018b, ApJ, 861, L14

Bañados E., et al., 2021, ApJ, 909, 80

Baek S., Semelin B., Di Matteo P., Revaz Y., Combes F., 2010, A&A, 523, A4

Bajtlik S., Duncan R. C., Ostriker J. P., 1988, ApJ, 327, 570

Banihashemi A., Khosravi N., Shirazi A. H., 2020, Phys. Rev. D, 101, 123521

Barger V., Gao Y., Mao Y., Marfatia D., 2009, Physics Letters B, 673, 173

Barkana R., Loeb A., 2001, Phys. Rep., 349, 125

Barkana R., Loeb A., 2005, ApJ, 626, 1

Barkana R., Outmezguine N. J., Redigol D., Volansky T., 2018, Phys. Rev. D, 98, 103005

Barry N., et al., 2019, ApJ, 884, 1

Beardsley A. P., et al., 2016, ApJ, 833, 102

Becker G. D., Bolton J. S., 2013, MNRAS, 436, 1023–1039

Becker G. D., Bolton J. S., Lidz A., 2015a, PASA, 32, e045

Becker G. D., Bolton J. S., Madau P., Pettini M., Ryan-Weber E. V., Venemans B. P., 2015b, MNRAS, 447, 3402

Becker G. D., D'Aloisio A., Christenson H. M., Zhu Y., Worseck G., Bolton J. S., 2021, MNRAS, 508, 1853

Begley R., et al., 2022, MNRAS, 513, 3510

Belladitta S., et al., 2020, A&A, 635, L7

Bennett C. L., et al., 2013, ApJS, 208, 20

Beutler F., et al., 2011, MNRAS, 416, 3017

Bhagwat A., Ciardi B., Zackrisson E., Schaye J., 2022, MNRAS

Bharadwaj S., Ali S. S., 2004, MNRAS, 352, 142

Bhattacharyya A., Alam U., Lal Pandey K., Das S., Pal S., 2019, ApJ, 876, 143

Bianco M., Giri S. K., Iliev I. T., Mellema G., 2021, MNRAS, 505, 3982

Biermann P. L., Nath B. B., Caramete L. I., Harms B. C., Stanev T., Becker Tjus J., 2014, MNRAS, 441, 1147

Blake C., et al., 2011, MNRAS, 418, 1707

Boera E., Becker G. D., Bolton J. S., Nasir F., 2019, ApJ, 872, 101

Bolgar F., Eames E., Hottier C., Semelin B., 2018, MNRAS, 478, 5564

Bolton J. S., Haehnelt M. G., 2007, MNRAS, 374, 493

Bolton J. S., Haehnelt M. G., Warren S. J., Hewett P. C., Mortlock D. J., Venemans B. P., McMahon R. G., Simpson C., 2011, MNRAS, 416, L70

Bolton J. S., Becker G. D., Raskutti S., Wyithe J. S. B., Haehnelt M. G., Sargent W. L. W., 2012, MNRAS, 419, 2880

Bolton J. S., Puchwein E., Sijacki D., Haehnelt M. G., Kim T.-S., Meiksin A., Regan J. A., Viel M., 2017, MNRAS, 464, 897

Bosman S. E. I., 2022, All z>5.7 quasars currently known, doi:10.5281/zenodo.6039724

Bosman S. E. I., Becker G. D., 2015, MNRAS, 452, 1105

Bosman S. E. I., Fan X., Jiang L., Reed S., Matsuoka Y., Becker G., Haehnelt M., 2018, MNRAS, 479, 1055

Bosman S. E. I., et al., 2022, MNRAS, 514, 55

Bouwens R. J., Illingworth G. D., Oesch P. A., Caruana J., Holwerda B., Smit R., Wilkins S., 2015, ApJ, 811, 140

Bovino S., Schleicher D. R. G., Grassi T., 2014, A&A, 561, A13

Bowman J. D., et al., 2013, PASA, 30, e031

Bowman J. D., Rogers A. E. E., Monsalve R. A., Mozdzen T. J., Mahesh N., 2018, Nature, 555, 67–70

Boyarsky A., Drewes M., Lasserre T., Mertens S., Ruchayskiy O., 2019, Progress in Particle and Nuclear Physics, 104, 1

Boylan-Kolchin M., 2022, arXiv e-prints, p. arXiv:2208.01611

Bradač M., Allen S. W., Treu T., Ebeling H., Massey R., Morris R. G., von der Linden A., Applegate D., 2008, ApJ, 687, 959

Braun R., Bonaldi A., Bourke T., Keane E., Wagg J., 2019, arXiv e-prints, p. arXiv:1912.12699

Bromm V., Loeb A., 2003, Nature, 425, 812

Bromm V., Coppi P. S., Larson R. B., 1999, ApJ, 527, L5

Brout D., et al., 2022, arXiv e-prints, p. arXiv:2202.04077

Burns J. O., et al., 2012, Advances in Space Research, 49, 433

Burns J., et al., 2021, arXiv e-prints, p. arXiv:2103.05085

Busca N. G., et al., 2013, A&A, 552, A96

Byrne R., et al., 2019, ApJ, 875, 70

Byrne R., Morales M. F., Hazelton B., Sullivan I., Barry N., Lynch C., Line J. L. B., Jacobs D. C., 2022, MNRAS, 510, 2011

Calverley A. P., Becker G. D., Haehnelt M. G., Bolton J. S., 2011, MNRAS, 412, 2543–2562

Cappelluti N., et al., 2017, ApJ, 837, 19

Carilli C. L., Gnedin N. Y., Owen F., 2002, ApJ, 577, 22

Carilli C. L., Wang R., van Hoven M. B., Dwarakanath K., Chengalur J. N., Wyithe S., 2007, AJ, 133, 2841

Carilli C. L., et al., 2010, ApJ, 714, 834

Carucci I. P., Villaescusa-Navarro F., Viel M., Lapi A., 2015, J. Cosmology Astropart. Phys., 2015, 047

Cen R., 1992, ApJS, 78, 341

Cen R., Haiman Z., 2000, ApJ, 542, L75

Chakraborty A., et al., 2021, ApJ, 907, L7

Chapman E., Jelić V., 2019, arXiv e-prints, p. arXiv:1909.12369

Chapman E., Santos M. G., 2019, MNRAS, 490, 1255

Chapman E., et al., 2012, MNRAS, 423, 2518

Chapman E., et al., 2015, in Advancing Astrophysics with the Square Kilometre Array (AASKA14). p. 5 (arXiv:1501.04429)

Chapman E., Zaroubi S., Abdalla F. B., Dulwich F., Jelić V., Mort B., 2016, MNRAS, 458, 2928

Chardin J., Puchwein E., Haehnelt M. G., 2017, MNRAS, 465, 3429

Chardin J., Kulkarni G., Haehnelt M. G., 2018, MNRAS, 478, 1065

Chen H., Gnedin N. Y., 2021a, ApJ, 911, 60

Chen H., Gnedin N. Y., 2021b, ApJ, 916, 118

Chen X., Miralda-Escudé J., 2004, ApJ, 602, 1

Chen Z., Xu Y., Wang Y., Chen X., 2019, ApJ, 885, 23

Chen X., Yan J., Deng L., Wu F., Wu L., Xu Y., Zhou L., 2021, Philosophical Transactions of the Royal Society of London Series A, 379, 20190566

Chen H., Croft R., Gnedin N. Y., 2022a, arXiv e-prints, p. arXiv:2208.13787

Chen H., et al., 2022b, ApJ, 931, 29

Chen S.-F., Vlah Z., White M., 2022c, J. Cosmology Astropart. Phys., 2022, 008

Cheng S., Yu H.-R., Inman D., Liao Q., Wu Q., Lin J., 2020, arXiv e-prints, p. arXiv:2003.03931

Chiaki G., Susa H., Hirano S., 2018, MNRAS, 475, 4378

Choudhury T. R., Paranjape A., Bosman S. E. I., 2021, MNRAS, 501, 5782

Christenson H. M., Becker G. D., Furlanetto S. R., Davies F. B., Malkan M. A., Zhu Y., Boera E., Trapp A., 2021, ApJ, 923, 87

Chuzhoy L., Shapiro P. R., 2006, ApJ, 651, 1–7

Chuzhoy L., Shapiro P. R., 2007, ApJ, 655, 843

Ciardi B., Salvaterra R., 2007, MNRAS, 381, 1137

Ciardi B., Salvaterra R., Di Matteo T., 2010, MNRAS, 401, 2635

Ciardi B., et al., 2013, MNRAS, 428, 1755

Ciardi B., Inoue S., Mack K., Xu Y., Bernardi G., 2015a, in Advancing Astrophysics with the Square Kilometre Array (AASKA14). p. 6 (arXiv:1501.04425)

Ciardi B., et al., 2015b, MNRAS, 453, 101

Clark P. C., Glover S. C. O., Klessen R. S., Bromm V., 2011, ApJ, 727, 110

Clesse S., García-Bellido J., 2018, Physics of the Dark Universe, 22, 137

Clowe D., Bradač M., Gonzalez A. H., Markevitch M., Randall S. W., Jones C., Zaritsky D., 2006, ApJ, 648, L109

Cohen A., Fialkov A., Barkana R., Lotem M., 2017, MNRAS, 472, 1915

Cole S., et al., 2005, MNRAS, 362, 505

Colombi S., Dodelson S., Widrow L. M., 1996, ApJ, 458, 1

Connor T., et al., 2021, ApJ, 911, 120

Conselice C. J., 2014, ARA&A, 52, 291

Corbelli E., Salucci P., 2000, MNRAS, 311, 441

Curran S. J., Whiting M. T., 2012, ApJ, 759, 117

Curran S. J., Tzanavaris P., Darling J. K., Whiting M. T., Webb J. K., Bignell C., Athreya R., Murphy M. T., 2010, MNRAS, 402, 35

D'Aloisio A., McQuinn M., Trac H., 2015, ApJ, 813, L38

D'Aloisio A., McQuinn M., Davies F. B., Furlanetto S. R., 2018, MNRAS, 473, 560–575

D'Aloisio A., McQuinn M., Maupin O., Davies F. B., Trac H., Fuller S., Upton Sanderbeck P. R., 2019, ApJ, 874, 154

D'Aloisio A., McQuinn M., Trac H., Cain C., Mesinger A., 2020, ApJ, 898, 149

Datta K. K., Friedrich M. M., Mellema G., Iliev I. T., Shapiro P. R., 2012, MNRAS, 424, 762

Davies F. B., Furlanetto S. R., 2016, MNRAS, 460, 1328

Davies F. B., et al., 2018, ApJ, 864, 142

Davies F. B., Hennawi J. F., Eilers A.-C., 2019, ApJ, 884, L19

Davies F. B., Hennawi J. F., Eilers A.-C., 2020, MNRAS, 493, 1330

Davies J. E., Croft R. A. C., Di-Matteo T., Greig B., Feng Y., Wyithe J. S. B., 2021, MNRAS, 501, 146

Davis M., Efstathiou G., Frenk C. S., White S. D. M., 1985, ApJ, 292, 371

DeBoer D. R., et al., 2017, PASP, 129, 045001

Delubac T., et al., 2015, A&A, 574, A59

Denzel P., Coles J. P., Saha P., Williams L. L. R., 2021, MNRAS, 501, 784

Dewdney P. E., Hall P. J., Schilizzi R. T., Lazio T. J. L. W., 2009, IEEE Proceedings, 97, 1482

Di Valentino E., Melchiorri A., Mena O., 2017, Phys. Rev. D, 96, 043503

Di Valentino E., et al., 2021, Classical and Quantum Gravity, 38, 153001

Dijkstra M., Haiman Z., Loeb A., 2004, ApJ, 613, 646

Dijkstra M., Haiman Z., Mesinger A., Wyithe J. S. B., 2008, MNRAS, 391, 1961

Dijkstra M., Gilfanov M., Loeb A., Sunyaev R., 2012, MNRAS, 421, 213

Dillon J. S., et al., 2014, Phys. Rev. D, 89, 023002

Dillon J. S., et al., 2015, Phys. Rev. D, 91, 123011

Dixon K. L., Iliev I. T., Mellema G., Ahn K., Shapiro P. R., 2016, MNRAS, 456, 3011

Djorgovski S. G., Castro S., Stern D., Mahabal A. A., 2001, ApJ, 560, L5

Dodelson S., Widrow L. M., 1994, Phys. Rev. Lett., 72, 17

Doughty C., Finlator K., Oppenheimer B. D., Davé R., Zackrisson E., 2018, MNRAS, 475, 4717

Dowell J., Taylor G. B., 2018, ApJ, 858, L9

Dutta R., Srianand R., 2022, MNRAS, 516, 4338

Dutta J., Nath B. B., Clark P. C., Klessen R. S., 2015, MNRAS, 450, 202

Dutta J., Sur S., Stacy A., Bagla J. S., 2020, ApJ, 901, 16

Eastwood M. W., et al., 2019, AJ, 158, 84

Eide M. B., Graziani L., Ciardi B., Feng Y., Kakiichi K., Di Matteo T., 2018, MNRAS, 476, 1174

Eide M. B., Ciardi B., Graziani L., Busch P., Feng Y., Di Matteo T., 2020, MNRAS, 498, 6083

Eilers A.-C., Davies F. B., Hennawi J. F., Prochaska J. X., Lukić Z., Mazzucchelli C., 2017, ApJ, 840, 24

Eilers A.-C., Davies F. B., Hennawi J. F., 2018, ApJ, 864, 53

Eilers A.-C., et al., 2020, ApJ, 900, 37

Eilers A.-C., Hennawi J. F., Davies F. B., Simcoe R. A., 2021, ApJ, 917, 38

Einstein A., 1917, Sitzungsberichte der Königlich Preußischen Akademie der Wissenschaften (Berlin), pp 142–152

Eisenstein D. J., et al., 2005, ApJ, 633, 560

Emberson J. D., Thomas R. M., Alvarez M. A., 2013, ApJ, 763, 146

Endsley R., Stark D. P., Chevallard J., Charlot S., 2021, MNRAS, 500, 5229

Endsley R., et al., 2022, arXiv e-prints, p. arXiv:2206.00018

Espinosa J. R., Racco D., Riotto A., 2018, Phys. Rev. Lett., 120, 121301

Essen L., Donaldson R. W., Bangham M. J., Hope E. G., 1971, Nature, 229, 110

Euclid Collaboration 2019, A&A, 631, A85

Ewall-Wice A., Dillon J. S., Mesinger A., Hewitt J., 2014, MNRAS, 441, 2476

Ewall-Wice A., et al., 2016, MNRAS, 460, 4320

Ewall-Wice A., Chang T. C., Lazio J., Doré O., Seiffert M., Monsalve R. A., 2018, ApJ, 868, 63

Ewen H. I., Purcell E. M., 1951, Nature, 168, 356

Fan X., et al., 2006, AJ, 132, 117

Farina E. P., et al., 2022, arXiv e-prints, p. arXiv:2207.05113

Feng C., Holder G., 2018, ApJ, 858, L17

Fialkov A., Barkana R., 2019, MNRAS, 486, 1763

Fialkov A., Loeb A., 2016, ApJ, 821, 59

Fialkov A., Barkana R., Visbal E., 2014, Nature, 506, 197

Fialkov A., Cohen A., Barkana R., Silk J., 2017, MNRAS, 464, 3498

Fialkov A., Barkana R., Cohen A., 2018, Phys. Rev. Lett., 121, 011101

Field G. B., 1958, Proceedings of the IRE, 46, 240

Field G. B., 1959, ApJ, 129, 551

Fields B. D., 2011, Annual Review of Nuclear and Particle Science, 61, 47

Finkelstein S. L., et al., 2019, ApJ, 879, 36

Fixsen D. J., 2009, ApJ, 707, 916

Fixsen D. J., et al., 2011, ApJ, 734, 5

Fraser S., et al., 2018, Physics Letters B, 785, 159

Freeman K. C., 1970, ApJ, 160, 811

Friedmann A., 1922, Zeitschrift fur Physik, 10, 377

Friedrich M. M., Mellema G., Alvarez M. A., Shapiro P. R., Iliev I. T., 2011, MNRAS, 413, 1353

Furlanetto S. R., 2006a, MNRAS, 370, 1867

Furlanetto S. R., 2006b, MNRAS, 371, 867

Furlanetto S. R., 2019, The Fundamentals of the 21-cm Line (arXiv:1909.13740)

Furlanetto S. R., Furlanetto M. R., 2007a, MNRAS, 374, 547

Furlanetto S. R., Furlanetto M. R., 2007b, MNRAS, 379, 130

Furlanetto S. R., Loeb A., 2002, ApJ, 579, 1

Furlanetto S. R., Oh S. P., 2008, ApJ, 681, 1

Furlanetto S. R., Pritchard J. R., 2006, MNRAS, 372, 1093

Furlanetto S. R., Stoever S. J., 2010, MNRAS, 404, 1869

Furlanetto S. R., Zaldarriaga M., Hernquist L., 2004a, ApJ, 613, 1

Furlanetto S. R., Zaldarriaga M., Hernquist L., 2004b, ApJ, 613, 16

Furlanetto S. R., Peng Oh S., Briggs F. H., 2006, Phys. Rep., 433, 181

Gaikwad P., et al., 2020, MNRAS, 494, 5091

Gamow G., 1946, Physical Review, 70, 572

Garzilli A., Theuns T., Schaye J., 2015, MNRAS, 450, 1465

Gehlot B. K., et al., 2019, MNRAS, 488, 4271

Geil P. M., Wyithe J. S. B., 2008, MNRAS, 386, 1683

Ghara R., Mellema G., 2020, MNRAS, 492, 634

Ghara R., Choudhury T. R., Datta K. K., 2015, MNRAS, 447, 1806

Ghara R., et al., 2020, MNRAS, 493, 4728

Gilfanov M., Grimm H. J., Sunyaev R., 2004, MNRAS, 347, L57

Giri S. K., Mellema G., Dixon K. L., Iliev I. T., 2018, MNRAS, 473, 2949

Giri S. K., Mellema G., Aldheimer T., Dixon K. L., Iliev I. T., 2019, MNRAS, 489, 1590

Giri S., Mellema G., Jensen H., 2020, The Journal of Open Source Software, 5, 2363

Gloudemans A. J., et al., 2022, arXiv e-prints, p. arXiv:2210.01811

Gnedin N. Y., 2014, ApJ, 793, 29

Gnedin N. Y., 2016, ApJ, 833, 66

Gnedin N. Y., Abel T., 2001, New Astron., 6, 437

Gnedin N. Y., Hui L., 1998, MNRAS, 296, 44

Gnedin N. Y., Madau P., 2022, arXiv e-prints, p. arXiv:2208.02260

Goldenberg H. M., Kleppner D., Ramsey N. F., 1960, Phys. Rev. Lett., 5, 361

Goldstein Samuel J. J., 1963, ApJ, 138, 978

Grazian A., et al., 2017, A&A, 602, A18

Greig B., Mesinger A., 2015, MNRAS, 449, 4246

Greig B., Mesinger A., Haiman Z., Simcoe R. A., 2017, MNRAS, 466, 4239

Greig B., Mesinger A., Bañados E., 2019, MNRAS, 484, 5094

Greig B., Trott C. M., Barry N., Mutch S. J., Pindor B., Webster R. L., Wyithe J. S. B., 2021a, MNRAS, 500, 5322

Greig B., et al., 2021b, MNRAS, 501, 1

Greig B., Mesinger A., Davies F. B., Wang F., Yang J., Hennawi J. F., 2022, MNRAS, 512, 5390

Grieb J. N., et al., 2017, MNRAS, 467, 2085

Griest K., 1993, in Akerlof C. W., Srednicki M. A., eds, Vol. 688, Texas/PASCOS '92: Relativistic Astrophysics and Particle Cosmology. p. 390 (arXiv:hep-ph/9303253), doi:10.1111/j.1749-6632.1993.tb43912.x

Grissom R. L., Ballantyne D. R., Wise J. H., 2014, A&A, 561, A90

Gu J., Xu H., Wang J., An T., Chen W., 2013, ApJ, 773, 38

Gunn J. E., Peterson B. A., 1965, ApJ, 142, 1633

Gupta N., Srianand R., Noterdaeme P., Petitjean P., Muzahid S., 2013, A&A, 558, A84

Guth A. H., 1981, Phys. Rev. D, 23, 347

Guth A. H., Pi S. Y., 1982, Phys. Rev. Lett., 49, 1110

Haardt F., Madau P., 1996, ApJ, 461, 20

Haehnelt M. G., Natarajan P., Rees M. J., 1998, MNRAS, 300, 817

Harker G., et al., 2010, MNRAS, 405, 2492

Hassan S., Davé R., Mitra S., Finlator K., Ciardi B., Santos M. G., 2018, MNRAS, 473, 227

Hawking S. W., 1982, Physics Letters B, 115, 295

Hennawi J. F., Davies F. B., Wang F., Oñorbe J., 2021, MNRAS, 506, 2963

Heymans C., et al., 2021, A&A, 646, A140

Hirano S., Hosokawa T., Yoshida N., Umeda H., Omukai K., Chiaki G., Yorke H. W., 2014, ApJ, 781, 60

Hirata C. M., 2006, MNRAS, 367, 259

Hong S. E., Jeong D., Hwang H. S., Kim J., 2021, ApJ, 913, 76

Hopkins P. F., Hernquist L., Martini P., Cox T. J., Robertson B., Di Matteo T., Springel V., 2005, ApJ, 625, L71

Hosokawa T., Omukai K., Yoshida N., Yorke H. W., 2011, Science, 334, 1250

Hosokawa T., Yorke H. W., Inayoshi K., Omukai K., Yoshida N., 2013, ApJ, 778, 178

Hou S. Q., He J. J., Parikh A., Kahl D., Bertulani C. A., Kajino T., Mathews G. J., Zhao G., 2017, ApJ, 834, 165

Houston N., Li C., Li T., Yang Q., Zhang X., 2018, Phys. Rev. Lett., 121, 111301

Hsyu T., Cooke R. J., Prochaska J. X., Bolte M., 2020, ApJ, 896, 77

Hubble E., 1929, Proceedings of the National Academy of Science, 15, 168

Hutter A., Dayal P., Yepes G., Gottlöber S., Legrand L., Ucci G., 2021, MNRAS, 503, 3698

Ighina L., Belladitta S., Caccianiga A., Broderick J. W., Drouart G., Moretti A., Seymour N., 2021, A&A, 647, L11

Iliev I. T., Mellema G., Pen U. L., Merz H., Shapiro P. R., Alvarez M. A., 2006, MNRAS, 369, 1625

Iliev I. T., Mellema G., Ahn K., Shapiro P. R., Mao Y., Pen U.-L., 2014, MNRAS, 439, 725

Inayoshi K., Visbal E., Haiman Z., 2020, ARA&A, 58, 27

Intema H. T., Jagannathan P., Mooley K. P., Frail D. A., 2017, A&A, 598, A78

Ioka K., Mészáros P., 2005, ApJ, 619, 684

Ishimoto R., et al., 2020, ApJ, 903, 60

Ishiyama T., et al., 2021, MNRAS, 506, 4210

Jaacks J., Thompson R., Finkelstein S. L., Bromm V., 2018, MNRAS, 475, 4396

Jana R., Nath B. B., Biermann P. L., 2019, MNRAS, 483, 5329

Jansky K., 1932, Proceedings of the Institute of Radio Engineers, 20, 1920

Jansky K., 1933, Proceedings of the Institute of Radio Engineers, 21, 1387

Jansky K., 1935, Proceedings of the Institute of Radio Engineers, 23, 1158

Jansky K., 1937, Proceedings of the Institute of Radio Engineers, 25, 1517

Jeffrey N., et al., 2021, MNRAS, 505, 4626

Jelić V., et al., 2008, MNRAS, 389, 1319

Jelić V., Zaroubi S., Labropoulos P., Bernardi G., de Bruyn A. G., Koopmans L. V. E., 2010, MNRAS, 409, 1647

Jiang L., et al., 2022, Nature Astronomy, 6, 850

Jungman G., Kamionkowski M., Griest K., 1996, Phys. Rep., 267, 195

Kadota K., Sekiguchi T., Tashiro H., 2021, Phys. Rev. D, 103, 023521

Kadota K., Villanueva-Domingo P., Ichiki K., Hasegawa K., 2022, arXiv e-prints, p. arXiv:2209.01305

Kakiichi K., et al., 2017, MNRAS, 471, 1936

Kannan R., Garaldi E., Smith A., Pakmor R., Springel V., Vogelsberger M., Hernquist L., 2022, MNRAS, 511, 4005

Kapteyn J. C., 1922, ApJ, 55, 302

Kariuki Chege J., Jordan C. H., Lynch C., Trott C. M., Line J. L. B., Pindor B., Yoshiura S., 2022, arXiv e-prints, p. arXiv:2207.12090

Kashino D., Lilly S. J., Shibuya T., Ouchi M., Kashikawa N., 2020, ApJ, 888, 6

Katz N., Weinberg D. H., Hernquist L., 1996, ApJS, 105, 19

Kaur H. D., Gillet N., Mesinger A., 2020, MNRAS, 495, 2354

Kaurov A. A., Venumadhav T., Dai L., Zaldarriaga M., 2018, ApJ, 864, L15

Keating L. C., Haehnelt M. G., Becker G. D., Bolton J. S., 2014, MNRAS, 438, 1820

Keating L. C., Haehnelt M. G., Cantalupo S., Puchwein E., 2015, MNRAS, 454, 681

Keating L. C., Puchwein E., Haehnelt M. G., 2018, MNRAS, 477, 5501

Keating L. C., Weinberger L. H., Kulkarni G., Haehnelt M. G., Chardin J., Aubert D., 2020, MNRAS, 491, 1736

Kern N. S., Liu A., Parsons A. R., Mesinger A., Greig B., 2017, ApJ, 848, 23

Khrykin I. S., Hennawi J. F., Worseck G., 2019, MNRAS, 484, 3897

Khrykin I. S., Hennawi J. F., Worseck G., Davies F. B., 2021, MNRAS, 505, 649

Kim H.-S., Wyithe J. S. B., Park J., Lacey C. G., 2013, MNRAS, 433, 2476

King A., Nixon C., 2015, MNRAS, 453, L46

Kirihara T., Hasegawa K., Umemura M., Mori M., Ishiyama T., 2020, MNRAS, 491, 4387

Knevitt G., Wynn G. A., Power C., Bolton J. S., 2014, MNRAS, 445, 2034

Kohler K., Gnedin N. Y., Miralda-Escudé J., Shaver P. A., 2005, ApJ, 633, 552

Kolopanis M., et al., 2019, ApJ, 883, 133

Kondapally R., et al., 2021, A&A, 648, A3

Koopmans L., et al., 2015, in Advancing Astrophysics with the Square Kilometre Array (AASKA14). p. 1 (arXiv:1505.07568), doi:10.22323/1.215.0001

Kuhlen M., Madau P., Montgomery R., 2006, ApJ, 637, L1

Kulkarni G., Hennawi J. F., Oñorbe J., Rorai A., Springel V., 2015, ApJ, 812, 30

Kulkarni G., Choudhury T. R., Puchwein E., Haehnelt M. G., 2017, MNRAS, 469, 4283

Kulkarni G., Keating L. C., Haehnelt M. G., Bosman S. E. I., Puchwein E., Chardin J., Aubert D., 2019, MNRAS, 485, L24

Kumar S., 2021, Physics of the Dark Universe, 33, 100862

Kumar S., Nunes R. C., 2016, Phys. Rev. D, 94, 123511

La Plante P., Trac H., Croft R., Cen R., 2017, ApJ, 841, 87

La Plante P., Trac H., Croft R., Cen R., 2018, ApJ, 868, 106

Labbé I., et al., 2022, arXiv e-prints, p. arXiv:2207.12446

Lee K.-G., Cen R., Gott J. Richard I., Trac H., 2008, ApJ, 675, 8

Lehmer B. D., et al., 2016, ApJ, 825, 7

Lemaître G., 1927, Annales de la Société Scientifique de Bruxelles, 47, 49

Lewis J. S. W., et al., 2020, MNRAS, 496, 4342

Lewis J. S. W., et al., 2022, MNRAS, 516, 3389

Li W., et al., 2019, ApJ, 887, 141

Lidz A., Oh S. P., Furlanetto S. R., 2006, ApJ, 639, L47

Lidz A., McQuinn M., Zaldarriaga M., Hernquist L., Dutta S., 2007, ApJ, 670, 39

Lin Y., Oh S. P., Furlanetto S. R., Sutter P. M., 2016, MNRAS, 461, 3361

Lin M.-X., Raveri M., Hu W., 2019, Phys. Rev. D, 99, 043514

Linde A. D., 1982, Physics Letters B, 108, 389

Liszt H., 2001, A&A, 371, 698

Liu A., Parsons A. R., 2016, MNRAS, 457, 1864

Liu Y., et al., 2021, ApJ, 908, 124

Loeb A., Rasio F. A., 1994, ApJ, 432, 52

Lukić Z., Stark C. W., Nugent P., White M., Meiksin A. A., Almgren A., 2015, MNRAS, 446, 3697

Lusso E., et al., 2010, A&A, 512, A34

Lusso E., Worseck G., Hennawi J. F., Prochaska J. X., Vignali C., Stern J., O'Meara J. M., 2015, MNRAS, 449, 4204

Ma Q.-B., Ciardi B., Kakiichi K., Zaroubi S., Zhi Q.-J., Busch P., 2020, ApJ, 888, 112

Mack K. J., Wyithe J. S. B., 2012, MNRAS, 425, 2988

Madau P., Dickinson M., 2014, ARA&A, 52, 415

Madau P., Efstathiou G., 1999, ApJ, 517, L9

Madau P., Haardt F., 2015, ApJ, 813, L8

Madau P., Rees M. J., 2000, ApJ, 542, L69

Madau P., Meiksin A., Rees M. J., 1997, ApJ, 475, 429

Madau P., Ferrara A., Rees M. J., 2001, ApJ, 555, 92

Madau P., Haardt F., Dotti M., 2014, ApJ, 784, L38

Maiolino R., et al., 2013, arXiv e-prints, p. arXiv:1310.3163

Majumdar S., Bharadwaj S., Choudhury T. R., 2012, MNRAS, 426, 3178

Majumdar S., Kamran M., Pritchard J. R., Mondal R., Mazumdar A., Bharadwaj S., Mellema G., 2020, MNRAS, 499, 5090

Mao Y., Tegmark M., McQuinn M., Zaldarriaga M., Zahn O., 2008, Phys. Rev. D, 78, 023529

Mao Y., Shapiro P. R., Mellema G., Iliev I. T., Koda J., Ahn K., 2012, MNRAS, 422, 926

Markevitch M., Gonzalez A. H., Clowe D., Vikhlinin A., Forman W., Jones C., Murray S., Tucker W., 2004, ApJ, 606, 819

Martini P., 2004, in Ho L. C., ed., Coevolution of Black Holes and Galaxies. p. 169 (arXiv:astro-ph/0304009)

Maselli A., Gallerani S., Ferrara A., Choudhury T. R., 2007, MNRAS, 376, L34

Mason C. A., Treu T., Dijkstra M., Mesinger A., Trenti M., Pentericci L., de Barros S., Vanzella E., 2018, ApJ, 856, 2

Mason C. A., et al., 2019, MNRAS, 485, 3947

Matsuoka Y., et al., 2018, ApJ, 869, 150

Matsuoka Y., et al., 2022, ApJS, 259, 18

Mazzucchelli C., et al., 2017, ApJ, 849, 91

McGreer I. D., Mesinger A., D'Odorico V., 2015, MNRAS, 447, 499

McKinley B., Trott C. M., Sokolowski M., Wayth R. B., Sutinjo A., Patra N., Nambissan T. J., Ung D. C. X., 2020, MNRAS, 499, 52

McQuinn M., 2012, MNRAS, 426, 1349

McQuinn M., Zahn O., Zaldarriaga M., Hernquist L., Furlanetto S. R., 2006, ApJ, 653, 815

Meiksin A., 2011, MNRAS, 417, 1480

Meiksin A., 2020, MNRAS, 491, 4884

Meiksin A., 2021, Research Notes of the American Astronomical Society, 5, 126

Mellema G., et al., 2013, Experimental Astronomy, 36, 235–318

Mertens F. G., et al., 2020, MNRAS, 493, 1662

Mertens F. G., Semelin B., Koopmans L. V. E., 2021, in Siebert A., et al., eds, SF2A-2021: Proceedings of the Annual meeting of the French Society of Astronomy and Astrophysics. pp 211–214 (arXiv:2109.10055)

Mesinger A., 2010, MNRAS, 407, 1328

Mesinger A., Furlanetto S., 2007, ApJ, 669, 663

Mesinger A., Furlanetto S. R., 2008, MNRAS, 385, 1348

Mesinger A., Furlanetto S., Cen R., 2011, MNRAS, 411, 955

Mesinger A., Greig B., Sobacchi E., 2016, MNRAS, 459, 2342

Miralda-Escudé J., Rees M. J., 1998, ApJ, 497, 21

Miralda-Escudé J., Cen R., Ostriker J. P., Rauch M., 1996, ApJ, 471, 582

Miralda-Escudé J., Haehnelt M., Rees M. J., 2000, ApJ, 530, 1

Mirocha J., 2014, MNRAS, 443, 1211

Mirocha J., Furlanetto S. R., 2019, MNRAS, 483, 1980

Mittal S., Kulkarni G., 2021, MNRAS, 503, 4264

Mittal S., Kulkarni G., 2022a, MNRAS, 510, 4992

Mittal S., Kulkarni G., 2022b, MNRAS, 515, 2901

Mittal S., Ray A., Kulkarni G., Dasgupta B., 2022, J. Cosmology Astropart. Phys., 2022, 030

Molaro M., et al., 2022, MNRAS, 509, 6119

Mondal R., et al., 2020, MNRAS, 498, 4178

Monsalve R. A., Rogers A. E. E., Bowman J. D., Mozdzen T. J., 2017, ApJ, 835, 49

Morales M. F., Hazelton B., Sullivan I., Beardsley A., 2012, ApJ, 752, 137

Morey K. A., Eilers A.-C., Davies F. B., Hennawi J. F., Simcoe R. A., 2021, ApJ, 921, 88

Mortlock D. J., et al., 2011, Nature, 474, 616

Mortlock A., et al., 2013, MNRAS, 433, 1185

Muñoz J. B., Loeb A., 2018, Nature, 557, 684

Mukhanov V. F., Chibisov G. V., 1981, Pisma v Zhurnal Eksperimentalnoi i Teoreticheskoi Fiziki, 33, 549

Mukherjee S., et al., 2020, arXiv e-prints, p. arXiv:2009.14199

Muller C. A., Oort J. H., 1951, Nature, 168, 357

Murdoch H. S., Hunstead R. W., Pettini M., Blades J. C., 1986, ApJ, 309, 19

Murray S., Greig B., Mesinger A., Muñoz J., Qin Y., Park J., Watkinson C., 2020, The Journal of Open Source Software, 5, 2582

Naidu R. P., Forrest B., Oesch P. A., Tran K.-V. H., Holden B. P., 2018, MNRAS, 478, 791

Nakatani R., Fialkov A., Yoshida N., 2020, ApJ, 905, 151

Nambissan T. J., et al., 2021, arXiv e-prints, p. arXiv:2104.01756

Nambissan T. J., McKinley B., Trott C. M., Jones J., Ung D. C. X., 2022, PASA, 39, e018

Nasir F., D'Aloisio A., 2020, MNRAS, 494, 3080

Nasir F., Bolton J. S., Becker G. D., 2016, MNRAS, 463, 2335

Natarajan P., et al., 2017, MNRAS, 468, 1962

Natwariya P. K., 2021, European Physical Journal C, 81, 394

Neben A. R., et al., 2016, ApJ, 826, 199

Nunes R. C., 2018, J. Cosmology Astropart. Phys., 2018, 052

Oñorbe J., Davies F. B., Lukić Z., Hennawi J. F., Sorini D., 2019, MNRAS, 486, 4075

Ocvirk P., et al., 2016, MNRAS, 463, 1462

Ocvirk P., et al., 2020, MNRAS, 496, 4087

Oesch P. A., et al., 2016, ApJ, 819, 129

Oh S. P., 2002, MNRAS, 336, 1021

Omukai K., Schneider R., Haiman Z., 2008, ApJ, 686, 801

Oyama Y., Shimizu A., Kohri K., 2013, Physics Letters B, 718, 1186

Paciga G., et al., 2013, MNRAS, 433, 639

Paczynski B., 1986, ApJ, 304, 1

Pagano L., Delouis J. M., Mottet S., Puget J. L., Vibert L., 2020, A&A, 635, A99

Pal A. K., Guha Sarkar T., 2016, MNRAS, 459, 3505

Pallottini A., Ferrara A., Gallerani S., Salvadori S., D'Odorico V., 2014, MNRAS, 440, 2498

Park H., Shapiro P. R., Choi J.-h., Yoshida N., Hirano S., Ahn K., 2016, ApJ, 831, 86

Parsa S., Dunlop J. S., McLure R. J., 2018, MNRAS, 474, 2904

Parsons A. R., et al., 2010, AJ, 139, 1468

Patil A. H., et al., 2017, ApJ, 838, 65

Patra N., Subrahmanyan R., Raghunathan A., Udaya Shankar N., 2013, Experimental Astronomy, 36, 319

Pawsey J. L., 1951, Nature, 168, 358

Peebles P. J. E., 1984, ApJ, 277, 470

Peebles P. J. E., Yu J. T., 1970, ApJ, 162, 815

Penzias A. A., Wilson R. W., 1965, ApJ, 142, 419

Penzias A. A., Wilson R. W., 1969, ApJ, 156, 799

Perlmutter S., et al., 1999, ApJ, 517, 565

Pezzulli E., Valiante R., Schneider R., 2016, MNRAS, 458, 3047

Philip L., et al., 2019, Journal of Astronomical Instrumentation, 8, 1950004

Planck Collaboration 2014, A&A, 571, A16

Planck Collaboration 2020, A&A, 641, A6

Pober J. C., et al., 2013, ApJ, 768, L36

Poole G. B., Angel P. W., Mutch S. J., Power C., Duffy A. R., Geil P. M., Mesinger A., Wyithe S. B., 2016, MNRAS, 459, 3025

Potter D., Stadel J., Teyssier R., 2017, Computational Astrophysics and Cosmology, 4, 2

Poulin V., Smith T. L., Karwal T., Kamionkowski M., 2019, Phys. Rev. Lett., 122, 221301

Pratt G. W., Arnaud M., Biviano A., Eckert D., Ettori S., Nagai D., Okabe N., Reiprich T. H., 2019, Space Sci. Rev., 215, 25

Price D. C., et al., 2018, MNRAS, 478, 4193

Pritchard J. R., Furlanetto S. R., 2006, MNRAS, 367, 1057

Pritchard J. R., Furlanetto S. R., 2007, MNRAS, 376, 1680

Pritchard J. R., Loeb A., 2010a, Phys. Rev. D, 82, 023006

Pritchard J., Loeb A., 2010b, Nature, 468, 772

Pritchard J. R., Loeb A., 2012, Reports on Progress in Physics, 75, 086901

Pritchard J. R., Pierpaoli E., 2008, Phys. Rev. D, 78, 065009

Puchwein E., Springel V., 2013, MNRAS, 428, 2966

Puchwein E., Bolton J. S., Haehnelt M. G., Madau P., Becker G. D., Haardt F., 2015, MNRAS, 450, 4081

Puchwein E., Haardt F., Haehnelt M. G., Madau P., 2019, MNRAS, 485, 47

Puchwein E., et al., 2022, arXiv e-prints, p. arXiv:2207.13098

Qin Y., Mesinger A., Bosman S. E. I., Viel M., 2021, MNRAS, 506, 2390

Reber G., 1940, ApJ, 91, 621

Reed S. L., et al., 2015, MNRAS, 454, 3952

Regan J. A., Visbal E., Wise J. H., Haiman Z., Johansson P. H., Bryan G. L., 2017, Nature Astronomy, 1, 0075

Reis I., Fialkov A., Barkana R., 2020, MNRAS, 499, 5993

Rhook K. J., Haehnelt M. G., 2006, MNRAS, 373, 623

Ricci C., et al., 2017, MNRAS, 468, 1273

Riess A. G., et al., 1998, AJ, 116, 1009

Riess A. G., et al., 2022, ApJ, 934, L7

Robertson B. E., Ellis R. S., Furlanetto S. R., Dunlop J. S., 2015, ApJ, 802, L19

Rosdahl J., et al., 2018, MNRAS, 479, 994

Ross H. E., Dixon K. L., Iliev I. T., Mellema G., 2017, MNRAS, 468, 3785

Rubin V. C., Ford W. Kent J., 1970, ApJ, 159, 379

Rubin V. C., Burley J., Kiasatpoor A., Klock B., Pease G., Rutscheidt E., Smith C., 1962, AJ, 67, 491

Safarzadeh M., Scannapieco E., Babul A., 2018, ApJ, 859, L18

Salpeter E. E., 1964, ApJ, 140, 796

Santos M. G., Amblard A., Pritchard J., Trac H., Cen R., Cooray A., 2008, ApJ, 689, 1–16

Santos M. G., Ferramacho L., Silva M. B., Amblard A., Cooray A., 2010, MNRAS, 406, 2421

Satyavolu S., Kulkarni G., Keating L. C., Haehnelt M. G., 2022, arXiv e-prints, p. arXiv:2209.08103

Saxena A., Röttgering H. J. A., Rigby E. E., 2017, MNRAS, 469, 4083

Schawinski K., Koss M., Berney S., Sartori L. F., 2015, MNRAS, 451, 2517

Schaye J., Theuns T., Leonard A., Efstathiou G., 1999, MNRAS, 310, 57

Schmidt M., 1965, ApJ, 141, 1295

Seiler J., Hutter A., Sinha M., Croton D., 2019, MNRAS, 487, 5739

Semelin B., 2016, MNRAS, 455, 962

Shakura N. I., Sunyaev R. A., 1973, A&A, 24, 337

Shapiro P. R., Giroux M. L., 1987, ApJ, 321, L107

Shaw A. K., Bharadwaj S., Mondal R., 2020, MNRAS, 498, 1480

Shen Y., 2021, ApJ, 921, 70

Shen Y., et al., 2007, AJ, 133, 2222

Shen X., Hopkins P. F., Faucher-Giguère C.-A., Alexander D. M., Richards G. T., Ross N. P., Hickox R. C., 2020, MNRAS, 495, 3252

Shimabukuro H., Ichiki K., Inoue S., Yokoyama S., 2014, Phys. Rev. D, 90

Shimabukuro H., Ichiki K., Kadota K., 2020, Phys. Rev. D, 102, 023522

Shimwell T. W., et al., 2017, A&A, 598, A104

Shull J. M., van Steenberg M. E., 1985, ApJ, 298, 268

Silk J., 1983, MNRAS, 205, 705

Singal J., et al., 2018, PASP, 130, 036001

Singh S., Subrahmanyan R., Shankar N. U., Rao M. S., Girish B. S., Raghunathan A., Somashekar R., Srivani K. S., 2018, Experimental Astronomy, 45, 269

Singh S., et al., 2022, Nature Astronomy, 6, 607

Sitwell M., Mesinger A., Ma Y.-Z., Sigurdson K., 2014, MNRAS, 438, 2664

Smith D. J. B., et al., 2016, in Reylé C., Richard J., Cambrésy L., Deleuil M., Pécontal E., Tresse L., Vauglin I., eds, SF2A-2016: Proceedings of the Annual meeting of the French Society of Astronomy and Astrophysics. pp 271–280 (arXiv:1611.02706)

Sokasian A., Yoshida N., Abel T., Hernquist L., Springel V., 2004, MNRAS, 350, 47

Sokolowski M., et al., 2015, PASA, 32, e004

Spinelli M., Bernardi G., Santos M. G., 2018, MNRAS, 479, 275

Springel V., 2005, MNRAS, 364, 1105

Springel V., et al., 2005, Nature, 435, 629

Springel V., Pakmor R., Zier O., Reinecke M., 2021, MNRAS, 506, 2871

Srianand R., Gupta N., Petitjean P., Noterdaeme P., Ledoux C., 2010, MNRAS, 405, 1888

Srianand R., et al., 2022, MNRAS, 516, 1339

Starobinsky A. A., 1980, Physics Letters B, 91, 99

Starobinsky A. A., 1982, Physics Letters B, 117, 175

Steffen A. T., Strateva I., Brandt W. N., Alexander D. M., Koekemoer A. M., Lehmer B. D., Schneider D. P., Vignali C., 2006, AJ, 131, 2826

Steidel C. C., Bogosavljević M., Shapley A. E., Reddy N. A., Rudie G. C., Pettini M., Trainor R. F., Strom A. L., 2018, ApJ, 869, 123

Sunyaev R. A., Zeldovich Y. B., 1970, Ap&SS, 7, 3

Swarup G., Ananthakrishnan S., Kapahi V. K., Rao A. P., Subrahmanya C. R., Kulkarni V. K., 1991, Current Science, 60, 95

Tepper-García T., 2006, MNRAS, 369, 2025

The HERA Collaboration 2022a, ApJ, 924, 51

The HERA Collaboration 2022b, ApJ, 925, 221

Theuns T., Leonard A., Efstathiou G., Pearce F. R., Thomas P. A., 1998, MNRAS, 301, 478

Thyagarajan N., 2020, ApJ, 899, 16

Tilvi V., et al., 2020, ApJ, 891, L10

Tittley E. R., Meiksin A., 2007, MNRAS, 380, 1369

Trebitsch M., et al., 2021, A&A, 653, A154

Trebitsch M., Hutter A., Dayal P., Gottlöber S., Legrand L., Yepes G., 2022, arXiv e-prints, p. arXiv:2202.02337

Trott C. M., et al., 2020, MNRAS, 493, 4711

Turner E. L., 1991, AJ, 101, 5

Upton Sanderbeck P., Bird S., 2020, MNRAS, 496, 4372

Venemans B. P., et al., 2015, ApJ, 801, L11

Venumadhav T., Dai L., Kaurov A., Zaldarriaga M., 2018, Phys. Rev. D, 98, 103513

Verner D. A., Ferland G. J., 1996, ApJS, 103, 467

Verner D. A., Ferland G. J., Korista K. T., Yakovlev D. G., 1996, ApJS, 465, 487

Viel M., Haehnelt M. G., Springel V., 2004, MNRAS, 354, 684

Viel M., Lesgourgues J., Haehnelt M. G., Matarrese S., Riotto A., 2005, Phys. Rev. D, 71, 063534

Villanueva-Domingo P., Ichiki K., 2022, PASJ

Villanueva-Domingo P., Mena O., Miralda-Escudé J., 2020, Phys. Rev. D, 101, 083502

Villasenor B., Robertson B., Madau P., Schneider E., 2022, ApJ, 933, 59

Volonteri M., Gnedin N. Y., 2009, ApJ, 703, 2113

Volonteri M., Silk J., Dubus G., 2015, ApJ, 804, 148

Voronov G., 1997, ADNDT, 65, 1

Voytek T. C., Natarajan A., Jáuregui García J. M., Peterson J. B., López-Cruz O., 2014, ApJ, 782, L9

Walther M., Oñorbe J., Hennawi J. F., Lukić Z., 2019, ApJ, 872, 13

Wang F., et al., 2019, ApJ, 884, 30

Wang F., et al., 2020, ApJ, 896, 23

Wayth R. B., et al., 2015, PASA, 32, e025

Weinberger L. H., Haehnelt M. G., Kulkarni G., 2019, MNRAS, 485, 1350

Weymann R., 1965, Physics of Fluids, 8, 2112

Whipple F. L., Greenstein J. L., 1937, Proceedings of the National Academy of Science, 23, 177

Whitney A., Ferreira L., Conselice C. J., Duncan K., 2021, ApJ, 919, 139

Wilensky M. J., Morales M. F., Hazelton B. J., Barry N., Byrne R., Roy S., 2019, PASP, 131, 114507

Willott C. J., et al., 2010, AJ, 140, 546

Wise J. H., 2019, Contemporary Physics, 60, 145

Wise J. H., Demchenko V. G., Halicek M. T., Norman M. L., Turk M. J., Abel T., Smith B. D., 2014, MNRAS, 442, 2560

Worseck G., Khrykin I. S., Hennawi J. F., Prochaska J. X., Farina E. P., 2021, MNRAS, 505, 5084

Wouthuysen S. A., 1952, AJ, 57, 31

Wu X.-B., et al., 2015, Nature, 518, 512

Wyithe J. S. B., 2008, MNRAS, 387, 469

Wyithe J. S. B., Loeb A., 2003, ApJ, 588, L69

Wyithe J. S. B., Loeb A., 2004a, Nature, 427, 815

Wyithe J. S. B., Loeb A., 2004b, Nature, 432, 194

Wyithe J. S. B., Bolton J. S., Haehnelt M. G., 2008, MNRAS, 383, 691

Xu Y., Chen X., Fan Z., Trac H., Cen R., 2009, ApJ, 704, 1396

Xu Y., Ferrara A., Chen X., 2011, MNRAS, 410, 2025

Xu Y., Yue B., Chen X., 2018, ApJ, 869, 42

Xu Y., Yue B., Chen X., 2021, ApJ, 923, 98

Yang Y., 2018, Phys. Rev. D, 98, 103503

Yang J., et al., 2020a, ApJ, 897, L14

Yang J., et al., 2020b, ApJ, 904, 26

Yoshiura S., et al., 2021, MNRAS, 505, 4775

Yu Q., Tremaine S., 2002, MNRAS, 335, 965

Yue B., Ciardi B., Scannapieco E., Chen X., 2009, MNRAS, 398, 2122

Zahn O., Lidz A., McQuinn M., Dutta S., Hernquist L., Zaldarriaga M., Furlanetto S. R., 2007, ApJ, 654, 12

Zaroubi S., 2012, ASSL, p. 45–101

Zeltyn G., Trakhtenbrot B., 2022, ApJ, 929, 21

Zhao C., et al., 2022, MNRAS, 511, 5492

Zhu Y., et al., 2022, ApJ, 932, 76

Zwaan M. A., Liske J., Péroux C., Murphy M. T., Bouché N., Curran S. J., Biggs A. D., 2015, MNRAS, 453, 1268

Zwicky F., 1933, Helvetica Physica Acta, 6, 110

Zygelman B., 2005, ApJ, 622, 1356

de Lera Acedo E., et al., 2022, Nature Astronomy, 6, 984

Šoltinský T., et al., 2021, MNRAS, 506, 5818

van Haarlem M. P., et al., 2013, A&A, 556, A2

van de Hulst H. C., 1945, Nederlandsch Tijdschrift voor Natuurkunde, 11, 210

van de Hulst H. C., 1998, ARA&A, 36, 1